

University of Louisville

ThinkIR: The University of Louisville's Institutional Repository

Electronic Theses and Dissertations

1-2021

Design for metal fused filament fabrication (DfMF3) of Ti-6Al-4V alloy.

Mohammad Qasim Shaikh
University of Louisville

Follow this and additional works at: <https://ir.library.louisville.edu/etd>



Part of the [Computer-Aided Engineering and Design Commons](#), and the [Manufacturing Commons](#)

Recommended Citation

Shaikh, Mohammad Qasim, "Design for metal fused filament fabrication (DfMF3) of Ti-6Al-4V alloy." (2021). *Electronic Theses and Dissertations*. Paper 3613.
<https://doi.org/10.18297/etd/3613>

This Doctoral Dissertation is brought to you for free and open access by ThinkIR: The University of Louisville's Institutional Repository. It has been accepted for inclusion in Electronic Theses and Dissertations by an authorized administrator of ThinkIR: The University of Louisville's Institutional Repository. This title appears here courtesy of the author, who has retained all other copyrights. For more information, please contact thinkir@louisville.edu.

DESIGN FOR METAL FUSED FILAMENT FABRICATION (DfMF³)
OF Ti-6Al-4V ALLOY

By

Mohammad Qasim Shaikh

A Dissertation

Submitted to the Faculty of the

J.B. Speed School of Engineering of the University of Louisville

in Fulfillment of the Requirements

for the Degree of

Doctor of Philosophy

in Mechanical Engineering

Department of Mechanical Engineering

University of Louisville

Louisville, Kentucky, United States

May 2021

Copyright 2021 by Mohammad Qasim Shaikh

All Rights Reserved

DESIGN FOR METAL FUSED FILAMENT FABRICATION (DfMF³)
OF Ti-6Al-4V ALLOY

By

Mohammad Qasim Shaikh

A Dissertation Approved on

April 5, 2021

by the following Dissertation Committee:

Dr. Sundar V. Atre
Dissertation Chair

Dr. Kunal H. Kate
Dissertation Member

Dr. Thomas A. Berfield
Dissertation Member

Dr. Gerald T. Grant
Dissertation Member

DEDICATION

To my mother Rabiya A. Jabbar and my late father Abdul Jabbar,
the reason for what I am today.

Thanks for supporting me through my endeavors in life
with your love, encouragement and sacrifices!

ACKNOWLEDGEMENTS

First, I owe a deep sense of gratitude to my advisor, Dr. Sundar V. Atre for his continuous support, guidance, and motivation throughout my journey as a Ph.D. student. I feel extremely grateful for the opportunity to get inspired by and learn from his vision, knowledge, and leadership. Having provided the ground to think, he always pushed me to raise the bar and strive for excellence. Dr. Atre has been a wonderful mentor and a friend forever. I would also like to thank his wife, Rachna, for her compassion and motivation as a family.

I profusely thank my committee members, Dr. Kunal H. Kate, Dr. Thomas A. Berfield and Dr. Gerald T. Grant for their invaluable time and feedback that consistently helped me enhance my research work. Dr. Kate has been a great collaborator and was supportive of several research collaborations. I will certainly cherish the wonderful time we spent working together. I am extremely thankful to Dr. Berfield for allowing me to use his laboratory facility and provide guidance on my research work. I would also to thank Dr. Grant for the opportunity of research collaboration with his dental research group and the access to his dental laboratory facility. He has always been exceptionally generous and supportive. Also, I would like to thank Dr. Vamsi K. Balla and Dr. Azim Gokce for sharing their expertise and guidance during their 1-year visit to the University of Louisville. I enjoyed all discussions and learning received from their research experience.

I offer my sincere thanks and praise to the MSC Software team, Pierre-Yves Lavertu, Casey Radigan, Dustin Souza and Kiranmayi Abburivenkata for their constant engagement and collaboration with the University of Louisville that played a crucial role in my research work. I would also like to thank Dr. Serena Graziosi from Politecnico di Milano and acknowledge her contribution through a research collaboration that constituted an important part of my thesis.

I gratefully acknowledge the funding received towards my Ph.D. from the National Aeronautics and Space Administration (NASA) and Minority Business Development Agency (MBDA) US Department of Commerce. I am thankful to each member of the NASA FABLAB team and Techshot team for giving me the opportunity to work with them and contribute to a great project. My thanks also go out to Jim Adams from the Material Powder Industries Federation (MPIF) for his generosity and support that allowed me to present at the international conference.

I must express my gratitude to Dr. Khalil Moussa, Martin Johnson, Dr. Edward Hortelano, and other colleagues at 3D Systems for their support and motivation. I acknowledge the crucial learning experience I gained working at 3D Systems, a global leader in the additive manufacturing space. Also, I thank Dr. Laurent Hazard for his trust and support during the final phase of my Ph.D. and for providing me with an opportunity to work at Solvay Specialty Polymers.

I also want to extend thanks and appreciation to my lab mates and colleagues Dr. Paramjot Singh, Dr. Subrata Deb Nath, Arulselvan Arumugham, Kavish Sudan, Saleh Khanjar, Pavankumar Ajjarapu, Dr. Anagh Deshpande, Dr. Alireza Tofangchi for their support and

help throughout my time at the University of Louisville. I also wish to sincerely thank my friends Arafat Mirza, Parag Siddique, Dr. Siva Pakanati, Dr. Sadakatali Gori for their support during the journey.

I take this opportunity to say thanks to my mother, Rabiya, and my sisters Amina, Zaitoon and Bashira for their prayers, love, encouragement, and support in my endeavors. I thank my wife Dr. Sana Amreen for keeping faith in me, being always supportive in my adventurous journey and having patience in these testing times. She has always been a source of courage and motivation; without her support, I would not have achieved this milestone. Finally, I am thankful to my 2 years old son, Khizar, for walking into my life; he has been truly a bundle of joy and a stressbuster to me during this crucial phase of life.

ABSTRACT
DESIGN FOR METAL FUSED FILAMENT FABRICATION (DfMF³)
OF Ti-6Al-4V ALLOY

Mohammad Qasim Shaikh

April 5, 2021

Additive manufacturing (AM) offers unmatched freedom of design with the ability to manufacture parts from a wide range of materials. The technology of producing three-dimensional parts by adding material layer-by-layer has become relevant in several areas for numerous industries not only for building visual and functional prototypes but also for small and medium series production. Among others, while metal AM technologies have been established as production method, their adoption has been limited by expensive equipment, anisotropy in part properties and safety concerns related to working with loose reactive metal powder. To address this challenge, the dissertation aims at developing the fundamental understanding required to print metal parts with bound metal powder filaments using an extrusion-based AM process, known as metal fused filament fabrication (MF³). MF³ of Ti-6Al-4V has been investigated, owing to significant interest in the material from aerospace and medical industries on account of their high strength-to-weight ratio, excellent corrosion resistance and biocompatibility.

To investigate the material-geometry-process interrelationship in MF³ printing, the current work looks into the process modeling and simulation, the influence of material composition

and resulting characteristics on printed part properties, effects of printing parameters and slicing strategies on part quality, and part design considerations for printability. The outcome of the work is expected to provide the basis of design for MF³ (DfMF³) that is essential to unlocking the full potential of additive manufacturing. Moreover, the layer-by-layer extrusion-based printing with the highly filled material involves several challenges associated with printability, distortion and dimensional variations, residual stresses, porosity, and complexity in dealing with support structures. Currently, a high dependency on experimental trial-and-error methods to address these challenges limits the scope and efficiency of investigations. Hence, the current work presents a framework of design for MF³ and evaluates a thermo-mechanical model for finite element simulation of the MF³ printing process for virtual analyses. The capability to estimate these outcomes allows optimization of the material composition, part design, and process parameters before getting on to the physical process, reducing time and cost.

The quantitative influence of material properties on MF³ printed part quality in terms of part deformation and dimensional variations was estimated using the simulation platform and results were corroborated by experiments. Also, a systematic procedure for sensitivity analysis has been presented that identified the most significant input parameters in MF³ from the material, geometry and process variables, and their relative influence on the print process outcome. Moreover, feasible geometry and process window were identified for supportless printing of Ti-6Al-4V lattice structures using the MF³ process, and an analytical approach has been presented to estimate the extrudate deflection at the unsupported overhangs in lattice structures. Finally, the design and fabrication of Ti-6Al-4V maxillofacial implants using MF³ technology are reported for the first time confirming the

feasibility to manufacture patient-specific implants by MF³. The outcome of the work is an enhanced understanding of material-geometry-process interrelationships in MF³ governing DfMF³ that will enable effective design and manufacturing.

TABLE OF CONTENTS

CHAPTER 1

INTRODUCTION	1
--------------------	---

CHAPTER 2

METAL FUSED FILAMENT FABRICATION (MF³) PROCESS SIMULATION:

DISTORTIONS PREDICTION AND EXPERIMENTAL VERIFICATION	10
--	----

2.1 INTRODUCTION	10
------------------------	----

2.1.1 Thermo-mechanical analysis of MF ³ process	14
---	----

2.1.2 Constitutive models	15
---------------------------------	----

2.2 METHODOLOGY	18
-----------------------	----

2.2.1 Process simulation	19
--------------------------------	----

2.2.2 Printing experiments.....	24
---------------------------------	----

2.3 RESULTS AND DISCUSSION	25
----------------------------------	----

2.3.1 Dimensional variation	27
-----------------------------------	----

2.3.2 Reverse warpage.....	33
----------------------------	----

2.3.3 Thermal history	37
-----------------------------	----

2.3.4 Residual stresses.....	40
------------------------------	----

2.4 CONCLUSIONS.....	41
----------------------	----

CHAPTER 3

PROCESS SENSITIVITY AND SIGNIFICANT PARAMETERS INVESTIGATION IN

METAL FUSED FILAMENT FABRICATION (MF ³) OF TI-6AL-4V	44
--	----

3.1	INTRODUCTION	44
3.1.1	FEA simulation of MF ³ process	49
3.2	METHODOLOGY	50
3.2.1	Sensitivity analysis.....	53
3.2.2	Input parameters	54
3.2.3	Simulation setup: Base case	57
3.3	RESULTS AND DISCUSSION	58
3.3.1	Simulation results: Base case for Design-I, Design-II & Design-III	58
3.3.2	Sensitivity Analysis.....	65
3.3.3	Identification of significant input parameters	71
3.3.4	Process sensitivity towards different geometries	80
3.4	CONCLUSIONS.....	82
CHAPTER 4		
SUPPORTLESS PRINTING OF LATTICE STRUCTURES BY METAL FUSED		
FILAMENT FABRICATION (MF ³) OF TI-6AL-4V: DESIGN AND ANALYSIS.....		
4.1	INTRODUCTION	84
4.2	MATERIAL AND METHODS.....	89
4.2.1	MF ³ printing experiments.....	89
4.2.2	Tuning of the printing parameters: effects on the printability of lattices.....	90
4.2.3	Lattice geometry parameters: effects on part deformation and relative density	93
4.2.4	MF ³ process simulation	97

4.3	RESULTS AND DISCUSSION	99
4.3.1	Effects of lattice geometry parameters	99
4.3.2	MF ³ process simulation results.....	101
4.3.3	Extrudate deflection	108
4.3.4	Sintered part quality	115
4.3.5	Multi-stacked lattice structures	117
4.4	CONCLUSIONS.....	118
CHAPTER 5		
PATIENT-SPECIFIC MAXILLOFACIAL IMPLANT USING METAL FUSED		
FILAMENT FABRICATION (MF ³): DESIGN, FABRICATION AND ANALYSIS..		
121		
5.1	INTRODUCTION	121
5.2	MATERIALS AND METHODS.....	126
5.2.1	Materials	126
5.2.2	Methods	127
5.2.3	Design of the implant	128
5.2.4	Fabrication of customized Ti-6Al-4V implant.....	134
5.2.5	Green and sintered parts characterization	137
5.2.6	MF ³ process simulation	138
5.3	RESULTS AND DISCUSSION	139
5.3.1	MF ³ printed green parts	139

5.3.2 Printing process simulations.....	140
5.3.3 Sintered Ti-6Al-4V parts characterization	143
5.4 CONCLUSIONS.....	151
CHAPTER 6	
CONCLUSIONS.....	154
CHAPTER 7	
FUTURE WORK.....	159
REFERENCES	162
APPENDIX A	
ESTIMATING POWDER-POLYMER MATERIAL PROPERTIES USED IN DESIGN FOR METAL FUSED FILAMENT FABRICATION (DfMF ³)	180
APPENDIX B-I	
SUPPLEMENTARY MATERIALS:	
PROCESS SENSITIVITY AND SIGNIFICANT PARAMETERS INVESTIGATION IN METAL FUSED FILAMENT FABRICATION (MF ³) OF TI-6AL-4V	218
APPENDIX B-II	
SUPPLEMENTARY MATERIALS:	
SUPPORTLESS PRINTING OF LATTICE STRUCTURES BY METAL FUSED FILAMENT FABRICATION (MF ³) OF TI-6AL-4V: DESIGN AND ANALYSIS.....	222
APPENDIX C-I	
RESIDUAL STRESSES IN MF ³ PRINTED PART: PREDICTIVE SIMULATION AND EXPERIMENTAL MEASUREMENT	226

APPENDIX C-II	
TEMPERATURE DISTRIBUTION AND THERMAL HISTORY IN MF ³ PRINTING: PREDICTIVE SIMULATION AND EXPERIMENTAL MEASUREMENT	244
APPENDIX C-III	
POROSITY DISRIBUTION IN MF ³ PRINTING: PREDICTIVE SIMULATION	248
APPENDIX C-IV	
MF ³ SINTERING PROCES SIMULATION: SIMUFACT ADDITIVE.....	251
APPENDIX C-V	
MF ³ PRINTING SIMULATION OF PARTS FROM NASA	259
CURRICULUM VITAE.....	262

LIST OF TABLES

Table 2.1. MF ³ printing process conditions	21
Table 2.2. Part dimension results; simulations and experiments with Ti-6Al-4V feedstock and unfilled ABS.....	30
Table 2.3. Part dimension results using compensated geometry in Iteration-II; simulations and experiments with Ti-6Al-4V feedstock and unfilled ABS.....	37
Table 3.1. Input parameters variation	55
Table 3.2. Input for the initial base case simulation	57
Table 3.3. (a) Sensitivity factors: (a) Design-I (b) Design-II (c) Design-III	66
Table 3.4. Infill pattern and print time per layer that change with variation in part wall thickness and bead width leading to variation in minimum substrate temperature	80
Table 3.5. MF ³ process sensitivity variation with part geometry, i.e. Design-I, Design-II, Design-III.....	81
Table 4.1. Processing condition-A is generally used to print Ti-6Al-4V by MF ³ for several different geometries. Condition-B identified as suitable specifically for lattice structure	91
Table 4.2. Effects of printing parameters evaluated by modifying one parameter at a time. Processing Condition-A (Table 4.1) systematically modified to print unit lattice cell. ...	93
Table 4.3. Printing parameters input for process simulation	99
Table 4.4. Part dimensions: CAD design vs. simulated part vs. printed green part	104
Table 4.5. Shrinkage relative to CAD design: simulated part vs. printed green part	105

Table 4.6. Extrudate deflection: experimental results	112
Table 4.7. Extrudate deflection: estimation vs. experimental results	114
Table 4.8. Shrinkage and relative density of sintered unit cells: element thickness 2.5 mm	116
Table 5.1. Printing process parameters	135
Table 5.2. Surface roughness of as-sintered parts.....	147
Table 5.3. Relative density and porosity.....	149
Table A.1. Material properties of Ti-6Al-4V alloy at room temperature	185
Table A.2. Experimental methods with respective ASTM standard for measuring the thermophysical properties of the binder system	186
Table A.3. Experimentally determined binder thermophysical properties	190
Table A.4. Specific heat of Ti-6Al-4V powder-binder feedstock at different filler volume fractions for different temperatures	193
Table A.5. Thermal conductivity of Ti-6Al-4V powder-binder feedstock at different filler volume fractions for different temperatures	194
Table A.6. Viscosity of Ti-6Al-4V powder-binder feedstock as a function of filler volume fraction, temperature, and shear rate.....	199
Table A.7. Cross-WLF constants to determine viscosity at varying shear-rate and temperature for binder and 0.60 volume fractions of Ti-6Al-4V powder in the feedstock	200
Table A.8. Specific volume of Ti-6Al-4V powder-binder feedstock as a function of filler volume fraction, temperature, and pressure	202

Table A.9. Dual-domain Tait constants for Ti-6Al-4V powder-binder feedstock at 0 and 0.59 volume fractions.....	204
Table A.10. Thermo-physical properties for major commercially used metals [33].....	209
Table B-I.1. Design I - Simulation results used for sensitivity factor calculation.....	219
Table B-I.2. Design II - Simulation results used for sensitivity factor calculation	220
Table B-I.3. Design III - Simulation results used for sensitivity factor calculation	221
Table B-II.1. Square cross-section unit cell green part characterization	222
Table B-II.2. Circular cross-section unit cell green part characterization	223
Table B-II.3. Square cross-section unit cell (3 mm thickness) sintered part characterization	224
Table B-II.4. Circular cross-section unit cell (3 mm thickness) sintered part characterization.....	225
Table C-I.1. Printing process parameters.....	229
Table C-I.2. Micro-strain measured experimentally with incremental slotting.....	234
Table C-I.3. Legendre polynomial basis matrix [Pij]	235
Table C-I.4. Strain value estimated from simulations (ABAQUS) represent the Compliance matrix [C] elements Cij.....	237
Table C-I.5. Residual stresses distribution: Experimental measurement	240
Table C-I.6. Residual stresses distribution: Process simulation prediction	241
Table C-IV.1. Material properties input	256
Table C-IV.2. Validation experimental data.....	256
Table C-IV.3. Sintering process parameters	257

Table C-IV.4. Green part properties considered equivalent to that of Ti-6Al-4V feedstock	257
Table C-IV.5. Ti-6Al-4V feedstock viscosity.....	257
Table C-IV.6. Sintered part - Young's modulus	258

LIST OF FIGURES

Figure 1.1. Overview of MF ³ process showing filament preparation, printing, debinding and sintering, and demonstrations of a typical part fabricated by MF ³ of Ti-6Al-4V	2
Figure 1.2. DfMF ³ : Overall approach leveraging predictive simulation.....	5
Figure 2.1. The methodology of predictive simulation and experimental verification of MF ³ printed part	18
Figure 2.2. Mechanical and thermal properties over a range of temperatures used in printing process simulations (a) Ti-6Al-4V feedstock (b) unfilled ABS	20
Figure 2.3. (a) ASTM E8 tensile bar dimensions (b) meshed model with voxel element size 0.3 mm (c) GCode data defines the 0-90° toolpath generated in slicing tool.....	23
Figure 2.4. MF ³ printing simulation progress by sequential element activation algorithm; temperature variation plot concerning time in sync with material deposition in the printing experiment of Ti-6Al-4V feedstock.....	26
Figure 2.5. Part deflection estimation: (a) Ti-6Al-4V feedstock (b) ABS.....	27
Figure 2.6. Part dimensions: simulation and experiment results (a) Ti-6Al-4V feedstock (b) ABS.....	28
Figure 2.7. Z-warpage: simulation and experiment results (a) Ti-6Al-4V feedstock (b) ABS	31
Figure 2.8. Part distortion along the Z-axis: simulation and optical surface profilometry results (a) Ti-6Al-4V feedstock (b) ABS.....	32

Figure 2.9. (a) and (b) Reverse-warped geometry (grey) overlapped with original design geometry (black) for Ti-6Al-4V feedstock and ABS, respectively. Larger warpage compensation was required in ABS. (c) and (d) Warped geometry (red) overlapped with original design geometry (green) for Ti-6Al-4V feedstock and ABS, respectively. Iteration-I and Iteration-II represent before and after warpage compensation, respectively. Warpage compensation leads to higher geometric conformity. 34

Figure 2.10. Part distortion along the Z-axis: optical surface profilometry results in experiments Iteration-II (a) Ti-6Al-4V feedstock (b) ABS 35

Figure 2.11. Temperature distribution at the end of printing; (a) Ti-6Al-4V feedstock (b) ABS (c) Thermal history estimation for Ti-6Al-4V feedstock part..... 39

Figure 2.12. Residual stresses (von Mises) at the end of printing; (a) Ti-6Al-4V feedstock (b) ABS 40

Figure 3.1. (a) MF³ process sensitivity study framework: input parameters (process conditions, component geometry, material properties) and output parameters (part quality) investigated. (b) Three different geometries were studied to investigate process sensitivity variation with part geometry. CAD and MF³ printed green and sintered parts 48

Figure 3.2. (a) FE model setup in Digimat: STL CAD file was used for slicing/ toolpath generation defined in GCode file, the same STL model meshed with 0.3 mm voxel elements (b) Mechanical and thermal properties of Ti-6Al-4V with 59 vol.% feedstock over a range of temperatures used in MF³ printing process simulations 51

Figure 3.3. Simulation results: (a) Deflection, overall (b) Z-warpage..... 60

Figure 3.4. Simulation results: Residual stresses (von Mises)..... 62

Figure 3.5. Simulation results: (a) Temperature distribution at the end of printing (b) Substrate temperature history	64
Figure 3.6. (a-c) Contribution from significant input parameters towards print time, (d-f) print time variation trends for significant input parameters.....	72
Figure 3.7. (a-c) Contribution from significant input parameters towards deflection, (d-e) deflection variation trends for significant input parameters	73
Figure 3.8. (a-c) Contribution from significant input parameters towards Z-warpage, (d-e) Z-warpage variation trends for significant input parameters	75
Figure 3.9. (a-c) Contribution from significant input parameters towards residual stresses, (d-f) residual stresses variation trends for significant input parameters	76
Figure 3.10. (a-c) Contribution from significant input parameters towards substrate temperature, (d-f) substrate temperature variation trends for significant input parameters	77
Figure 3.11. Infill pattern for varying part wall thickness and bead width.....	78
Figure 4.1. Overview of MF ³ process showing filament preparation, 3D printing, debinding and sintering, and demonstration of a lattice structure fabricated with Ti-6Al-4V	86
Figure 4.2. Rectilinear vs. concentric toolpath. Rectilinear infill led to low geometric fidelity of narrow and tiny cross-sectional print area in the lattice unit cell, whereas concentric perimeters follow the outline more precisely, leading to higher fidelity both in the case of circular and square beams cross-section.	92
Figure 4.3. Unit cells with square and circular cross-section printed with varying element length and thickness to evaluate the effects of lattice geometry parameters on printed parts	94

Figure 4.4. Unit cells with varying element thickness (3 mm, 2.5 mm, 2 mm) and overhang (8 mm, 7 mm, 6 mm) were printed for both square and circular c/s: (a) 3 mm element thickness; (b) 2 mm element thickness; (c) 2.5 mm element thickness.....	95
Figure 4.5. Simulation setup of square and circular c/s unit cells (element length 7 mm, element thickness 2.5 mm); (a) meshed model with voxel element size 0.1 mm (b) G-Code data defines the concentric toolpath generated in slicing tool	98
Figure 4.6. (a) Effect of lattice element thickness and length on XY-shrinkage (b) Effect of lattice element thickness and length on Z-shrinkage (c) Effect of lattice element thickness and length on green part relative density	100
Figure 4.7. (a) Part deflection estimation from simulation of unit cell. (b) Deflection location and pattern were found similar in both simulation and experiments	103
Figure 4.8. Representation of the A-B-C-D dimensions listed in Table 4.....	105
Figure 4.9. Porosity estimation of square and circular c/s unit cells (element length 7 mm, element thickness 2.5 mm)	106
Figure 4.10. Residual stresses estimation from simulation of unit cells.....	107
Figure 4.11. Large deflection observed in experimental printing in unsupported regions, whereas simulation did not provide an estimation of such deflection	109
Figure 4.12. (a) Extrudate in unsupported overhang was considered equivalent to a simply supported beam under uniformly distributed load; (b) extrudate deflection in unsupported region measured in printed green parts	110
Figure 4.13. (a) Effect of overhang length on extrudate deflection in the unsupported region of square c/s. (b) Effect of overhang length on extrudate deflection in the unsupported	

region of circular c/s. (c) Effect of lattice element cross-section extrudate deflection in the unsupported overhang (comparison between 4.13a and 4.13b).....	113
Figure 4.14. Sintered unit cells	115
Figure 4.15. Lack of diffusion between beads was observed in the bottom-facing surface of the unsupported overhang feature as an effect of extrudate sagging in the green part	116
Figure 4.16. Stacked Ti-6Al-4V lattice structure (green and sintered parts) of various configurations fabricated by MF ³	117
Figure 5.1. Overview of MF ³ process showing filament preparation, 3D printing, debinding, sintering, and demonstration of custom implant part fabricated by MF ³ with Ti-6Al-4V	124
Figure 5.2. CBCT scan of the patient showing the defect	126
Figure 5.3. The workflow of patient-specific implant fabrication using the MF ³ process	127
Figure 5.4. (a) Segmentation of maxilla and mandible bones from the overall facial anatomy; coronal, axial, sagittal and front views (b) Hounsfield radiodensity scale	129
Figure 5.5. SLA process flow to fabricate 3D printed maxilla structure biomodel of the patient.....	130
Figure 5.6. (a). Implant design requirement as defined by the oral/ maxillofacial surgeons considering the current condition of the patient's maxilla structure bone and dental implant requirements. (b) Implant geometries generated from digital biomodel using 3-Matic. (c) First-generation design of the implant. The implant was divided into three components, (RH, Middle & LH parts).....	132

Figure 5.7. (a) Build setup showing sliced model, toolpath support structure of the middle part (b) MF³-printed green part (c) printing without appropriate support structure failed, optimal support led to successful printing of the RH part 135

Figure 5.8. (a) MF³-printed maxillofacial implants green parts with a support structure (b) optical surface profilometry the green parts 139

Figure 5.9. MF³ printing process simulation results: (a) part deflection overlapped on original CAD design (b) residual stresses (von Mises) estimation..... 142

Figure 5.10. Typical dimensions of LH part of the customized implant: (a) CAD design (b) simulation estimation (c) printed green part 143

Figure 5.11. (a) sintered metal parts with a support structure (b) sintered metal parts after support structure removal (c) green part vs. sintered part dimensions showed 16% shrinkage in sintering..... 144

Figure 5.12. (a) Stair-step effects from layer-by-layer printing due to Z-gradient of the implant surface (b) Surface roughness measured in LH & Middle unpolished sintered parts in 0° and 90° (c) SEM (unetched unpolished condition) 146

Figure 5.13. (a) Optical microscopy (etched polished condition) (b) SEM (etched polished condition) 150

Figure A.1. The present work for determining the input material parameters for conducting process simulations 181

Figure A.2. Typical defects observed in MF³ 3D printing process demonstrated for Ti-6Al-4V alloy system fabricated by our group showing (a) dark regions representing pores within a cut-cross section of a powder-polymer filament, (b) gaps between layers within an MF³

fabricated green part, (c) crack propagation observed after debinding and (d) the presence of micro and macro pores present within the sintered MF ³ part.....	182
Figure A.3. Estimated (a) Feedstock density, and (b) Young’s modulus for Ti-6Al-4V filler-binder feedstock at different volume fractions	189
Figure A.4. Estimated thermal properties of composite Ti-6Al-4V powder-binder feedstock at different volume fractions for (a) specific heat and (b) thermal conductivity as a function of temperature, and (c) coefficient of thermal expansion	196
Figure A.5. Estimated viscosity of the Ti-6Al-4V powder-binder feedstock for a shear rate of 20-1600s ⁻¹ at (a) 413K and (b) 423K with different volume fractions.....	197
Figure A.6. Estimated specific volume of Ti-6Al-4V powder-binder feedstock at different filler volume fractions for (a) 0 MPa and (b) 50 MPa	202
Figure A.7. Experimental and simulation result verifications using estimated values: (a) CAD file for ASTM E8 tensile sample with dimensions, (b) Simulation of the part using the estimated material properties for 59 vol.% Ti-6Al-4V + binder feedstock (c) Printed green parts with 0.59 vol.% of Ti-6Al-4V + binder feedstock, (d) Simulation of the ABS part using the available material database in Digimat-AM, (e) Printed part with ABS material filament, (f) Warpage analysis resulting from experiments and simulation for 59 vol.% Ti-6Al-4V+ binder feedstock and ABS.....	205
Figure A.8. Dimensions for an ASTM E8 tensile sample obtained from simulations and experiments for 59 vol. % solids loading Ti-6Al-4V feedstock and ABS.....	207
Figure A.9. Examples for Digimat-AM simulations that show typical outputs such as (a) warpage, and (b) residual stress in case studies for parts an end-of-arm tool (top) and automotive brake lever (bottom).....	208

Figure C-I.1. Methodology followed for estimation of residual stresses through process simulation, and verification by experimental measurement	228
Figure C-I.2. (a) ASTM E8 tensile bar dimensions (a) meshed model with voxel element size 0.3mm (b) GCode data defines the 0-90° toolpath generated in slicing tool	229
Figure C-I.3. Mechanical and thermal properties of Ti-6Al-4V feedstock over a range of temperatures used in printing process simulations	230
Figure C-I.4. Residual stresses (maximum principal stresses) estimation for Ti-6Al-4V feedstock part	230
Figure C-I.5. Full block geometry model showing cut slot and strain gauge on the opposite side	231
Figure C-I.6. Experimental setup: (a) strain gauges connected to test specimen (b) specimen broken after slotting	233
Figure C-I.7. FEA simulation setup: pressure load applied along Y-axis on 0.2mm slotted face, symmetry boundary condition applied at the cutting plane	236
Figure. C-I.8. Displacement results from ABAQUS. Strain along Y-axis calculated at Y=2.25 mm (representing strain gauge length used in experimental measurement).....	236
Figure C-I.9. Residual stresses distribution across thickness: Experimental measurement	240
Figure C-I.10. Residual stresses distribution across thickness: Process simulation prediction	241
Figure C-I.11. Residual stresses distribution at cutting plane cross-section: Process simulation prediction	242

Figure C-II.1. Experimental setup for real-time measurement calibration of the thermal imaging camera using memory logger and FLIR ResearchIR Max software	244
Figure C-II.2. (a) Thermocouple connected to the print bed reading temperature in the memory logger (b) Memory logger showing print bed temperature 75.7 °C	245
Figure C-II.3. FLIR software showing real-time measurement of print bed temperature distribution ranging between 24.2 °C and 83.5 °C	246
Figure C-II.4. Two square bar placed at a distance were chosen as test specimen to allow sufficient time for clear reading of the latest layer temperature and evaluate temperature drop between two layers	246
Figure C-II.5. (a) MF ³ printing (b) FLIR software recording the real-time temperature measurement of the print bed, printed layers, nozzle and extruder, temperature distribution ranging between 20.9 °C and 145.9 °C.....	247
Figure C-III.1. Unit lattice cell (a) MF ³ printed green part (b) voxel mesh (c) toolpath	248
Figure C-III.2. Porosity estimation by Digimat-AM	248
Figure C-III.3. PathCoverage results from GENOA: considerable voids/ porosity between tracks found at the corners within a single layer.....	249
Figure C-III.4. EmptySpots results from GENOA: considerable voids/ porosity observed at the corners between tracks as well as between layers.....	249
Figure C-III.5. VoidRatio results from GENOA: 0.3~4% voids observed at macro level (a) bottom of the unit cell (b) mid-section along the vertical axis	250
Figure C-IV.1. Shrinkage and distortion predicted by sintering simulation using Simufact Additive: Helical Bevel Gear	252

Figure C-IV.2. Geometry compensation taking into account the predicted shrinkage and distortions: (a)Original CAD geometry and after sintered geometry (b) pre-compensated geometry and original CAD geometry (c) final sintered shape of pre-compensated geometry and original CAD geometry.....	253
Figure C-IV.3. Comparison of surface deviation of the original CAD geometry with the after sintered shape (left) and original CAD geometry and after-sintered shape of pre-compensated geometry (right)	254
Figure C-IV.4. (a) Deformation along Z-axis (b) Deformation profiles at the top surface (half the circumference).....	255
Figure C-V.1. Clutch adaptor (a) CAD in STL format (b) toolpath from slicer software imported in Digimat-AM (c) voxel mesh (d) residual stresses (e) thermal history (f) deformation.....	259
Figure C-V.2. Hinge base (a) CAD in STL format ((b) residual stresses (c) deformation	260
Figure C-V.3. Impellor (a) CAD in STL format (b) deformation	260
Figure C-V.4. Motor Support (a) CAD in STL format (b) deformation.....	261
Figure C-V.5. Test artifact (a) CAD in STL format (b) deformation	261

CHAPTER 1

INTRODUCTION

Additive manufacturing (AM), also known as 3D printing, can fabricate three-dimensional (3D) objects by adding material layer upon layer, as opposed to subtractive and formative methods of manufacturing [1]. The ability of AM to deal with highly complex geometry and produce parts in small quantity yet economically has attracted industries such as aerospace, automotive, medical, dentistry, and consumer to produce application-specific end-user parts [2]. The past few decades have witnessed enormous developments and the adoption of both polymer and metal AM technologies. In particular, several metal AM processes have been established as production methods, such as laser powder bed fusion (L-PBF), electron beam melting (EBM), direct energy deposition (DED), and binder jetting. However, very high capital investment in machines besides unique challenges and safety concerns due to directly working with loose reactive metal powder tends to limit the accessibility of these technologies at different scales. Moreover, there are process-related challenges, such as localized heating, rapid cooling, high thermal gradients induce residual stresses, non-equilibrium microstructures, and microstructural anisotropy leading to differences in physical and mechanical properties in the laser/electron beam-based technologies [3,4]. Binder jetting faces other difficulties arising from powder-binder interactions, fewer material options, de-powdering of green parts, and low part density [5].

Alternatively, extrusion-based AM processes are emerging for fabricating metal parts using feed material in the form of a paste, filament, or granular feedstock. These processes can eliminate loose powder health hazards and produce isotropic parts and are also accessible at low-cost desktop-level printing [6-8]. The current work presents a filament-based AM process known as metal fused filament fabrication (MF³) that can effectively manufacture metal parts. As shown in **Figure 1.1**, MF³ uses a highly filled metal powder-polymer filament, the metal powder content generally varies between 55 to 60% volume of powder-binder mixture. The feedstock is extruded to form a 1.75 mm diameter filament, that can be used on an extrusion-based desktop printer to build a 3D part. The printed part referred to as a ‘green part’, is subsequently subjected to solvent and thermal debinding to remove polymer binder, leading to a ‘brown part’. Finally, sintering is conducted in an inert environment at elevated temperatures, providing a fully dense ‘sintered metal part’.

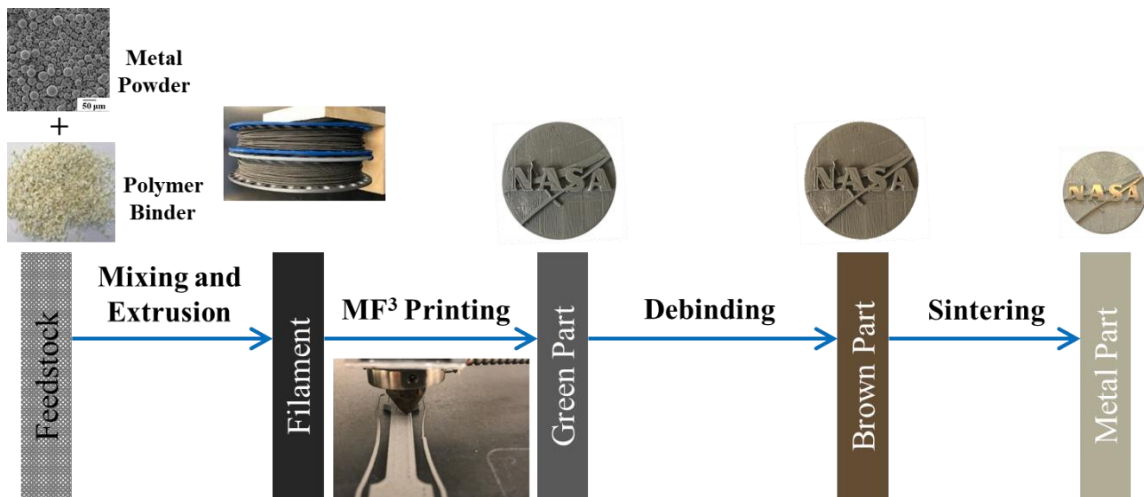


Figure 1.1. Overview of MF³ process showing filament preparation, printing, debinding and sintering, and demonstrations of a typical part fabricated by MF³ of Ti-6Al-4V

In this work, the MF³ process has been demonstrated to fabricate Ti-6Al-4V alloy parts. Titanium and its alloys find a wide range of applications, particularly, in aerospace and medical applications owing to their high specific strength, excellent corrosion resistance and biocompatibility [9]. As the acceptance for MF³ is growing, AM leaders, such as BASF, Markforged, Desktop Metal have commercialized their MF³ solutions in terms of material, hardware or services.

However, while the extrusion-based AM processes of polymers, such as fused deposition modeling (FDM), are well established and have been widely used for decades now, MF³ is still in a nascent stage. Though MF³ has got enormous potentials, very few materials have been developed so far. There exist several research gaps in MF³, such as lack of understanding about the influence of material composition and resulting properties on printed part properties, effects of printing parameters and slicing strategies on part quality, part design considerations for printability, process modeling and simulation to aid design for MF³. The paucity of literature on these research areas has resulted in a lot of dependencies on the trial-and-error approach that ultimately retards the overall developments and growth of the technology. A few research groups have been working with different materials [6-8, 10-12], however, most of the studies are based on experiments, trial-and-error or empirical models. Hence, the work presented in the dissertation has addressed the identified research gaps.

Moreover, the fundamental understanding of design for MF³ (DfMF³) is essential for unlocking the full potential of additive manufacturing, such as design freedom, light-weighting, design integration/ part consolidation, ability to deal with highly intricate shapes of production parts, and ultimately, applications development for MF³. In addition, the

layer-by-layer printing with the highly filled powder-binder compound leads to several challenges, such as warpage and distortions, residual stresses, porosity within and between layers, low geometric fidelity of fine features like lattice structures, increased difficulties in printing unsupported regions due to high material density, and complexities in dealing with support structures in green as well as in sintered stage. To address these challenges, there is a need for investigations of material-geometry-process interrelationships in detail. Such investigations through an experimental approach and trial-and-error method would not be feasible or efficient and have limited scope. Here, computational simulation and virtual analyses can help overcome the limitation.

Application of predictive simulations in AM has already been proven for different technologies both in metals and polymers using simulation tools like Ansys, Abaqus, etc. [13-17]. However, no work has been done on the simulation of the MF³ process so far. There is a need for a design platform, a simulation solution to analyze the MF³ process, and enable design for MF³. Hence, the current work presents a framework of design for MF³ leveraging an FEA-based simulation tool, Digimat from MSC Software as shown in **Figure 1.2**. Digimat is an advanced simulation tool used for multi-scale material modeling and anisotropic analysis.

First, data was gathered for input parameters such as material thermo-mechanical properties as a function of temperature, part geometry, and printing process parameters. Using a thermo-mechanical process model, the MF³ printing process was simulated, enabling the prediction of part deformation, warpage, dimensional variations, residual stresses and thermal history. The capability to estimate these outcomes allows optimization of material composition, part design and process parameters before getting on to the

physical process. This approach enables the development of the “right part” for printing and getting it printed “right first time”, eliminating the waste in experimental trial-and-error methodology.

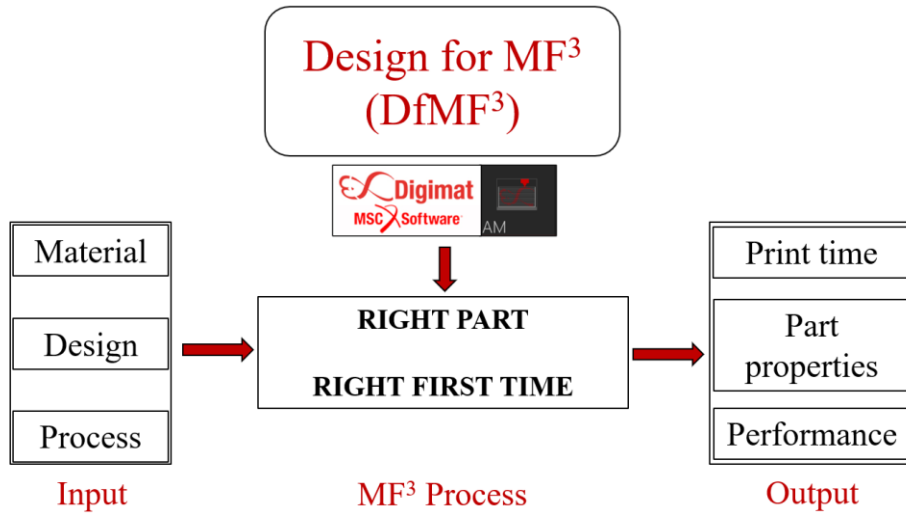


Figure 1.2. DfMF³: Overall approach leveraging predictive simulation

The approach would certainly reduce time and cost, and lead to efficient design and manufacturing. Moreover, the predictive simulation would enhance the understanding of the material-geometry-process interrelationships in MF³ and accelerate the research through reduced dependency on experimental studies.

Building on the initial work of material and process development, the goal of the current work is to establish a fundamental understanding of design for MF³ of Ti-6Al-4V by investigating the material-geometry-process interrelationships and their influence on printed part quality. It is expected that the overall findings will enable effective fabrication of complex parts and significantly reduce dependency on the trial-and-error approach.

CHAPTER 2 presents an introduction to the MF³ printing process simulation as an enabler to design for MF³. In this study, the applicability of a thermo-mechanical model for finite element simulation of MF³ printing of Ti-6Al-4V has been investigated. The quantitative influence of material properties on MF³ printed part quality was estimated using the simulation platform. The simulation results of two materials, a Ti-6Al-4V filled polymer and an unfilled ABS copolymer, were corroborated by experiments. It was determined that the unfilled polymer parts showed greater warpage and dimensional variations than that of the Ti-6Al-4V filled polymer, both in simulations and experiments. Further, the warpage pattern was consistent between experiments and simulation results for both materials. Finally, the warpage compensation algorithms showed improvement in dimensional control for both materials in simulations and were consistent with experimental results. **CHAPTER 2** findings have been published in the Journal of Materials Engineering and Performance in the special issue of Additive Manufacturing (DOI: <https://doi.org/10.1007/s11665-021-05733-0>).

CHAPTER 3 investigates the sensitivity of key output parameters towards each of the input parameters in MF³ printing. Process simulations were used to estimate the process outcome in terms of part deformation, warpage, residual stresses, thermal history and print time, in response to variable inputs from the material, geometry and printing process standpoint. A systematic procedure for sensitivity analysis has been presented. Dimensionless sensitivity values for all output parameters were calculated in the response of each input parameter, which allows parameters with different units to be compared quantitatively with a single yardstick. Moreover, three different part geometries were studied to identify how the process sensitivity varies with part design. For each output

parameter, the most influential input parameters were identified from the whole set of input parameters, and their influence trends were evaluated for different part designs. **CHAPTER 3** findings have been published in the Journal of Materials Engineering and Performance in the special issue of Additive Manufacturing (DOI: <https://doi.org/10.1007/s11665-021-05666-8>).

CHAPTER 4 investigates supportless printing of Ti-6Al-4V lattice structures using the MF³ process for the first time. A unit cell was used as a starting point, which was then extended to multi-stacked lattice structures. Feasible MF³ processing conditions were identified to fabricate defect-free lattice structures. The effects of lattice geometry parameters on part deflection and relative density were investigated at the unit cell level. Computational simulations using the finite element method were employed to predict the part quality, and results were verified by experimental printing. Having identified the simulation limitation, an analytical approach has been presented to estimate the extrudate deflection at the unsupported overhangs in lattice structures. Finally, using the identified processing and geometry parameters, multi-stacked lattice structures were successfully printed and sintered without defects. The outcome of the work is an understanding of geometry-processing-properties interrelationships governing the design and fabrication of lattice structures by MF³. **CHAPTER 4** manuscript has been accepted for publication by the *Rapid Prototyping Journal* and is currently in the publication process.

CHAPTER 5 evaluates the feasibility of MF³ to manufacture patient-specific maxillofacial implants based on an elderly patient with osteoporotic maxillary structure. The design and fabrication of Ti-6Al-4V maxillofacial implants using MF³ technology are being reported for the first time. The CBCT image data of the patient's oral anatomy was

digitally processed to design 3D CAD models of maxillofacial implants that match the patient's anatomy and dental implant requirement. The patient-specific implants were fabricated by MF³ printing, followed by debinding and sintering, using support structures for the first time. Sintered parts were characterized after cutting the support structures off. An overall 15-20% shrinkage was observed in the sintered parts relative to the green parts. A relative density of 81% indicated 19% total porosity, including 13% open interconnected porosity in the sintered parts, which would favor bone healing and high osteointegration in implants. Considerable surface roughness (Ra: 13~23 μm) and stair-step effects were noticed. Also, a Rockwell hardness of 6.52 ± 0.8 HRC was observed. The outcome of the work proves that MF³ is a potential process to manufacture patient-specific custom implants out of Ti-6Al-4V. The work presented in **CHAPTER 5** contributes towards a manuscript that is being submitted to the *Annals of 3D Printed Medicine*.

Appendix A reports the evaluation of estimation models that were used to determine Ti-6Al-4V feedstock material properties used to define the material behavior in the simulation platform. Physical and thermo-mechanical properties including density, specific heat, modulus, thermal conductivity, coefficient of thermal expansion, viscosity and specific volume were estimated as a function of temperature. These findings have been published in *JOM*, 2020 (DOI: <https://doi.org/10.1007/s11837-019-03920-y>).

Appendix B: B-I consists of some valuable raw data that was generated during the MF³ sensitivity analyses (Chapter 3). A total of 78 simulation jobs were conducted in this study for three different part designs. The data includes the simulation results used for sensitivity factor calculations of all the designs. **B-II** consists of details from lattice structure fabrication experiments and characterization data (Chapter 4).

Appendix C: **C-I** presents the work done towards verification of the simulation prediction of residual stresses developed in MF³ printing. An experimental approach based on the ‘Crack Compliance’ method was used. It involved a two-step process: (i) measurement of micro-strain using strain gauge by incremental slotting of the specimens (ii) structural simulation using an FEA tool. The residual stresses estimated by Digimat-AM showed a correlation with experimental measurement. Findings from this work contribute towards a manuscript that is in progress. **C-II** comprises preliminary details on the real-time measurement of temperature distribution during MF³ printing. It would enable verification of simulation results by facilitating the evaluation of thermal gradient and temperature history during the process. It would also provide an enhanced understanding of the influence of thermal attributes on resulting part quality and performance. **C-III** briefs about the initial progress towards the capability of estimating porosity distribution in the MF³ printed green part. It would also provide an estimation of relative density distribution within the printed green part. Apart from Digimat-AM, another simulation tool, GENOA (AlphaStar), was investigated in this work. Though not fully capable yet, both tools have some initial developments on this feature. **C-IV** consists of a demonstration of the sintering simulations model developed through the collaboration between MSC Software and the University of Louisville. A new module has been added in Simufact Additive (MSC) and is presently being tested. This development underlines the extension of MF³ printing simulation to the sintering process. **C-V** demonstrates some of the NASA parts simulated for MF³ printing as part of the FabLab project. These simulation results were used for design analysis from a printing standpoint. NASA also wanted to conduct sintering simulations on these parts to predict the final part quality.

CHAPTER 2

METAL FUSED FILAMENT FABRICATION (MF³) PROCESS SIMULATION: DISTORTIONS PREDICTION AND EXPERIMENTAL VERIFICATION

2.1 INTRODUCTION

Additive manufacturing (AM) is used for fabricating three-dimensional (3D) objects from a virtual 3D model by adding material layer upon layer, as opposed to subtractive and formative methods of manufacturing [1]. The main advantage of AM over conventional manufacturing processes is the ability to deal with geometric and material complexities that cannot be created, technically or economically, using conventional manufacturing processes [2]. Metal fused filament fabrication (MF³) is an emerging AM technology for fabricating metal parts. MF³ uses a highly filled metal powder-polymer filament in an extrusion-based printing platform [6-8]. The metal powder content generally varies between 55 to 60% volume of powder-binder mixture. The feedstock is extruded to form a 1.75 mm diameter filament, that can be used on an extrusion-based desktop printer to build a 3D part.

In the MF³ printing process, the filament is first heated to a semi-molten state and extruded through a nozzle. The extrudate gets deposited on a build plate as the nozzle moves, following a predefined printing path. The deposited material dissipates heat to the environment through convection and radiation. Also, conduction between the previously

printed material and build plate leads to heat transfer [18]. While the previously deposited material cools down and is in a near-solid phase, the new layer of semi-molten material is at a higher temperature. This temperature difference exists along the Z-axis throughout the build. It develops thermal gradients along Z-axis resulting in residual stresses in the printed component in an anisotropic manner. These stresses consequently produce part distortion and nonuniform variations in dimensions, during the printing process as well as after component removal from the build plate [13, 18]. Part distortions and dimensional variations are the most significant quality challenges that hinder acceptance of the MF³ process and printed parts in potential functional applications. Hence, the influence of each input variable on part quality needs to be investigated. The capability of predicting the thermal gradient, residual stresses and distortion if MF³ may help reduce the dependence on trial-and-error methods which is time-consuming and expensive. Also, such a predictive solution can facilitate design for MF³. However, no research work has been published towards such investigations in MF³.

Computational simulations aimed at predicting residual stresses and part deformation are attracting increasing interest in additive manufacturing to study the effects of process parameters on the quality of 3D printed parts. In fused filament fabrication (FFF), several recent studies focused on the prediction of mechanical behavior of FFF printed components. Among the others, Armillotta et al. [14] presented an empirical model for warpage prediction by varying part geometry and layer thickness for acrylonitrile butadiene styrene (ABS). The study suggested that a lower dimension along build direction led to lower bending stiffness and thus to larger distortions. Watanabe et al. [15] investigated warpage and residual stresses through simulation of polypropylene (PP) using Ansys

Polyflow. The effects of adjusting process variable settings, such as extrusion temperature, deposition speed, and layer height, on part warpage were analyzed computationally and experimentally. Cattenone et al. [13] investigated the impact of process parameters and modeling choices (e.g., mesh size, material model, time step size) on simulation outcomes using Abaqus for ABS filament. Croccolo et al. [19] proposed an analytical model to predict the strength and the stiffness properties based on input parameter variations for FFF of ABS. A model was proposed taking into account the effects of building direction and the number of contours in mechanical strength prediction. Phan et al. [20] used a computational fluid dynamics simulation to model the melting process of polylactic acid (PLA) through the extruder nozzle. It revealed a recirculation vortex that has a large viscosity which explains why no material is observed to spill out of FFF printers from the large backpressures. Zhang et al. [21] used a finite difference method to look into the influence of process parameters on temperature variation. The influence of temperature settings, layer thickness and print speed were identified. Brenken et al. [22] investigated polymer crystallization kinetics and thermo-viscoelastic models based on the thermal history of polyphenylene sulfide (PPS).

Similarly, simulations of metal AM processes have been investigated by several researchers. Li C et al. [16] investigated a predictive model of part distortion and residual stress in the selective laser melting (SLM) process of AlSi10Mg using Abaqus. To overcome the limitations of the single-track conventional simulation approach, a temperature-thread multiscale modeling approach was proposed to predict residual stress and part distortion. Song J et al. [17] used an FE-based thermomechanical model using

FORTRAN to predict the time-dependent temperature field, residual stress and resultant deformation of the Ti-6Al-4V part using the SLM process.

However, no work has been done towards process modeling and simulation of extrusion-based printing with metal-filled materials. The use of FEA tools to perform material and process simulations of MF³ is yet to be explored. There are only a few works on MF³ research that have been published. Most of the work has been done towards material and process development, and experimental or analytical studies to understand process dynamics [1, 6-8, 23, 24]. Prior work performed by our group looked into estimating the feedstock material properties such as physical, thermal, rheological and mechanical for highly filled powder-polymer systems [10], and printability challenges in MF³ [11]. In order to design for MF³ and overcome part quality issues, there is a need to investigate the material-geometry-process interrelationships. However, such investigations using an experimental trial-and-error approach or empirical methods have limited scope towards problem-solving in a timely or cost-effective manner. Hence, computational simulation and design solutions are required for MF³ as an enabler to widespread industrial application of the process.

In this study, the applicability of the thermo-mechanical model using a finite element simulation for the MF³ printing process was investigated. The material system used in MF³ comprises a novel formulation of metal powder mixed with a multi-component custom polymer binder. Here, the question arises on how the properties of powder-binder feedstock in MF³ influence the printing process outcome and quality of the printed part. A thermo-mechanical material model was considered for Ti-6Al-4V feedstock material containing 59 vol.% metal powder. Printed part quality was evaluated in terms of part distortion and

changes in dimensions. Simulation results were verified with experimental printing and measurements, including optical surface profilometry. Furthermore, the sensitivity of the simulation model to material properties was verified by simulation and experimental printing of unfilled ABS material. The experimental matrix also enabled the influence evaluation of material composition and resulting properties on printed part quality. It is expected that the present study will lead to a predictive simulation solution for MF³ that will provide an assessment of the printing process outcomes at the component design stage based on part geometry, material properties, print strategy and process conditions, enabling design for MF³ (DfMF³). It will further enable the identification of optimal processing conditions and component design to get the part right and print right the first time, as opposed to the traditional approach based on experience and trial-and-error.

2.1.1 Thermo-mechanical analysis of MF³ process

To analyze the MF³ printing process, FEA simulations were conducted using Digimat software [25]. The GCode data was obtained from a slicing tool (Simplify 3D) and a sequential thermo-mechanical simulation was performed. The analysis was divided into two steps. First, a thermal analysis was conducted, solving the heat transfer equations to evaluate the time-spatial temperature field evolution during the printing process. Subsequently, the resulting temperature field was adopted as loading input in a mechanical analysis to evaluate residual stresses and part distortions. To simulate the extrusion-based printing process, the sequential element activation function was used in Digimat. As per the toolpath defined by GCode data, a chunk of elements representing a small part of the deposited extrudate was activated in each time step. Once all the elements were activated,

the final results were then used for a thermo-mechanical analysis to simulate the solidification and cooling phase.

2.1.2 Constitutive models

Thermal analysis

The extrusion-based printing process involves transient heat transfer. As the heated extrudate gets deposited on a substrate, the temperature drops from extrusion temperature towards chamber and substrate temperatures. The simulation uses a heat transfer model to calculate temperature variations in the part being printed through the entire printing process and at the end after cooling. The transient heat transfer is modeled by the governing partial differential equation [14]:

$$\rho C_p \frac{\partial T}{\partial t} = k \left(\frac{\partial^2 T}{\partial x^2} + \frac{\partial^2 T}{\partial y^2} + \frac{\partial^2 T}{\partial z^2} \right) \quad (1)$$

where T , ρ , C_p , and k represent the temperature, density, specific heat capacity, and thermal conductivity of the powder-binder feedstock, respectively. The phase solidification energy per layer is given as:

$$H = \int \rho C_p(T) dT \quad (2)$$

where H represents enthalpy.

As print progresses, the newly deposited layer, initially at extrusion temperature, cools down quickly to a lower temperature. The lowered temperature and rate of cooling depend upon the build chamber and substrate temperature. A few underlying layers are re-heated by conduction heat flow from new layers, and their temperature exceeds glass transition

temperature again, leading to further diffusion between the layers. The evolution of the temperature in z-direction for each position satisfies the following heat equation [14]:

$$\rho C_p \frac{\partial T}{\partial t} = k \frac{\partial^2 T}{\partial z^2} \quad (3)$$

The variation of temperature throughout the part thickness is obtained as:

$$T = T_c + (T_m - T_c) \frac{\Delta h}{\sqrt{\pi \varphi t}} \exp\left(-\frac{Z^2}{4\varphi t}\right) \quad (4)$$

where $\varphi = k/\rho C_p$ is thermal diffusivity, T_m , T_c , Δh and Z are melting temperature, chamber temperature, layer thickness and position in Z-direction.

Mechanical analysis

The governing equations for mechanical analysis are the stress equilibrium with thermal strain included [26].

$$\begin{aligned} \frac{\partial \sigma_x}{\partial x} + \frac{\partial \tau_{yx}}{\partial y} + \frac{\partial \tau_{zx}}{\partial z} &= 0 \\ \frac{\partial \tau_{yx}}{\partial x} + \frac{\partial \sigma_y}{\partial y} + \frac{\partial \tau_{zy}}{\partial z} &= 0 \\ \frac{\partial \tau_{xz}}{\partial x} + \frac{\partial \tau_{yz}}{\partial y} + \frac{\partial \sigma_z}{\partial z} &= 0 \end{aligned} \quad (5)$$

Thermal strain, ϵ_{th} , is given by

$$\epsilon_{th} = \alpha_e \Delta T \quad (6)$$

Where, α_e is coefficient of thermal expansion and ΔT is the change in temperature

By Hooke's law, stress is related to strain by

$$\{\sigma\} = [D]\{\epsilon^e\} \quad (7)$$

Where, ϵ^e is elastic strain and D is the stiffness matrix

$$\{\epsilon^e\} = [D]^{-1}\{\sigma\} \quad (8)$$

For the thermo-elastic model, total strain, ϵ is given by

$$\{\epsilon\} = [D]^{-1}\{\sigma\} + \{\epsilon^{th}\} \quad (9)$$

In 3D form, this relationship is given as [27]:

$$\begin{pmatrix} \epsilon_{11} \\ \epsilon_{22} \\ \epsilon_{33} \\ \gamma_{12} \\ \gamma_{23} \\ \gamma_{31} \end{pmatrix} = \begin{pmatrix} 1/E_{11} & -\nu_{12}/E_{11} & -\nu_{13}/E_{11} & 0 & 0 & 0 \\ & 1/E_{22} & -\nu_{23}/E_{22} & 0 & 0 & 0 \\ & & 1/E_{33} & 0 & 0 & 0 \\ & & & 1/G_{23} & 0 & 0 \\ & & & & 1/G_{13} & 0 \\ & & & & & 1/G_{12} \end{pmatrix} \begin{pmatrix} \sigma_{11} \\ \sigma_{22} \\ \sigma_{33} \\ \tau_{12} \\ \tau_{23} \\ \tau_{31} \end{pmatrix} + \begin{pmatrix} \epsilon_{th,11} \\ \epsilon_{th,22} \\ \epsilon_{th,33} \\ \gamma_{th,12} \\ \gamma_{th,23} \\ \gamma_{th,31} \end{pmatrix} \quad (10)$$

Once the six stress components are calculated from the above equations, the principal stresses ($\sigma_1, \sigma_2, \sigma_3$) are calculated from the stress components by the cubic equation,

$$\begin{vmatrix} \sigma_{11} - \sigma_p & \tau_{12} & \tau_{31} \\ \tau_{12} & \sigma_{22} - \sigma_p & \tau_{23} \\ \tau_{31} & \tau_{23} & \sigma_{33} - \sigma_p \end{vmatrix} = 0 \quad (11)$$

The von Mises stress, σ' , is calculated as [28];

$$\sigma' = \sqrt{\frac{1}{2}[(\sigma_1 - \sigma_2)^2 + (\sigma_2 - \sigma_3)^2 + (\sigma_3 - \sigma_1)^2]} \quad (12)$$

2.2 METHODOLOGY

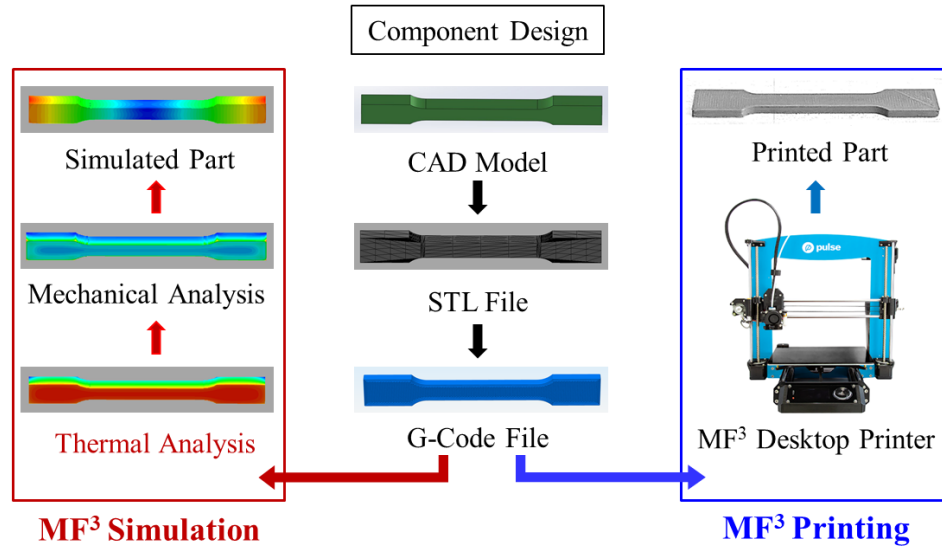


Figure 2.1. The methodology of predictive simulation and experimental verification of MF³ printed part

The simulations in this study focused only on the printing stage of the MF³ process chain. Simulation solutions for debinding and sintering stages are being worked on and will be reported separately. The overall approach followed in this study is shown in **Figure 2.1**. A 3D model of ASTM E8 tensile bar was developed using CAD software (Solidworks), which is then converted to STL format having a triangular mesh of the external surface. A slicing software (Simplify3D) is fed with the STL file as geometry input, slicing parameters as toolpath input and printing parameters as process conditions input. A GCode file is obtained that contains the printing process instructions. The same GCode file is used in MF³ printing simulations as well as printing experiments. This ensures consistency of input and boundary conditions between simulations and experiments. The information in the GCode file was used to set up FEA simulations in Digimat 2019.0 following a sequential

thermo-mechanical simulation approach. Estimation of a thermal gradient, residual stresses and distortions in the printed part was provided by the simulation. In MF³ printing experiments, the same GCode information was fed to a desktop FFF printer, Pulse (MatterHackers, Lake Forest, California), that prints a 3D part by adding material as per GCode instructions. The printed part is generally referred to as the ‘green part’.

2.2.1 Process simulation

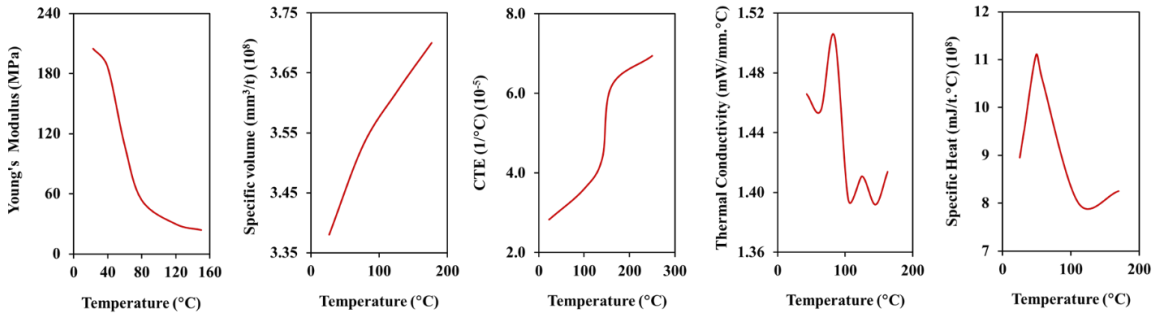
To model and simulate the MF³ printing process, accurate information is required to define the thermo-mechanical behavior of the novel powder-binder composite material, part geometry and printing process parameters. The accuracy of simulation prediction depends upon the accuracy of input data and the thermo-mechanical simulation model.

Material properties

In this study, the printing of the filaments with 59 vol.% of Ti-6Al-4V powder dispersed in a multi-component custom polymer matrix was simulated. Thermo-mechanical properties of the novel material were generated using empirical estimation models. A recent publication by the authors involved the use of experimentally measured polymer binder properties and estimation models to generate thermo-mechanical properties of Ti-6Al-4V feedstock material [10]. **Figure 2.2a** shows the mechanical and thermal properties of the material over a range of temperatures. In order to evaluate the effects of material properties on the printed part quality as well as to verify the sensitivity of the simulation model to changing material properties, simulations and printing experiments were conducted with an unfilled acrylonitrile butadiene styrene (ABS) polymer as well. ABS

was selected due to the availability of thermo-mechanical material properties in the database of the simulation tool. **Figure 2.2b** shows the mechanical and thermal properties of unfilled ABS polymer over a range of temperatures.

(a) Ti-6Al-4V feedstock



(b) Unfilled ABS

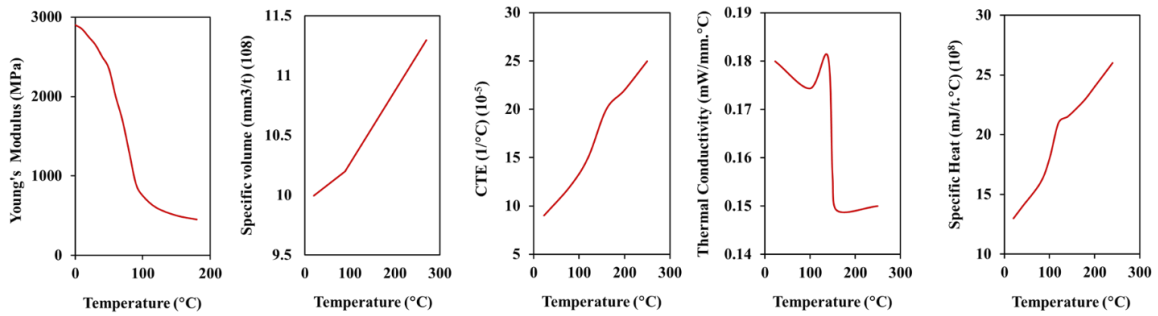


Figure 2.2. Mechanical and thermal properties over a range of temperatures used in printing process simulations (a) Ti-6Al-4V feedstock (b) unfilled ABS

Geometry

An ASTM E8 tensile bar was used for both printing simulations and experiments in this study. **Figure 2.3a** shows the dimension of the part. The tensile bar was used to evaluate

the mechanical and physical properties of printed parts, both at the green and sintered stage in the ongoing MF³ research at MIG; hence the same geometry was selected for simulation.

Printing parameters

The printing process in MF³ involves several input parameters. **Table 2.1** presents the key process parameters used in this study and their typical values selected based on experience.

Table 2.1. MF³ printing process conditions

Process parameters	Settings
Layer thickness (mm)	0.15
Bead width (mm)	0.48
Extrusion temperature (°C)	240
Build plate temperature (°C)	65
Build chamber temperature (°C)	20
Printing speed (mm/s)	5
Toolpath (°)	0 – 90

Layer thickness defines the height of each layer of material deposited during printing. While a smaller layer thickness discretizes the build into higher resolution leading to better accuracy and surface quality, it leads to higher printing time. Typically, a layer thickness of 0.1 – 0.2 mm is used in MF³ printing. In this study, a layer thickness of 0.15 mm was used. Bead width defines the discretization of each layer in the XY plane. It is decided considering the desired accuracy of geometric exactness and print speed. Nozzle size is selected according to intended bead width. A layer width of 0.48mm was obtained using a

0.4 mm diameter nozzle. Extrusion temperature of 240 °C and build plate temperature of 65 °C was used. Build chamber temperature was considered equal to ambient temperature as the desktop printer used in this study did not have a closed build chamber. A lower speed is more suited in MF³, the melt being highly viscous and the filament less stiff compared to standard polymer filaments like ABS [11]. A print speed of 5 mm/s was used in MF³ of Ti-6Al-4V. A toolpath was defined with alternating raster angle 0-90°.

Simulation setup

In this study, a thermo-mechanical model was used for finite element simulations in Digimat to model the MF³ printing process. The CAD model of the ASTM E8 tensile bar in STL format was imported in Digimat-AM. It was discretized into voxel mesh. To accurately reproduce the printing process, it is required that the typical element height is equal to a sub-multiple of the layer thickness. Also, if the element width can be equal to or a sub-multiple of the filament width, it provides consistency with the real process. But in some cases, this meshing strategy can lead to finite element models with a very large number of elements ($> 10^5$), which requires substantial computational resources. For this reason, we considered a meshing consistent with the height but not with the width of the deposited filament. However, the mesh size cannot be smaller than the layer thickness. Considering the computational time, a mesh size of 0.3 mm was used, leading to 89,606 voxel elements as shown in **Figure 2.3b**. The temperature-dependent mechanical and thermal material properties were defined over a range of temperatures for both Ti-6Al-4V feedstock and unfilled ABS, as shown in **Figure 2.2**. Processing parameters shown in **Table 2.1** were used in simulation as well as printing experiments. The GCode file from

Simplify3D defines the toolpath, layer thickness, and printing speed. This file includes the time and spatial position of the nozzle, material deposition description and contour of the part. An alternating 0° and 90° raster angle toolpath was generated in the slicing tool as shown in **Figure 2.3c**. Other printing parameters such as bead width, extrusion temperature, build plate temperature, chamber temperature, convection coefficient were defined through the simulation tool graphical user interface.

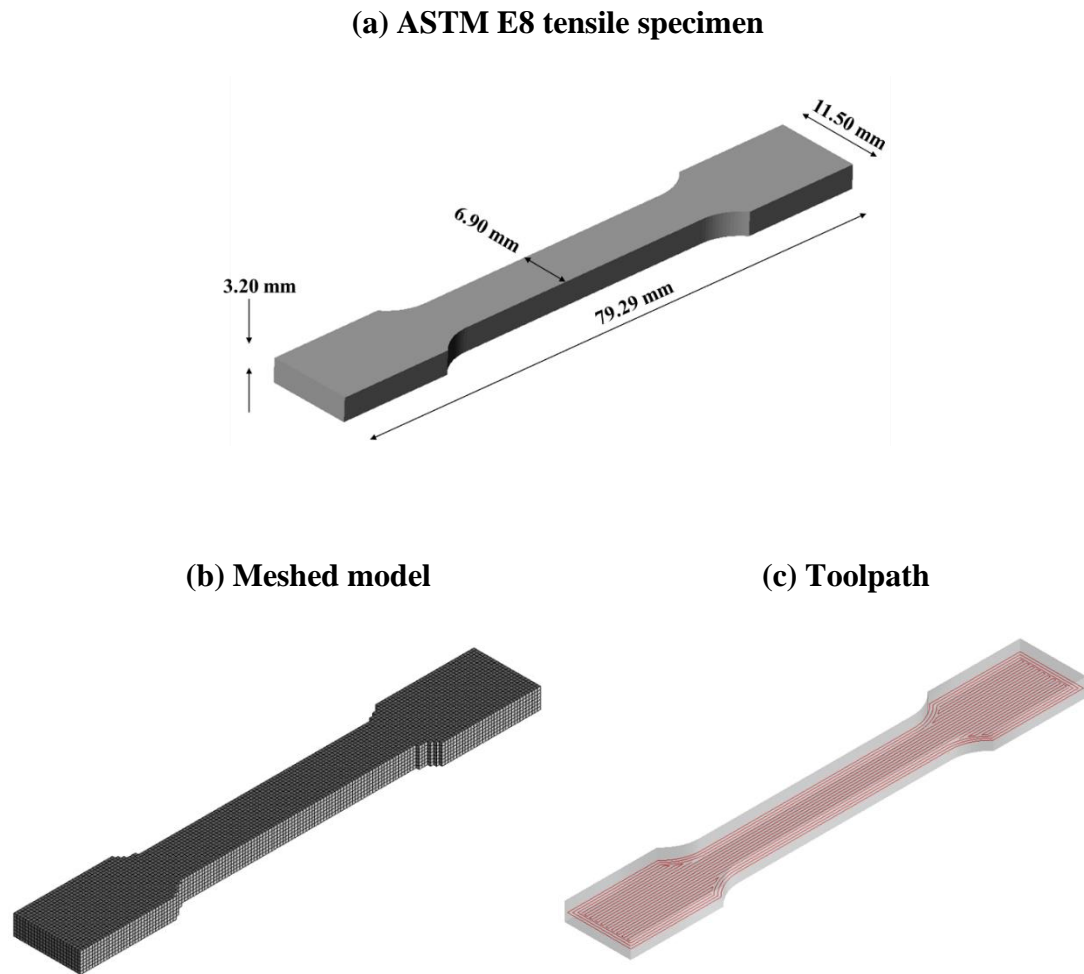


Figure 2.3. (a) ASTM E8 tensile bar dimensions (b) meshed model with voxel element size 0.3 mm (c) GCode data defines the 0 - 90° toolpath generated in the slicing tool

To simulate the progress in the printing process as defined in GCode, simulation provides two approaches. A ‘layer-by-layer discretization’ method, where the voxel elements are activated, and results are computed for one layer at a time. Whereas in the ‘filament discretization’ method, a chunk of elements representing filament deposition gets activated and computed at a time. While the filament discretization method provides more insights into thermal evolution within each layer, it was difficult for a full tensile bar model due to computational limitations. Hence, a layer-by-layer discretization’ method was used in this study. Having defined the material, geometry, toolpath, and process parameters, the job was submitted for thermo-mechanical simulation. The printing process and printed part quality were evaluated by post-processing the simulation results.

2.2.2 Printing experiments

To verify MF³ printing simulation results, printing experiments were performed using the same geometry, material, and processing conditions as used in simulations. The ASTM E8 tensile bar STL file was processed through Simplify3D to generate GCode instructions. Filaments with Ti-6Al-4V of 59 vol.% feedstock and unfilled ABS were used in a spooled form. The filament diameter was 1.75 mm, which is standard for most desktop printers. An FFF desktop printer, Pulse from MatterHackers, was used for printing. Five samples were printed with a given set of input parameters. The processing parameters used were the same as those used in simulations, as shown in **Table 2.1**. A few additional control parameters were defined in experimental printing, like extrusion multiplier, which was kept as 1.0 because simulation does not take this variable into account. Similarly, the skirt was defined to overcome oozing by purging and get a smooth flow through the nozzle, though

simulation does not model these features. Also, a 100 % infill was used to get a fully dense part.

The printed parts were characterized for dimensional changes and distortions compared to the original CAD design. A Vernier caliper was used for measuring the dimensions of the printed parts. Optical microscopy was used to evaluate Z-warpage. Additionally, an optical surface profiler (Keyence VR-5000) was used to generate the 3D surface geometry of the printed parts. These results were compared with simulated part geometry and original design geometry for verification.

2.3 RESULTS AND DISCUSSION

In the MF³ printing process, the material softens and partially melts when pushed through the extruder-nozzle. **Figure 2.4** shows the temperature evolution results from the thermal analysis of Ti-6Al-4V feedstock for the initial two layers by sequential element activation in the ‘filament discretization’ method during the printing process. It was observed that temperature was ranging between 96 °C and 63 °C. As the extrudate was deposited on a substrate, a chunk of elements was graphically activated representing a small portion of the deposited bead at a higher temperature. As the printing progressed, the previously deposited extrudate cooled down to a temperature close to that of the heated bed, 65°C. This can be attributed to the heat loss to the environment due to lower ambient temperature in the absence of a closed heated chamber [29].

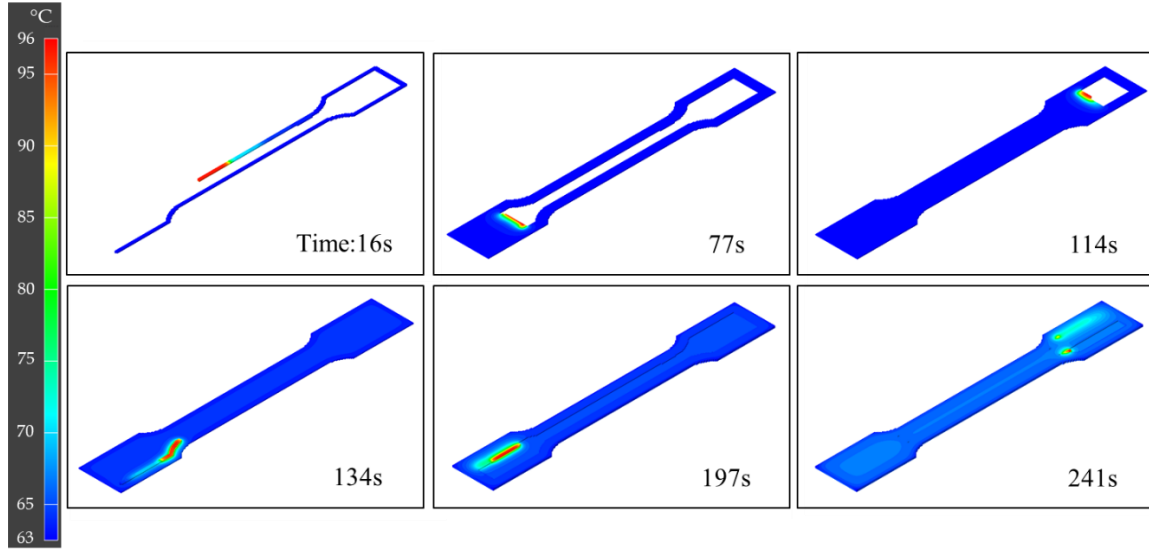


Figure 2.4. MF³ printing simulation progress by sequential element activation algorithm; temperature variation plot concerning time in sync with material deposition in the printing experiment of Ti-6Al-4V feedstock

As the extrudate from the nozzle was deposited on a substrate, it cooled down and solidified. With the addition of subsequent layers, repeated cycles of heating and cooling led to the development of a thermal gradient along the Z-axis. This gradient combined with non-uniform cooling leads to inherent thermal strains in the printed part. The extent of the strain varies according to the thermal gradient and coefficient of thermal expansion (CTE) of the material. The thermal strain causes deflection and warpage, finally leading to deviations in printed part dimensions and shape as opposed to original CAD geometry [30]. Hence, to achieve the desired part quality and dimensional tolerances, it is important to understand and control the deflection and warpage phenomenon during MF³ printing.

The mechanical simulation provides an estimation of deflections in X, Y, Z directions as well as the overall deflection results for a given material, geometry, and process

parameters. The estimated maximum deflection for the ASTM E8 tensile bar with Ti-6Al-4V feedstock was found to be 0.44 mm, as shown in **Figure 2.5a**. As the deposited extrudate underwent phase change during the printing process, a considerable amount of shrinkage occurred, depending upon the CTE of the material leading to part deflection and changes in dimensions. Unfilled ABS showed a higher deflection value, 0.83 mm, as shown in **Figure 2.5b**. This can be attributed to the higher CTE value of unfilled ABS than that of Ti-6Al-4V feedstock having 59 vol.% of metal powder. However, the deflection pattern was found to be the same for both materials.

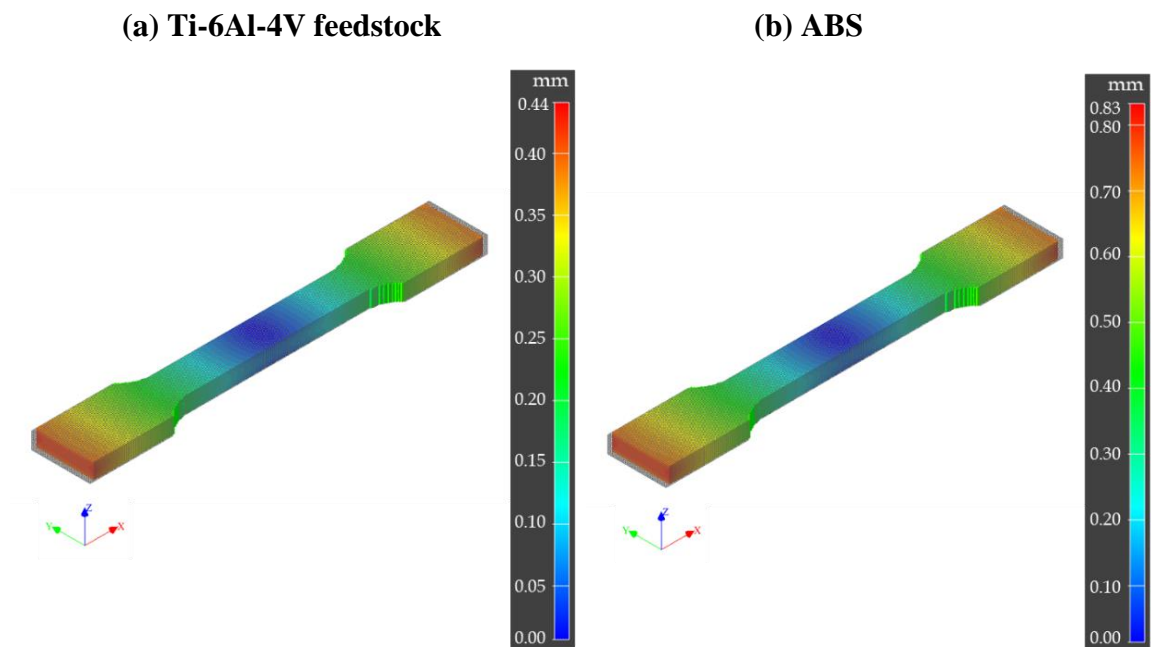


Figure 2.5. Part deflection estimation: (a) Ti-6Al-4V feedstock (b) ABS

2.3.1 Dimensional variation

The simulation tool does not directly provide simulated part dimensions. To estimate the part dimensions from deflection results, the deformed part geometry was exported from the

simulation results in STL format. This file was then imported into CAD software (SolidWorks) to generate a 3D model, and dimensions of the deformed part were measured in SolidWorks. These dimensions represent the estimated dimensions of the printed part with given material and processing parameters. To verify the simulation results, the respective dimensions of physically printed parts were measured using a Vernier caliper. **Figure 2.6** shows the dimension results from simulation and experiments for Ti-6Al-4V feedstock and unfilled ABS.

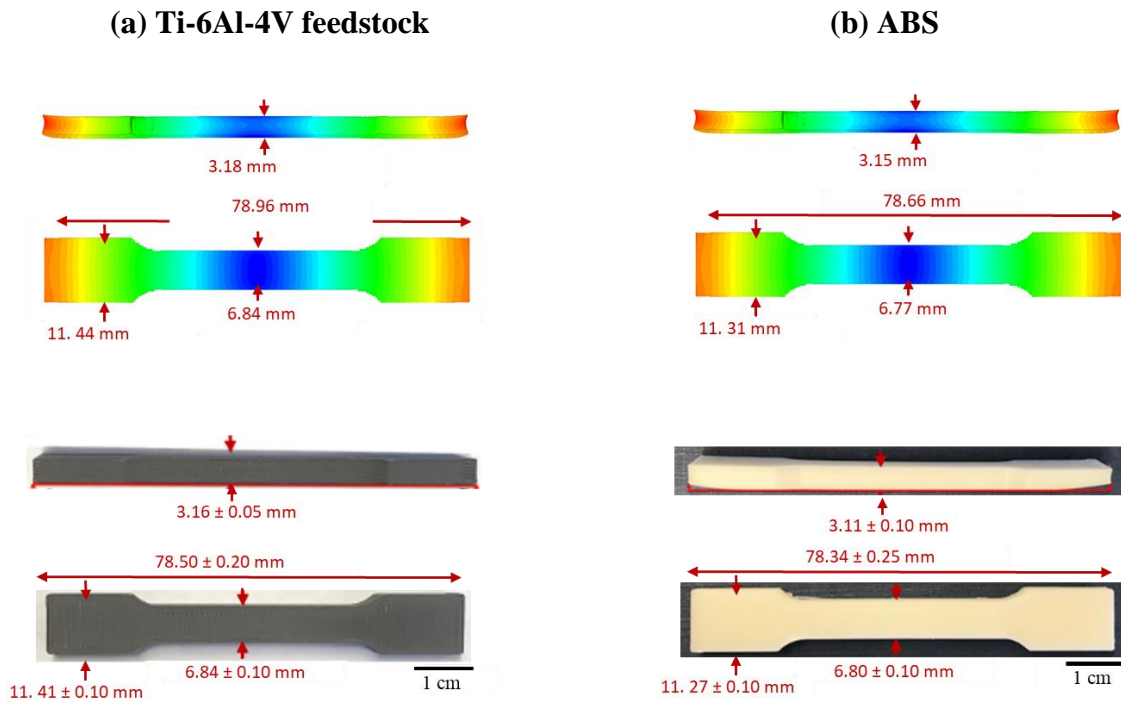


Figure 2.6. Part dimensions: simulation and experiment results (a) Ti-6Al-4V feedstock (b) ABS

As shown in **Figure 2.6a**, both simulation and experiment with Ti-6Al-4V feedstock showed shrinkage in all three directions (X, Y, Z) consistently. Simulation results showed

a maximum 1 % change in dimensions in XY-plane and a 1.5 % change in Z-dimension. In comparison, the experimental results showed 0.6 % and 0.9 %, respectively. Experimental part dimensions fairly matched with that of the simulated part. The shrinkage was observed to be higher along Z-axis than in the XY plane in simulation as well as experiments. This can be attributed to a higher thermal gradient along Z-axis than in XY-plane, due to layer-by-layer printing. Moreover, it was noted that simulations showed an overall higher shrinkage than experiments. This may be due to the stress relaxation effect in experiments tending to lower residual stress and lower overall deflection. In contrast, the simulation model currently does not take the stress relaxation effect into account, leading to higher residual stresses during printing which tends to develop higher deflections at the end of printing.

Similarly, for ABS, both simulation and experiment results showed shrinkage in all three directions (X, Y, Z) consistently, as shown in **Figure 2.6b**. Also, experimental part dimensions fairly matched with that of the simulated part. However, it was observed that ABS showed a higher amount of dimensional variations compared to Ti-6Al-4V feedstock in both simulations and experiments. Simulation results showed a maximum 1.9 % change in dimension in XY-plane and a 2.8 % change in Z-dimension, whereas the experimental results showed 1.4 % and 2.2 %, respectively. Shrinkage along Z-axis was observed to be higher than that in the XY-plane in simulation as well as experiments. **Table 2.2** summarizes the simulation and experiment dimensions compared to theoretical dimensions for both materials. Compared to Ti-6Al-4V feedstock, ABS parts showed higher dimensional changes. It is attributed to higher shrinkage resulting from the higher CTE

value of ABS unfilled copolymer. This difference indicates the influence of material composition and resulting material properties on printed part quality in the extrusion-based additive manufacturing process. Also, this sensitivity of the simulation model to material properties variations was verified by experimental results from both materials.

Table 2.2. Part dimension results; simulations and experiments with Ti-6Al-4V feedstock and unfilled ABS

Description	Length (mm)	Grip-width (mm)	Gauge-width (mm)	Thickness (mm)	Z-warpage (mm)
CAD Dimensions	79.29	11.50	6.90	3.20	0.00
Ti-6Al-4V: Simulation	78.50	11.42	6.84	3.15	0.15
Ti-6Al-4V: Experiment	78.86 ± 0.20	11.44 ± 0.10	6.86 ± 0.10	3.17 ± 0.05	0.28 ± 0.05
ABS: Simulation	77.80	11.34	6.81	3.11	0.27
ABS: Experiment	78.14 ± 0.25	11.29 ± 0.10	6.77 ± 0.10	3.10 ± 0.10	0.63 ± 0.10

Part distortion

Apart from dimensional changes, distortion of part geometry was observed consistently for both materials in simulations as well as experiments. The non-uniform shrinkage caused by differential cooling during printing led to a non-uniform distribution of thermal strains causing warpage and distortion of part shape.

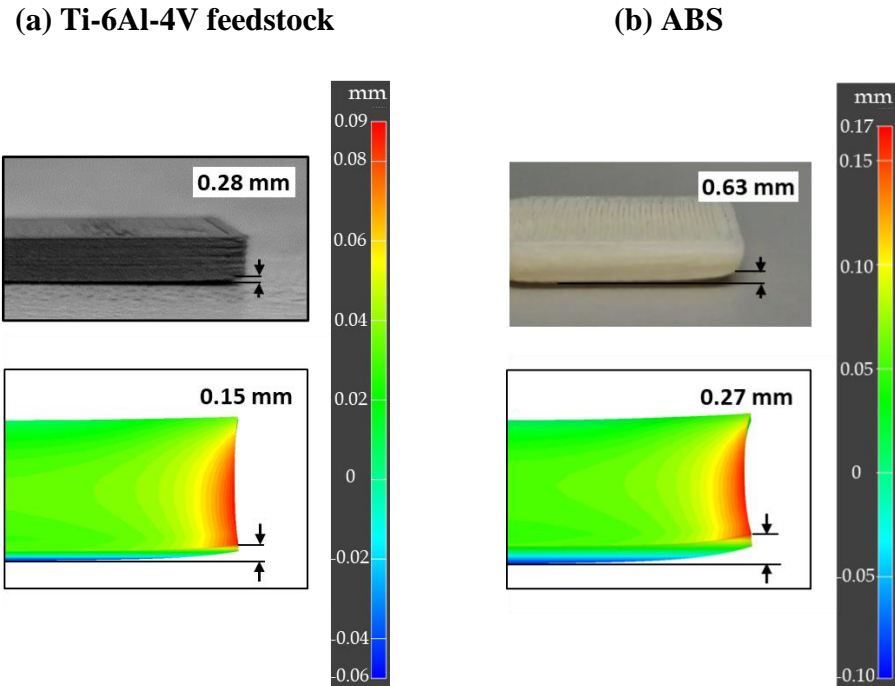


Figure 2.7. Z-warpage: simulation and experiment results (a) Ti-6Al-4V feedstock (b) ABS

The part distortion was seen to be more significant along the Z-axis. As shown in **Figure 2.7a**, the estimated maximum Z-warpage for the Ti-6Al-4V feedstock tensile bar was 0.15 mm, whereas experiments showed 0.28 mm. Similarly, ABS showed 0.27 mm and 0.63 mm Z-warpage in the simulation and experiment, respectively, as shown in **Figure 2.7b**. Following the same trend as dimensional change results, Z-warpage was found to be higher in ABS compared to Ti-6Al-4V feedstock, due to the higher CTE value.

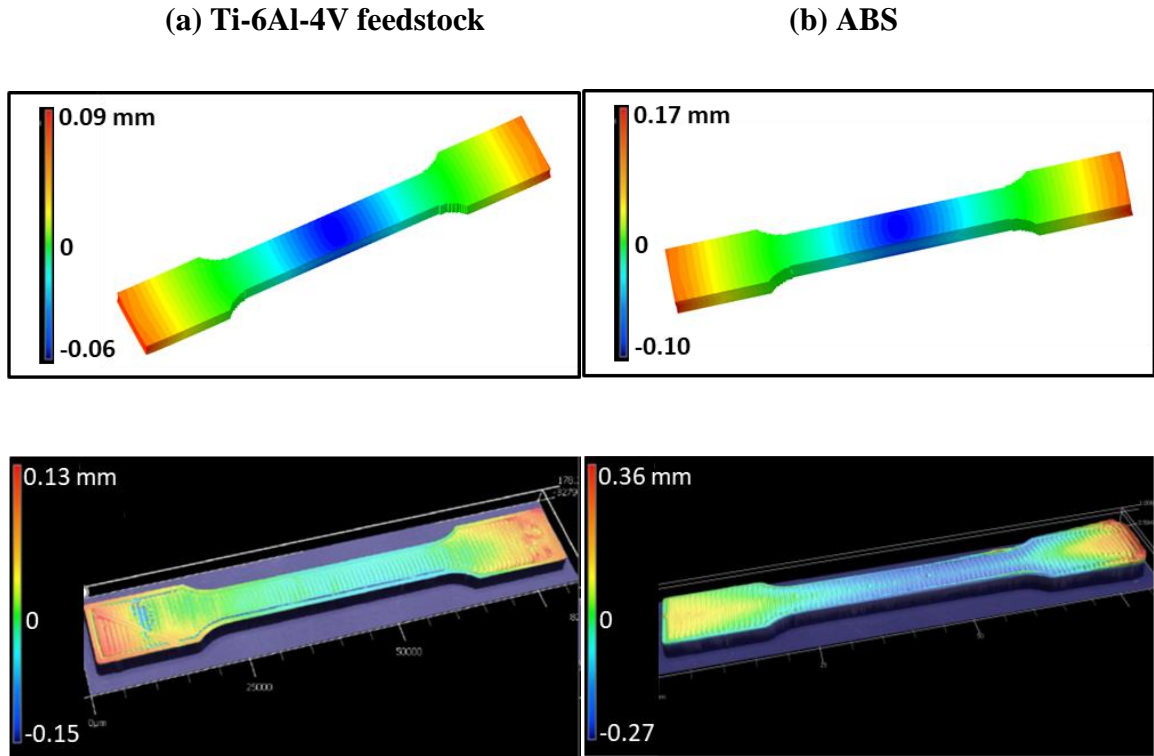


Figure 2.8. Part distortion along the Z-axis: simulation and optical surface profilometry results (a) Ti-6Al-4V feedstock (b) ABS

Moreover, the higher Z-warpage in experiments than in simulations may be attributed to imperfect adhesion of part base to the heated print bed. As printing progressed, the temperature at the bottom layer dropped to bed temperature, leading to a phase change from viscous melt to solid. Non-uniform cooling of the part developed thermal strains and residual stresses. The residual stresses at the base were high enough to overcome the adhesion between the part base and print bed; subsequently, it caused peeling off at the part base edges and corners leading to the increased Z-warpage. After partial detachment, due to lesser resistance, the part base tended to warp to a greater extent in experiments. However, the simulation assumes a perfect adhesion between part base and print bed, and

this boundary condition remains constant throughout the printing stage of simulation and is taken off during the cooling stage. Simulation and printing experiments showed similar warpage patterns and locations for both materials. **Figure 2.8** shows the overall part distortion along the Z-axis. The scanned printed part surface models obtained from optical surface profilometry showed agreement with the simulated part distortion. Extreme ends of the part were found to be deflecting the most. This can be attributed to a higher rate of heat loss by convection and faster cooling at the two ends. Also, the bending distortion resulting from tension-compression stresses developed across the part thickness leads to maximum deflection at the ends of the part geometry. The distortion pattern was similar in both materials, whereas unfilled ABS showed a higher magnitude due to a higher CTE value than that of Ti-6Al-4V feedstock.

2.3.2 Reverse warpage

Besides the estimation of part deformation, the simulated deformed part geometry was used to optimize the original design to achieve the desired target dimensions keeping material and processing parameters unchanged. The deformed simulated geometry was scaled by a compensation factor of -1.0 to develop a reverse warpage model. The model was exported in STL format from Digimat and imported into SolidWorks. In **Figures 2.9a** and **b**, the grey part is the reverse-warped geometry, and the black part is the original design geometry CAD models. From the overlapped CAD models, it was observed that the reverse-warped geometry is slightly larger in dimensions than the original design and warped in a pattern opposite to the estimated warpage pattern. The required geometry compensation for unfilled ABS was observed to be higher than that for the Ti-6Al-4V feedstock.

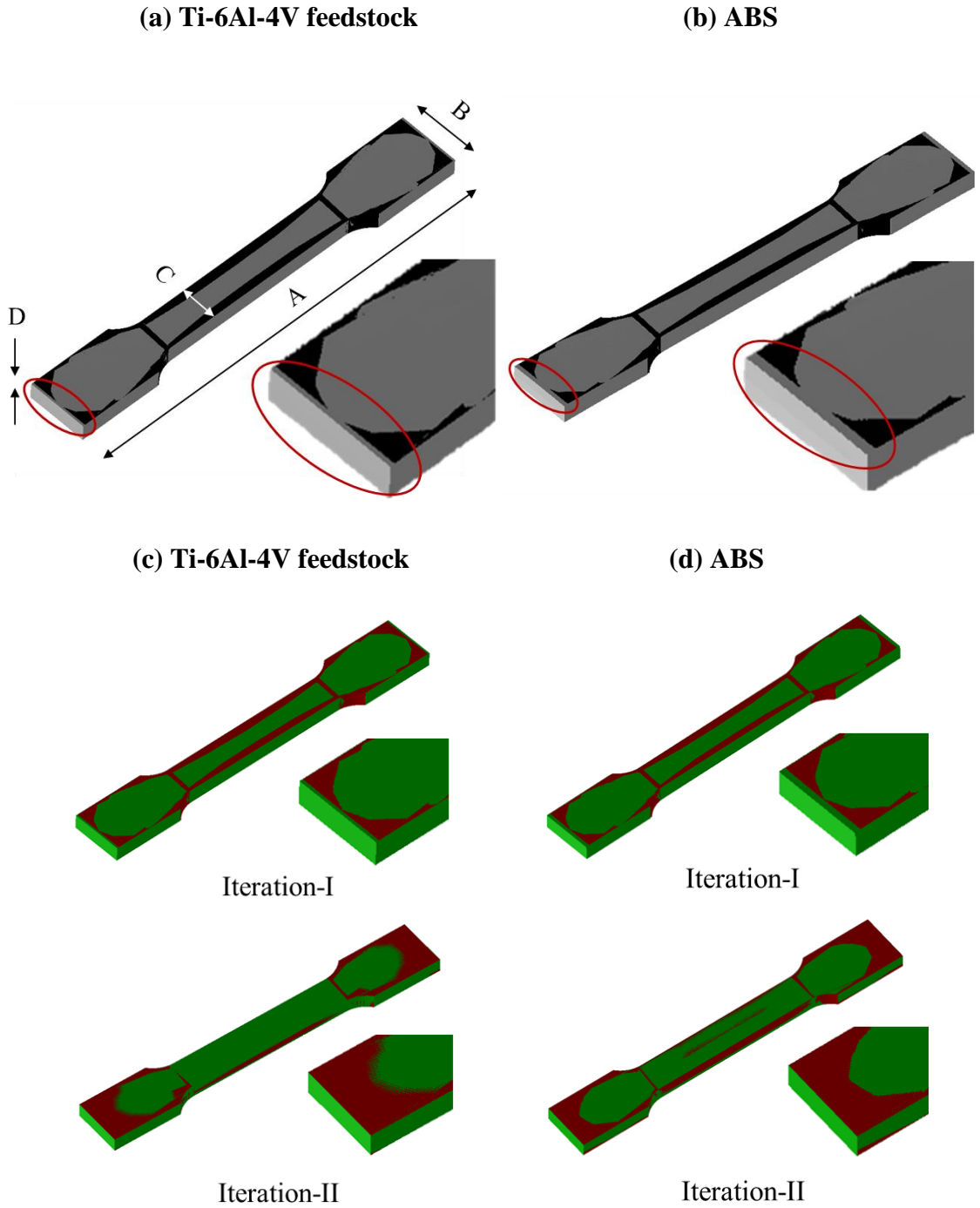


Figure 2.9. (a) and (b) Reverse-warped geometry (grey) overlapped with original design geometry (black) for Ti-6Al-4V feedstock and ABS, respectively. Larger warpage compensation was required in ABS. (c) and (d) Warped geometry (red) overlapped with original design geometry (green) for Ti-6Al-4V feedstock and ABS, respectively. Iteration-

I and Iteration-II represent before and after warpage compensation, respectively. Warpage compensation leads to higher geometric conformity.

The reverse warpage model was used as a compensated geometry to counter the shrinkage and distortion that took place during the printing process. With compensated geometry, the next iteration of the simulation was conducted keeping the rest of the input unchanged. The simulation results showed a similar phenomenon of the thermal gradient, residual stresses and deflection as in the first iteration. However, the resulting part geometry matched with the as-designed CAD geometry. **Figure 2.9c** and **d** show the comparison of as-designed geometry (green) with as-printed warped geometry (red). Iteration-I simulation results indicate that without warpage compensation there was a lack of shape fidelity and geometric precision. However, the part geometry from the Iteration-II simulation taking into account the geometry compensation was matching closely with the as-designed CAD geometry. The reverse-warped geometry was further used in the Iteration-II of printing experiments for both materials.

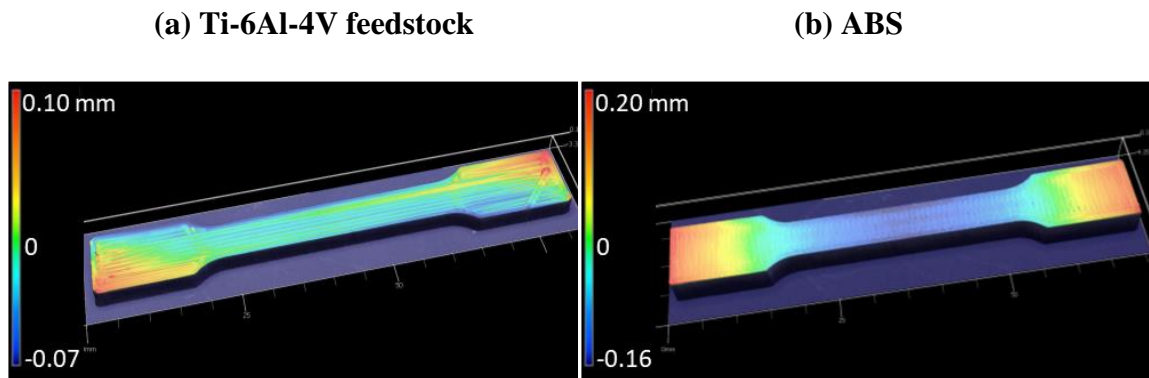


Figure 2.10. Part distortion along the Z-axis: optical surface profilometry results in experiments Iteration-II (a) Ti-6Al-4V feedstock (b) ABS

The optical surface profilometry as shown in **Figure 2.10** validated that warpage compensation in geometry led to a lower Z-warpage compared to the ones from the original CAD geometry as shown in **Figure 2.8**.

The printed part dimensions were measured and compared with simulated part dimensions as shown in **Table 2.3**. Simulation results showed all the dimensions in Iteration-II closely matched the theoretical CAD dimensions, and the Z-warpage was found negligible for both materials. Similarly, printed part dimensions showed improvement in overcoming the shrinkage. However, all the dimensions in the printed part were found to be greater than the theoretical CAD dimensions. This could be attributed to the fact that in simulation, stress relaxation was not taken into account, resulting in higher residual stresses and increased deflection at the end of printing, and ultimately leading to a larger amount of geometric compensation than needed experimentally. However, this discrepancy can be addressed by further adjusting the geometry compensation through multiple iterations to identify a typical compensation factor. The investigation of the iterative procedure to achieve desired dimensions in printed parts for various geometries through simulation will be conducted in future studies to provide a protocol for correctly printing the part right the first time.

Table 2.3. Part dimension results using compensated geometry in Iteration-II; simulations and experiments with Ti-6Al-4V feedstock and unfilled ABS

Description	Length (mm)	Grip-width (mm)	Gauge-width (mm)	Thickness (mm)	Z-warp (mm)
CAD Dimension	79.29	11.50	6.90	3.20	0.00
Ti-6Al-4V - Simulation (Iteration-II)	79.27	11.49	6.89	3.20	0.01
Ti-6Al-4V: Experiment (Iteration-II)	79.54 ± 0.20	11.53 ± 0.10	6.92 ± 0.10	3.21 ± 0.05	0.09 ± 0.05
ABS: Simulation results (Iteration-II)	79.24	11.49	6.90	3.19	0.04
ABS: Experiment (Iteration-II)	79.68 ± 0.15	11.55 ± 0.10	6.93 ± 0.10	3.23 ± 0.10	0.52 ± 0.10

2.3.3 Thermal history

In the extrusion-based printing process, the thermal history of deposited material influences phase transition from a viscous fluid to a solid. Repeated cycles of heating and cooling can lead to the development of a significant thermal gradient in Z-direction. Also, the heat loss differential between the central zone and outer periphery builds up a thermal gradient in XY-plane. The thermal gradients lead to residual stresses and distortion in the printed part.

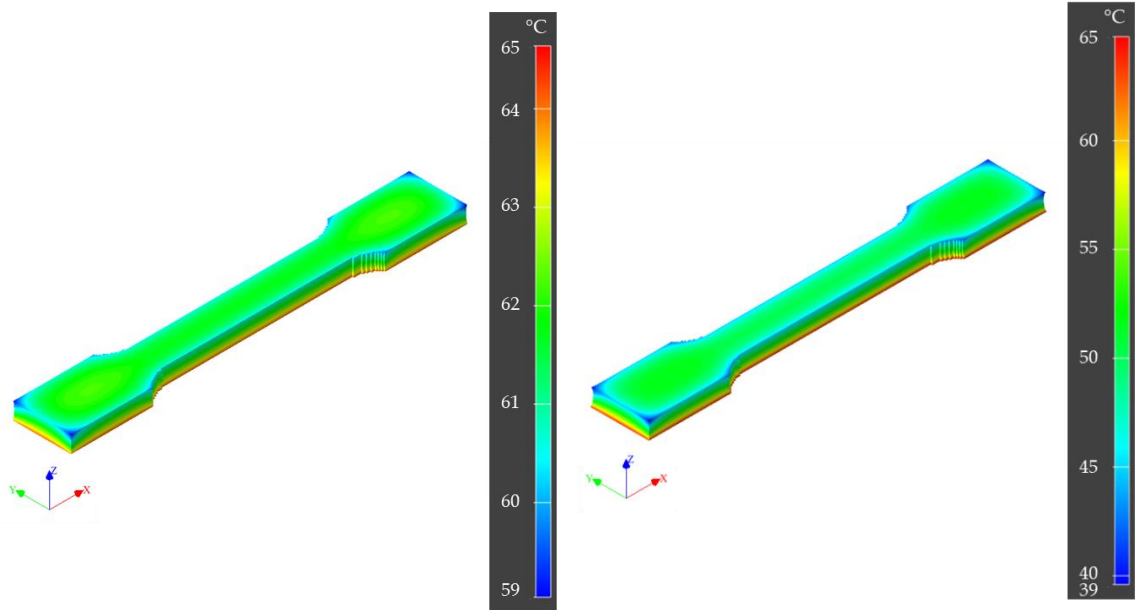
The simulation was able to predict the temperature distribution and thermal history utilizing a transient thermal analysis. **Figure 2.11a** and **b** show the temperature variation indicating the thermal gradient at the end of printing, before the cooling stage. For the Ti-6Al-4V feedstock, the temperature distribution in printed layers was found to be in the range of 65 °C to 59 °C. The extrusion temperature used was 240°C. However, the

temperature results are calculated at the end of printing each layer. As the print time per layer was long enough (680s), by the time a layer was finished, the deposited material in that layer had sufficient time to cool down before the next layer was deposited. However, the print bed was maintained at 65°C, which corresponds to the bottom layer temperature. For unfilled ABS, the temperature distribution in printed layers was found to be in the range of 65 °C to 39 °C. The lower minimum temperature in ABS may be attributed to the lower thermal conductivity of unfilled ABS polymer than that of Ti-6Al-4V feedstock material. Moreover, the larger thermal gradient in ABS is expected to lead to higher thermal strains and part distortion in ABS.

The study of local temperature evolution during the process is of importance as it affects the phase transition and crystallization process, and hence the resulting part properties. In particular, the temperature of the previously deposited layer and the new incoming layer have a significant impact on interlayer bond strength [31, 32]. **Figure 2.11c** shows the local temperature evolution across the part thickness for the Ti-6Al-4V feedstock part. It was observed that the temperature of a deposited layer at the time of subsequent layer deposition decreases along Z-direction. It can be attributed to limited heat transfer from the heated bed to deposited layers as Z-height increases. Hence, it can be argued that the interlayer bond strength in the top layers would be lower than that in the bottom layers.

(a) Ti-6Al-4V feedstock

(b) ABS



(c) Thermal history

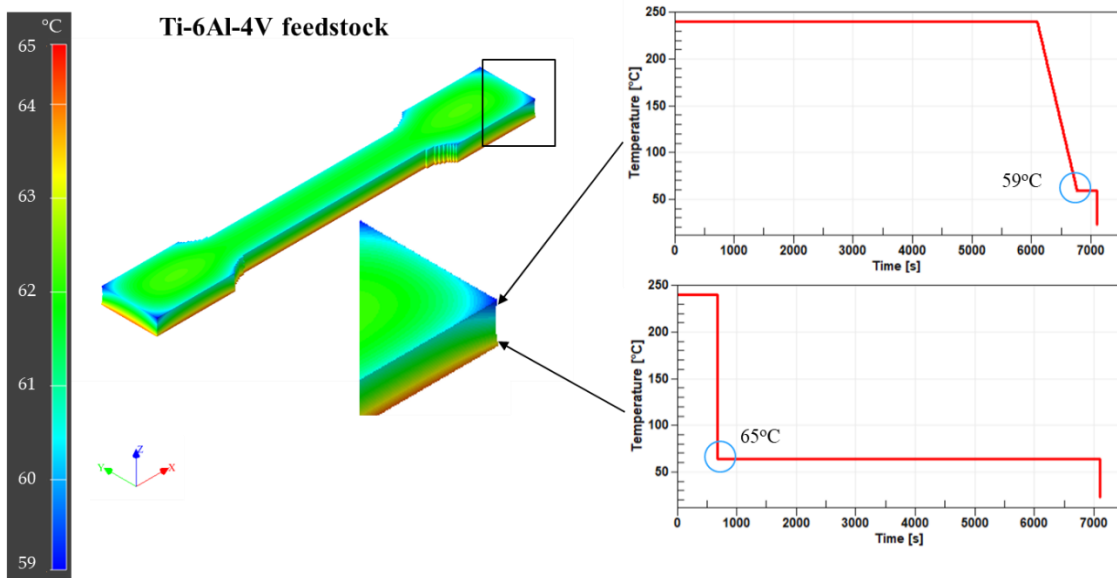


Figure 2.11. Temperature distribution at the end of printing; (a) Ti-6Al-4V feedstock (b) ABS (c) Thermal history estimation for Ti-6Al-4V feedstock part

2.3.4 Residual stresses

The simulation also provides an estimation of residual stresses induced during and at the end of the MF³ printing process. **Figure 2.12** shows the von Mises stresses as residual stresses developed at the end of printing that can be primarily attributed to the thermal gradient along the Z-axis as a result of layer-by-layer stacking combined with non-uniform cooling. Also, the heat loss differential between the central zone and outer periphery builds up the thermal gradient in XY-plane and adds to residual stresses along the plane.

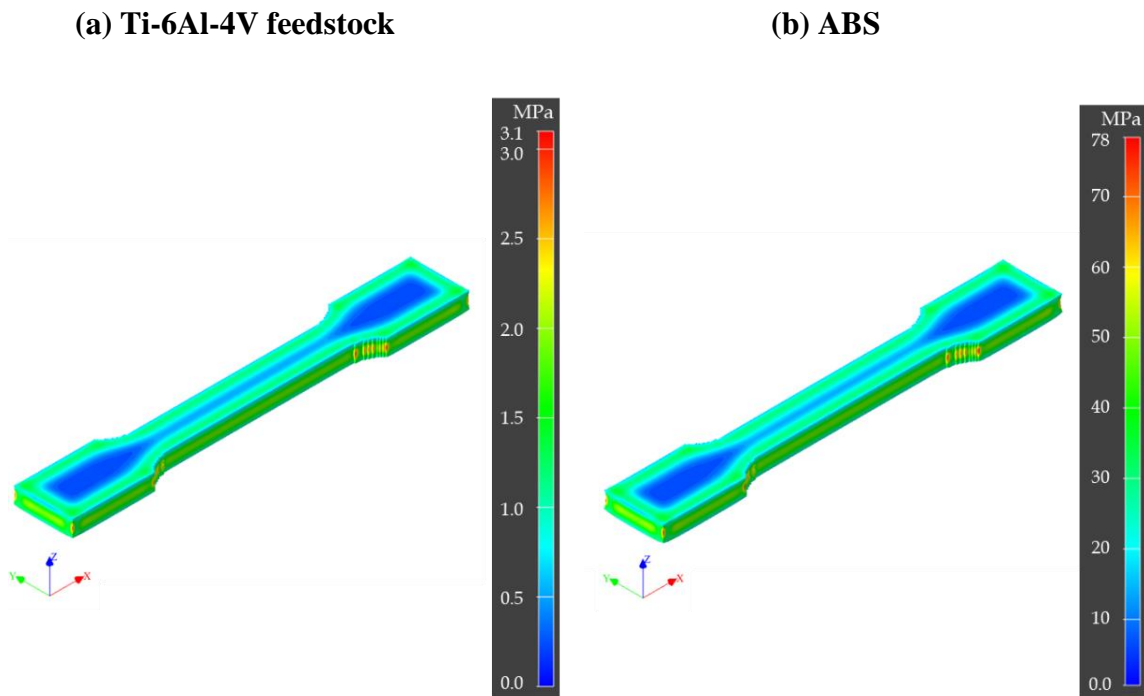


Figure 2.12. Residual stresses (von Mises) at the end of printing; (a) Ti-6Al-4V feedstock
(b) ABS

For the Ti-6Al-4V feedstock, the maximum residual stress of 3.1 MPa was observed at four corners and the outer periphery. ABS showed a similar pattern of residual stress

distribution, but with a higher magnitude of 78 MPa. The higher stress value was attributed to higher material stiffness, Young's modulus, of ABS that was taken into account in the thermomechanical simulation model.

Residual stresses distort the printed part and affect its mechanical strength. In MF³, high residual stresses may lead to cracks or damage the part during the debinding and sintering processes. Lower thermal gradient, uniform and slower cooling helps in reducing residual stresses. Hence a closed chamber-controlled temperature printing environment would provide better part quality. The effects of material properties and process parameters on residual stresses in MF³ are currently being investigated by our group. Experimental verification using the crack compliance approach is being investigated and will be reported in the future.

2.4 CONCLUSIONS

MF³ printing process was simulated for the first time and results were verified with experiments. Following conclusions emerge from the present work:

1. Simulations and printing experiments showed similar warpage patterns and locations, and shrinkage in all three directions (X, Y, Z) consistently for both Ti-6Al-4V and ABS. Shrinkage along Z-axis was observed to be higher than that in XY-plane in both simulation and experiment due to a higher thermal gradient along the Z-axis. Also, simulations showed an overall higher shrinkage than experiments because the stress relaxation effects are not considered in the simulation platform.

The higher dimensional change in ABS parts than that in Ti-6Al-4V feedstock was attributed to the higher CTE of the unfilled ABS polymer.

2. The estimated maximum Z-warping was lower than the experiment results for both materials. It can be attributed to imperfect adhesion of the part to the heated bed in experiments, which is ignored in simulation.
3. Ti-6Al-4V feedstock showed a lower thermal gradient than ABS due to higher thermal conductivity brought in by the Ti-6Al-4V alloy. A larger temperature gradient in ABS resulted in higher thermal strains and part distortion.
4. Simulation of Ti-6Al-4V feedstock and ABS showed a similar pattern of residual stress distribution but a significantly higher magnitude was observed in ABS. The higher stress value was attributed to the higher material stiffness of ABS that was considered in the thermomechanical simulation model.
5. The difference in material properties between Ti-6Al-4V and ABS led to differences in part dimensions, warpage. It also verified the sensitivity of the simulation model to material properties that were further corroborated by the experimental results.
6. Warpage compensation algorithms showed improvement in dimensional control for both materials in simulations and were consistent with experimental results.

Looking into the perspectives for avoiding or minimizing distortion and achieving higher dimensional accuracy, materials with lower CTE tend to undergo a smaller volumetric change for a given temperature differential. Also, lower extrusion temperature and reduced thermal gradients in all three directions would lead to lower distortions. The authors are

investigating a process sensitivity analysis of MF³ to look into more details. Moreover, for a semi-crystalline material, the print bed and surrounding temperature would have considerable effects on the crystallization process affecting the degree of crystallinity and part's physical and mechanical properties. Having a closed chamber-controlled temperature and print bed temperature above the crystallization point would lead to slower cooling and low distortions. It would be useful to investigate these aspects in MF³ feedstock containing a multi-component polymer binder highly filled with metal powder.

The identified gap between simulation and experimental results can be attributed to more than one factor, such as stress relaxation behavior of polymer composite, imperfect sticking of the bottom layer to print bed and crystallization process that were not yet taken into account in the simulation. Moreover, melt rheology would also have impacts on part distortions as it affects the diffusion between layers and tracks. Investigations into considering these phenomena in simulations would be imperative to improve prediction accuracy. Based on the current study, the above aspects are being explored as future studies.

CHAPTER 3

PROCESS SENSITIVITY AND SIGNIFICANT PARAMETERS INVESTIGATION IN METAL FUSED FILAMENT FABRICATION (MF³) OF TI-6AL-4V

3.1 INTRODUCTION

Additive manufacturing (AM) is a technology for fabricating 3D objects by adding material layer upon layer, as opposed to subtractive and formative manufacturing technologies. AM is being increasingly used for fabricating three-dimensional parts from polymers, metals, or ceramics used in various applications [1]. Metal fused filament fabrication (MF³) is a hybrid AM process used to fabricate custom 3D metal components [10]. The established metal additive manufacturing processes such as laser-powder bed fusion, direct metal laser sintering, and direct energy deposition are energy-intensive and not suited for certain specific requirements like in-space manufacturing. MF³ provides the best alternative to address these challenges. It is a multi-step process that involves: (a) mixing and extrusion of a powder-polymer mixture into filaments, (b) 3D printing of a green part, (c) polymer removal from the 3D printed green part by debinding to get a brown part, and (d) densifying the brown part to achieve a fully dense metal part by sintering. MF³ has been found capable of metal additive manufacturing of materials like Ti-6Al-4V, bronze, copper, 17-4 PH stainless steel, 316L stainless steel [6-8, 33].

The material system used in MF³ comprises an optimum composition of metal powder mixed with a multi-component custom polymer binder, like in powder injection molding (PIM). The solids loading and binder composition are varied for different material systems to enable efficient debinding and sintering, or to meet specific application needs [34]. Consequently, the properties of new material may vary considerably. Now, questions arise as to how these changes in material properties in MF³ would influence the process outcome, and consequently, the properties and performance of the end product. The powder-binder composites filament is processed by an extrusion-based 3D printing process, fused filament fabrication (FFF), which is typically used to get a 3D shape with polymers [1]. The printing process has several input variables, like extrusion temperature, build plate temperature, printing speed, layer thickness, extrusion width, toolpath and slicing strategy. These process parameters have significant effects on printed part quality and performance. The layer-by-layer material deposition develops temperature gradients leading to warpage and residual stresses in the printed part which are influenced by printing parameters [14, 35]. Hence, there is a need for establishing optimized parameter settings for specific materials. The common trial-and-error experimental approach is often costly and time-consuming, and sometimes not even feasible. Moreover, the empirical relationships between input and output parameters are often not straightforward which compels a greater understanding of the process dynamics.

Computational simulation techniques provide effective alternative means to predict the printing process outcome by estimating the thermo-mechanical behavior of the material being printed [18, 27, 29, 36, 37]. The availability of FEA-based simulation tools has shown promise for aiding engineers to resolve the interrelated problems involving material-

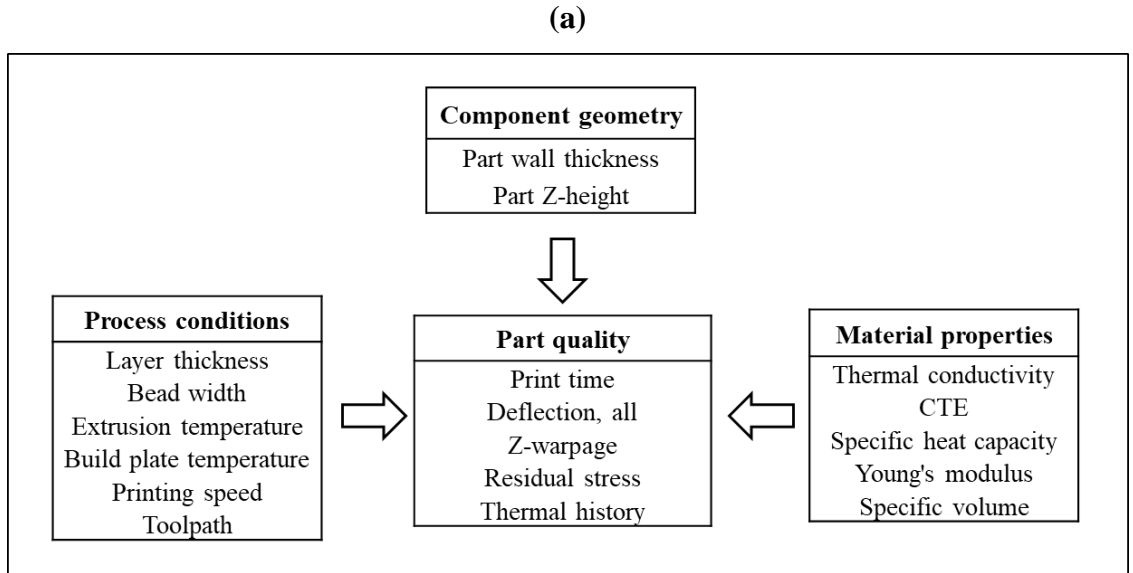
process-geometry in the FFF process [13, 26]. However, the use of such tools to perform material and process simulations of the MF³ printing process is yet to be explored, which will favor the widespread use of MF³ to manufacture parts with different materials for a variety of applications [38].

A lot of research has been published on experimental or analytical methodologies for the optimization of process parameters or study of the influence of process parameters on the outcome of fused deposition modeling (FDM) process [39-45]. However, in each study, only a few selected process parameters were investigated, though there exist definite interrelationships between material, process and geometry. Hence, there is a need for the identification of significant input parameters and the extent of sensitivity of process output parameters to each input parameter. Atre et al. used a process simulation tool for sensitivity study and identification of significant material, process and geometry parameters in powder injection molding [46]. A similar approach has been followed for MF³ in this study. Additionally, various geometries were studied to investigate how sensitivity and influence may vary with part geometry.

Moreover, understanding the constraints imposed by the extrusion-based additive manufacturing process and highly filled material used in MF³ is crucial for successful design and manufacturing. Hence, there is a need for design for MF³ (DfMF³) approach, supported by relevant design tools. Also, the development of the end product calls for several factor considerations to improve the functional and aesthetic attributes of the part. It may lead to multiple design changes. Here, the questions arise as to how the changes in product design influence the process outcome. Moreover, any variations in powder-polymer composition can consequently affect filament properties, filament processing, 3D

printing, debinding, and sintering. Accordingly, material compositional variations can affect the printed part attributes. However, little information is available on the sensitivity of predictions by CAE simulation tools to the variations in material property values. Additionally, as several process settings need to be changed and controlled during the MF³ printing process, it is important to understand how a CAE simulation tool captures the influence of such process variations in its predictions.

The above crucial questions are addressed in the current study by analyzing the MF³ process for the sensitivity of the key output variables to the material, geometry and process input variables as shown in **Figure 3.1a**. FEA-based simulations are used to estimate the process outcome in response to variable inputs. CAE simulation tool, Digimat (MSC Software Inc., Newport Beach, CA, USA), was used for integrated thermo-mechanical process simulation. Process simulation helps in predicting and minimizing warpage and residual stresses, achieving intended dimensions through reverse warpage, and estimating the structural performance of the 3D printed parts. The quantitative relationships on the dependence of many MF³ process output parameters on changes in component geometry, process parameters and material properties are presented. A dimensionless sensitivity factor was calculated that allows the parameters with different units to be compared quantitatively with a single yardstick. It also facilitated the identification of dominant input parameters and relative contribution to each output parameter. The results provide important insights into the geometry-process-material interrelationships in the MF³ process.



(b)


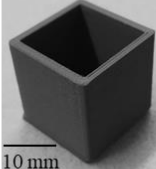
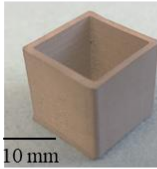

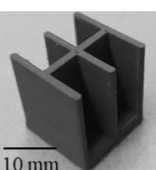
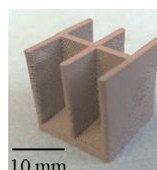

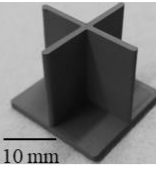
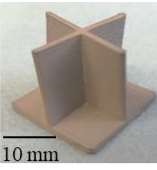
	CAD	Printed green part	Sintered part
Design I 1.5mm thick hollow cube 20mm x 20mm x 20mm			
Design II 1.5mm thick structure 20mm x 20mm x 20mm			
Design III 1.5mm thick structure 20mm x 20mm x 20mm			

Figure 3.1. (a) MF³ process sensitivity study framework: input parameters (process conditions, component geometry, material properties) and output parameters (part quality) investigated. (b) CAD and MF³ printed green and sintered parts. Three different geometries were studied to investigate process sensitivity variation with part geometry.

For each output parameter, the most significant input parameters were identified from the whole set of input parameters and their influence trends were evaluated for different part geometries. Such findings are expected to be useful in streamlining further development exercises including experimental studies that are now feasible and more meaningful. The present sensitivity analysis procedure can be used as a tool not only for process parameters optimization but also for the development of material and part geometry for MF³, hence, enabling design for MF³ (DfMF³). This study provides a powerful approach that can be applied to identify the parameters that need to be optimized in the design stage and carefully monitored and controlled in the production stage. Also, during material formulation development, the tool can provide insights about sensitivity evolution with different solids loading and binder compositions to optimize the formulations for MF³. The simulations in this study only focused on the printing stage of the MF³ process, as simulation solutions for debinding and sintering processes are under development.

3.1.1 FEA simulation of MF³ process


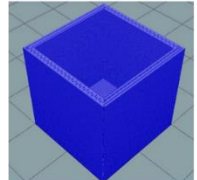
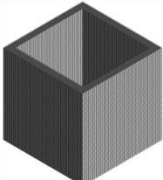

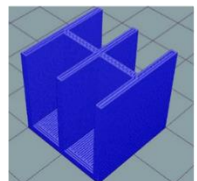
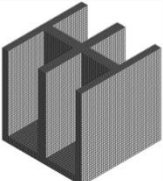

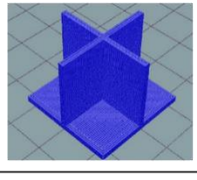
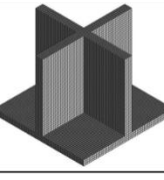
In this study, a commercially available simulation software, Digimat was used to perform finite element-based (FE) process simulations of the MF³ printing process. The tool provides the capability of using sequentially coupled thermomechanical analysis for both stress and heat analysis [28, 47]. It enables numerical analyses of the complex thermomechanical loadings that occur during the layer-by-layer deposition of the material and subsequent cooling of the part. The thermal gradient developed across the deposited material generates differential shrinkage between adjacent beads or layers. Through the element activation function in Digimat, a small part of the geometry was activated

sequentially that represents filament-wise printing that progresses layer-by-layer [25]. Once all the elements were activated, the final thermal history results are then used for a thermomechanical coupled analysis to simulate the solidification process and the cooling phase. Extrusion-based printing of highly filled powder polymer mixture in MF³ exhibits strong dependency on the filament material thermal, mechanical and physical properties. In this study, the properties used for Ti-6Al-4V with 59 vol.% solids loading in custom polymer binders were obtained from estimation models [10]. These properties represent the feedstock as well as the filament properties. The FE simulations were used to estimate print time, deflection/ warpage, residual stresses and thermal history that take place in the printing process. These estimations can enable design and process engineers to not only come-up with optimal material, geometry and processing parameters but also identify potential issues and troubleshoot them at the early stage of design.

3.2 METHODOLOGY

The simulations in this study focused only on the printing stage of the MF³ process. Simulation solutions for the debinding and sintering stages of the MF³ process are being developed and will be reported separately. In the present study, three different component geometries were selected and simulated as shown in **Figure 3.1b** to evaluate the printing process sensitivity variation with changing part geometry. An optimal formulation of Ti-6Al-4V with 59 vol. solids loading in a custom polymer binder for MF³ was developed by our research group [10, 11]. The same material was evaluated for process sensitivity in this study. To conduct a thermomechanical process simulation, a set of thermal and mechanical properties of feedstock material is needed.

(a)

	CAD - STL	GCode toolpath	Voxel mesh
Design I			
Design II			
Design III			

(b)

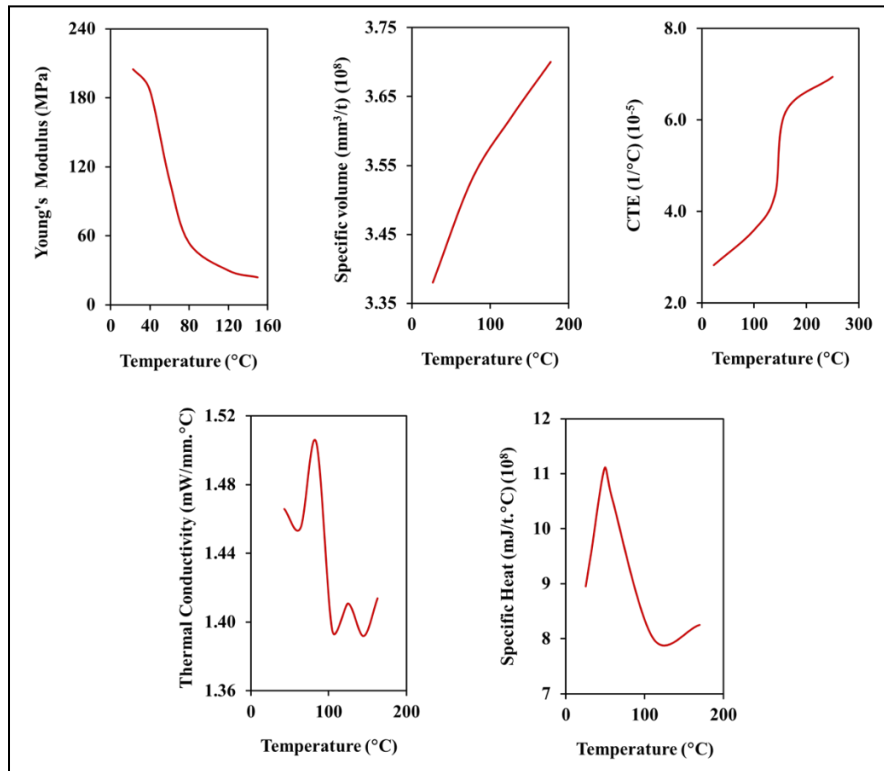


Figure 3.2. (a) FE model setup in Digimat: STL CAD file was used for slicing/ toolpath generation defined in GCode file, the same STL model meshed with 0.3 mm voxel

elements (b) Mechanical and thermal properties of Ti-6Al-4V with 59 vol.% feedstock over a range of temperatures used in MF³ printing process simulations

Figure 3.2b shows the properties of Ti-6Al-4V with 59 vol.% feedstock over a range of temperatures used to define the thermo-mechanical behavior of the material in the simulation tool, Digimat. A CAD model in STL format defines the part geometry to be simulated. It was discretized into voxel mesh, as shown in **Figure 3.2a**. The voxel mesh size is decided according to layer thickness and part geometry. A GCode file from a slicing tool, Simplify3D (Simplify3D, Cincinnati, OH, USA), defines the toolpath, layer thickness and printing speed. Other printing parameters like layer width, extrusion temperature, build plate temperature, chamber temperature, convection coefficient are defined through the simulation tool graphical user interface. Having the material, geometry and process input defined, thermo-mechanical simulations were performed for each of the three geometries.

For each geometry, first, a base case MF³ printing process was simulated with the given geometry, material properties, and typical process conditions as input parameters. Then, each input parameter was varied one at a time within a meaningful window, and the influence on the process outcome was noted. For each input variation, a simulation job was performed, and simulation results are reported as output parameters.

The input parameters for this study have been divided into three subgroups:

- component geometry parameters
- process conditions
- material properties

The output parameters evaluated in the study include:

- print time
- deflection
- Z-warpage
- residual stresses
- substrate temperature

The goal of this sensitivity analysis is to evaluate the sensitivity of output parameters to each of the input parameters and subsequently identify the most significant input parameters for each output parameter in the MF³ printing process.

3.2.1 Sensitivity analysis

For the sensitivity analysis, each input parameter was varied within a feasibility window. The response of each output parameter was recorded to evaluate its sensitivity to variations in input parameters. The sensitivity was calculated as the gradient or slope of the dimensionless dependent variable concerning the dimensionless independent variable according to the following equation [46]:

$$\text{Sensitivity} = \frac{\% \text{ change in output}}{\% \text{ change in input}} = \frac{\text{increment in output/ initial value of output}}{\text{increment in input/ initial value of input}}$$

This definition of sensitivity was used to investigate the input and output parameters having different units. The sensitivity factor in this study represents the percentage change in the output parameter for a 10 % change in the given input parameter. For example, a sensitivity factor of -5 means the percentage decrement of the output is 5 % if the percentage

increment of the given input is 10 % and is independent of the units of the input and output parameters.

3.2.2 Input parameters

Table 3.1 shows the input parameter variations that were investigated in this study. Each input parameter was varied over a range of interest and feasibility to streamline the parameters for further optimizations.

Component geometry parameters

Figure 3.1b shows three geometries used in the present study. Three distinct geometries were studied to investigate process sensitivity variation with part geometry. Part wall thickness and Z-height were varied as component geometry parameters. The values of selected parameters for sensitivity analysis are presented in **Table 3.1**.

Process parameters

The printing process in MF³ involves several input parameters. In the present study, a set of major process parameters was studied. **Table 3.1** presents the typical values of selected process parameters identified based on experience. Layer thickness defines the height of each layer of printing. While a smaller layer thickness discretizes the build into higher resolution leading to better accuracy and surface quality, it leads to higher print time. Typically, a layer thickness of 0.2 mm is used in MF³. Variations to 0.1 mm and 0.3 mm layer thickness were investigated for sensitivity in this study. Bead width defines the discretization of each layer in the XY plane. Bead width is decided considering the desired

print speed and accuracy of exactness. Nozzle size is selected according to the intended bead width. In the present study, a 0.48 mm bead width, varying between 0.36 mm and 0.60 mm, was considered. Extrusion temperature defines the material temperature for softening it just enough to overcome its viscosity and extrude through the nozzle smoothly. While a too-low extrusion temperature may lead to a lack of diffusion between tracks and layers, giving poor part quality, a too-high extrusion temperature leads to challenges of process control and print resolution. An extrusion temperature of 240°C with variations to 220°C and 260°C was evaluated. The build plate was heated to keep the substrate temperature high enough to enable efficient diffusion between two layers. It also provides a slower cooling that helps to minimize part warpage.

Table 3.1. Input parameters variation

Input Parameters		Units	Variations
Component geometry	Part wall thickness	(mm)	1.5 ± 0.5
	Part Z-height	(mm)	20 ± 10
Process conditions	Layer thickness	(mm)	0.2 ± 0.1
	Bead width	(m)	0.48 ± 0.12
	Extrusion temperature	(°C)	240 ± 20
	Build plate temperature	(°C)	65 ± 20
	Printing speed	(mm/s)	10 ± 5
	Toolpath	(°)	$0^\circ-90^\circ / 45^\circ-135^\circ$
Material properties	Thermal conductivity	(W/m·°C)	$1.466 \pm 20 \%$
	CTE	(1/°C) (10^{-6})	$28.3 \pm 20 \%$
	Specific heat capacity	(J/kg·°C)	$895 \pm 20 \%$
	Young's modulus	(MPa)	$205 \pm 20 \%$
	Specific volume	(m ³ /kg) (10^{-4})	$3.38 \pm 20 \%$

The influence of build plate temperature of 65 °C with variations to 45 °C and 85 °C is evaluated. Printing speed defines the travel speed of the nozzle while it extrudes material to print. As it directly relates to print time, it is always desirable to get a higher print speed. However, it is limited by several parameters like material viscosity, filament stiffness to push through the nozzle, and desired print quality. In MF³, the filament being highly viscous and less stiff compared to standard polymer filaments like ABS, PLA and PA, a lower speed is more suited. Typically, a print speed of 10 mm/s is used in MF³ of Ti-6Al-4V. Variations to 5 mm/s and 15 mm/s were investigated for sensitivity in this study. Finally, the toolpath defined by the raster angle is considered an important process parameter as it affects the orientation of porosity in the printed part thereby affecting part strength anisotropy. It also affects the temperature difference between two subsequent tracks in the same layer as the length of the track varies with the raster angle. Two raster angles, 0°–90° and 45°–135°, were investigated in this study.

Powder-binder material properties

In this study, the properties of Ti-6Al-4V with 59 vol.% solids loading with custom polymer binder were obtained from estimation models. The material definition for simulation includes a set of mechanical and thermal properties over a range of temperatures. **Table 3.1** summarizes the material properties at 23 °C. The given material properties were varied to +/- 20 % to investigate the influence on the printing process outcome. These variations can be looked at as representative of changes in the material formulation in terms of solids loading and a custom polymer binder.

3.2.3 Simulation setup: Base case

In this study, finite element analysis (FEA) simulations are conducted using Digimat to estimate the outcome from the MF³ printing process. **Table 3.2** lists the component geometry, process conditions and material properties initial values used in the base case simulation for each of the three geometries.

Table 3.2. Input for the initial base case simulation

Input parameters		
Component geometry	Part wall thickness	2 mm
	Part Z-height	20 mm
Process conditions	Layer thickness	0.2 mm
	Bead width	0.48 mm
	Extrusion temperature	240 °C
	Build plate temperature	65 °C
	Printing speed	10 mm/s
	Toolpath	0° – 90°
Material properties	Thermal conductivity	1.466 mW/mm·°C
	Coefficient of thermal expansion	2.83 E-05 1/°C
	Specific heat capacity	8.95 E+08 mJ/t·°C
	Young's modulus	205 MPa
	Specific volume	3.38 E+08 mm ³ /t

The CAD model was imported in STL format. It was discretized into voxel mesh as shown in **Figure 3.2a**. The mesh size influences the prediction of residual stresses but has a minor influence on displacement/ warpage results [25]. However, the mesh size cannot be smaller than the layer thickness. Considering the computational time, a mesh size of 0.3 mm was used in this study. A GCode file defined toolpath, layer thickness and printing speed. Other

printing parameters like layer width, extrusion temperature, build plate temperature, chamber temperature and convection coefficient were defined through the simulation tool graphical user interface. The material behavior definition for simulation includes mechanical and thermal properties over a range of temperatures. The thermo-mechanical behavior of the material is defined in the simulation tool, Digimat using the properties of Ti-6Al-4V 59 vol.% feedstock over a range of temperatures. Considering the computational time and number of simulation jobs, a layer-by-layer activation method was used to simulate the printing process. Here, a set of elements representing one layer are activated at a time in the FE model, whereas in the filament discretization method, a chunk of filaments representing deposited filament gets activated.

3.3 RESULTS AND DISCUSSION

First, the results of the base case simulations for all three geometries are explained in detail concerning print time, deflection, Z-warpage, residual stress and substrate temperature. Then, having conducted all the simulation jobs by varying each of the input parameters, the sensitivity analysis results of all three designs are discussed. Moreover, simulation results were further used to identify the most significant input parameters for each output parameter and their variation trends are discussed for all three geometries. Finally, variation in MF³ process sensitivity with variation in part geometry is discussed.

3.3.1 Simulation results: Base case for Design-I, Design-II & Design-III

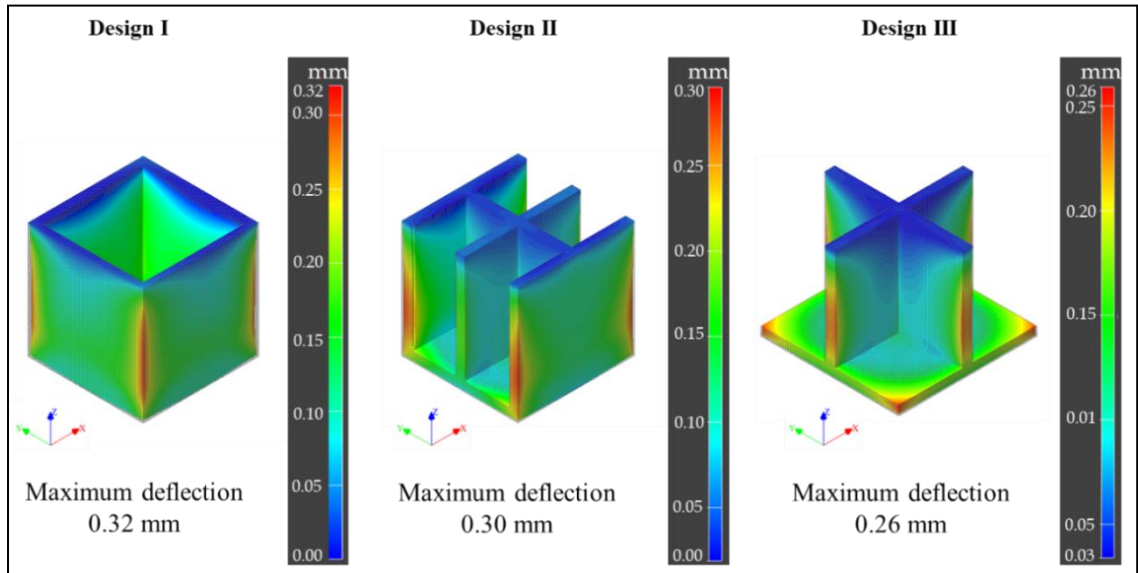
Print time

Like in any manufacturing process, print time is an important aspect of an AM process. While lower print time indicates a higher commercial advantage, it is generally accompanied by quality compromise. Simulation provides an estimate of the time required to print a given part under set process parameters for a given material. Print time is dependent upon component geometry parameters (part wall thickness, layer cross-sectional area, part maximum height) and process parameters (printing speed, part orientation, build height, layer width, layer thickness, toolpath). The estimated print time for the initial base case of Design-I, Design-II & Design-III was 123 min, 125 min & 108 min, respectively. Print time for Design-I and Design-II were almost the same because the part volume and surface area per layer were almost the same. Compared to Design-I, in Design-II two of the vertical walls were repositioned. However, in Design-III, two vertical walls were eliminated that led to lower part volume and surface area per layer, hence a lower print time.

Deflection

In the MF³ printing process, the material is subjected to softening and partial melting, pushed through an extruder-nozzle, deposited on a substrate layer-by-layer, and then allowed to cool down and solidify. Afterward, it is subjected to repeated cycles of heating and cooling with each new layer getting deposited on top of it. This leads to the development of thermal gradient and inherent thermal strains in the printed part [25, 47]. The extent of the strain varies according to the thermal gradient and coefficient of thermal expansion of the material. The thermal strain causes deflection and warpage, finally leading to deviations in printed part dimensions from defined CAD geometry.

(a)



(b)

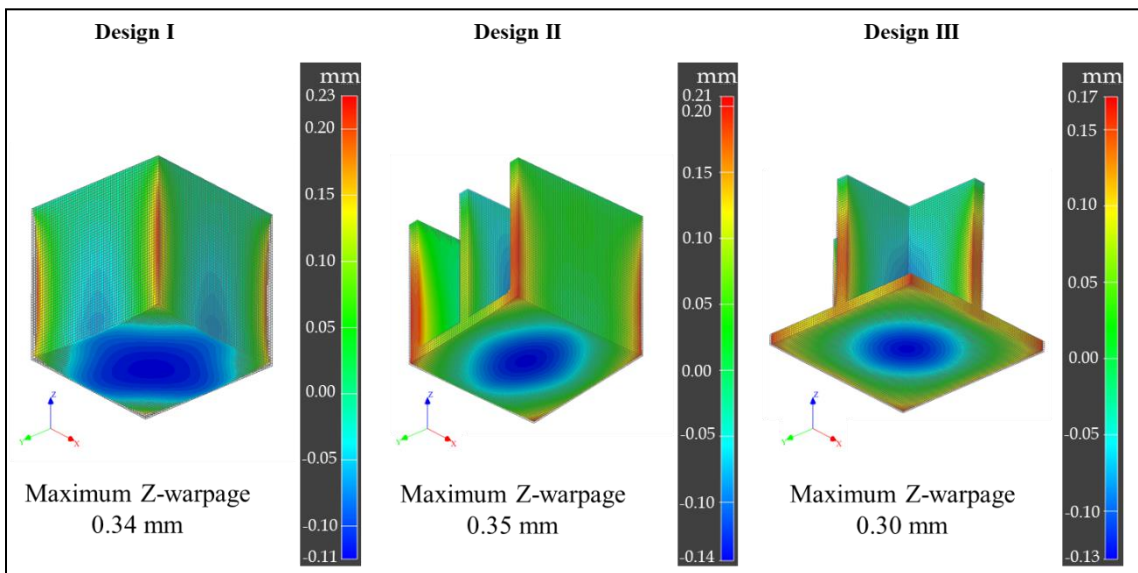


Figure 3.3. Simulation results: (a) Deflection, overall (b) Z-warpage

Simulation provides an estimation of deflection in X, Y, Z direction as well as overall deflection results. It is primarily dependent upon temperature-related process parameters

(extrusion temperature, build plate temperature) and material properties (coefficient of thermal expansion). Moreover, time-related parameters (print speed) and geometry-related parameters (part thickness, height, layer thickness, bead width) also influence deflection in a printed part. As shown in **Figure 3.3a**, the estimated maximum overall deflection for the initial base case of Design-I, Design-II & Design-III was 0.32 mm, 0.30 mm & 0.26 mm, respectively. The deflection was found to be maximum at outer corners for all three geometries as a result of a higher rate of convection heat transfer compared to inner volume, combined with lower structural stiffness at corners to resist deformation. The deflection was oriented along Z-axis which was attributed to the thermal gradient along Z-axis.

Z-warpage

As thermal strains lead to deflection in the printed part, it is combined with nonuniform shrinkage resulting from uneven cooling due to layer-by-layer printing. This leads to warpage which is more significant along Z-axis. As shown in **Figure 3.3b**, the simulation estimated maximum Z-warpage for the initial base case of Design-I, Design-II & Design-III was 0.34 mm, 0.35 mm and 0.30 mm, respectively. The experimental printing showed 0.56 mm, 0.59 mm and 0.51 mm Z-warpage for the three designs, respectively. The higher value in experiments can be attributed to imperfect sticking of the first layer to the heated bed as the print progresses, whereas in the simulation it is assumed to be perfectly sticking to the bed as a boundary condition throughout the printing process. Z-warpage was found to be maximum at the outer corners for all three geometries as a result of a higher rate of convection heat transfer compared to inner volume, combined with lower structural stiffness to resist deformation.

Residual stress

The process simulation provides an estimation of residual stresses induced during and at the end of the printing and cooling processes as a result of a thermal gradient, non-uniform cooling and material shrinkage. **Figure 3.4** indicates the von Mises stress as residual stress developed at the end that can be attributed to thermal gradient due to layer-by-layer stacking as well as differential heat loss from the central zone and outer periphery. Lower thermal gradient, uniform and slower cooling helps in reducing residual stresses. The estimated maximum residual stress for the initial base case of Design-I, Design-II & Design-III was 10.9 MPa, 7.5 MPa & 7.2 MPa, respectively. Like deflection results, residual stresses were found to be maximum at the outer corners and oriented along Z-axis for all three geometries for the same reasons of differential heat transfer and thermal gradient along the Z-axis, respectively.

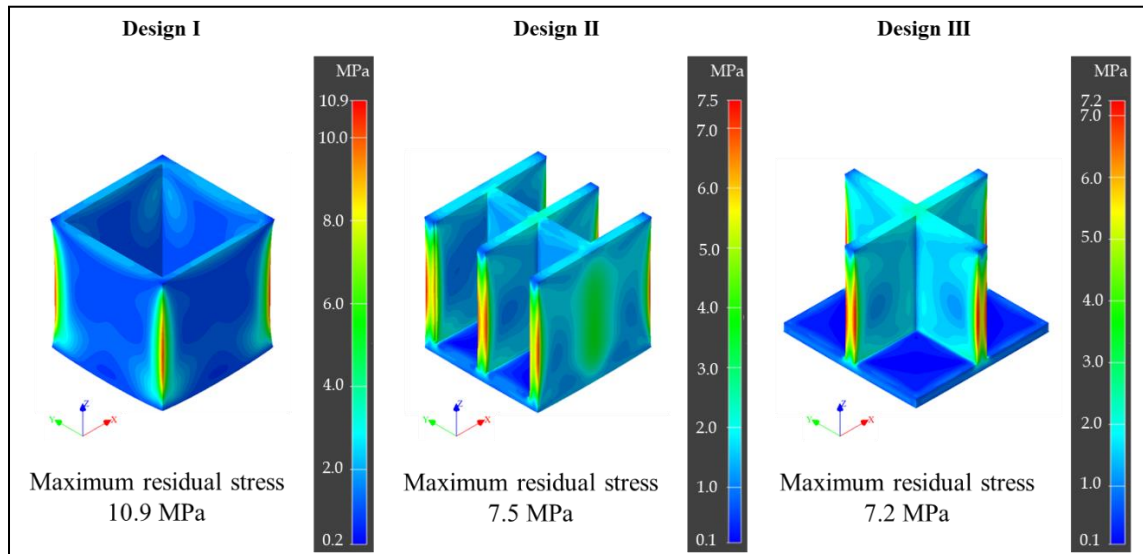
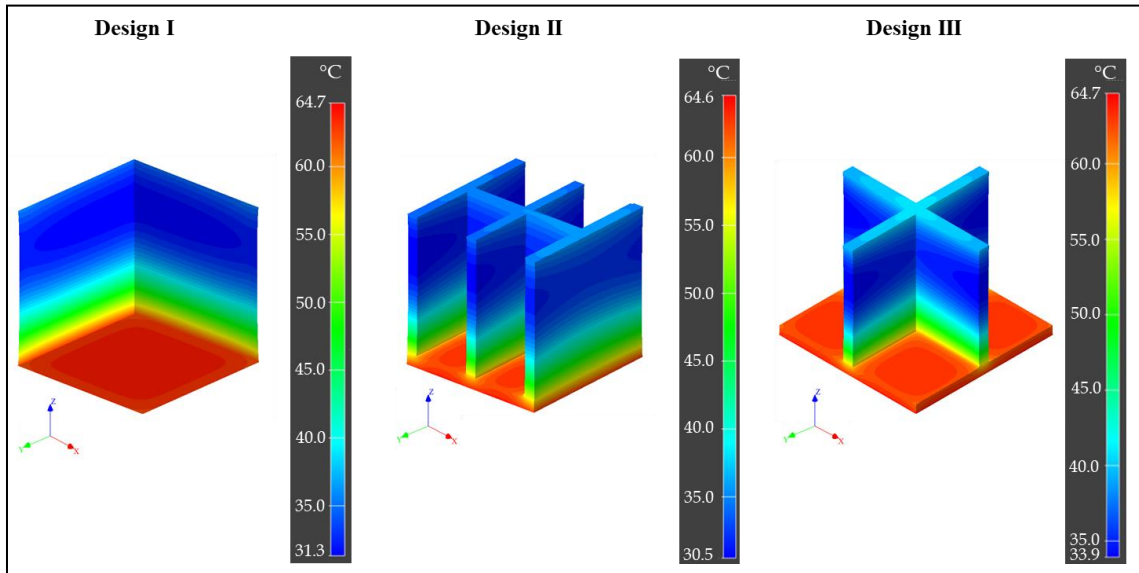


Figure 3.4. Simulation results: Residual stresses (von Mises)

Substrate temperature

The simulation predicts the temperature history of the printing process employing a transient thermal analysis that provides insights into local temperature evolution during the process. **Figure 3.5a** shows the temperature distribution indicating the thermal gradient at the end of printing. The viscous material from the nozzle is extruded and deposited on the substrate at a set extrusion temperature of 240°C. However, by the time the next layer is deposited, the previous layer cools down to a much lower temperature. This is due to heat loss to the environment as an open chamber printer was considered in the study. The chamber temperature was set to ambient temperature, 20°C, in the simulations. However, the build plate was kept at 65°C. So, the printed layers lose heat to the environment (20°C) through convection and temperature drops. Below a certain equilibrium point, these layers start gaining heat from the heated bed (65°C) through conduction. The heat flux depends upon the temperature gradient, the surface area for convection heat transfer and the thermal conductivity of the material. As a result of simultaneous heat loss and heat gain, the layers at the bottom of the build are found to be close to 65°C when the next layer comes in. It can be said that the substrate temperature of this next layer is 65°C. As the build progresses, substrate temperature decreases with an increase in build height or layer distance from the build plate. The substrate temperature in the top portion of the build is found to be 31°C for Design-I. Here, the amount of heat gain from the build plate was much lower than heat loss to the environment. This is because of the limited thermal conductivity of the material, while convection heat loss was more significant.

(a)



(b)

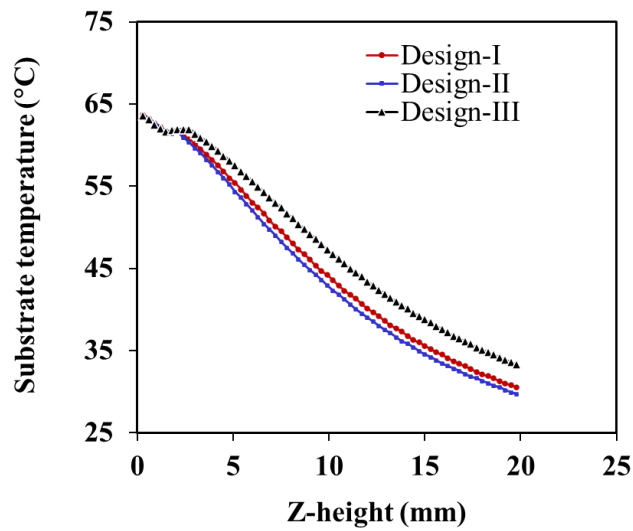


Figure 3.5. Simulation results: (a) Temperature distribution at the end of printing (b) Substrate temperature history

The phenomenon of heat gain through conduction and heat loss through convection also depends on the surface area of exposure, Z-height, time taken to print each layer which

ultimately depends on part geometry as well as printing parameters. The estimated minimum substrate temperature for the initial base case of Design-I, Design-II & Design-III was 31 °C, 30 °C & 34 °C, respectively, as shown in **Figure 3.5b**. The importance of substrate temperature is that a lower substrate temperature leads to a lower amount of diffusion between two layers, hence, lower interlayer bond strength leading to a lower mechanical strength [31, 32]. Hence, it is an important consideration from not only the build setup or process parameters standpoint but also geometry and material design standpoint.

3.3.2 Sensitivity Analysis

Each of the input parameters was varied to an upper and lower value, and a simulation job was conducted for each variation keeping all the other inputs the same as in the initial base case. For each input variable, two simulation jobs were conducted. So, for the given 13 input parameters, 26 jobs were conducted for each part design. Hence, a total of 78 simulation jobs was conducted for three designs in this study. As described, equation (1) provides the sensitivity factor (SF) calculation for every individual output parameter response to the variation in each input parameter. **Table 3.3(a-c)** summarizes the SF results for Design-I, Design-II & Design-III. SF is categorized as ‘highly significant’ if $SF > 10$, ‘significant’ if $10 > SF > 5$, ‘less significant’ if $5 > SF > 1$ and ‘no significance’ if $1 > SF$.

Table 3.3. (a) Sensitivity factors: (a) Design-I (b) Design-II (c) Design-III

(a)

Input Parameters		Print time	Deflection	Z-Warpage	Residual stresses	Substrate temperature
Component geometry	Part wall thickness	14.27	0.48	0.61	2.94	4.15
	Part Z-height	8.64	2.42	4.10	5.80	7.64
Process conditions	Layer thickness	18.93	0.22	0.35	0.31	2.24
	Bead width	18.48	3.25	3.78	7.87	1.28
	Extrusion temperature	0.00	17.41	17.88	17.39	1.78
	Buildplate temperature	0.00	0.49	0.45	0.21	2.13
	Printing speed	19.98	0.53	0.82	0.74	3.40
	Toolpath	0.17	0.00	0.01	0.02	0.08
Material properties	Thermal conductivity	0.00	0.16	0.37	0.18	1.27
	CTE	0.00	10.51	10.35	10.41	0.01
	Specific heat capacity	0.00	0.22	0.36	0.32	2.20
	Young's modulus	0.00	0.00	0.00	10.01	0.00
	Specific volume	0.00	0.27	0.45	0.41	2.67

Sensitivity Factor	SF > 10
	10 > SF > 5
	5 > SF > 1
	1 > SF

(b)

Input Parameters		Print time	Deflection	Z-Warpage	Residual stresses	Substrate temperature
Component geometry	Part wall thickness	14.41	0.75	0.71	2.84	4.36
	Part Z-height	8.67	2.86	5.58	6.58	7.60
Process conditions	Layer thickness	21.30	3.23	4.97	3.02	2.56
	Bead width	18.63	2.37	2.84	2.04	0.60
	Extrusion temperature	0.00	20.29	16.51	17.18	1.70
	Buildplate temperature	0.00	1.44	1.84	2.36	2.01
	Printing speed	19.98	0.50	0.69	0.72	3.29
	Toolpath	0.84	0.03	0.02	0.03	0.15
Material properties	Thermal conductivity	0.00	0.19	0.30	0.15	1.32
	CTE	0.00	10.77	9.87	10.33	0.01
	Specific heat capacity	0.00	0.19	0.27	0.27	2.09
	Young's modulus	0.00	0.00	0.00	10.00	0.00
	Specific volume	0.00	0.24	0.34	0.35	2.56

(c)

Input Parameters		Print time	Deflection	Z-Warpage	Residual stresses	Substrate temperature
Component geometry	Part wall thickness	14.40	1.51	3.41	3.50	5.22
	Part Z-height	6.88	2.69	7.13	5.95	6.65
Process conditions	Layer thickness	15.72	0.22	0.53	0.48	2.51
	Bead width	17.10	1.14	2.69	2.51	12.53
	Extrusion temperature	0.00	16.40	16.79	17.18	2.33
	Buildplate temperature	0.00	0.44	0.71	0.16	2.17
	Printing speed	19.98	0.46	1.15	1.05	4.05
	Toolpath	0.48	0.02	0.04	0.03	0.19
Material properties	Thermal conductivity	0.00	0.10	0.25	0.13	1.03
	CTE	0.00	10.02	9.91	10.28	0.03
	Specific heat capacity	0.00	0.21	0.53	0.48	2.72
	Young's modulus	0.00	0.00	0.00	10.00	0.00
	Specific volume	0.00	0.27	0.66	0.59	3.31

Print time

According to the simulation results, print time was found to be sensitive to component geometry and process parameters. It was not influenced by any of the material properties. As part wall thickness increases, print time increases. A strong sensitivity was observed in print time towards part wall thickness. It was obvious that a higher print area of each layer of the vertical walls and a larger height of the bottom horizontal portion of the geometry led to larger print time. Print time also showed high sensitivity to part Z-height or build height as the number of layers required to finish the build varies proportionately. Print time is greatly influenced by layer thickness. Print increases when the layer thickness decreases and vice versa. Similarly, bead width has a significant influence on print time. With wider tracks, the time to print infill of each layer decreases. Printing speed has a direct and significant influence on print time. Toolpath was found to have a negligible effect on print time. However, none of the material parameters influenced print time as the sensitivity factor remained zero. Hence, as per simulation results, material properties do not influence print time. However, it is important to note the fact that if some specific properties of the material were changed experimentally, such as viscosity, that might require a change in printing speed to be extruded through the nozzle optimally. This change will ultimately influence print time. But, at present the simulation tool is unable to capture the rheological behavior of the material, hence, its influence could not be included in the study.

Deflection, all

The deflection results showed low sensitivity towards component geometry parameters like part wall thickness and Z-height. Among process parameters, layer thickness and layer

width showed a low influence on the deflection. Extrusion temperature influences deflection strongly as it defines the thermal gradient. Higher extrusion temperature leads to higher deflection and vice versa because higher temperature causes a larger extent of phase change in the extrudate material that is accompanied by greater volumetric changes in the material. The sensitivity to build plate temperature was low. Printing speed and toolpath showed no influence on the deflection. While the coefficient of thermal expansion showed a strong effect, all other material properties did not influence the deflection at all. CTE defines the volumetric changes with temperature change, which is used for deflection calculation in simulation.

Z-warpage

Z-warpage showed a sensitivity pattern similar to that of deflection as the physical phenomenon and computational approaches are similar for both. Part wall thickness showed a low impact on Z-warpage. However, part Z-height had considerable influence on Z-warpage because the deflection in build direction depends upon the thermal gradient in Z-direction that varies with build height. On the processing side, layer thickness and bead width showed no influence. Extrusion temperature influenced Z-warpage strongly, for the same reason as that for deflection. Higher extrusion temperature led to a higher Z-warpage. The sensitivity to build plate temperature was low. Printing speed and toolpath showed no influence. From material properties, CTE again showed a strong effect, while all other properties did not influence at all.

Residual stresses

From a component geometry standpoint, the residual stress results showed low sensitivity to part wall thickness, and considerable sensitivity to part Z-height. On the process front, layer thickness and bead width had negligible impacts. A strong sensitivity was observed towards extrusion temperature for the same reason as that for deflection and warpage. Lower extrusion temperature helps reducing residual stresses as it reduces the thermal gradient and the extent of phase change in the extrudate material. Build plate temperature, printing speed and toolpath showed negligible influences on residual stresses. The coefficient of thermal expansion showed a high influence, it dictates the amount of volumetric change of the material during the thermal process. Young's modulus was found to influence the residual stresses only. As residual stress is the result of resistance to deflection from the material, it is proportionate with material stiffness. Hence, higher Young's modulus and higher CTE values lead to higher residual stresses, and vice versa.

Substrate temperature

Substrate temperature showed sensitivity to most of the input parameters, though the level of sensitivity was considerable enough only for a few input variables. From component geometry, wall thickness showed considerable influence. As part thickness increases, print time per layer increases. This allows more time to dissipate heat before the next layer comes in, leading to lower substrate temperature. High sensitivity was observed towards part Z-height. As the build height increases, the substrate temperature decreases due to a larger distance from the heated build plate. Among the process parameters, print speed, build plate temperature, extrusion temperature and layer thickness showed an influence on the

substrate temperature. On the material front, sensitivity was considerable for thermal conductivity and negligible for specific heat capacity and specific volume, and zero for CTE and Young's modulus.

3.3.3 Identification of significant input parameters

The sensitivity analysis provides a means to identify significant input parameters for each of the output parameters. The sensitivity factor facilitates a quantitative yardstick to identify the significant parameters. It is worth looking into the distribution of influence of various input parameters for each output parameter. Such examination gives insight into how a particular process outcome can be varied and controlled by adjusting input parameters. If it is assumed that the input parameters considered in this study are the only parameters that affect the listed output parameters, the sensitivity factor can be considered as the contribution of the input parameter towards the outcome of the respective output parameter. Accordingly, a contribution chart was generated for each output parameter showing contribution from the most significant input parameters.

The relationship between an input and an output parameter may or may not be linear. In the graphs of the input (X-axis) and output (Y-axis) parameters relationship, a curve drawn over three given points of calculation indicates if there exists a linear or nonlinear relation. Also, the slope of variations between three points of measurement gives an idea of non-linearity or biases. Moreover, the slope of variation differs with part design, both in nonlinear and linear relationships. These observations signify the effect of each input parameter as well as part design on the output parameters.

Print time

Figure 3.6 shows the contribution from significant input parameters towards print time for the three geometries. **Figure 3.6(a-c)** indicates that printing speed, layer thickness and bead width were the major contributors to print time consistently for all three geometries. These three input parameters put together contributed 69 % to 72 %. It provides a clear idea that these input parameters need to be optimized to minimize the print time.

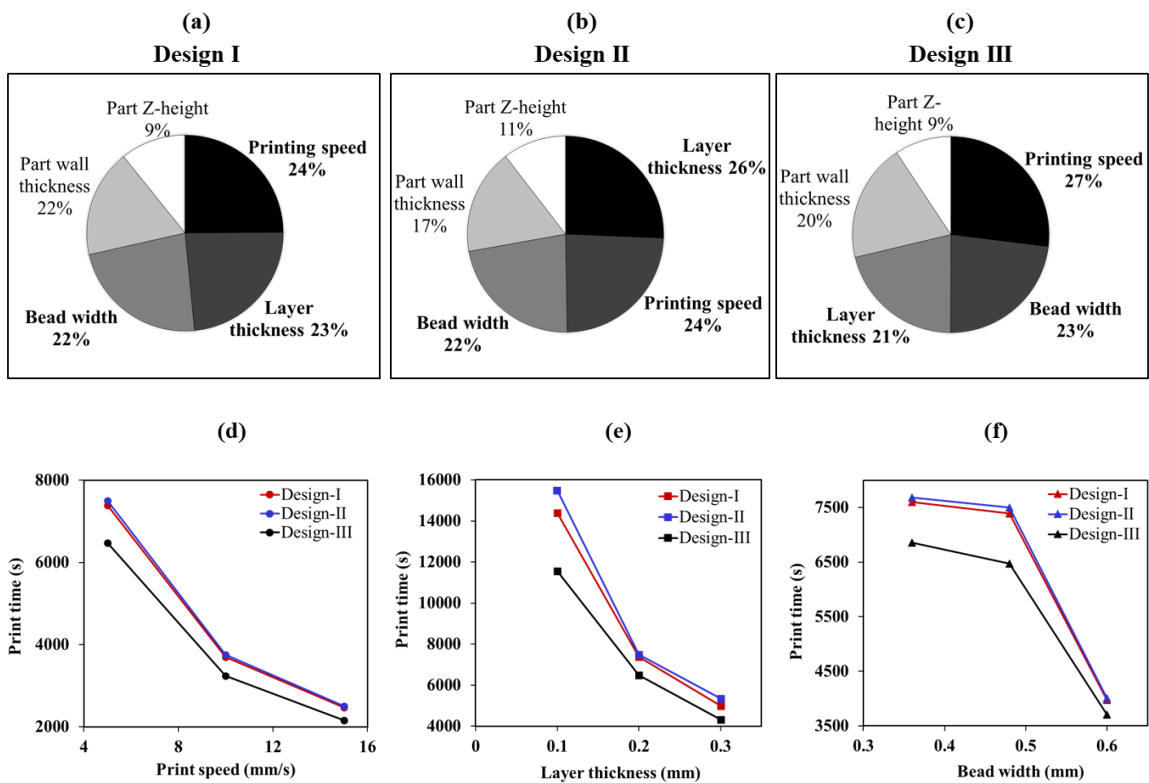


Figure 3.6. (a-c) Contribution from significant input parameters towards print time, (d-f) print time variation trends for significant input parameters

Figure 3.6(d-f) shows variation trends of print time with the printing speed, layer thickness and bead width for the three geometries. Print time decreased with an increase in these

three input variables, though the slope of variation varied among the three variables as well as within each variable. However, the slopes did not change much from one part design to another.

Deflection, all

Extrusion temperature and CTE were found to be the most significant input parameters for part maximum deflection. These two input parameters together contributed 72 % to 79 % for all three geometries as shown in **Figure 3.7(a-c)**.

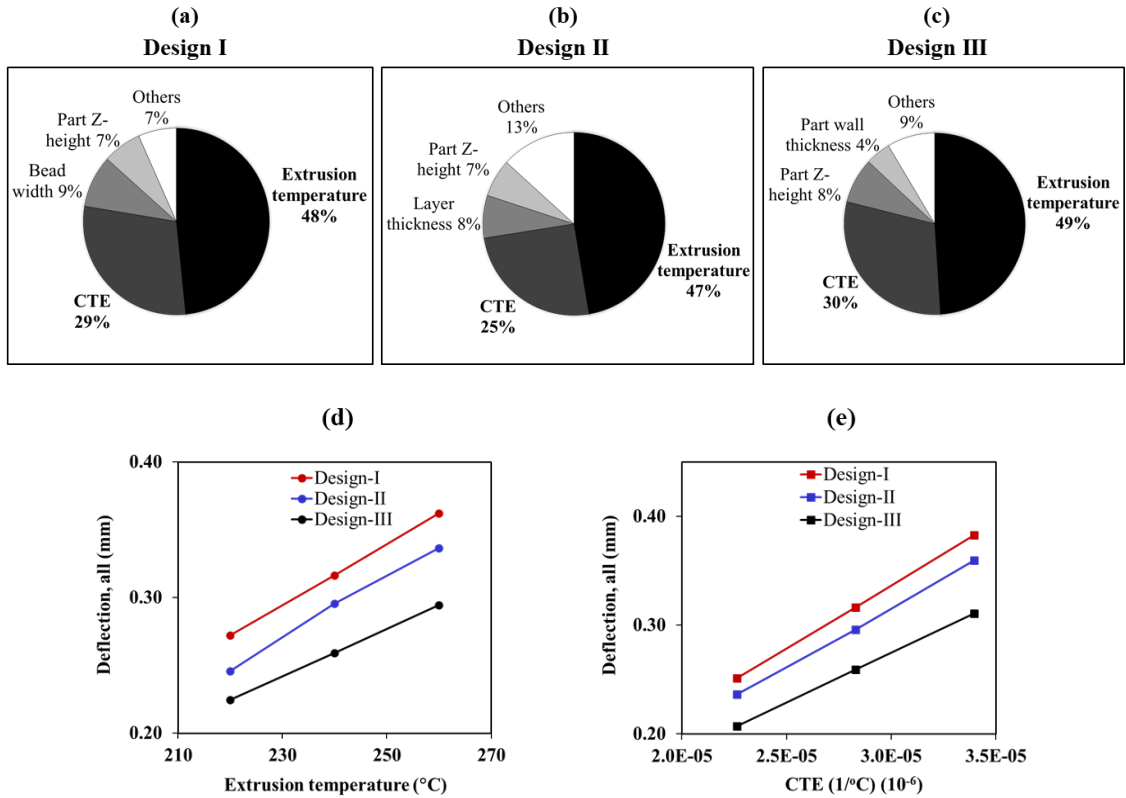


Figure 3.7. (a-c) Contribution from significant input parameters towards deflection, (d-e) deflection variation trends for significant input parameters

The influence of these input parameters on part deflection did not vary much with part geometry, whereas the influence of the less significant input parameters was found to vary with part geometry. **Figure 3.7(d-e)** shows variation trends of deflection with the extrusion temperature and CTE for the three geometries. Maximum deflection increased with an increase in these two input variables. The slope of variation by and large remained the same among the variables as well as within each variable.

Z-warpage

Figure 3.8(a-c) indicates that extrusion temperature and CTE are the major contributors to Z-warpage for all three geometries. These two input parameters together contributed 60 % to 71 %. The influence of these significant input parameters did not vary much with part geometry, whereas that of the less significant input parameters did. **Figure 3.8(d-e)** shows variation trends of deflection with the extrusion temperature and CTE for three geometries. Maximum deflection increased with an increase in these two input variables. The slope of variation remained unchanged between the two variables as well as within each variable indicating a direct proportionality for all three geometries. While Design-I and Design-II showed the same slope, Design-III showed slightly a lower slope than the other two designs. The deflection and Z-warpage can be reduced by a lower extrusion temperature as they lead to a lower thermal gradient and limits the material phase transfer and volumetric changes. Similarly, a material with lower CTE undergoes a smaller amount of volumetric changes under given process conditions, leading to lower deflection and Z-warpage.

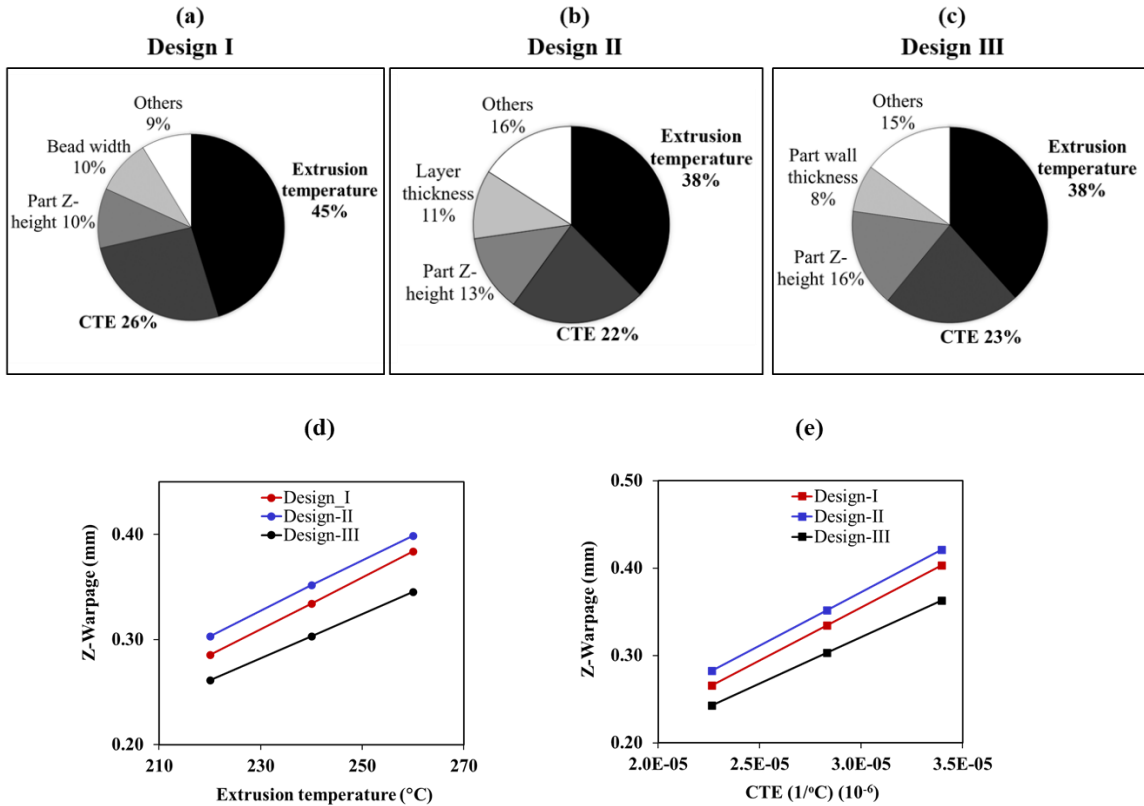


Figure 3.8. (a-c) Contribution from significant input parameters towards Z-warpage, (d-e) Z-warpage variation trends for significant input parameters

Residual stresses

Extrusion temperature, CTE and Young's modulus were found to be the most significant input parameters for residual stresses developed in the printed part. These three input parameters together contributed 67% - 72% for all three geometries as shown in **Figure 3.9(a-c)**. The influence of these input parameters on residual stresses did not vary much with part geometry, whereas the influence of the less significant input parameters was found to vary with part geometry. **Figure 3.9(d-f)** shows variation trends of maximum residual stress with the extrusion temperature, CTE and Young's modulus for three geometries. Residual stresses increase with an increase in these three input variables,

hence, by optimizing these three input parameters, residual stresses can be minimized. It was interesting to know that the higher stiffness of material leads to higher residual stresses. It is an important consideration for applications requiring higher material stiffness to get printed parts with high strength and stiffness.

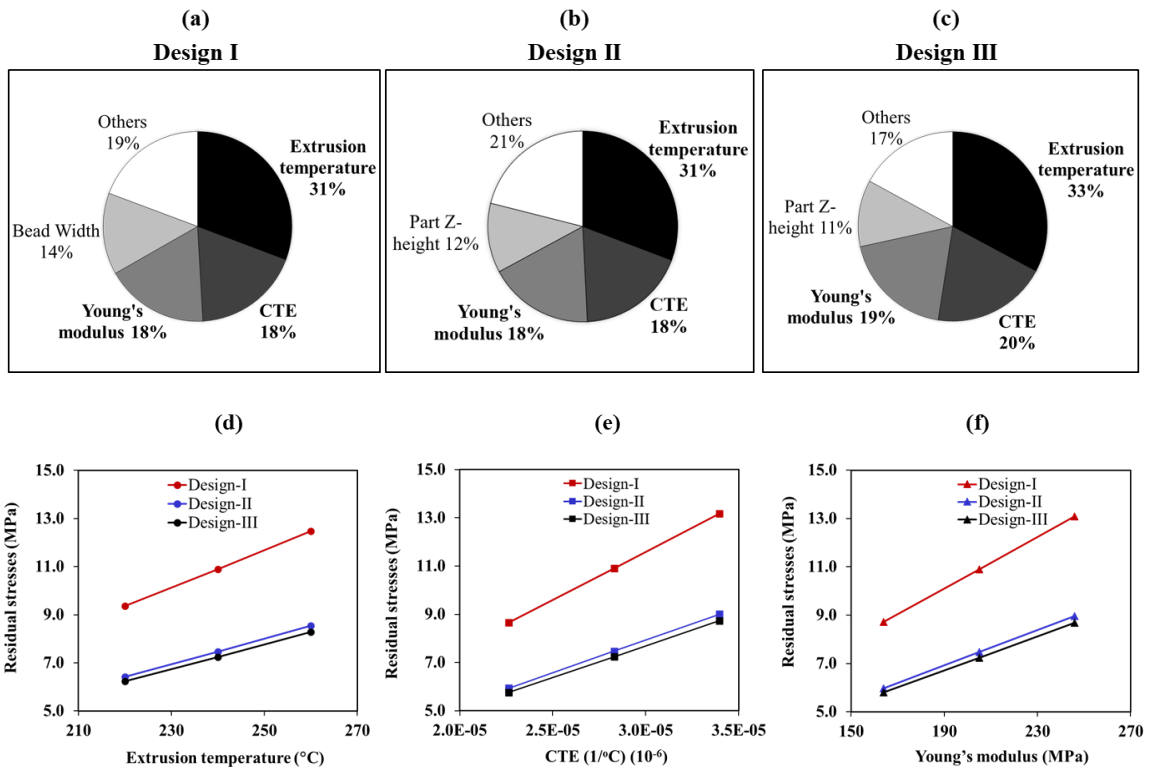


Figure 3.9. (a-c) Contribution from significant input parameters towards residual stresses, (d-f) residual stresses variation trends for significant input parameters

The slope of variation remained unchanged between the three variables as well as within each variable having a direct proportionality for all three geometries. While Design-II and Design-III showed the same slope, Design-I showed a considerably higher slope than the other two designs. This difference could be attributed to the higher structural stiffness of

Design-I geometry compared to the other designs that have free vertical edges having lesser structural stiffness.

Substrate temperature

Substrate temperature did not show a very high sensitivity to any input parameters though part Z-height, wall thickness and bead width were among the highest influencers. **Figure 3.10(a-c)** indicates that part Z-height, wall thickness and printing speed were the major influencers for substrate temperature in Design-I and Design-II, whereas bead width, Z-height and wall thickness were the major contributors in Design-III.

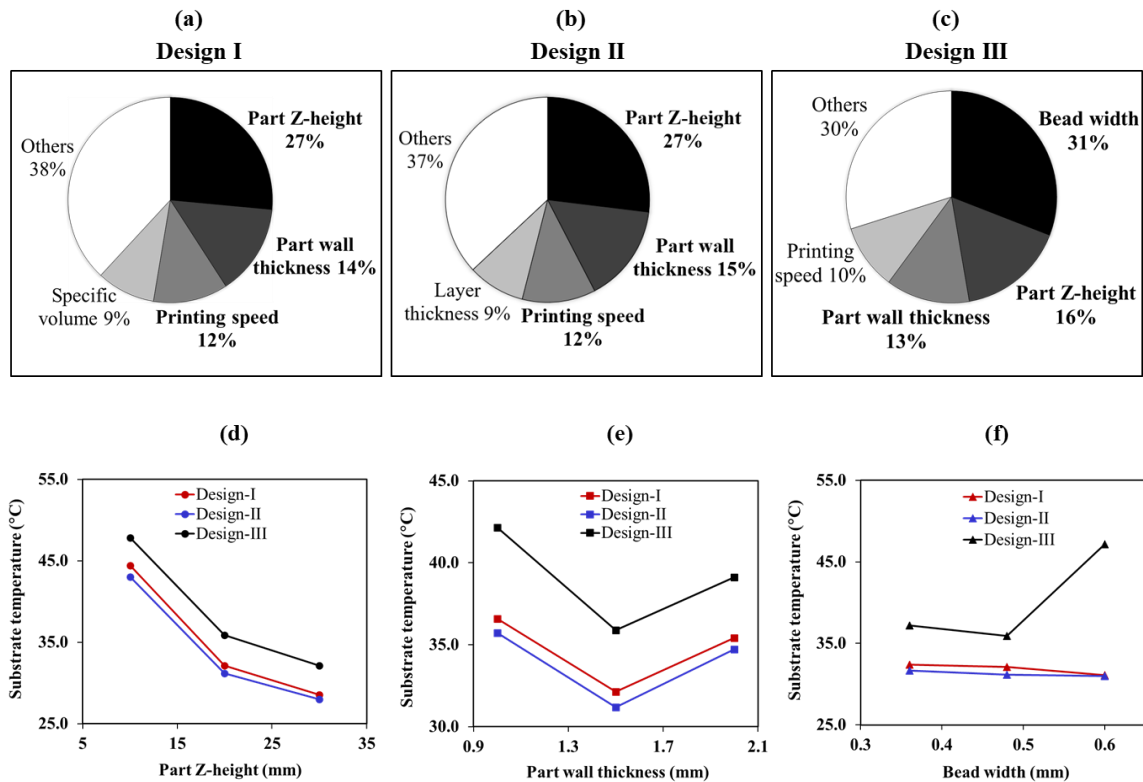


Figure 3.10. (a-c) Contribution from significant input parameters towards substrate temperature, (d-f) substrate temperature variation trends for significant input parameters

Figure 3.10(d-f) shows variation trends with part Z-height, wall thickness and bead width for the three geometries. The slope of variation varied between the three variables as well as within each variable. However, for part Z-height and wall thickness, the slopes did not change much from one part design to another, as opposed to that for bead width. As shown in **Figure 3.10d**, substrate temperature decreases with an increase in part Z-height, initially at a higher rate and later at a lower rate. Substrate temperature decreases with an increase in part Z-height due to the high thermal gradient resulting from low thermal conductivity and low ambient temperature. Similarly, as shown in **Figure 3.10e**, it decreases with an increase in part wall thickness from 1 mm to 1.5 mm, due to higher printable area per layer leading to higher print time allowing more cooling time.

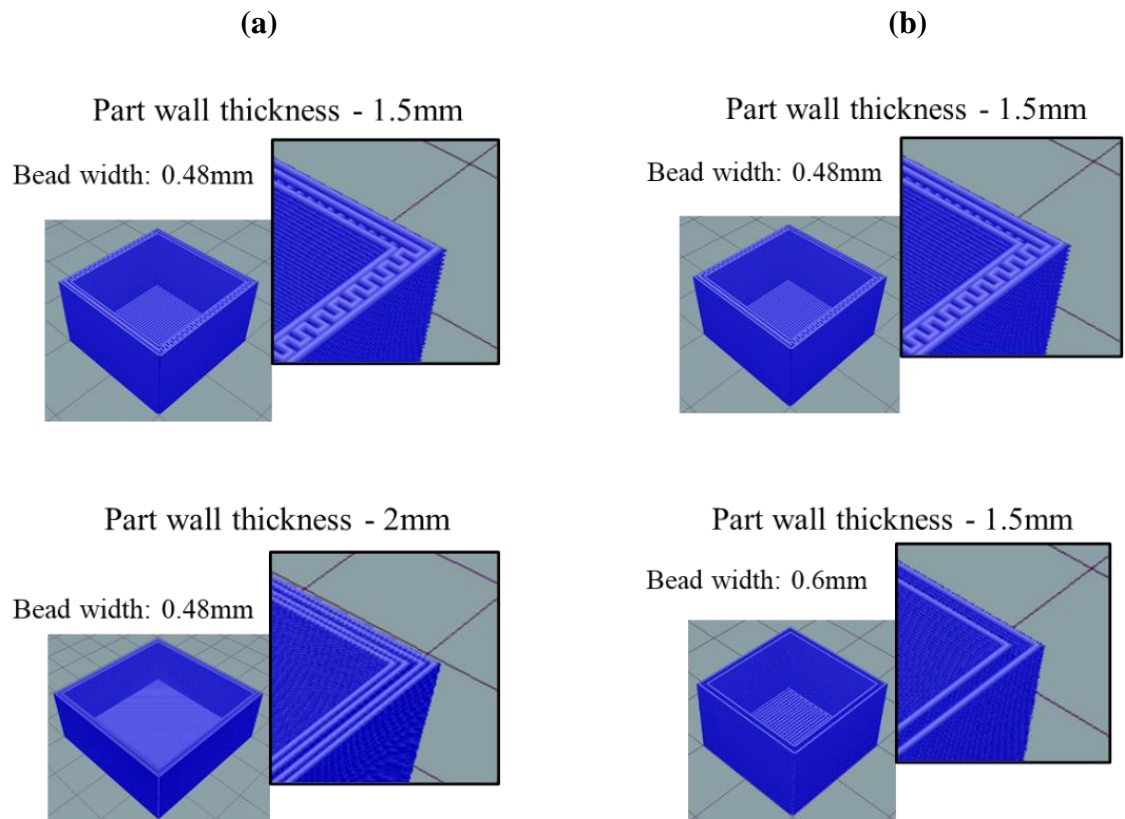


Figure 3.11. Infill pattern for varying part wall thickness and bead width

However, when wall thickness increases from 1.5 mm to 2 mm, the temperature increases considerably, which was opposite to the expectations. This is because of the change of the infill pattern. **Figure 3.11a** shows the infill pattern for the two different wall thicknesses of 2 mm and 1.5 mm for bead width 0.48 mm. It was observed that 1.5 mm part wall thickness, infill contains zig-zag lines as opposed to straight-lines with 2 mm wall thickness. Hence the print time per layer is lesser for the 2 mm thick part, despite increased wall thickness. **Figure 3.10f** shows the bead width had no significant effect on substrate temperature in Design-I and Design-II. Also, in Design-III, bead width had no considerable influence when varied from 0.36 mm to 0.48 mm. However, when it was varied from 0.48 mm to 0.6 mm, the substrate temperature increased significantly. This difference is because of the changed infill pattern. **Figure 3.11b** shows the infill pattern with the two different bead widths of 0.48 mm and 0.6 mm for part wall thickness of 1.5 mm.

Table 3.4 summarizes the infill pattern and print time per layer that changed with variation in part wall thickness and bead width for different geometries leading to variation in minimum substrate temperature. The slicing tool decides an infill pattern according to the infill space available that changes with part wall thickness, and bead width. For 0.48 mm bead width, the infill contains zig-zag lines as opposed to no infill with 0.6 mm bead width. Hence the print time per layer was considerably lower for 0.6 mm bead width leading to a very low total print time. However, the effect of such reduction in print time on substrate temperature was not significant for Design-I and Design-II as the print time remained still high due to large print area per layer, whereas in Design-III having print area per layer half of that in the other two designs, reduction in print time had significant effects on thermal history. Hence, lower cooling time leads to higher substrate temperature in Design-III. As

part Z-height was a significant contributor, by reducing part Z-height or keeping the build height small through part orientation optimization, the minimum substrate temperature can be considerably increased. It would eventually lead to higher interlayer diffusion and bond strength providing higher mechanical properties in printed parts.

Table 3.4. Infill pattern and print time per layer that change with variation in part wall thickness and bead width leading to variation in minimum substrate temperature

Part wall thickness (mm)	Bead width (mm)	Infill	Print time/ layer (min)*			Minimum substrate temperature (°C)		
			D-I	D-II	D-III	D-I	D-II	D-III
1.0	0.48	No infill	0.77	0.78	0.50	36.6	35.7	42.1
1.5	0.48	Zigzag	1.57	1.63	1.12	32.1	31.2	35.9
2.0	0.48	Straight lines	1.47	1.50	0.98	35.4	34.7	39.1
1.5	0.36	Straight lines	1.50	1.52	0.98	32.4	31.6	37.2
1.5	0.48	Zigzag	1.57	1.63	1.12	32.1	31.2	35.9
1.5	0.60	No infill	0.77	0.78	0.50	31.1	31.0	47.1
* Print time/layer taken into account excluding the horizontal bases portion of the part that remains the same for all three designs.								

3.3.4 Process sensitivity towards different geometries

Table 3.5 shows the MF³ printing process sensitivity for all three parts designs. Different geometries led to varying part volume, print area per layer, the surface area for heat transfer

and structural stiffness. It was observed that the influence of the identified significant input parameters did not vary with part geometry, such as part wall thickness, layer thickness, bead width and printing speed remained highly significant towards print time for all three geometries.

Table 3.5. MF³ process sensitivity variation with part geometry, i.e., Design-I, Design-II, Design-III

Input Parameters	Print time			Deflection, all			Z-Warpage			Residual Stress			Substrate temperature		
	Design I, II, III														
	I	II	III	I	II	III	I	II	III	I	II	III	I	II	III
Part wall thickness	■	■	■			■			■	■	■	■	■	■	■
Part Z-height	■	■	■	■	■	■	■	■	■	■	■	■	■	■	■
Layer thickness	■	■	■		■			■			■		■	■	■
Bead width	■	■	■	■	■	■	■	■	■	■	■	■	■		■
Extrusion temp				■	■	■	■	■	■	■	■	■	■	■	■
Build plate temp					■			■			■		■	■	■
Printing speed	■	■	■							■	■	■	■	■	■
Toolpath															
Thermal conductivity													■	■	■
CTE				■	■	■	■	■	■	■	■	■			
Specific heat capacity													■	■	■
Young's modulus										■	■	■			
Specific volume													■	■	■

Similarly, extrusion temperature and CTE showed consistently high significance for deflection and Z-warpage, whereas extrusion temperature, CTE and Young’s modulus

remained highly significant for residual stresses irrespective of part geometry. Such input parameters identified as highly significant can be used for further optimization studies over a wide range of part geometry. However, the sensitivity for input parameters at lower significance levels varied with part geometry, such as the sensitivity of deflection and Z-warpage towards part wall thickness and Z-height varied with part geometry. Similarly, the influence of layer thickness, build plate temperature and printing speed towards deflection, Z-warpage and residual stresses kept varying with geometry. Also, the significance of bead width towards substrate temperature was considerably different for all three geometries. Such identification provides a clear idea about the impact of part geometry on process sensitivity. Input parameters identified as highly significant can be used for further optimization studies according to sensitivity level with part geometry.

3.4 CONCLUSIONS

The MF³ printing was simulated and analyzed for the first time using a systematic procedure based on sensitivity analysis principles. The sensitivity analyses facilitated the identification of dominant input parameters in MF³ printing of Ti-6Al-4V feedstock.

The investigations in this study led to the following conclusions:

1. Print time was influenced by process conditions and part geometry, but it was completely insensitive to material parameters. Print speed, layer thickness and bead width were the most significant influencers. Print time decreased with an increase in these three input variables, at different rates, though the rates did not change from one geometry to another.

2. Deflections and Z-warpage showed very high sensitivities to extrusion temperature and CTE, having direct proportionality. The slope of variation remained almost the same for the two input variables and did not change with part geometry.
3. Residual stresses showed very high sensitivities to extrusion temperature, CTE and Young's modulus having direct proportionality. The slope of variation remained almost the same for all three input variables and did not change with part geometry.
4. Substrate temperature did not show a very high sensitivity to any input parameters, though part Z-height, wall thickness and bead width were among the highest influencers. The temperature decreased with an increase in part Z-height due to limited thermal conductivity leading to a high thermal gradient. However, a mixed response was observed with a change in wall thickness and bead width due to varied infill patterns and the subsequent effect on print time.
5. The procedure identified the relative importance of specific attributes of parts geometry, processing conditions, slicing strategies, powder-binder material properties on MF³ printing based on correlations between input and output parameters.

The identification of significant input parameters would enable streamlining further development exercise. Experimental studies or design of experiments, involving the significant input parameters only, are now feasible and more meaningful, which was not the case while dealing with all thirteen input parameters. In the next step, it would be effective to conduct a detailed design of experiments (DOE) with the identified significant input parameters only to investigate the interactions between parameters. Also, an experimental DOE would now be feasible and more efficient, which was not the case while dealing with all thirteen input parameters.

CHAPTER 4

SUPPORTLESS PRINTING OF LATTICE STRUCTURES BY METAL FUSED FILAMENT FABRICATION (MF³) OF TI-6AL-4V: DESIGN AND ANALYSIS

4.1 INTRODUCTION

Lattice structure represents a design concept for products where user-specific physical and mechanical properties are required [48]. It brings enormous scope for design, performance, and light-weighting in several applications [49]. Lattice structures are favored in various fields because they possess useful properties such as high strength-to-weight ratio, high stiffness-to-weight ratio, negative Poisson's ratio, high energy absorption, low thermal expansion coefficient, and high heat dissipation rate through active cooling [50-55].

Due to these excellent characteristics, lattice structures have been extensively implemented in engineering applications, including ultralight structures, energy absorbers, low thermal expansion structures, impact-resistant and conformal cooling structures in automotive, aerospace, biomedical, construction, and other applications [56-61]. In addition, lattice structures are widely used as biocompatible materials for orthopedic implants and tissue engineering [62-64].

While lattice structure brings in distinguished potentials due to its specific geometric configuration, the fabrication processes of these geometries are usually more complicated than those of the bulk materials [65]. In the past, the complexity of lattice structure design

was severely restricted by traditional manufacturing techniques, such as casting, sheet metal forming and wire bonding, hot press molding, laser cutting, water cutting, which were employed for lattice structure fabrications [66]. Moreover, complex molds, high cost and manufacture defects, low productivity made them unable to fully exploit the potentials of lattice structures [67]. While the subtractive and formative methods of manufacturing have limitations for lattice structures, additive manufacturing has proved its potential and suitability for lattice structure fabrication [49].

Additive manufacturing (AM) is used for fabricating three-dimensional (3D) objects from 3D model virtual data by adding material layer upon layer, as opposed to subtractive and formative methods of manufacturing [1]. Recent progress in additive manufacturing (AM) has enabled its capabilities to manufacture complex parts, and lattice structures in particular [67]. Many lattice structures fabricated by various additive manufacturing technologies were reported recently, such as direct metal deposition (DMD), electron beam melting (EBM), and selective laser melting (SLM) for metal lattice structures [68], and fused filament fabrication (FFF), selective laser sintering (SLS), multi-jet fusion (MJF) for polymer lattice structures [48, 69, 70]. The current work investigated the applicability of an advanced metal additive manufacturing process, called metal fused filament fabrication, to fabricate Ti-6Al-4V lattice geometries.

As shown in **Figure 4.1**, MF³ involves a filament-based printing process, with additional subsequent steps involving binder removal and sintering at elevated temperatures to densify the printed parts [10]. It starts with sinterable metal powder, which is Ti-6Al-4V in this study, bonded in a multi-component polymer-based binder. The metal powder content generally varies between 55% and 60 % volume of powder-binder mixture. The

feedstock is extruded to form a 1.75 mm diameter filament that can be used on an extrusion-based desktop printer to build a 3D part. The diameter of the filament can be modified to match the requirement of a specific printer. The printed part is subsequently subjected to debinding to remove the polymer binder and sintering to get a fully dense metal part.

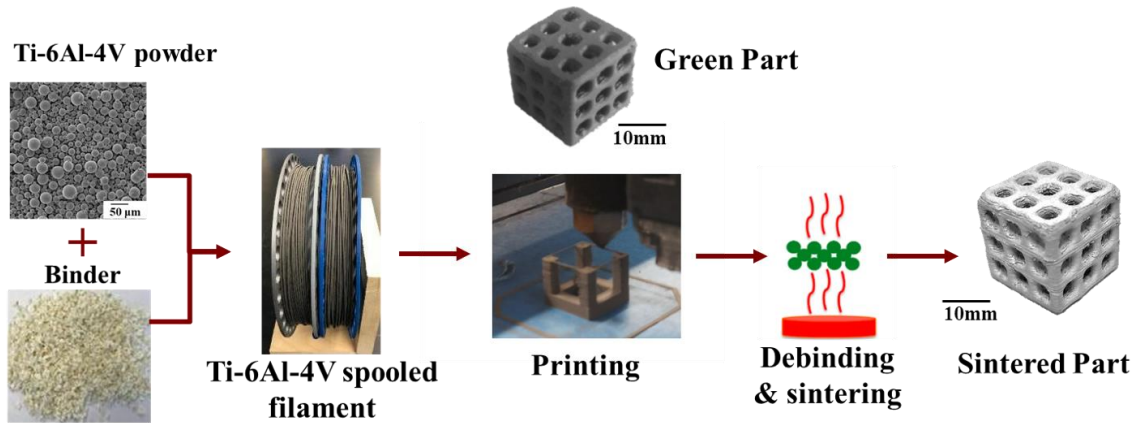


Figure 4.1. Overview of MF³ process showing filament preparation, 3D printing, debinding and sintering, and demonstration of a lattice structure fabricated with Ti-6Al-4V

Moreover, Ti-6Al-4V is a widely used material in aerospace and automotive applications due to its high strength-to-weight ratio, corrosion resistance, and good mechanical properties [71, 72]. Due to its high biocompatibility, it is considered one of the most suitable biomaterials for medical applications [73]. If these differentiating characteristics of the material can be leveraged to complement the capabilities of lattice structures, it would further enable strong potentials for customized designs and greater performance in several industrial applications. MF³ has been successfully used to print Ti-6Al-4V parts of varying geometries, as reported in previous publications by our research group [11]. To enable the fabrication of more complex geometries such as lattice structures, investigations on material-process-properties interrelationships was required.

A literature survey has indicated that the rapid developments of AM have proved its potential and suitability for the fabrication of lattice structures, and hence many lattice structures fabricated by additive manufacture were reported recently [49, 74]. AM, through layer-by-layer material addition, brings new vitality to fabricate lattice structures. However, each manufacturing technology has its limitations, and AM is no exception. Particularly, extrusion-based processes, such as MF³ or FDM, have a well-known limitation of the need for support structures on down-facing surfaces [75], when the maximum printable bridge length is exceeded.

Generally, when printing overhang features with an extrusion-based process, a support structure is provided throughout the printing process if threshold values are overcome so that the overhang geometry is printed defect-free and accurate without any distortion or sagging [48]. This support material is removed during post-processing either by mechanical or chemical methods [76]. However, it leads to extra cost and time in terms of the printing material and printing time and brings vulnerability of the part surface to potential damage when the support is removed eventually.

For lattice structures, it would be extremely difficult or even impossible to remove any interior support after the part is printed. In addition, for MF³, there is no sacrificial material that could be used as support, and hence the same material is used as support. These support structures are kept intact through the debinding and sintering processes to avoid potential collapse due to binder removal. However, removal of these supports mechanically from the sintered metal part is very difficult and nearly impossible for lattice structures due to the intricate geometry. From this point of view, supportless lattice structures [77] are highly desirable and advantageous since they are self-supporting and do not require any support

structure during the AM process. However, if not designed and printed optimally, an unsupported overhang may exhibit geometrical errors such as dimensional inaccuracy and sagging [51]. Hence, for a given AM technology and material, there is a need to develop optimal geometry and process parameters for a supportless lattice structure. There have been several works regarding how to design lattice structures for AM [76, 78-81], but none of them focused on sagging deflection in overhang features of the unsupported lattice structure. Moreover, being highly filled with metal powder, the high-density material in MF³ tends to sag in unsupported areas more than unfilled polymers in FDM. No literature is available on designing supportless lattice structures for additive manufacturing of highly filled material, such as the MF³ process with Ti-6Al-4V.

The quality of a printed part is equally important as its mechanical properties. Part with high mechanical strength may not be accepted if the part quality is poor. Hence, suitable processing conditions and feasible geometry parameters of the lattice structure need to be identified for MF³ that would address both the requirements. The printability of a given part and quality of the printed part highly depend upon processing conditions, geometry parameters, and material characteristics. The design of a lattice structure is influenced by material properties, the topology (shape and size) of the selected unit cell, and the relative density [77, 82]. In this study, the effects of processing conditions and lattice geometry on printed part quality were investigated for the given material formulation.

Moreover, in recent times, computational simulations aimed at predicting part deformation, residual stresses, and mechanical properties are attracting increasing interest in additive manufacturing to study the effects of the process, geometry, and material on the quality of 3D printed parts [22, 81]. Previous work published by our group presented an FEA

simulation of the MF³ process to predict printed part quality [10]. Computational simulation of lattice structure can further aid the prediction of lattice part quality and enable design for MF³.

The objective of this research is to investigate the applicability of MF³ to fabricate a supportless lattice structure and identify the processing window by establishing printability with the Ti-6Al-4V filament. Also, the experimental study investigated the effects of lattice geometry parameters on printed part quality from dimensional variations, sagging, and relative density standpoint. Moreover, finite element simulation was employed to estimate the part quality, and results were corroborated with experimental verification. Finally, an analytical model was proposed to estimate the extrudate deflection in unsupported overhangs in unit cells of different geometric configurations.

4.2 MATERIAL AND METHODS

4.2.1 MF³ printing experiments

In this study, 59 vol.% of Ti-6Al-4V powder dispersed in a multi-component custom polymer matrix was used in a filament form. The 1.75 mm diameter filament is processed by an extrusion-based desktop printer, Pulse (MatterHackers, Lake Forest, California), to print lattices. Printed green parts were eventually processed through solvent and thermal debinding followed by sintering. Initial attempts to print lattice structure by MF³ using usual conditions led to poor printability and highly defective parts. To understand the process-geometry-properties relationships better and identify feasible process and geometry parameters for lattice, Simple Cubic unit cells were investigated first, and it further enabled the successful fabrication of multi-stacked lattice structures. This unit cell

was selected not only for its simple design but also because of the presence of down-facing surfaces easy to inspect. Firstly, existing processing parameters were tuned to achieve defect-free printing of lattice geometry with the given material. Defect evolution as the results of the effect of each parameter change was recorded. Secondly, unit cells with square and circular cross-sections were printed with varying element thickness and length to evaluate the effects of geometry parameters on printed part quality in terms of dimensional variations and relative density.

4.2.2 Tuning of the printing parameters: effects on the printability of lattices

A unit cell of circular cross-section with element thickness 3 mm and element length 8 mm was initially printed using usual MF³ printing conditions identified based on the Ti-6Al-4V printing experience so far [10, 11]. The parameters that work well for solid geometries did not work for lattices primarily due to unsupported overhangs. Moreover, poor geometric fidelity was observed from the extrusion-based printing because of the small and narrow print areas in vertical and horizontal elements of lattice, respectively. Process condition-A shown in **Table 4.1** represents the usual MF³ printing conditions. Initial printing with condition-A led to defects and very poor lattice printability. Among several challenges, the extrusion of excess and unwanted material from the nozzle was a major issue. The inertia of the melt from the nozzle combined with filament pressure caused unwanted extrusion between small print areas. To overcome this issue, the filament retraction function was turned on in a slicer (Repetier-Host) that pulls the filament back by 0.3 mm (condition-B, **Table 4.1**) during the non-printing travel of the nozzle. This change led to a large improvement in geometric fidelity.

Table 4.1. Processing condition-A is generally used to print Ti-6Al-4V by MF³ for several different geometries. Condition-B identified as suitable specifically for lattice structure

Processing condition	A	B
Layer thickness (mm)	0.15	0.10
Printing speed (mm/s)	15	5
Nozzle diameter (mm)	0.4	0.35
Bead width (mm)	0.48	0.42
Extrusion multiplier	1.125	0.900
Extrusion temp °C	240	240
Bed temp °C	65	65
Build chamber temp °C	20	20
Toolpath	0-90	Concentric
Filament retraction (mm)	0.0	0.3

Next, in the toolpath definition, the rectilinear infill led to low geometric fidelity of the narrow and tiny cross-sectional print area of the lattice. A concentric infill was considered that follows perimeters more precisely, leading to higher fidelity. **Figure 4.2** shows the difference between rectilinear and concentric infill schemes for square and circular cross-section and the effect on printed part quality. Further improvement was achieved by dropping the extrusion multiplier that is usually kept 1.125 (condition-A, **Table 4.1**) to push more material relative to nozzle travel. This provides higher packing by pushing excess material.

However, in lattice having very small print areas pushing any extra material led to falling outside the print area. A value of 0.9 (condition-B, **Table 4.1**) was optimal for lattice, while further lower values led to voids in the infill. Printing speed in MF³ is generally 15 mm/s,

which is relatively lower when compared to FFF with unfilled polymers. This is due to high solids loading that builds up high viscosity and interparticle friction of fine metal powder. While 15 mm/s works well for solid geometries, for lattice, it was found to be too high for frequent switchovers between print and non-print due to flow control and inertia effects. 5 mm/s (condition-B, **Table 4.1**) led to considerable improvement over 15 mm/s (condition-A, **Table 4.1**). Smaller layer thickness, like in any AM process, improved the part resolution along Z-axis. A drop from 0.15 mm to 0.1 mm further contributed toward geometric fidelity. Finally, the bead width was dropped from 0.48 mm to 0.42 mm by switching to a 0.35 mm nozzle from an initial 0.4 mm. Significant improvement in XY resolution was achieved with a smaller bead width.

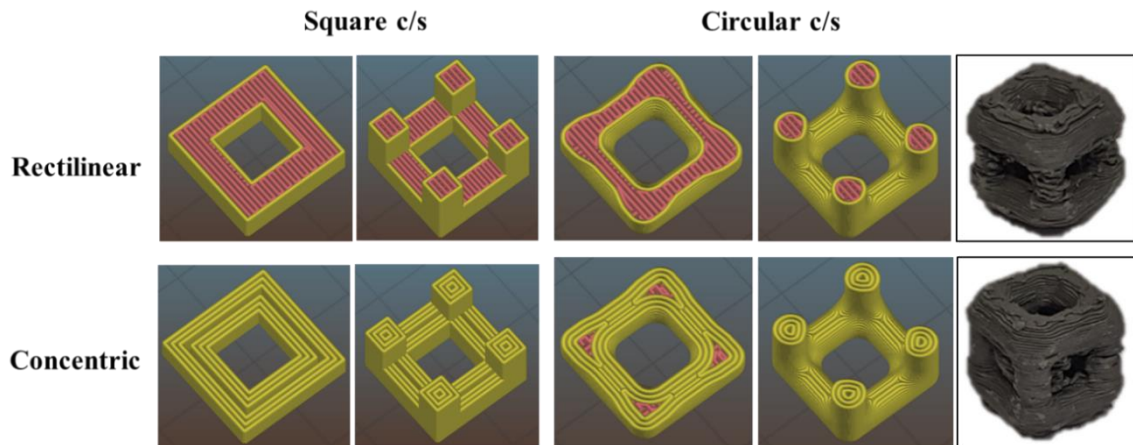
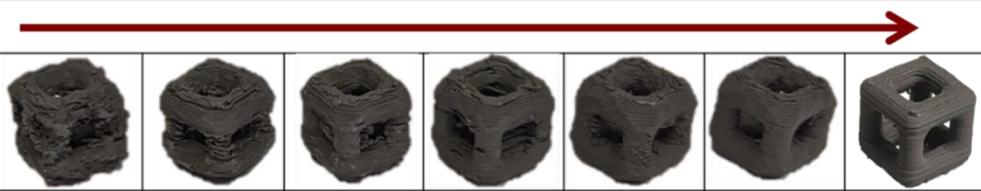


Figure 4.2. Rectilinear vs. concentric toolpath. Rectilinear infill led to low geometric fidelity of narrow and tiny cross-sectional print area in the lattice unit cell, whereas concentric perimeters follow the outline more precisely, leading to higher fidelity both in the case of circular and square beams cross-section.

Through this systematic modification of individual parameters, as shown in **Table 4.2**, process condition-B was identified for the given material that led to the printing of defect-free unit cells by MF³. It also paved the path for further experimental studies to investigate the effects of lattice geometry parameters on printed part quality, and subsequently successful printing and sintering of multi-stacked lattice structures by MF³.

Table 4.2. Effects of printing parameters evaluated by modifying one parameter at a time.

Processing Condition-A (Table 4.1) systematically modified to print unit lattice cell.



Process parameters	Started with Condition-A	Filament retraction	Toolpath	Extrusion multiplier	Printing speed	Layer thickness	Bead width
Condition-A	Condition-A	0 mm	Rectilinear	1.125	15 mm/s	0.15	0.48 mm
Modified		0.3 mm	Concentric	0.9000	5 mm/s	0.10	0.42 mm

4.2.3 Lattice geometry parameters: effects on part deformation and relative density

Having identified a feasible processing window for lattice, the effects of geometry parameters on part quality were investigated. Green parts were characterized for deflection and shrinkage relative to the CAD design and relative density. Unit cells were printed with varying geometric configurations. Square and circular, two types of cross-sections were studied. Element thickness of 3 mm, 2.5 mm, 2 mm, and element length of 6 mm, 7 mm, 8 mm were considered as shown in **Figure 4.3**.

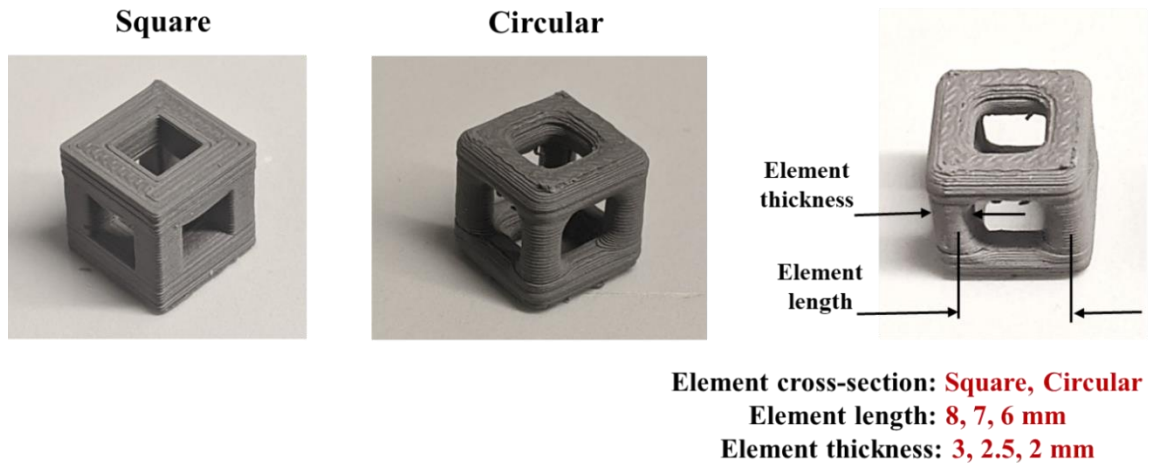
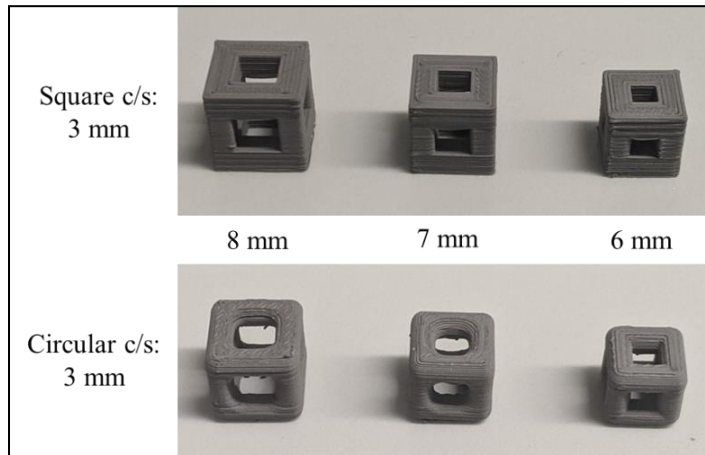


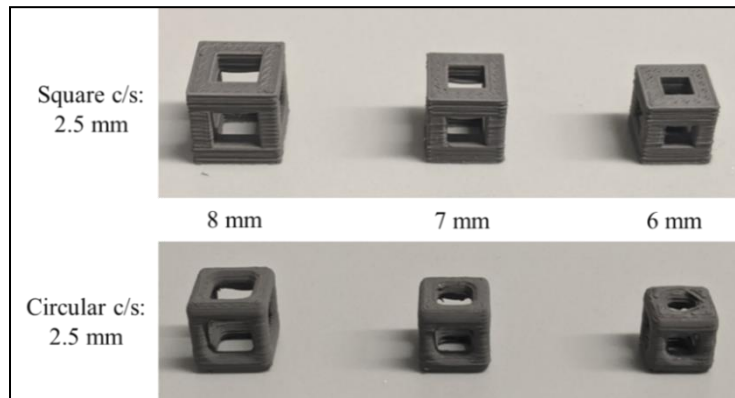
Figure 4.3. Unit cells with square and circular cross-section printed with varying element length and thickness to evaluate the effects of lattice geometry parameters on printed parts

Starting with element thickness 3 mm, unit cells of three different element lengths were printed for both cross-sections. All six parts were printed without any defects, as shown in **Figure 4.4a**. Eventually, twelve unit lattice cells of 2.5 mm and 2 mm element thickness were also printed, as shown in **Figure 4.4b** and **c**, respectively. However, it was also observed that parts with 2 mm thickness had some extrudates hanging in the unsupported region due to too tiny and narrow print areas in both cross-section types, but parts with 2.5 mm element thickness were printed without defects. This indicates the lower limit of element thickness with the given material and process conditions.

(a)



(b)



(c)

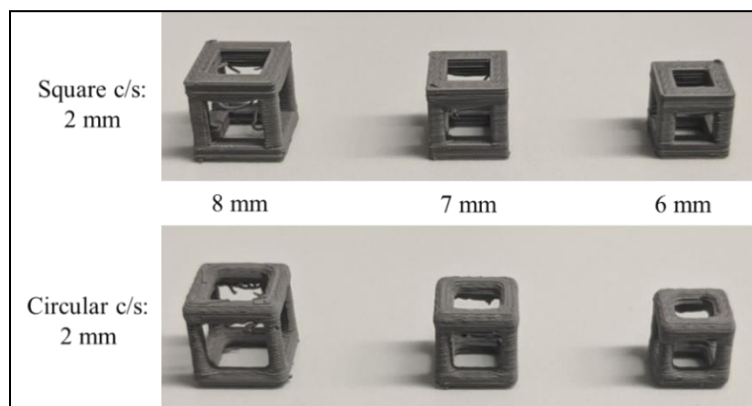


Figure 4.4. Unit cells with varying element thickness (3 mm, 2.5 mm, 2 mm) and overhang (8 mm, 7 mm, 6 mm) were printed for both square and circular c/s: (a) 3 mm element thickness; (b) 2 mm element thickness; (c) 2.5 mm element thickness

Part deformation

The printed green parts were characterized for dimensional changes and distortions compared to the original CAD design. % deformation was measured in both XY plane and along Z-axis using the below equation;

$$\text{Deformation (\%)} = \frac{\text{Original dimension}_{\text{CAD}} - \text{Actual dimension}_{\text{green part}}}{\text{Original dimension}_{\text{CAD}}} \quad (1)$$

A vernier caliper was used for measuring the dimensions of the printed parts. Deviations in part dimensions were evaluated as a function of lattice element thickness and element length. These results were further compared with simulated part geometry and original design geometry for verification.

Relative density

Archimedes' density of the printed parts was measured using Mettler Toledo's analytical balance. The relative density of green parts was calculated relative to the powder-binder feedstock density, which was 3.02 g/cc.

$$\text{Relative density}_{\text{green}} = \frac{\rho_{\text{Arch-green}}}{\rho_{\text{feedstock}}} \quad (2)$$

where, $\rho_{\text{Arch-green}}$ = Archimedes density of the green part

$\rho_{\text{feedstock}}$ = Theoretical density of the powder-binder feedstock (3.02 g/cc)

Variations in relative density were evaluated as a function of lattice element thickness and element length. These results were further correlated with porosity estimation from simulation for verification.

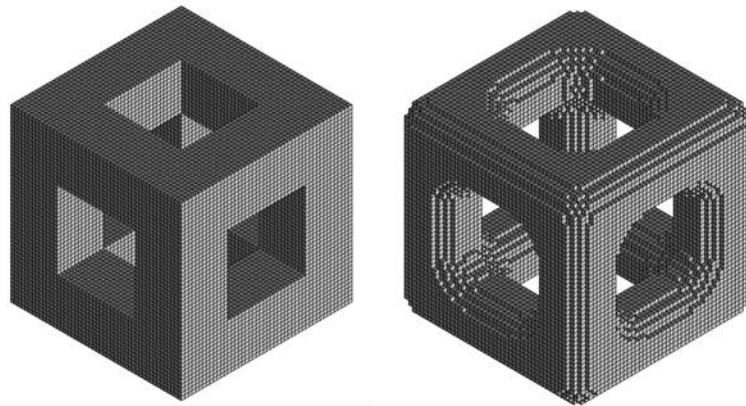
4.2.4 MF³ process simulation

To enable the prediction of MF3 printed lattice part quality, a thermo-mechanical model was used for finite element simulations using Digimat to simulate the MF3 printing process [47, 83]. To enable the prediction of MF³ printed lattice part quality, a thermo-mechanical model was used for finite element simulations using Digimat to simulate the MF³ printing process. Printing of filaments with 59 vol.% of Ti-6Al-4V powder dispersed in a multi-component custom polymer matrix was simulated. Thermo-mechanical properties of the novel material were generated using empirical estimation models. A recent publication by the authors involved the use of experimentally-measured polymer binder properties and estimation models to generate thermo-mechanical properties of Ti-6Al-4V feedstock material [10]. The CAD model of the square and circular cross-section unit cell of average size, element thickness 2.5 mm and element length 7 mm, was imported in STL format in Digimat-AM. It was discretized into a voxel mesh of element size 0.1 mm, as shown in **Figure 4.5a**.

Processing parameters used in the simulation were the same as those used in printing experiments (condition-B, **Table 4.1**). However, the simulation tool currently considers only key process parameters, as shown in **Table 4.3**. The GCode file from Repetier defines the toolpath, layer thickness, and printing speed. This file includes the time and spatial position of the nozzle, material deposition description, and contour of the part. Other printing parameters such as bead width, extrusion temperature, build plate temperature and chamber temperature were defined through the simulation tool graphical user interface. A concentric toolpath was generated in the slicing tool, as shown in **Figure 4.5b**. A ‘layer-by-layer discretization’ method is used, where the voxel elements are activated, and results

are computed for one layer at a time. Having defined the material, geometry, toolpath and process parameters, the job was submitted for thermo-mechanical simulation. The printing process and printed part quality were evaluated by post-processing the simulation results.

(a) Voxel mesh



(b) Toolpath from G-Code

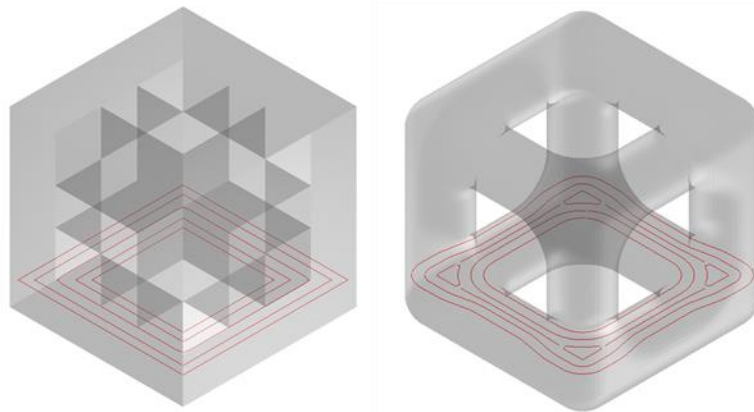


Figure 4.5. Simulation setup of square and circular c/s unit cells (element length 7 mm, element thickness 2.5 mm); (a) meshed model with voxel element size 0.1 mm (b) G-Code data defines the concentric toolpath generated in slicing tool

Table 4.3. Printing parameters input for process simulation

Process parameters	Variations
Layer thickness (mm)	0.10
Layer width (mm)	0.42
Extrusion temperature (°C)	240
Build plate temperature (°C)	65
Build chamber temperature (°C)	20
Printing speed (mm/s)	5
Toolpath	Concentric

4.3 RESULTS AND DISCUSSION

In this section, first, the effects of lattice geometry parameters on part deformation and relative density are discussed based on the findings from experimental printing of unit cells. Next, MF³ printing process simulation results such as deformation, residual stresses, and porosity in the green part are reported. Also, extrudate deflection in unsupported regions in a lattice is discussed, and an analytical approach is presented to estimate the extrudate deflection and verified by experimental results. Finally, multi-stacked lattice structures of different designs were printed and successfully sintered to fully dense Ti-6Al-4V parts.

4.3.1 Effects of lattice geometry parameters

The printed green parts were characterized for dimensional changes and distortions compared to the original CAD design. Distortion of part geometry was observed consistently for both cross-sections that resulted in dimensional changes. The non-uniform shrinkage caused by differential cooling during printing led to a non-uniform distribution

of thermal strains distorting the part shape. Printed green parts of unit cells of chosen element thickness, length, and cross-sections were measured for dimensional variations relative to CAD design. Shrinkage was observed in all three X, Y, Z directions consistently.

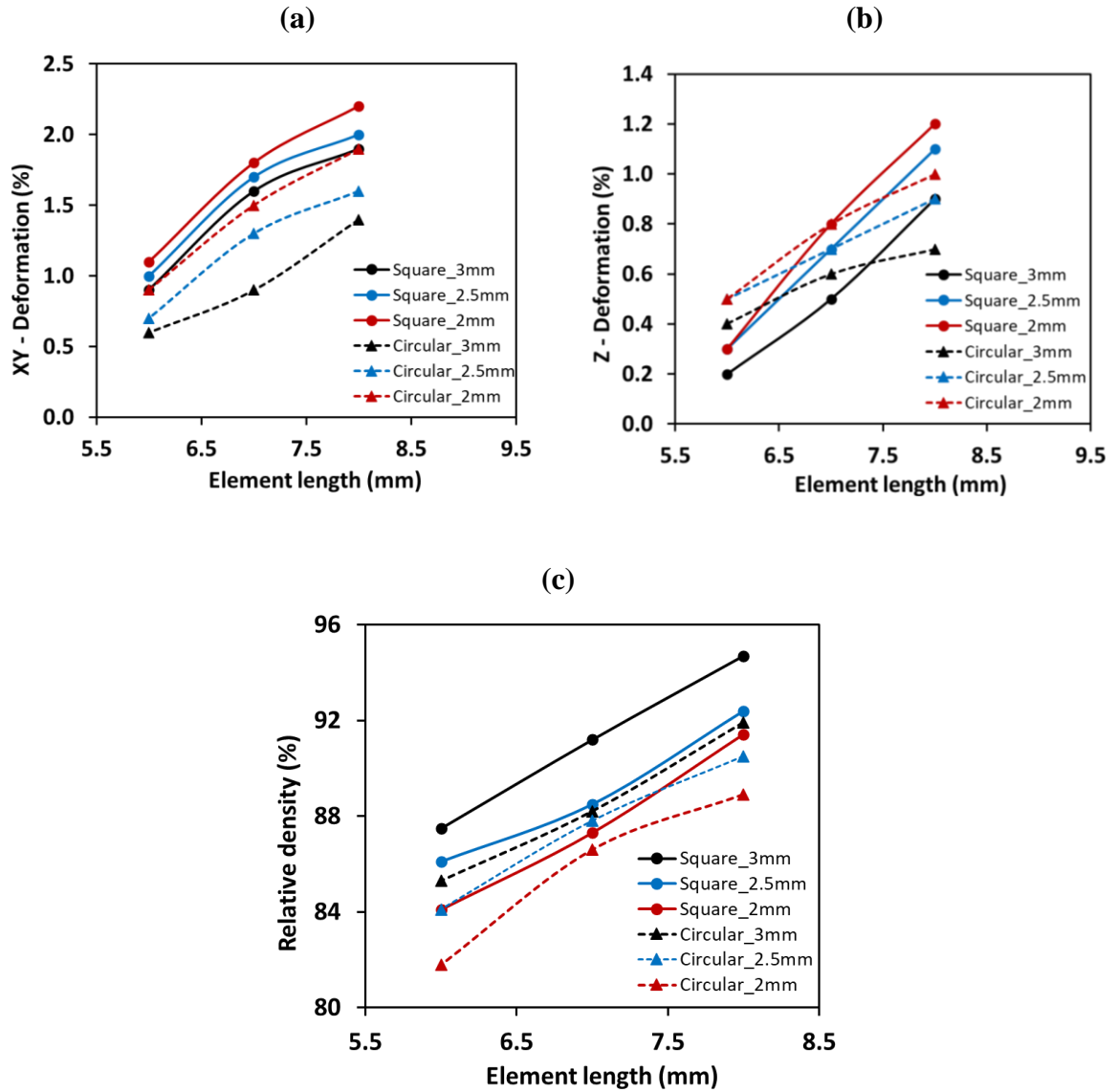


Figure 4.6. (a) Effect of lattice element thickness and length on XY-shrinkage (b) Effect of lattice element thickness and length on Z-shrinkage (c) Effect of lattice element thickness and length on green part relative density

As shown in **Figure 4.6a** and **b**, both XY and Z-deformation increased with element length for both cross-sections. The shrinkage also increased with a decrease in element thickness. These responses can be attributed to the increased aspect ratio (L/d) of lattice elements leading to higher longitudinal shrinkage. Square c/s showed higher shrinkage than circular c/s. Also, the response curves were different for the two cross-sections. The relative density of the green part was found to increase with lattice element length and element thickness for both cross-sections, as shown in **Figure 4.6c**. However, square c/s showed a higher relative density than circular c/s. Also, the response curves were different for the two cross-sections. The similar trends of shrinkage and relative density variation over element length indicate that higher shrinkage leads to higher relative density in green parts. Relative density can be considered indicative of packing density and strength in the green part, and it eventually affects the rebound and sintered part quality [11].

4.3.2 MF³ process simulation results

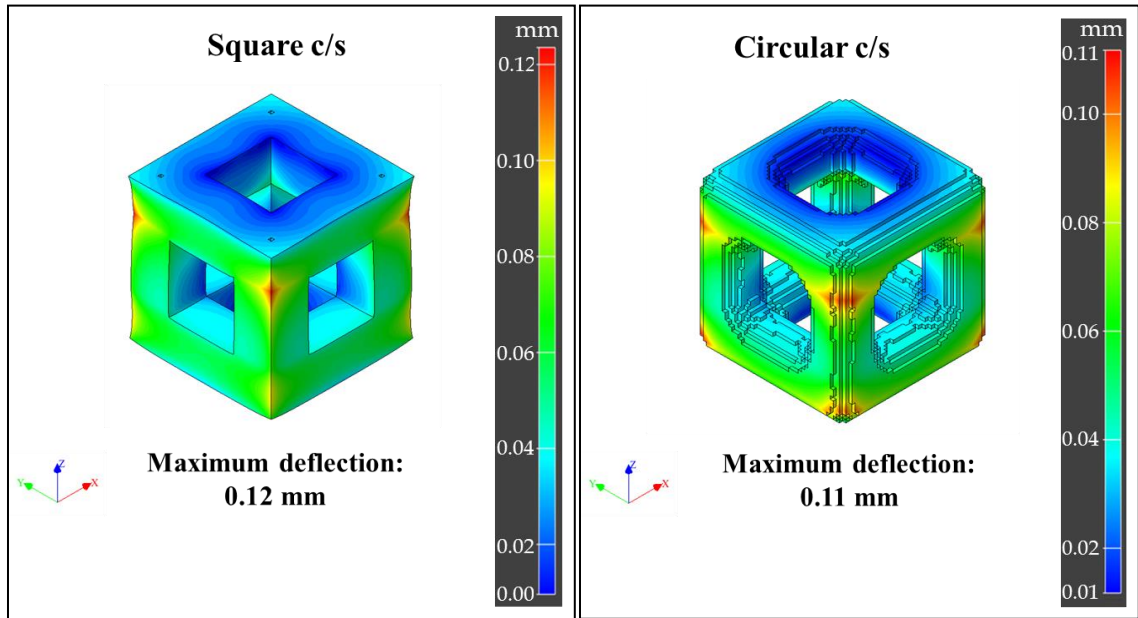
The process simulation was conducted using a sequential thermo-mechanical simulation approach. The thermal simulation modeled a layer-by-layer printing by the extrusion-based process. By solving the transient dynamic heat transfer equation using the material, geometry, and processing conditions as input, thermal history, and gradients were calculated by Digimat. These results were used as input for mechanical simulation in an integrated approach. The mechanical simulation provided an estimation of deflections in X, Y, Z directions as well as the overall deflection, residual stresses, and porosity in the printed part.

Deflection and dimensional variations

As the extrudate from the nozzle gets deposited on a substrate forming a layer, it cooled down and solidified. When the next layer was deposited, it transferred heat to the previous layer through conduction. With the addition of subsequent layers, repeated cycles of heating and cooling led to the development of a thermal gradient along the Z-axis. This gradient combined with non-uniform cooling leads to inherent thermal strains in the printed part. The extent of the strain varies according to the thermal gradient and coefficient of thermal expansion (CTE) of the material. The thermal strain causes deflection and warpage, finally leading to deviations in printed part dimensions and shape as opposed to original CAD geometry [84]. Simulation results showed similar deflection patterns and location for both c/s, as shown in **Figure 4.7a**.

The four corners of the unit cells, having a relatively large surface area, experience a higher rate of heat loss by convection and faster cooling. Also, the thermal gradient along Z-axis varies according to print surface area variation. These two aspects lead to the highest deflection in the four corners at the height of transition from the vertical to horizontal elements in the lattice geometry (**Figure 4.7a**), thereby increasing the print area considerably. It was also observed that printing experiments showed similar deflection patterns and locations as predicted by simulations for both c/s, as shown in **Figure 4.7b**. The non-uniform shrinkage caused by differential cooling during printing led to a non-uniform distribution of thermal strains, causing warpage and distortion of part shape.

(a)



(b)

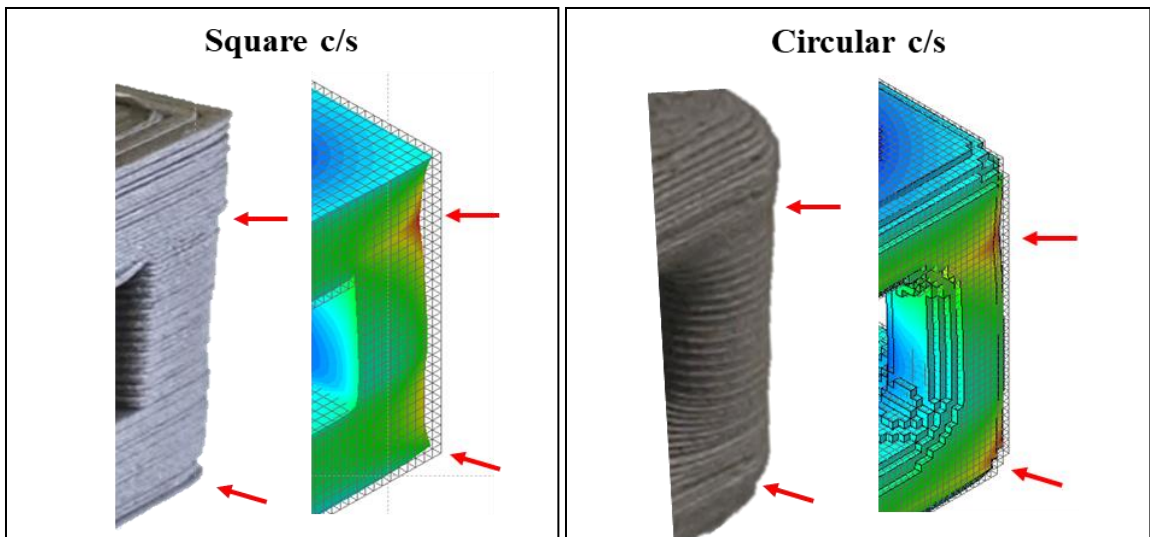


Figure 4.7. (a) Part deflection estimation from simulation of unit cell. (b) Deflection location and pattern were found similar in both simulation and experiments

Table 4.4. Part dimensions: CAD design vs. simulated part vs. printed green part

Part dimensions		A (mm)	B (mm)	C (mm)	D (mm)
Square c/s	CAD design	9.50	9.50	9.50	2.50
	Simulation results	9.35	9.35	9.41	2.45
	Experiment results	9.36	9.36	9.43	2.40
Circular c/s	CAD design	9.50	9.50	9.50	2.50
	Simulation results	9.37	9.37	9.47	2.45
	Experiment results	9.39	9.39	9.45	2.42

For quantitative verification of simulation results, simulated part dimensions were measured and compared with experimental results. The simulation tool does not directly provide simulated part dimensions. In order to estimate the part dimensions from deflection results, the deformed part geometry was exported from the simulation results in STL format. This file was then imported into CAD software (SolidWorks) to generate a 3D model, and dimensions of the deformed part were measured in SolidWorks. The respective dimensions of printed physical parts were measured using a vernier caliper. **Table 4.4** shows the dimension results from simulation and experiments compared with original CAD dimensions of unit cells of both c/s, while **Figure 4.8** explains what these dimensions represent. Experimental part dimensions fairly matched with that of the simulated part.

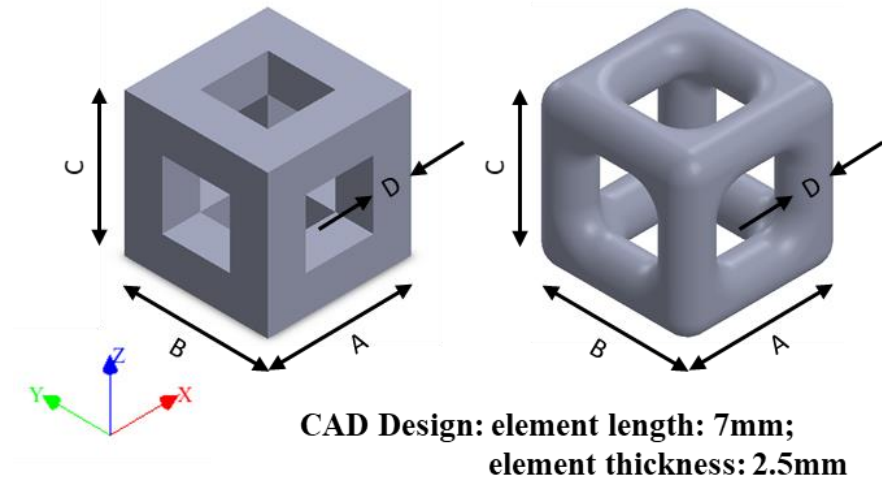


Figure 4.8. Representation of the A-B-C-D dimensions listed in Table 4

Table 4.5. Shrinkage relative to CAD design: simulated part vs. printed green part

		XY Shrinkage (%)	Z Shrinkage (%)
Square	Simulation	1.6	1.0
	Experiment	1.5	0.7
Circular	Simulation	1.4	0.3
	Experiment	1.2	0.5

As shown in **Table 4.5**, both simulation and experiment (**Figure 4.5**) showed shrinkage in all three directions (X, Y, Z) consistently. However, it was noted that simulations showed an overall higher shrinkage than experiments. This may be due to the stress relaxation effect in experiments tending to lower residual stress and lower overall deflection. The simulation model currently does not take the stress relaxation effect into account, leading to higher residual stresses during printing, which tends to develop higher deflections at the end of printing. Simulation results showed a maximum 1.6 % change in dimensions in XY-

plane and a 1 % change in Z-dimension for square c/s, whereas, in experiments, it was 1.5 % and 0.7 %, respectively. Overall, lower shrinkage was observed in circular c/s in both simulation and experiments.

Porosity estimation

The layer-by-layer printing using an extrusion-based process tends to develop macro porosity while trying to approximate the geometric profile. Several parameters such as the printing process, geometric complexity and material properties affect porosity formation, both in the infill and outer surface. The MF³ process simulation also provided an estimation of porosity distribution in the printed green part (**Figure 4.9**).

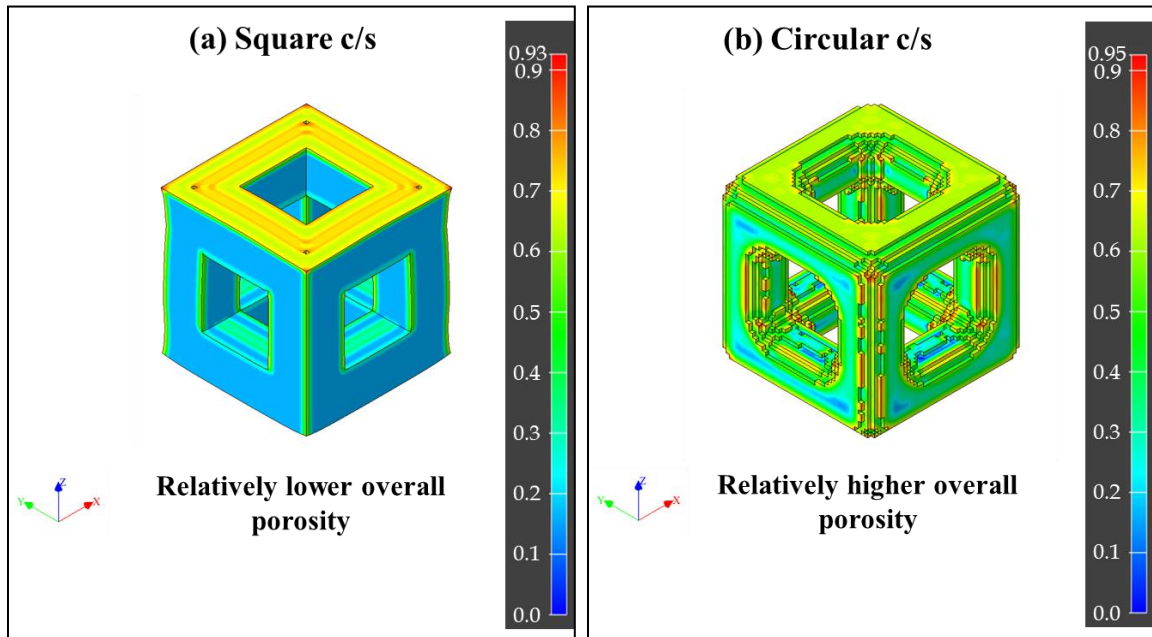


Figure 4.9. Porosity estimation of square and circular c/s unit cells (element length 7 mm, element thickness 2.5 mm)

It considers the part geometry, bead width, layer thickness, and toolpath (**Table 4.3**) to estimate the volume fraction of voids at each voxel mesh. An overall lower porosity was estimated in square c/s than in circular c/s. This can be correlated to higher relative density in square c/s than in circular c/s, as observed in experimental results. Toolpath having straight lines and a more uniform print area along Z-axis in square c/s led to lower porosity than in circular c/s.

Residual stress estimation

The process simulation provides an estimation of residual stresses induced during and at the end of the printing and cooling processes as a result of a thermal gradient, non-uniform cooling, and material shrinkage. **Figure 4.10** indicates the von Mises stress as residual stress developed at the end that can be attributed to thermal gradient due to layer-by-layer stacking as well as differential heat loss from the central zone and outer periphery.

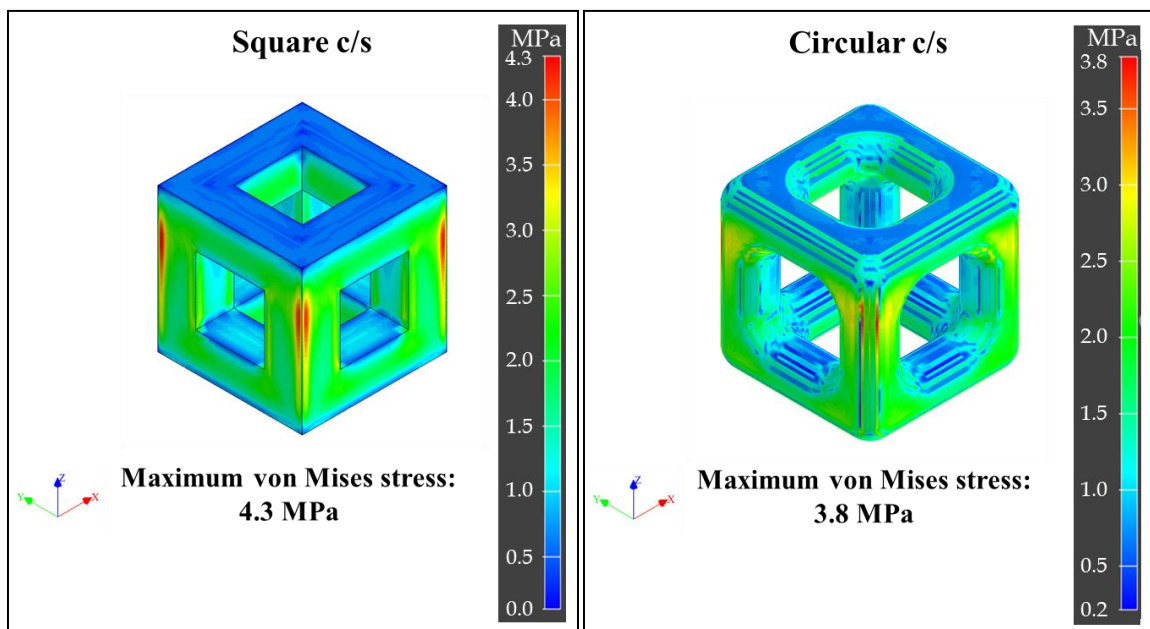


Figure 4.10. Residual stresses estimation from simulation of unit cells

The estimated maximum residual stress for the square and circular c/s was 4.3 MPa and 3.8 MPa, respectively. Sharp corners in square c/s led to slightly higher residual stresses than in the circular one. Like deflection results, residual stresses were found to be maximum at the outer corners and oriented along Z-axis for the same reasons of differential heat transfer and thermal gradient along the Z-axis, respectively. Residual stresses distort the printed part and affect its mechanical strength. In MF³, high residual stresses may lead to cracks or damage the part during the debinding and sintering processes. Lower thermal gradient, uniform and slower cooling helps in reducing residual stresses. Hence a closed chamber-controlled temperature printing environment would provide better part quality.

4.3.3 Extrudate deflection

The experimental printing of lattice showed large deflection in unsupported overhang due to gravity. It can be considered as a defect that stems from the inherent overhang feature in any lattice structure. The sagging deflections were observed consistently in both c/s; however, the amount of deflection varied with cross-section type and geometric configuration. It indicated that the sagging deflection is geometry-dependent and can be controlled by part design optimization. A capability to predict the sagging as a function of lattice geometry, material properties, and printing parameters would further enable design for lattice structure. Simulation results were investigated to see extrudate deflection estimation.

However, it was observed that simulation did not provide an estimation of such deflection, as shown in **Figure 4.11**. The reason being the current voxel-based simulation model not

considering gravity. As an alternative, an analytical hypothesis has been proposed and investigated for extrudate deflection estimation.

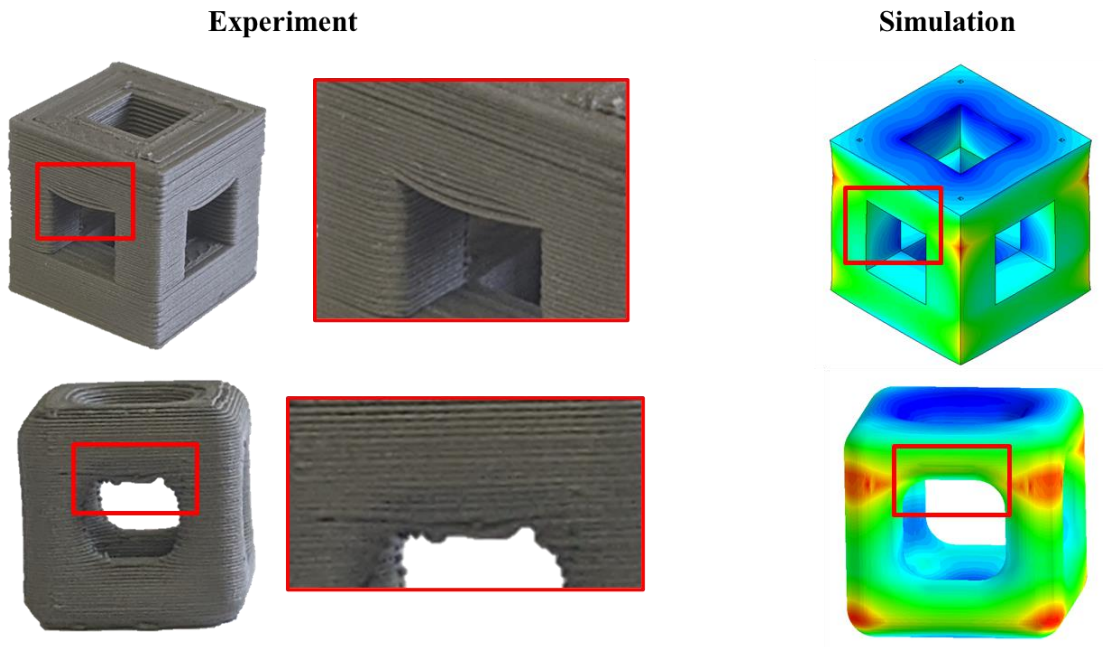


Figure 4.11. Large deflection observed in experimental printing in unsupported regions, whereas simulation did not provide an estimation of such deflection

Extrudate in the unsupported region was considered equivalent to a simply supported beam under uniformly distributed load. The geometry of a single extrudate was considered equivalent to the beam geometry, material properties at the extrusion temperature equivalent to the beam material, and the self-weight of the extrudate as the uniformly distributed load on the beam, as shown in **Figure 4.12a**.

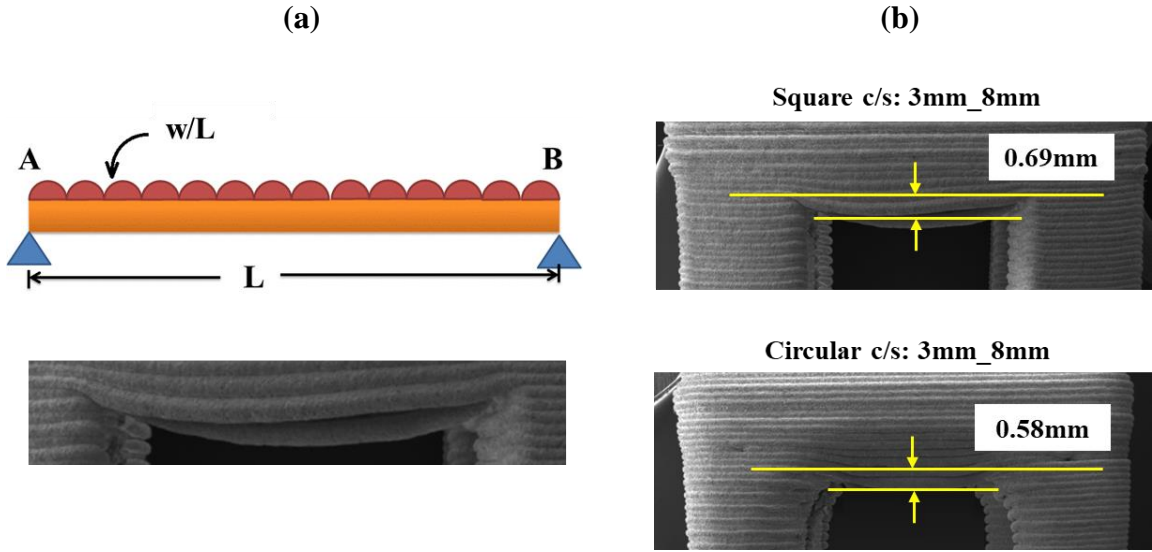


Figure 4.12. (a) Extrudate in unsupported overhang was considered equivalent to a simply supported beam under uniformly distributed load; (b) extrudate deflection in unsupported region measured in printed green parts

Deflection (δ) of a UDL beam is given by [85]

$$\text{Deflection, } \delta = \frac{5wL^4}{384EI} \quad (3)$$

where

$$w = \text{self-weight / length} = \frac{\rho\pi d^2}{4}$$

ρ = extrudate density at extrusion temperature

d = extrudate diameter (nozzle diameter)

L = overhang length

E = Young's modulus at extrusion temperature

$$I = \text{moment of inertia} = \frac{\pi d^2}{64}$$

Rearranging **Equation 3**,

$$\delta = \frac{5 \times 64}{384 \times 4} \frac{\rho}{E} \frac{L^4}{d^2} \quad (4)$$

Here,

$\frac{\rho}{E}$ = material variable; $\frac{1}{d^2}$ = machine variable (d = nozzle dia.); L = part geometry variable

Deflection can be minimized by optimizing the material, machine, and geometry variables.

$$\delta_{\min} = \left(\frac{\rho}{E}\right)_{\min} \times \left(\frac{1}{d^2}\right)_{\min} \times (L^4)_{\min} \quad (5)$$

In this study, the material, printing parameters, and nozzle diameter were kept unchanged, so the material and machine variables were constant. Hence, the deflection was a function of part geometry only.

$$\delta = f(L) \quad (6)$$

To define the extrudate deflection as a function of element length, the deflection was measured in unit cells of 3 mm and 2.5 mm element thickness and element lengths 8 mm, 7 mm, and 6 mm printed with square and circular c/s, as shown in **Figure 4.12b**. The extrudate deflection amount was found to vary with not only element length and thickness but also cross-section type, as shown in **Table 4.6**.

Table 4.6. Extrudate deflection: experimental results

Cross-section	Element length (mm)	Overhang length (mm)	Deflection (Experimental) (mm)
Square: 3 mm	8	5	0.69
	7	4	0.58
	6	3	0.45
Square: 2.5 mm	8	5.5	0.78
	7	4.5	0.60
	6	3.5	0.53
Circular: 3 mm	8	5	0.58
	7	4	0.46
	6	3	0.33
Circular: 2.5 mm	8	5.5	0.61
	7	4.5	0.53
	6	3.5	0.39

A power equation was derived by plotting the experimental deflection graph as a function of overhang length. As shown in **Figure 4.13a** and **13b**, deflection increases with overhang length for both cross-sections. However, a lower deflection was observed in circular c/s than in square one, as shown in **Figure 4.13c**.

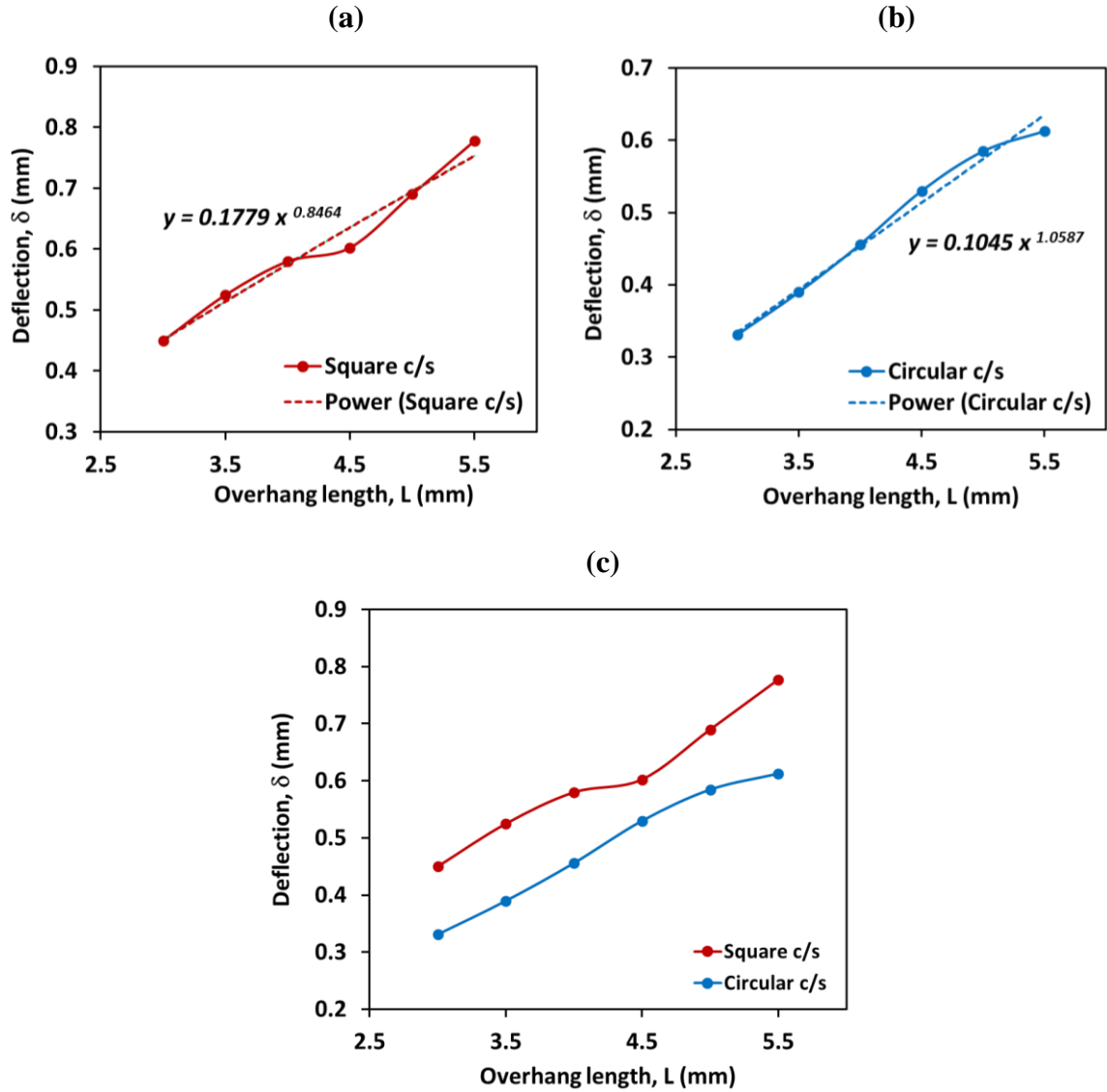


Figure 4.13. (a) Effect of overhang length on extrudate deflection in the unsupported region of square c/s. (b) Effect of overhang length on extrudate deflection in the unsupported region of circular c/s. (c) Effect of lattice element cross-section extrudate deflection in the unsupported overhang (comparison between 4.13a and 4.13b)

Therefore, the following equations were derived:

Deflection in square c/s;

$$\delta = 0.1779 (L)^{0.8464} \quad (7)$$

Deflection in circular c/s;

$$\delta = 0.1045 (L)^{1.0587} \quad (8)$$

Eq. (7) and (8) can be generalized to represent the extrudate deflection as a function of element overhang length;

$$\delta = f(L) = K(L)^a \quad (9)$$

where K: constant of the equation; a: exponent

‘K’ and ‘a’ are dependent on element cross-section geometry. Moreover, any change in material, process, and machine variables would also lead to variation in these constants of the empirical equation.

To verify the proposed hypothesis and validate the presented empirical relationship, it was used to estimate the sagging deflection in the unit cells of 2 mm element thickness and element length 8 mm, 7 mm, and 5 mm. The estimated deflections were verified with experimental results and a fair agreement was observed between them, shown in **Table 4.7**.

Table 4.7. Extrudate deflection: estimation vs. experimental results

Element thickness	Element length, L (mm)	δ (Estimation) (mm)	δ (Experiment) (mm)
Square: 2 mm	8	0.81	0.79
	7	0.69	0.66
	6	0.57	0.59
Circular: 2 mm	8	0.70	0.72
	7	0.57	0.60
	6	0.45	0.48

4.3.4 Sintered part quality

Green parts of defect-free unit cells printed using identified printing conditions were further subjected to post-printing processes. Polymer binder was eliminated by solvent debinding in heptane solution and thermal debinding. Finally, thermal sintering in an inert environment provided fully dense Ti-6Al-4V parts, as shown in **Figure 4.14**. The unsupported overhang features in both square and circular cross-sections survived without collapse and distortion during debinding and sintering processes.

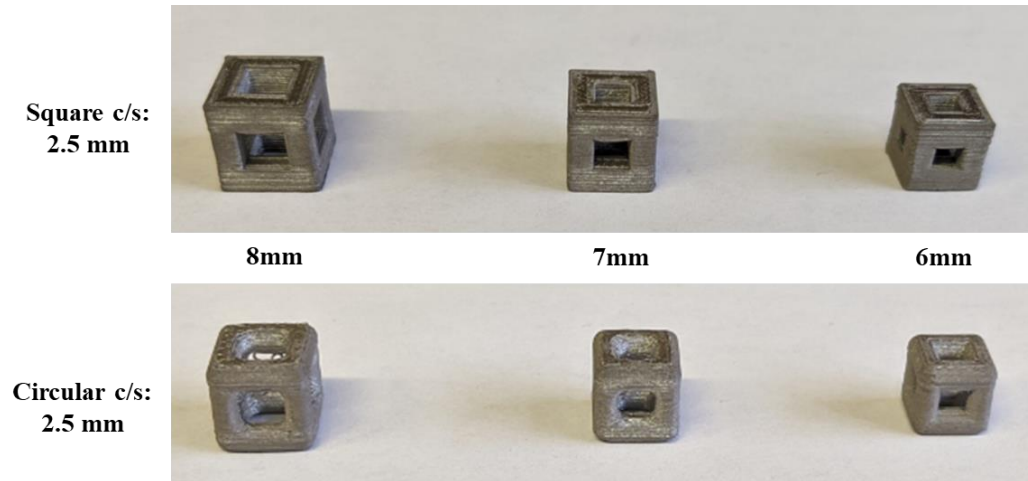


Figure 4.14. Sintered unit cells

Removal of polymer binder that constitutes 41 % volume of the filament material leads to a large amount of shrinkage during the debinding process. Moreover, thermal sintering provides densification of the metal, which further adds shrinkage. Sintered part dimensions were measured for shrinkage characterization. An overall 15~17 % shrinkage was observed in all three (X, Y, Z) directions (**Table 4.8**). Additionally, sintered parts Archimedes density was measured, and relative density was calculated using the below equation:

$$\text{Relative density}_{\text{sintered}} = \frac{\rho_{\text{Arch. sintered}}}{\rho_{\text{Ti64}}} \quad (10)$$

where, $\rho_{\text{Arch. sintered}}$ = Archimedes density of the sintered part

ρ_{Ti64} = Theoretical density of Ti-6Al-4V (4.43 g/cc)

Table 4.8. Shrinkage and relative density of sintered unit cells: element thickness 2.5 mm

	XY-Shrinkage (%)	Z-Shrinkage (%)	Relative density (%)
Square c/s	15.7	14.8	94.3
Circular c/s	17.0	15.4	93.5

Further, to investigate how the extrudate sagging in the unsupported overhang in the green part affects sintered part quality, the unit cells were cut in the middle Z-axis.

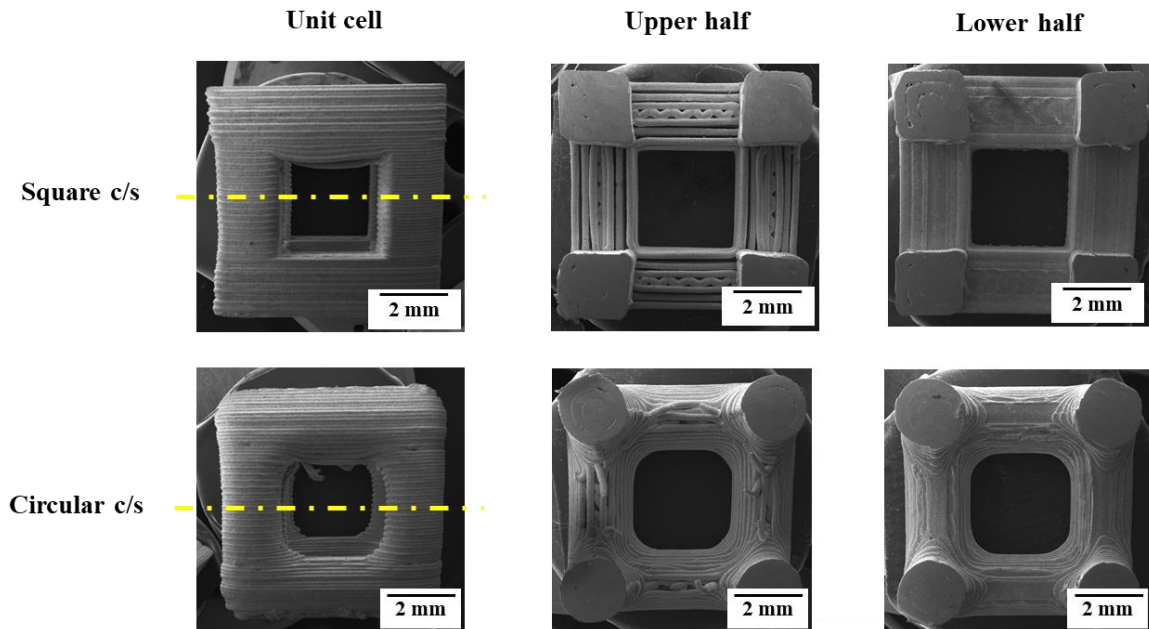


Figure 4.15. Lack of diffusion between beads was observed in the bottom-facing surface of the unsupported overhang feature as an effect of extrudate sagging in the green part

As shown in **Figure 4.15**, poorly diffused and loose beads were observed in the bottom-facing surface of unsupported overhangs, whereas adequate diffusion and packing of densification were observed in the lower half of the cell.

4.3.5 Multi-stacked lattice structures

Identification of processing conditions and geometry parameters optimal for lattice structure led to the successful fabrication of multi-stacked and complex shaped Ti-6Al-4V lattice structures by MF³ that were not possible before the study. Design-I shown in **Figure 4.16**, was designed using the circular c/s of element length 7 mm and diameter 2.5 mm, which was studied at unit cell level earlier in this study.

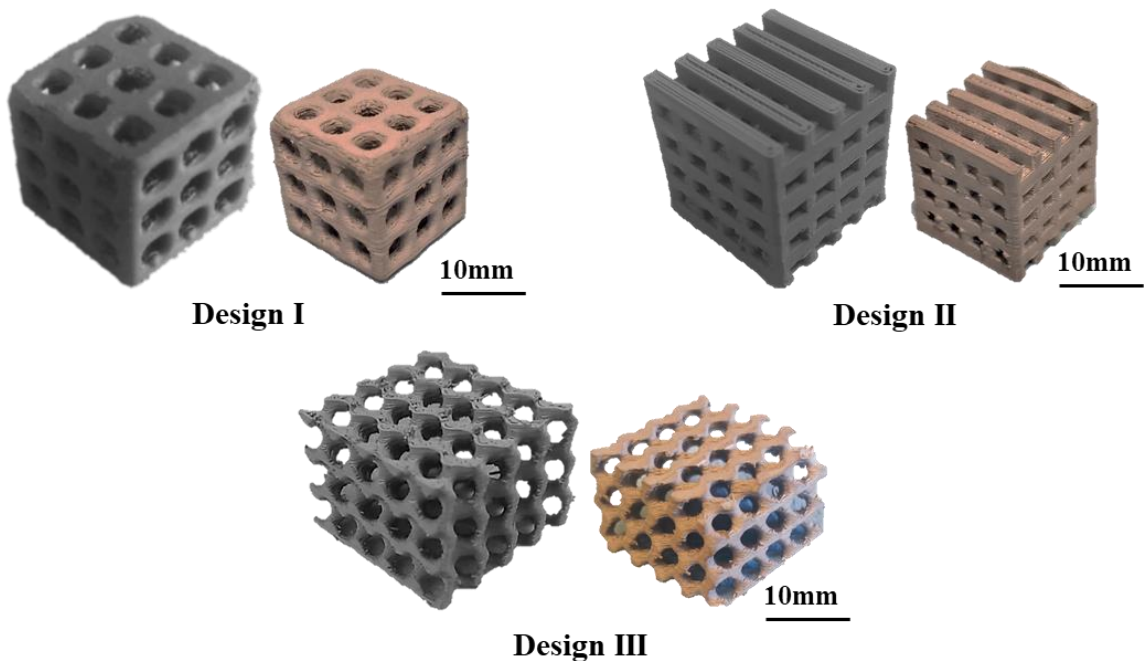


Figure 4.16. Stacked Ti-6Al-4V lattice structure (green and sintered parts) of various configurations fabricated by MF³

The multi-stacked lattice structures were printed without defects using a 0.35 mm diameter nozzle and printing condition-B (**Table 4.1**). Printed parts were able to survive solvent debinding without collapsing. Moreover, thermal debinding and sintering were conducted using the conditions used for bulk geometries [10, 11], and the lattice structures survived without collapse and distortion. Similarly, Design-II and Design-III lattice structures (**Figure 4.16**) suitable for various applications were printed and sintered. Design-III is an example of a Triply Periodic Minimal Surface structure based on the gyroid unit cell. It demonstrates the potential of MF³ to fabricate beam-based and surface-based lattices.

4.4 CONCLUSIONS

MF³ printing of lattice structure was investigated for the first time using experimental and analytical approaches. Feasible processing conditions were identified for Ti-6Al-4V to fabricate defect-free lattices. The effects of lattice geometry parameters on part deflection and relative density at the unit cell level were reported. Computational simulations using the finite element method were employed to predict the part quality, and results were verified by experimental printing. Having identified the simulation limitation, an analytical approach has been presented to estimate the extrudate deflection in unsupported regions of lattice structures. Finally, using the identified processing and geometry parameters, multi-stacked lattice structures were successfully printed and sintered.

Following conclusions emerge from the present work:

1. The unsupported overhang feature and narrow/ tiny cross-sectional print area in lattice structures required considerable changes in MF³ printing parameters

compared to printing bulk parts, e.g., filament retraction, concentric toolpath, extrusion multiplier < 1 , low printing speed, small layer thickness, and bead width.

2. XY, as well as Z dimensional variations in green parts, were found to be increasing with an increase in lattice element length or decrease in element thickness for both types of cross-sections. It can be attributed to a higher aspect ratio (L/d), leading to higher longitudinal shrinkage. Square c/s showed higher deformation than circular c/s. Also, the response curves were different for the two cross-sections.
3. Relative density in green parts was found to increase with lattice element length and element thickness for both cross-sections. However, square c/s showed an overall higher relative density than circular c/s. Also, the response curves were different for the two cross-sections.
4. Simulations and printing experiments of unit cells showed similar deflection patterns and locations, and shrinkage in all three directions (X, Y, Z) consistently for both cross-sections. Circular c/s showed lower shrinkage resulting in lower variation in dimensions compared to square c/s in both simulation and experiments.
5. Simulation estimated an overall lower porosity in square c/s than in circular c/s. This can be correlated to higher relative density in square c/s than in circular c/s observed in experimental results. Toolpath having straight lines and a more uniform print area along Z-axis led to lower porosity in square c/s than in circular c/s.
6. The experimental printing of lattice showed large deflection/sagging in unsupported regions due to gravity, whereas simulation was unable to estimate such deflection. An analytical model was presented to estimate extrudate deflections and verified with experimental results.

7. Extrudate deflection in unsupported regions was found increasing with overhang length, which is a function of lattice element thickness and length. Square c/s lattice showed larger extrudate deflection than circular c/s.
8. Lack of diffusion between beads was observed in the bottom facing surface of unsupported geometry of sintered unit cells as an effect of extrudate sagging in the green part stage.

This study proves that MF³ can fabricate fully dense Ti-6Al-4V lattice structures that appear to be a promising candidate for applications where mechanical performance, light-weighting, and design customization are required. The outcome of the work is an understanding of geometry-processing-properties interrelationships governing the design and fabrication of lattice structures by MF³. The insights gained through the work will enhance the design for MF³ (DfMF³).

CHAPTER 5

PATIENT-SPECIFIC MAXILLOFACIAL IMPLANT USING METAL FUSED FILAMENT FABRICATION (MF³): DESIGN, FABRICATION AND ANALYSIS

5.1 INTRODUCTION

Over the last few decades, dental restoration of edentulous patients has been significantly enhanced by implant dentistry, especially when conventional complete dentures find difficulty in retaining their stability in the long-term [86-88]. For the success of dental implants, anatomic conditions such as sufficient bone height, thickness and density, play a deciding role [88]. Bone regeneration by grafting is widely employed to grow new bone in weak jawbone areas by autografting, using other bone as a scaffold [89, 90]. However, in the case of severe bone resorption, extensive bone regeneration requirement represents clinical treatment challenges leading to hesitation from patients [91]. The development of a patient-specific implant would suffice the need for adequate bone structure to support dental implants. Particularly for elderly patients, such an implant is of great importance as they cannot or may not want to undergo complex regenerative surgeries, but need a fixed dental restoration [92, 93].

Apart from dental rehabilitation, maxilla and mandible reconstructions find applications in treating bone defects caused by tumors, injuries, or infections [94, 95]. However, such reconstruction represents major challenges from both engineering and medical aspect [94]. On the one hand, the complexity of facial anatomy, vital adjacent organs, the possibility of

infection, and the uniqueness of each patient are the challenge for doctors, on the other hand, complex facial bone structure design, the unique morphology of each patient, high demand on reconstruction material and performance, and limitations of manufacturing process pose great deal challenges for engineers [96]. Moreover, high osteoporotic structure in elderly patients makes it more challenging for doctors due to low regeneration tendency, and engineers due to reduced bone structure area and strength to support custom implants.

However, several developments in digital technology have made the fabrication of custom-made implants that perfectly match the anatomy and local morphology of the patient feasible [92, 97]. Modern technologies such as cone beam computed tomography (CBCT) for patient data acquisition, high-speed intraoral scanner to capture a direct optical impression, digital software for clinical analyses and surgical planning, 3D printers for a wide range of high-performance materials have fueled the progress in implant dentistry and maxillofacial reconstruction [93, 96, 98, 99].

In particular, additive manufacturing (AM) has enabled the fabrication of patient-specific implants for individual patients [94, 100]. Although the existence of AM technologies has been there for several decades, they have been leveraged more intensively over the last decade in the field of biomedical engineering [94, 100-103]. The method, also known as 3D printing or rapid prototyping, builds a three-dimensional (3D) part by adding the material layer-by-layer as opposed to a subtractive or formative method of manufacturing [1]. The technology is capable of building any complex shape in a variety of geometries without using specific molds, making it the best-suited process for custom-made implants. Moreover, the AM process can produce porous structures that help in optimizing the

effective stiffness, and thus reduce stress shielding in implants [99]. Such porosity also provides anchor sites to the bone tissue and promotes accelerated osseointegration [88, 104]. Hence, 3D printed implants could adequately transfer the stresses between implant and bone, thereby increasing the life of the implant and implant-supported restoration. AM brings a considerable reduction in wastes of material and time when compared with the conventional manufacturing methods such as the milling process specifically for implants with complex geometries [88]. In addition, AM has enabled the fabrication of physical biomodels of a patient's anatomy that serve as a great tool for operational planning and simulations [100-103].

While AM brings in promising capabilities for dental and maxillofacial implants, from the material front, limited compatible choices are available due to versatile demands on mechanical, physical and chemical characteristics of the implant material [105, 106]. Among others, titanium is a widely used material in implants and other biomedical applications due to its high strength-to-weight ratio, corrosion resistance, low density and non-magnetic properties [99, 107, 108]. In particular, Ti-6Al-4V (90 % titanium, 6 % aluminum, and 4 % vanadium), due to its high biocompatibility, is considered one of the most suitable biocompatible materials for medical applications [73]. Fabrication of Ti-6Al-4V implants has been investigated with various AM technologies [109].

Metal AM technologies such as selective laser melting (SLM), electron beam melting (EBM) or direct energy deposition (DED) have been widely explored for metal implant fabrications [107, 108, 110-113]. However, the limitations of these processes are (i) very high initial capital investment (ii) safety concerns due to directly working with loose reactive metal powder. Moreover, the high energy consumption of the only choice of

industrial level operation limits the economic viability of small-batch manufacturing. In addition, high thermal gradients, localized heat, and rapid cooling rates induce residual stresses, distortion, non-equilibrium microstructures and anisotropy leading to structural property differences [114, 115]. These limitations act as a barrier in the widespread implementation of metal AM technologies in implant dentistry and maxillofacial reconstructions. To overcome the above limitations, an advanced AM technology, known as metal fused filament fabrication (MF³), is rapidly emerging. It enables 3D printing of metal parts using desktop-level FFF printers [1, 7, 116, 117].

MF³ is essentially an extrusion-based printing process that uses highly filled metal powder-polymer binder filaments, where the polymer binder holds metal particles together in a feedstock and assists in material flow and deposition during printing [11, 47, 118]. **Figure 5.1** shows the MF³ process demonstrating the fabrication of a patient-specific implant.

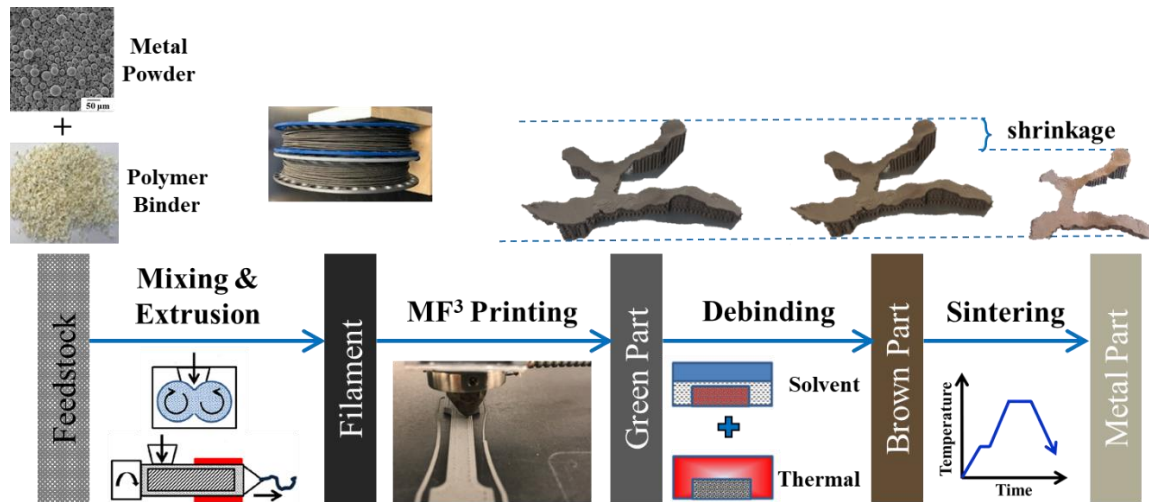


Figure 5.1. Overview of MF³ process showing filament preparation, printing, debinding, sintering, and demonstration of custom implant part fabricated by MF³ with Ti-6Al-4V.

MF³ has been successfully used to print Ti-6Al-4V and ceramic parts of varying geometries, as reported in the previous publications by our research group [10-12, 47, 118]. As identified in the literature survey, implant dentistry and maxillofacial reconstruction have a pressing need for fabrication technologies that could manufacture custom-made implants efficiently and economically at small to moderate scales. Building on the findings in Ti-6Al-4V printing with MF³, in this work we investigated the feasibility and suitability of Ti-6Al-4V printing with MF³ to manufacture patient-specific maxillofacial implants.

The purpose of this investigation is to examine the applicability of MF³ to manufacture custom-made 3D-printed implants in general, and in particular, a patient-specific maxillofacial implant for dental restoration of elderly patients with osteoporotic maxillary structure. We described the methodology followed in the design and fabrication of Ti-6Al-4V maxillofacial implants using MF³ technology. The methodology from processing the digital data of the patient's oral anatomy to the design development and fabrication of implant is discussed. There was a specific emphasis on the applicability of MF³ for custom implants in terms of manufacturability with the inclusion of support structures for the first time. Also, MF³ printing of the implants was simulated to investigate potential deformation and residual stresses. Moreover, the sintered parts were characterized for surface topography, density, porosity, microstructure, and hardness that would affect the implant performance.

This study is based on a real clinical case of an 85-year-old partially edentulous female patient. With the complaints of difficulty in eating and speech, she intended to get dental restoration. Her CBCT scan revealed severe resorption of the upper jaw and maxillary bone and no teeth in the upper jaw as shown in **Figure 5. 2**. To provide for dental implants,

adequate reconstruction of the maxillary structure was needed. Considering the patient's age, bone regeneration was not a suitable option. Hence, the custom-made maxillofacial implant was the best solution.

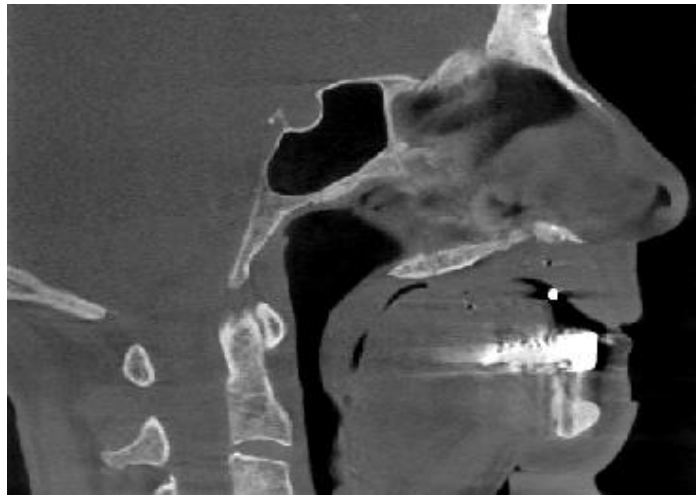


Figure 5.2. CBCT scan of the patient showing the defect

5.2 MATERIALS AND METHODS

5.2.1 Materials

The patient's CBCT data was required to design and fabricate the physical models of the patient's anatomy and maxillofacial implant. A photocurable acrylate material FLGPWH04 (Formlabs, Somerville, MA, USA) was used to fabricate the anatomical model by the SLA method using Form 2 (Formlabs, Somerville, Massachusetts) printer. The implant prototypes were printed by MF³ using the filament, which has 59 vol.% of Ti-6Al-4V powder dispersed in a multi-component custom polymer matrix using a desktop printer, Pulse (MatterHackers, Lake Forest, CA, USA).

5.2.2 Methods

The workflow started with the patient's anatomical data in 2D DICOM format obtained from CBCT scan. This data was imported into a biomedical software, Mimics (Materialise, Leuven, Belgium), for image processing and segmentation to develop a 3D CAD of the patient's facial bone and dental structure. This 3D model in STL format was used to fabricate a physical biomodel by SLA process. The biomodel helped the oral and maxillofacial surgeons to evaluate the current condition of the maxilla structure and implant requirements and accordingly propose a patient-specific implant solution. Using this input, an implant design was developed matching the patient's maxilla structure, and 3D CAD of the implant was generated using modeling software, 3-Matic (Materialise, Leuven, Belgium), considering the maxilla structure geometry as reference.

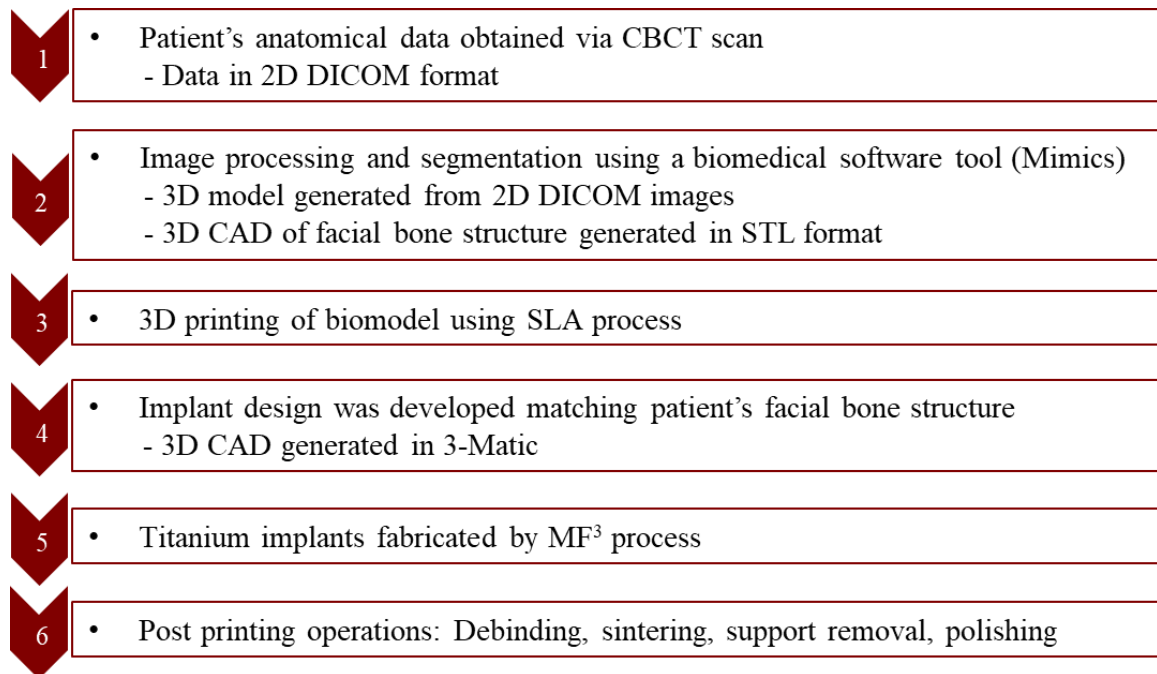


Figure 5.3. The workflow of patient-specific implant fabrication using the MF³ process

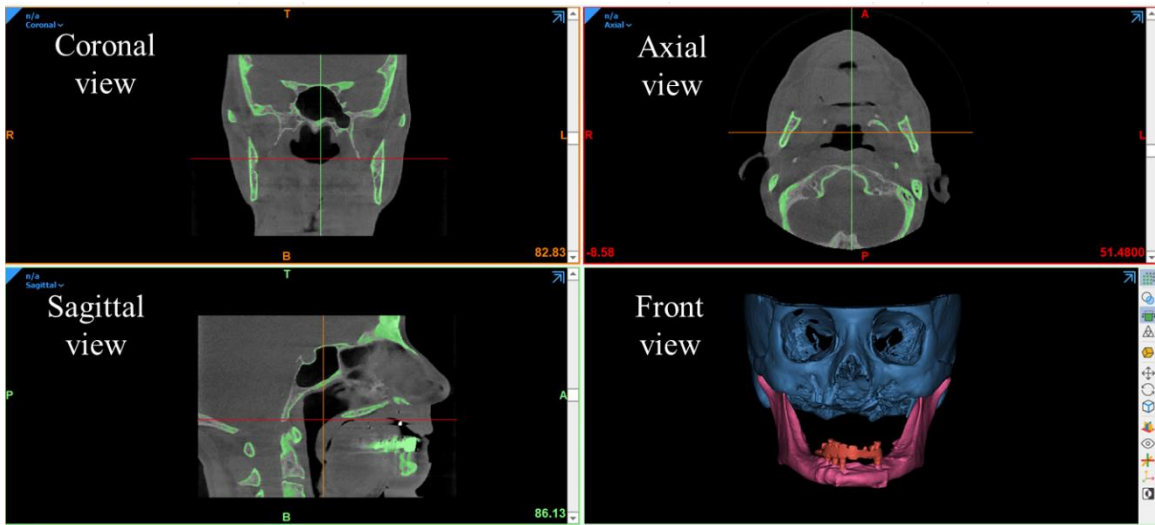
Using the STL files, implant components were printed by MF³, and the green parts were debound and sintered to get fully dense Ti-6Al-4V parts. Also, the MF³ printing process was simulated using a CAE simulation tool, Digimat (MSC Software, Newport Beach, CA, USA), to estimate part deflections and residual stresses. Finally, the resulting part attributes, such as geometric fidelity, density, porosity, surface morphology, metallography and hardness were evaluated as they affected the implant performance. A typical workflow of patient-specific implant fabrication using the MF³ process is shown in **Figure 5.3**.

5.2.3 Design of the implant

Image processing and segmentation

The latest facial morphology of the patient was obtained through a CBCT scan in 2D DICOM format. This 2D data was imported in Mimics for image processing and segmentation, and a 3D model of facial anatomy was generated from the 2D images. The vital aspect of this process was extracting the region of interest from DICOM images without much compromise to actual anatomical details.

(a)



(b)

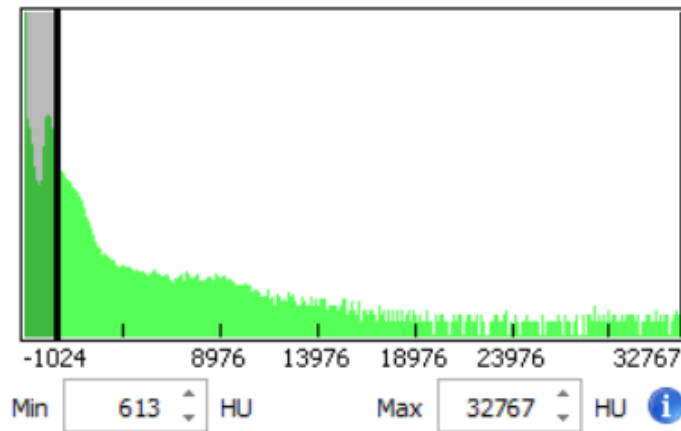


Figure 5.4. (a) Segmentation of maxilla and mandible bones from the overall facial anatomy; coronal, axial, sagittal and front views (b) Hounsfield radiodensity scale

Subsequently, the hard bone elements were segmented using the Hounsfield radiodensity scale in Mimics by filtering out a radiodensity of less than ~610 HU. A 3D CAD of bone and the dental structure was developed by segmenting the soft tissues out, as shown in **Figure 5.4**. The patient's osteoporotic bone in maxilla structure and absence of maxillary

dentition clearly showed the need for maxillofacial and dental implants, respectively. The mandible structure was separated from the maxilla, and a 3D CAD of the maxillary structure was exported in STL format. This data was further used not only in the fabrication of a biomodel by SLA but also as a reference to develop a patient-specific implant design to ensure a close geometric fit.

3D printed physical anatomical model

A physical model of a biological structure, generally referred to as a ‘biomodel’, has been used in several craniomaxillofacial surgery investigations to not only facilitate and improve treatment planning but also reduce the risk, time, and cost to patients and hospital [116-121].

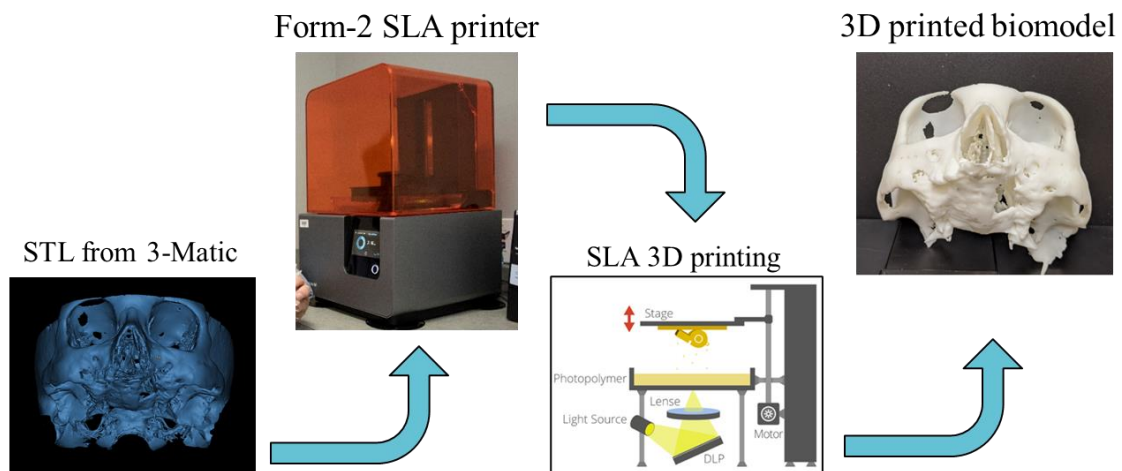


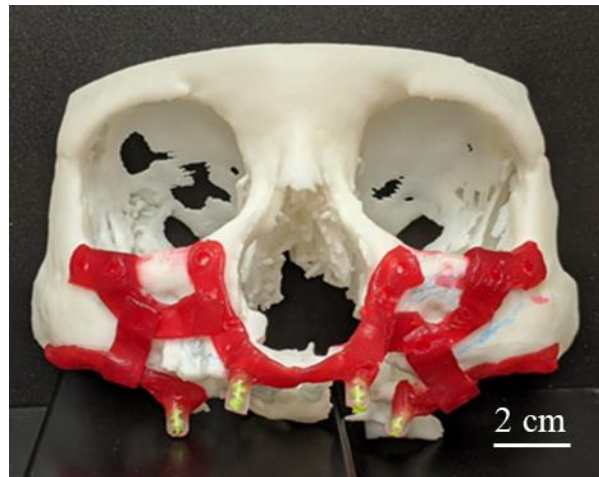
Figure 5.5. SLA process flow to fabricate 3D printed maxilla structure biomodel of the patient

The digital biomodel of the patient's maxilla structure obtained from Mimics in STL format was used to fabricate a physical biomodel using SLA, as shown in **Figure 5.5**. The STL file was processed through PreForm software (Formlabs, Somerville, Massachusetts) that was used for build-setup to define the part layout, orientation, supports, slicing, and printing parameters. An SLA printer, Form 2 (Formlabs, Somerville, Massachusetts), was used to build a 3D part through layer-by-layer photopolymerization by ultraviolet light. After printing, the part was rinsed in isopropyl alcohol (IPA) to remove any uncured resin from its surface. After drying the rinsed part, it was post-cured by exposing it to light and heat to achieve the highest possible strength and stability of the material. Finally, supports were removed from the part and remaining support marks were sanded for a clean finish.

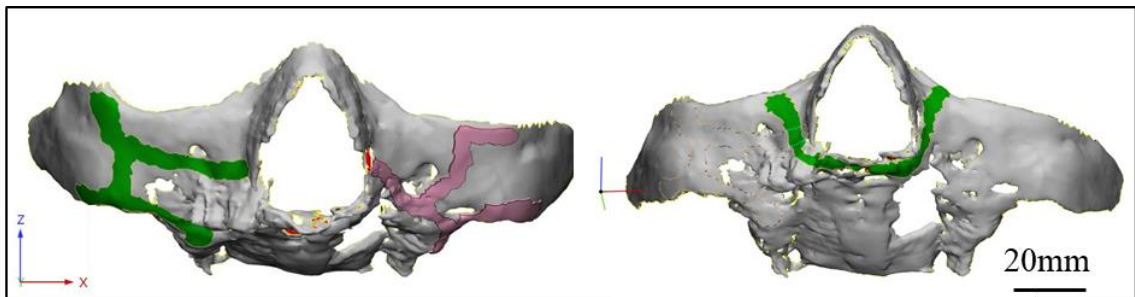
Implant design development

The physical biomodel enhanced visualization and understanding of the current bone loss condition in the patient's maxilla structure. **Figure 5.6a** shows the implant design requirement defined by oral & maxillofacial surgeons after thorough investigations of the patient's condition, the osteoporotic maxillary bone, and dental implant requirements. In this process, care needed to be taken to ensure the position of important nerves and other soft tissues were investigated while identifying bone with adequate density for fixation of the implant [93]. The maxillofacial implant was split into three components to mitigate surgery difficulties and allow for a certain amount of flexibility in positioning that might be identified during surgery, as indicated by surgeons. Moreover, it was recommended from an engineering point of view as well because of simplification in part design and wider allowable geometric tolerance in fabrication.

(a)



(b)



(c)

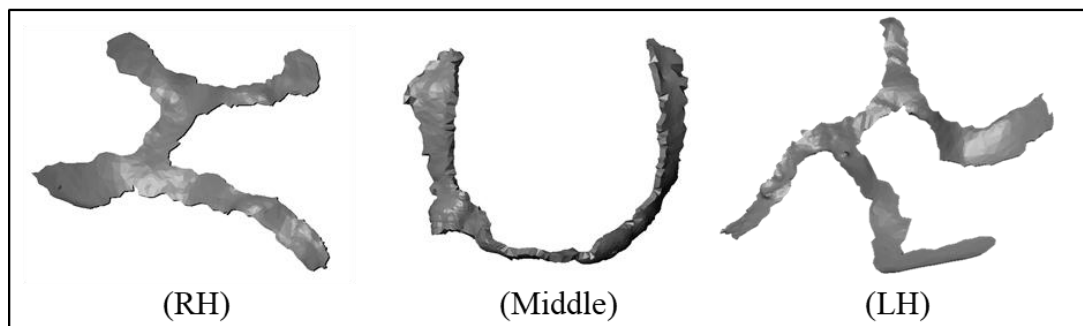


Figure 5.6. (a). Implant design requirement as defined by the oral/ maxillofacial surgeons considering the current condition of the patient's maxilla structure bone and dental implant requirements. (b) Implant geometries generated from digital biomodel using 3-Matic. (c) First-generation design of the implant. The implant was divided into three components, (RH, middle & LH parts)

Also, larger support structures would be required to print the implant in one piece, as opposed to smaller supports needed in simplified relatively flatter geometries. The implant was split into three parts, the Right Hand (RH), middle, and Left Hand (LH) components, as shown in **Figure 5.6c**. Here, RH and LH refer to the patient's LH and RH side, respectively. Each part consisted of mounting posts in the form of a cylindrical boss that would eventually support dental implants. Also, mounting holes were provided to fix the implants on the existing maxilla structure of the patient at the best position having sufficient bone density to support the implants.

Having developed the design concept, digital biomodel enabled the development of implant geometry to match the patient's anatomical condition and identified implant solution. Implant geometries were generated in STL format from digital biomodel using 3-Matic software (Materialise, Leuven, Belgium). Biomodel surfaces were extracted and offset to build the implant geometry as shown in **Figure 5.6b**, to ensure a perfect fit between the implant and maxilla structure. For each implant component, an STL file having tessellated surfaces was exported to Solidworks for geometric fine-tuning, edge correction and STL density reduction. In the proof-of-concept stage, the initial design did not include mounting posts and holes, as the objective was to investigate the applicability of MF³ to manufacture such custom implants. These models were used for MF³ printing of the implants.

5.2.4 Fabrication of customized Ti-6Al-4V implants

An extrusion-based desktop printer, Pulse (MatterHackers, Lake Forest, CA, USA), was used to print the implants. Green parts were fabricated using 1.75 mm filaments of 59 vol.% of Ti-6Al-4V powder dispersed in a multi-component custom polymer binder. The feedstock and filament were prepared based on our earlier investigations [10, 11]. The implant STL file was processed through Simplify3D software to generate GCode instructions. The processing parameters used are shown in **Table 5.1**. The printing parameters were selected based on several preliminary printing experiments of various geometries using different parameters. A lower printing speed and smaller layer thickness, as opposed to printing simpler solid geometries, were used to ensure the geometric fidelity of the thin-walled complex geometry of the implants. A layer thickness of 0.1-0.15 mm was chosen to achieve suitable resolution considering the 1 mm thickness of the implant. A 0.4 mm diameter nozzle was selected to achieve a bead width in the range of 0.48-0.60 mm that provides adequate in-plane geometric accuracy. Extrusion and build plate temperatures were chosen in the range of 240-260° C and 65-75 °C, respectively. A lower printing speed, 5 mm/s, was considered to achieve better detailing of the intricate geometries, as opposed to 10-15 mm/s used generally. A concentric infill toolpath was found more suitable than 0-90° that works well for regular geometries. Based on these preliminary experiments, the optimized parameters used to print the actual implant are shown in **Table 5.1**.

Table 5.1. Printing process parameters

Process parameters	Settings
Layer thickness (mm)	0.1
Bead width (mm)	0.48
Extrusion temperature (°C)	240
Build plate temperature (°C)	65
Extrusion multiplier	1
Printing speed (mm/s)	5
Toolpath (°)	Concentric

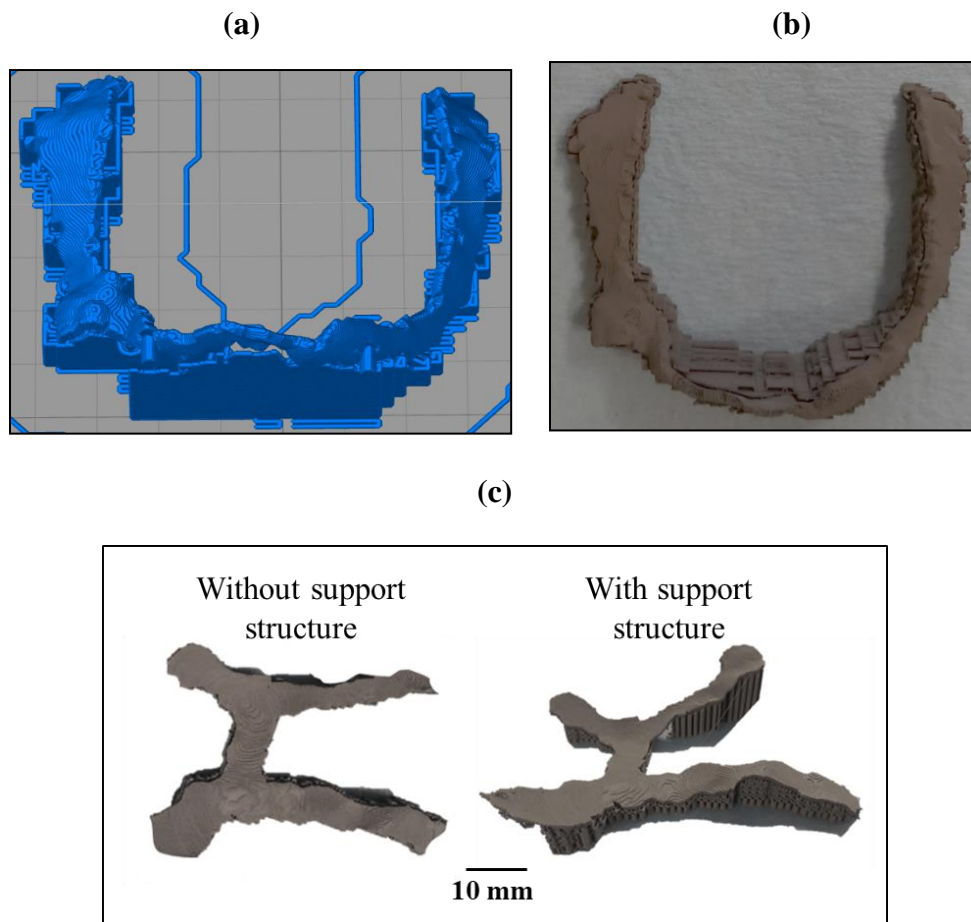


Figure 5.7. (a) Build setup showing sliced model, toolpath support structure of the middle part (b) MF³-printed green part (c) printing without appropriate support structure failed, optimal support led to successful printing of the RH part

Support structure

Initial attempts to print the implants by MF³ led to poor printability and highly defective parts due to irregular geometry, overhangs, and unsupported features. Hence, the use of a support structure was considered for the first time in MF³. Support structure in MF³ brings several challenges such as no sacrificial material can be used for supports that can be dissolved in a solvent because of the risk of losing the integrity of the green part. The other option of support structure using the parent material itself has a challenge because cutting the supports off in the green stage may easily damage the part. Hence, in this study, the support structures printed using the parent material were kept intact through the debinding and sintering stage as well. Moreover, cutting the support off in the sintered metal stage was difficult in this case due to irregular geometry and uneven surfaces of the implant. Hence, minimal support structures were employed to print the thin-walled implants. Eventually, the introduction of support structures improved the printability as shown in **Figure 5.7c**. For each geometry, an optimal support structure was designed using the slicer tool. All three components were printed, debound and sintered keeping the support structure that was finally cut off from the sintered part using a diamond-wire machine saw and diamond-wheel handsaw.

Debinding and sintering

Green parts of the implant components were subsequently subjected to post-printing processes. To completely remove the polymer binder components, a two-step debinding procedure was used to reduce thermal debinding time and debinding-related defects. First, the MF³ printed green parts were kept in heptane at 50 °C for 45min for solvent debinding.

After drying the parts in an oven at 80 °C to remove residual solvent, thermal debinding was carried out in a partial vacuum of 600 mTorr with argon sweep (TM Furnaces) at a heating rate of 1 °C/min and held for 3-10 hours below 600°C. Finally, the thermally debound parts were sintered in the same vacuum furnace at temperatures from 1200-1400 °C for 1-4 h with argon as cover gas and a typical heating rate of 3 °C/min [122]. Thermal sintering, finally, provided fully dense Ti-6Al-4V implants.

5.2.5 Green and sintered parts characterization

The MF³ printed green parts were evaluated for geometric fidelity using an optical surface profiler, Keyence VR 5000 (Keyence, Cincinnati, OH, USA). The overall dimensions were verified relative to the CAD model. The sintered parts were characterized for surface topography, density, porosity, microstructure and hardness that would affect the implant performance. Relative density and porosity were investigated using the Mettler Toledo scale by Archimedes method. Also, bulk density was calculated that indicates the amount of interconnected open porosity on part surfaces which is not taken into account by Archimedes density. The following equation was used considering the soaked weight.

$$\text{Bulk density} = \frac{\text{Dry weight}}{\text{Soaked weight} - \text{Suspended weight}} \times 100 \quad (1)$$

Archimedes density and bulk density together provide an estimation of open interconnected and closed porosities. Surface topography was evaluated by optical microscopy and scanning electron microscopy (SEM). Moreover, surface roughness was measured using a Mitutoyo portable surface roughness tester. Hardness was tested using a Rockwell hardness tester. The microstructure was evaluated by etched microscopy and SEM.

5.2.6 MF³ process simulation

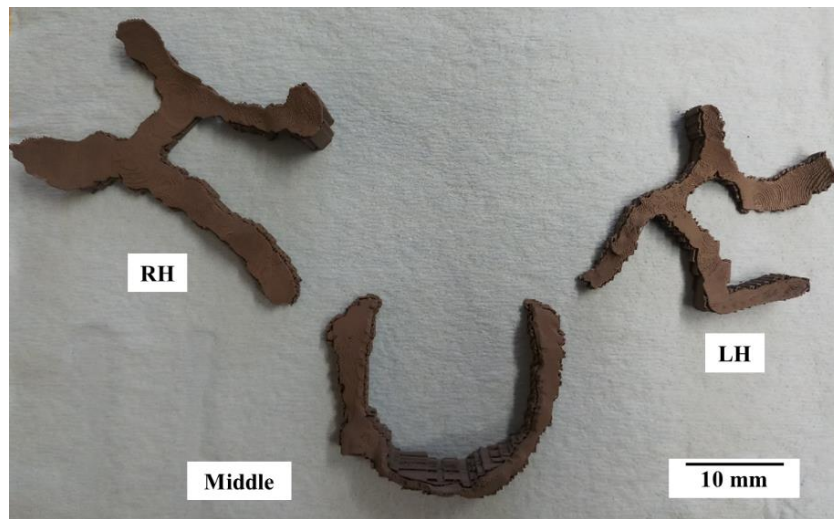
To enable the prediction of MF³ printed implant part quality in terms of dimensional variations, warpage, and residual stresses, a thermo-mechanical model was used for finite element simulations using Digimat to simulate the MF³ printing process. The 3D CAD model of the implant was imported in STL format in Digimat-AM and discretized into a voxel mesh of element size 0.1 mm. Thermo-mechanical properties of the novel material were obtained using empirical estimation models from a previously published research work by the authors [10]. Processing parameters used in the simulation were the same as those used in the printing experiments (**Table 5.1**). The build plate and ambient temperature define the boundary conditions while the melt extrusion temperature defines the thermal loading. The GCode file from Simplify3D defines the toolpath, layer thickness, and printing speed. Following the toolpath, each layer is activated for the calculation to simulate the physical printing process. Currently, the simulation is not able to consider the presence of or recognize the need for support structures during printing since the software does not include gravity effects in the modeling. The printing process and printed part quality were estimated by post-processing the simulation results. The thermo-mechanical process simulation provided a prediction of part deflection and residual stresses that develop as results of shrinkage and non-uniform cooling that stems from thermal gradient due to layer-by-layer printing. The simulated part dimensions were verified with MF³ printed green part dimensions. Moreover, the simulation results can be used in further optimization of the implant design, in future studies.

5.3 RESULTS AND DISCUSSION

5.3.1 MF³ printed green parts

Having followed through the specific digital workflow and using suitable support structures, all three components (RH, middle, LH) of the maxillofacial implant were successfully printed by MF³ of Ti-6Al-4V. **Figure 5.8a** shows the printed green parts.

(a)



(b)

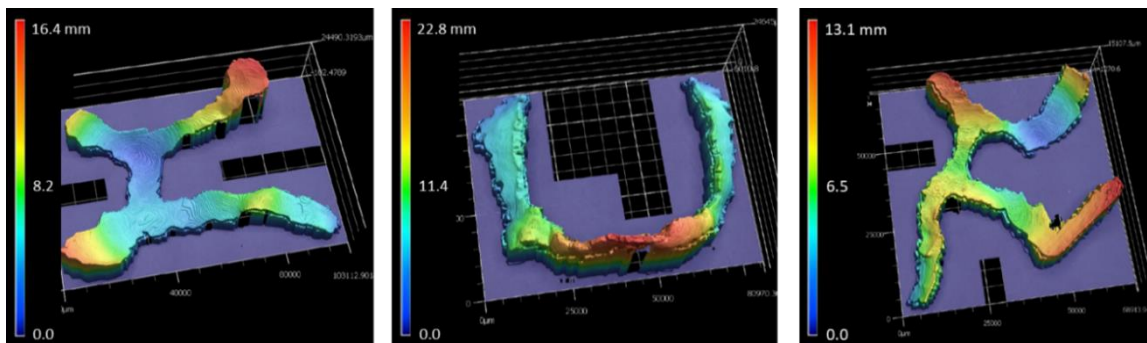


Figure 5.8. (a) MF³-printed maxillofacial implants green parts with a support structure (b) optical surface profilometry the green parts

The support structure of each part was generated by the slicing software depending on part geometry and orientation on the print bed. Post printing, this support was further kept intact to retain part geometry and minimize potential damage in the green stage. Moreover, the removal of the support structure at this stage had associated risks of part damage. Hence, support structures were not removed in the green stage. The geometric fidelity of printed parts was evaluated using an optical surface profiler, as shown in **Figure 5.8b**. It enabled the verification of maxillofacial implants with complex unique geometries that cannot be measured using conventional scales. The Z-axis positioning of millions of scanned points on the surface is plotted that can be used to verify the accuracy with original 3D CAD geometry. The surface profile generated by the tool can further be processed through a CAD tool and overlapped with the STL geometry to verify the deviations. Moreover, this data is useful in surface roughness investigations.

5.3.2 Printing process simulations

MF³ printing process simulations were conducted by modeling the layer-by-layer printing of the extrusion-based process. The sequential thermo-mechanical simulation by Digimat provided an estimation of deflections in X, Y, Z directions as well as the overall deflection, and residual stresses in the printed part [47, 83]. Thermal gradient combined with non-uniform cooling during printing led to inherent thermal strains in printed parts. The strain varied according to the thermal gradient and coefficient of thermal expansion (CTE) of material [31]. The thermal strain caused residual stresses, deflection and warpage, finally leading to deviations in printed part dimensions and shape as opposed to the original CAD geometry as shown in **Figure 5.9**.

The implant edges were found to experience a higher rate of heat loss by convection and faster cooling due to larger surface areas, leading to earlier crystallization and solidification than the central regions. The resulting non-uniform volumetric shrinkage caused greater deflection and residual stresses at these locations. Moreover, the lack of structural constraints at these free ends contributed to large deflections. Maximum deflection in the RH, middle and LH implant ends were observed to be 1.9 mm, 0.85 mm and 1.24 mm, respectively, while in the central zone the deflections were as low as zero. The difference among the parts can be attributed to geometry aspect ratio (Length/Thickness), structural stiffness and overhang length difference. The LH part with a relatively higher aspect ratio, lower structural stiffness, and larger overhang length led to higher deflections while the middle part showed the least. **Figure 5.9** also indicates the von Mises stress as residual stresses developed at the end of printing. Maximum residual stresses in the RH, middle and LH parts were observed to be 3.1 MPa, 3 MPa and 2.6 MPa, respectively. Differential heat transfer and thermal gradient along the print direction (Z-axis) as well as across print cross-section (XY-plane) led to such differences among parts and within a single part. Residual stresses distort the printed part and affect its mechanical strength. In MF³, high residual stresses may also lead to cracks or damage the part during the debinding and sintering processes. Lower thermal gradient, uniform and slower cooling would help in reducing residual stresses.

While the simulation of the MF³ printing process enabled a fair estimation of printed green part geometry and residual stresses, it is important to note that currently, the simulation tool does not consider support structure in modeling. It may affect the accuracy of simulation prediction.

(a) Deflection

(b) Residual Stresses

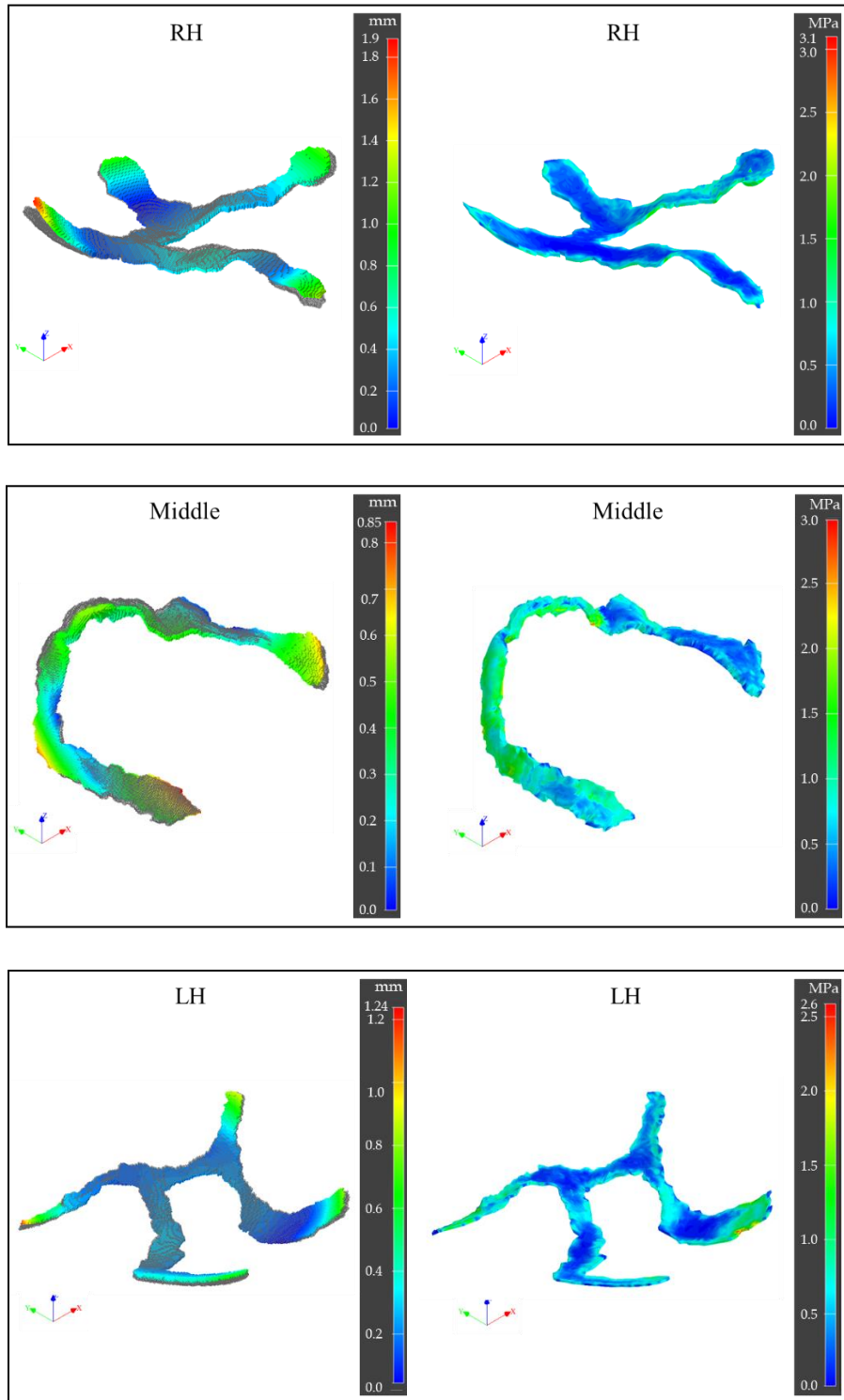


Figure 5.9. MF³ printing process simulation results: (a) part deflection overlapped on original CAD design (b) residual stresses (von Mises) estimation

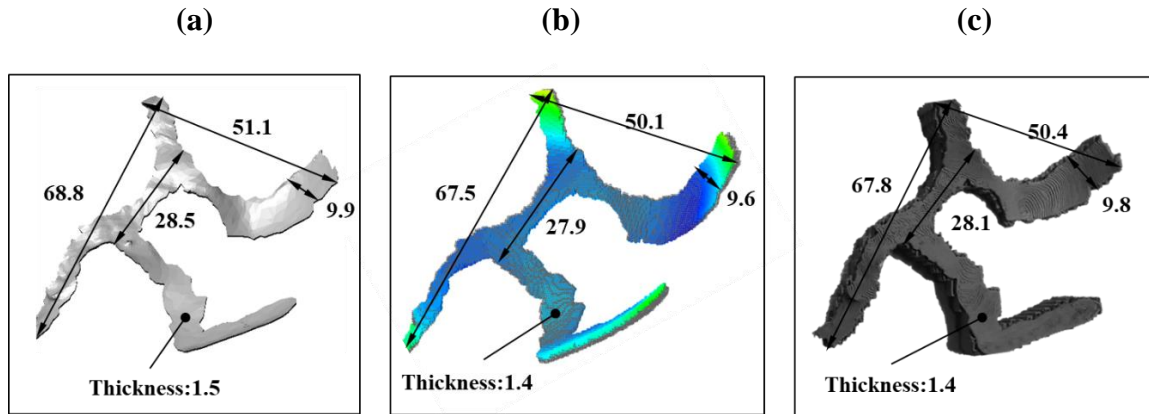


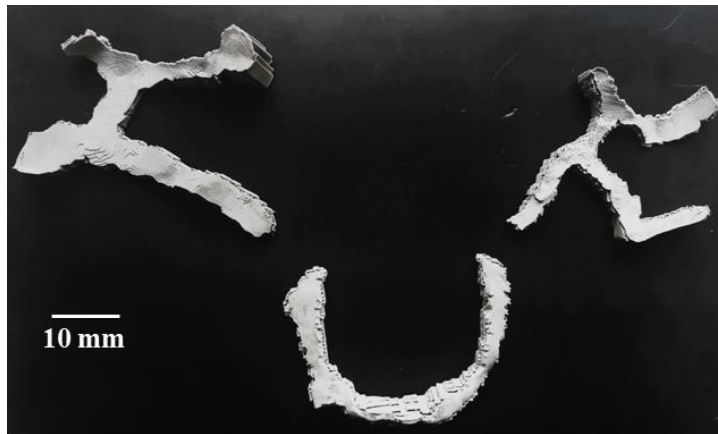
Figure 5.10. Typical dimensions of the LH part of the customized implant: (a) CAD design (b) simulation estimation (c) printed green part

For quantitative verification of simulation results, simulated part dimensions were measured and compared with experimental results. **Figure 5.10** shows the dimension results from simulation and experiments compared with original CAD dimensions of the LH part. Experimental part dimensions fairly matched with that of the simulated part. Simulated parts showed an overall shrinkage of 1.96 % from CAD dimensions, whereas in experiments it was found to be 1.37 %. With the inclusion of the support structure in simulations, the accuracy of estimation can further be improved.

5.3.3 Sintered Ti-6Al-4V parts characterization

Support structures were retained during debinding and sintering processes to avoid a potential collapse of unsupported geometry and minimize part distortion. **Figure 5.11a** shows the sintered Ti-6Al-4V implant components with the support structure.

(a)



(b)



(c)

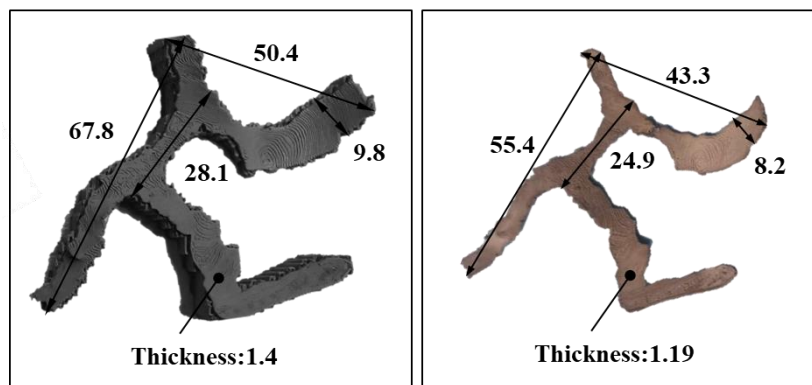


Figure 5.11. (a) sintered metal parts with a support structure (b) sintered metal parts after support structure removal (c) green part vs. sintered part dimensions showed 16% shrinkage in sintering

While the support structure helped in retaining the shape and minimizing distortion in the thin-walled implant parts, on the other hand, it was extremely challenging to cut the support off implant geometry in a fully sintered metal phase. Firstly, cutting the supports off the sintered parts was not easy for conventional metal cutting methods, particularly, due to the irregular geometry and wavy surfaces of the implants. Secondly, the thin-walled geometry was part of the problem because the parts could easily be damaged while chipping the supports off. Also, the vertical walls of the support structure were thicker than the part itself, contributing to the possibility of part breakage. These issues can be addressed by investigating the feasibility of maximum angle and length of unsupported overhang that can be printed. Also, the design and optimization of the support structure are needed to achieve adequate support using a minimal support structure. However, these aspects were beyond the scope of the current investigation. Diamond wire machine saw and diamond wheel hand saw were used to gradually cut the supports off. **Figure 5.11b** shows the sintered implant components without a support structure.

Surface morphology

A considerable stair-steps effect was observed in the sintered implants. As a 3D model is discretized into horizontal layers in MF³ printing, the presence of a sharp change in the curvature of the implant surface causes such an effect. Hence, the maxillofacial implant surfaces matching human anatomy developed significant stair-step effects, as shown in **Figure 5.13a**.

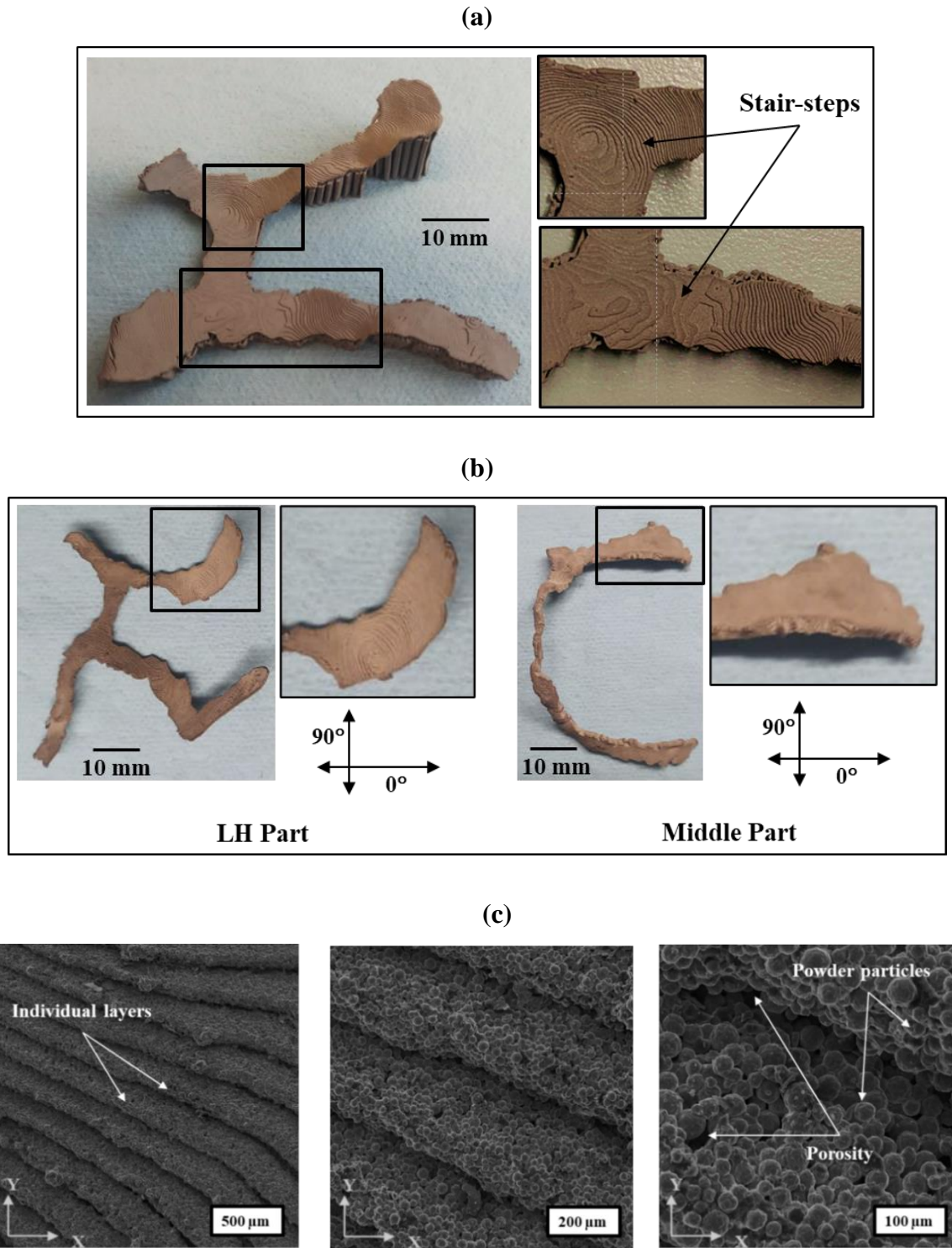


Figure 5.12. (a) Stair-step effects from layer-by-layer printing due to Z-gradient of the implant surface (b) Surface roughness measured in the LH & middle unpolished sintered parts in 0° and 90° (c) SEM (unetched unpolished condition)

The offset between adjacent layers having varying cross-sections along the print axis led to such deviations from the desired geometry. It further contributed to the surface roughness of the implants. Hence, a finer layer thickness was chosen to minimize this effect and get higher exactness to the CAD geometry. Moreover, the layer-by-layer and bead-by-bead printing by the extrusion-based process of MF³ printing leads to surface roughness that follows the toolpath as shown in high magnification of SEM micrographs in **Figure 5.13c**. It could be attributed to the lack of diffusion between layers and beads. Also, the overall surface roughness caused by the combined effects of stair-step and lack of layer-to-layer and bead-to-bead diffusion depends on part orientation and surface angle with the horizontal plane. The surface roughness was measured in 0° and 90° on as-sintered parts as shown in **Figure 5.13b**.

Table 5.2. Surface roughness of as-sintered parts

Part	Measurement angle (°)	Ra (µm)
LH	0	23.3 ± 1.0
	90	12.9 ± 1.2
Middle	0	13.5 ± 1.0
	90	12.7 ± 0.7

The difference in part geometry and orientation on the print bed led to different surface angles and toolpath, hence the variation in surface roughness, accordingly, as shown in **Table 5.2**. The LH part showed higher roughness (Ra 23.3 µm) in 0° than that of middle part (Ra 13.5µm), while in 90 ° both parts showed the same results (Ra ~12.7 µm). Higher

surface roughness was observed with a higher surface angle with build plate (horizontal plane). Hence, part orientation in the build plate becomes an important aspect apart from other slicing and printing parameters such as layer thickness, bead width, and extrusion temperature that affect surface roughness.

The SEM images in **Figure 5.13c** further show the implant surface roughness on different scales. The stair-step effect at layer thickness level shows a typical pattern that stems from part geometry, part orientation and slicing strategy (toolpath, layer thickness, bead width). The stair-step contributes to macro-level surface roughness. Secondly, at the individual layer level, powder particles and porosity can be seen that contribute to micro-level surface roughness. These topological features are expected to favor the maxillofacial implant as they would enhance the implant's ability to integrate into the surrounding tissue and augment the biological response to the implant [123]. Further investigation and optimization of surface roughness would be worth looking into this aspect.

Relative density and porosity

The printed samples were characterized for density using the Archimedes method. Sintered metal parts were evaluated for relative density and porosity considering Ti-6Al-4V has a theoretical density of 4.23 g/cc. The relative density (bulk density-based) of the middle part was found to be 81 % indicating the total porosity (containing both open interconnected porosity and closed porosity) of 19 %. Archimedes-based relative density was 94 % indicating 6 % closed porosity, hence, 13 % open interconnected porosity. These results indicate a considerable amount of interconnected open porosity.

Table 5.3. Relative density and porosity

	Archimedes density (g/cc)	Relative density (%) (AD-based)	Bulk density (g/cc)	Relative density (%) (BD-based)
Middle part	4.18	94.3	3.60	81.2

The optical micrographs revealed considerable porosities with sizes of 50 μ m as shown in **Figure 5.14a**. The open interconnected porosity has engaging characteristics that accelerate the healing of the bone and enhanced osteointegration of metallic implants [88, 104]. Such porosity provides anchor sites to the bone tissue and promotes accelerated osseointegration. By optimizing the open interconnected pore system, osseointegration can be biologically enhanced in implants. Moreover, microporosity better mimics the natural bone in terms of elastic modulus (cancellous: 1.5-11.2 GPa and cortical: 7-20 GPa) as opposed to fully dense Ti-6Al-4V (105 \pm 2 GPa) [125, 126]. This, in turn, leads to a more uniform stress distribution between the implant and adjoining bones.

Metallography

The SEM images revealed an average grain size of 14.8 \pm 1.6 μ m, as shown in **Figure 5.13**. In comparison to microstructure seen in typical L-PBF, the as-printed samples revealed martensite titanium and reduced intensities of beta titanium. One of the primary reasons for such observation could be the higher cooling rates of the L-PBF process with extremely small cycle times involved in powder spreading – melting – solidification of the Ti-6Al-4V powder which does not allow for the acicular martensite titanium, characteristic of higher cooling rates involved in L-PBF, to decompose into alpha titanium and prior beta

titanium grains. In comparison, the MF3 fabricated samples are sintered at around 1200-1400°C which allows for sufficient time for the formation of equiaxed alpha titanium and grain boundary beta titanium. Such a difference in microstructure between L-PBF and MF³ fabricated Ti-6Al-4V could affect the mechanical properties of the printed parts [122], with the MF³ fabricated parts possessing a higher elongation than the L-PBF parts, possibly due to the equiaxed microstructure. The higher ductility offered by MF³ fabricated Ti-6Al-4V implants directly aids in osteointegration of the implants [124].

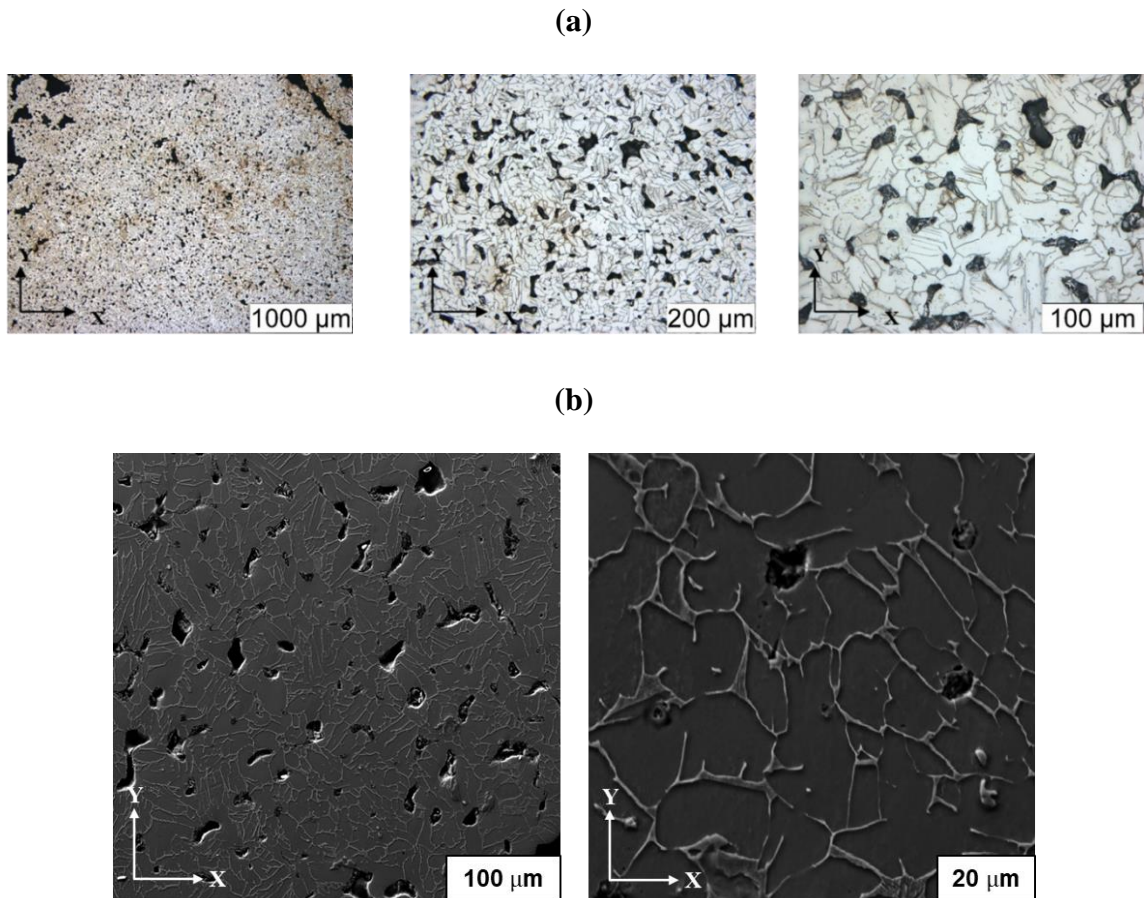


Figure 5.13. (a) Optical microscopy (etched polished condition) (b) SEM (etched polished condition)

Using a Rockwell hardness tester, the hardness of the printed implant samples was measured, and 6.52 ± 0.8 HRC was observed. For EBM and SLM printed parts it was found to be 37-57 HRC [127]. The lower hardness value of MF³ printed implants could be attributed to the porosity that can be further investigated and optimized. However, the lower hardness value of MF³ printed implants as opposed to EBM and SLM printed parts would mimic the bone characteristics more effectively and favor the implant performance as it could better match the bone hardness which is 40-44 HV [128].

5.4 CONCLUSIONS

MF³ printing of custom implants was studied for the first time using experimental and analytical investigations. Fabrication of patient's biomodel and custom maxillofacial implants using additive manufacturing technologies is demonstrated. The sintered metal implants were characterized for density, porosity, surface roughness, hardness and microstructure that play important role in the performance of an implant.

The following conclusions emerge from the study:

1. Fabrication of patient-specific custom maxillofacial implants out of Ti-6Al-4V by MF³ is found feasible and demonstrated through the experimental study.
2. A specific digital workflow is required to convert the patient's CBCT data into a 3D printable format that made additive manufacturing of the anatomical model and the maxillofacial implants possible.

3. MF³ printing with support structures was reported for the first time. Optimal support structures were required in MF³ for custom implant geometries to ensure geometric fidelity not only during printing but also debinding and sintering processes.
4. MF³ process simulation estimated maximum deflections of 0.9-1.9 mm and maximum residual stresses of 2.6-3.1 MPa in printed green parts. However, the accuracy of prediction would be affected by the absence of support structures in simulations as opposed to experimental printing.
5. The relative density (bulk density-based) of the middle part was found to be 81% indicating the total porosity of 19%, which includes 6% closed porosity and 13% open interconnected porosity that would provide anchor sites to the bone tissue and promotes accelerated osseointegration
6. Stair-step effects and lack of diffusion between layers contributed to surface roughness at the macro scale, whereas powder particles and porosity within a layer affected at the micro-scale. The LH part showed higher roughness (Ra-23.3 μm) in 0° than that of middle part (Ra-13.5 μm), while in 90° both parts showed the same results (Ra-~12.7 μm). The difference in part geometry and orientation on the print bed led to different surface angles and toolpath, hence the variation in surface roughness, accordingly. Higher surface roughness was observed with a higher surface angle with the build plate.
7. The hardness of 6.52 ± 0.8 HRC was observed in the Ti-6Al-4V implants printed by MF³ as opposed to 37-57 HRC in EBM and SLM. It mimics the bore more effectively and favors implant performance.

The outcome of the work proves that MF³ is a potential process to manufacture patient-specific custom implants out of Ti-6Al-4V. It also represents a part of the treatment procedure for complex surgery in elderly patients with a severely atrophic posterior maxilla eliminating the need for regenerative bone therapies. Moreover, the study demonstrates how additive manufacturing technologies could help the surgeon to improve pre-operative planning in implant surgery. The findings from this study will further allow the development of a beta version of the implants that would enable the dental research team to test and validate through surgical procedures on patient-specific biomodels. It would include refined geometries having smooth curves and surfaces developed matching the patient's anatomy. Also, multiple mounting posts for dental implants and holes for mounting the implants on the maxilla structure are to be provided. In future work, the second-generation design is to be fabricated by MF³ and the beta prototype tested for the clinical procedure. In addition, corrosion of the material can severely limit its fatigue life and mechanical strength. Even though titanium alloys are exceptionally corrosion-resistant because of the stability of the TiO₂ oxide layer, they are not inert to corrosive attack. Hence, maxillofacial implants need to be tested for corrosion in solutions that mimic biofluids like blood.

CHAPTER 6

CONCLUSIONS

The dissertation presents a novel attempt to address the design for metal fused filament fabrication (DfMF³) by investigating the material-geometry-process interrelationships observed in fabricating complex geometries with Ti-6Al-4V alloy. It also introduces and implements predictive simulation of MF³ to enable DfMF³. The following conclusions emerged from the presented work:

- The work confirmed the applicability of a thermo-mechanical model for finite element simulation of the MF³ printing process. It has been successfully demonstrated that simulation could predict the warpage, deformation and dimensional variations, and the results were corroborated by the experimental printing of Ti-6Al-4V parts. The simulation results showed a maximum 1% change in dimensions in XY-plane and a 1.5% change in Z-dimensions. Whereas the experimental results showed 0.6% and 0.9%, respectively. The experimental part dimensions fairly matched with that of the simulated part. In addition, the simulation provided an estimation of temperature distribution, porosity and residual stresses. Experimental verification of these estimations is in progress. Moreover, the application of warpage compensation calculated from the initial simulation led to an improvement in dimensional control in the subsequent iteration for both simulations and experiments.

- The ability of the process simulation to estimate the quantitative influence of material properties on printed part quality was verified by simulating two different materials, a Ti-6Al-4V filled polymer and an unfilled ABS copolymer, and the results were verified by experiments. Due to lower CTE, Ti-6Al-4V filled polymer showed lower shrinkage and warpage than unfilled ABS polymer, both in simulations and experiments. Similarly, Ti-6Al-4V feedstock showed a lower thermal gradient than ABS due to higher thermal conductivity brought in by Ti-6Al-4V alloy. A larger temperature gradient in ABS further contributed to higher thermal strains and part distortion. Significantly higher residual stress observed in ABS was attributed to its higher stiffness. These findings also verified the sensitivity of the simulation model to material properties.
- The sensitivity analyses facilitated the identification of dominant input parameters in MF³ printing of Ti-6Al-4V feedstock. The procedure identified the relative importance of specific attributes of geometry, processing conditions, slicing strategies, powder-binder material properties on MF³ printing based on correlations between input and output parameters. Moreover, the sensitivity response was found to vary with part designs.
- It was determined that process conditions and part geometry influenced print which was completely insensitive to material parameters. Deflections and Z-warpage showed very high sensitivities to extrusion temperature and CTE. Residual stresses showed very high sensitivities to extrusion temperature, CTE and Young's modulus having direct proportionality. Substrate temperature did not show a very high sensitivity to any

input parameters, though part Z-height, wall thickness and bead width were among the highest influencers.

- Supportless printing of lattice structures using the MF³ process was investigated for the first time using experimental and analytical approaches. Feasible printing conditions and lattice geometry parameters were identified for Ti-6Al-4V to fabricate defect-free lattices. As opposed to printing bulk parts, unsupported overhang feature and narrow/tiny cross-sectional print area in lattice structures required considerable changes in MF³ printing parameters, e.g., filament retraction, concentric toolpath, extrusion multiplier < 1, low printing speed, small layer thickness and small bead width. Both XY and Z dimensional variations in green parts were found to be increasing with an increase in lattice element length or decrease in element thickness for both types of cross-sections. This effect can be attributed to the higher aspect ratio (L/d), leading to a higher longitudinal shrinkage. The simulations also estimated an overall lower porosity in square c/s than in circular c/s. This can be correlated to higher relative density in square c/s than in circular c/s observed in experimental results. Tool path having straight lines and a more uniform print area along Z-axis led to lower porosity in square c/s than in circular c/s.
- The experimental printing of lattice showed large deflections in unsupported regions due to gravity, whereas simulation was unable to predict such deflections. Hence, an analytical model was presented to estimate extrudate deflections and verified with experimental results. The extrudate deflection in unsupported regions was found increasing with overhang length, which is a function of lattice element thickness and length. Square c/s lattice showed larger extrudate deflection than circular c/s. In the

sintered parts, lack of diffusion between beads was observed in the bottom facing surface of unsupported geometry as an effect of extrudate sagging in the green parts.

- The design and fabrication of Ti-6Al-4V maxillofacial implants using the MF³ process were demonstrated successfully confirming the feasibility of the technology to manufacture patient-specific implants. A specific digital workflow was required to convert the patient's CBCT data into a 3D printable format that made additive manufacturing of the anatomical model and the maxillofacial implants possible. MF³ printing with support structures was reported for the first time. Optimal support structures were required in MF³ for custom implant geometries to ensure geometric fidelity not only during printing but also debinding and sintering processes. However, the current simulation model does not consider support structure in the modeling, which may affect the prediction accuracy. However, the experimental green part dimensions fairly matched with that of the simulated part. Simulated parts showed an overall shrinkage of 1.96% relative to the CAD dimensions, whereas in experiments it was found to be 1.37%.
- Characterization of the sintered Ti6Al-4V implant indicated 81% relative density and 19% porosity including 6% closed porosity and 13% open interconnected porosity that would provide anchor sites to the bone tissue and promote accelerated osseointegration. Stair-step effects and lack of diffusion between layers contributed to surface roughness at the macro scale, whereas powder particles and porosity within a layer contributed at the micro-scale. The difference in part geometry and orientation on the print bed led to different surface angles and toolpath causing variation in surface roughness

accordingly. Higher surface roughness was observed with a higher surface angle with the build plate.

- Having established a simulation solution for the MF³ process, design for MF³ was looked into from multiple perspectives including validation of material behavior defined by estimation models, evaluation of the effects of material composition, part geometry and process parameters on printing outcome, identification of feasible printing and geometry window, and demonstration fabricating complex geometries using support structures or by supportless printing. The enhanced understanding of material-geometry-process interrelationships enabled design for MF³, and it would push MF³ technology several steps closer to be adopted as an effective industrial manufacturing process.

CHAPTER 7

FUTURE WORK

The work in the dissertation contributed towards the design for MF³ (DfMF³). This work addressed some key challenges towards understanding the material-geometry-process interrelationships, and how the properties of MF³ printed Ti-6Al-4V parts were affected. The applicability of an FEA-based thermo-mechanical process simulation model for MF³ printing was investigated. The evaluation identified the simulation as a valuable DfMF³ tool. The study also identified the gap between the simulation and physical process and opens up the scope for further scientific developments to enhance its prediction accuracy. It also expands the simulation capability to the sintering process. The recommendation for future research which can be built off from the current work includes:

- MF³ printing of complex geometry with overhang features using support structures has been investigated in this work. However, the current simulation model does not consider support structure in modeling, decreasing the prediction accuracy. The capability of identifying the need for support and, subsequently, including support geometry in the simulation model to predict its influence on part distortion, warpage and residual stresses would be valuable. It can be an enabler in designing optimal support structures and extending MF³ printing to parts that require support.

- The capability to estimate porosity distribution in the MF³ printed green part using predictive simulation has also been explored in the current work. It also provides an estimation of relative density distribution within the part. Though not fully capable, simulation tools have got initial developments on this feature. Simulation results would need to be experimentally verified, and the influence of porosity on part performance can be further investigated.
- The sensitivity analyses facilitated the identification of dominant input parameters in MF³ printing. Identification of such significant input parameters enables streamlining further development exercise. Building on such identification, more focused experimental studies or design of experiments, involving the significant input parameters only, can be investigated. Such studies are now feasible and more meaningful, which was not the case while dealing with all thirteen input parameters.
- The current work investigated the simulation of the MF³ printing process only, providing an extended understanding of and capability to design for the MF³ printing. This capability can be extended to the thermal debinding and sintering process enabling estimation of part deformations, dimensions, residual stresses, and relative density of sintered metal parts. An integrated solution of printing and sintering simulation would be an ultimate tool for DfMF³.
- Simulating the in-space conditions: As this NASA-funded project marks the extension of manufacturing by MF³ to in-space microgravity conditions, the effect material, process and geometry studied on earth can be extended to microgravity

environments. It would require the incorporation of gravity and its effects on the multi-physics in the process simulation model. Moreover, experimentation in microgravity would be required to validate the prediction model. This aspect provides a basis for a novel work of Design for Manufacturing in-Space (DfMiS).

- In the current work, MF³ printing simulation and experimental verification were investigated for Ti-6Al-4V with 59 vol.% filaments only. The findings from the work and established simulation solution can be leveraged to investigate different material compositions in terms of solids loading, binder composition and filler powder of a wider range, thereby extending the adaptability of MF³ through DfMF³.

REFERENCES

1. J.G. Gutierrez, S. Cano, S. Schuschnigg, C. Kukla, J. Sapkota, C. Holzer, Additive manufacturing of metallic and ceramic components by the material extrusion of highly filled polymers: a review and future perspectives, *Materials*, 2018, 11(5): p.840
2. H.A. Hegab, Design for additive manufacturing of composite materials and potential alloys: a review, *Manufacturing Review*, 2016, 3: 11
3. Y. Kok, X.P. Tan, P. Wang, M.L.S. Nai, N.H. Loh, E. Liu, S.B. Tor, Anisotropy and heterogeneity of microstructure and mechanical properties in metal additive manufacturing: A critical review, *Materials and Design*, 2018, 139: p.565-586
4. J.J. Lewandowski, M. Seifi, Metal Additive Manufacturing: A Review of Mechanical Properties, *Annual Review of Materials Research*, 2016, 46: p.151-186
5. S. Mirzababaei, S. Pasebani, A Review on Binder Jet Additive Manufacturing of 316L Stainless Steel, *Journal of Manufacturing and Materials Processing*, 2019, 3(3): 82
6. W. Lengauer, I. Duretek, M. Fürst, V. Schwarz, J.G. Gutierrez, Fabrication and properties of extrusion-based 3D-printed hardmetal and cermet components, *International Journal of Refractory Metals and Hard Materials*, 2019, 82: p.141-149
7. Y. Thompson, J.G. Gutierrez, C. Kukla, P. Felfer, Fused filament fabrication, debinding and sintering as a low-cost additive manufacturing method of 316L stainless steel, *Additive Manufacturing*, 2019, 30: 100861

8. G. Wu, N.A. Langrana, R. Sadanji, S. Danforth, Solid freeform fabrication of metal components using fused deposition of metals, *Materials & Design*, 2002, 23(1): p.97-105
9. Z.Z. Fang, J.D. Paramore, P. Sun, K.S.R. Chandran, Y. Zhang, Y. Xia, F. Cao, M. Koopman, M. Free, Powder metallurgy of titanium – past, present, and future, *International Materials Reviews*, 2018, 63(7): p.407-459
10. P. Singh, Q. Shaikh, V.K. Balla, S.V. Atre, K.H. Kate, Estimating powder-polymer material properties used in design for metal fused filament fabrication (DfMF³), *Journal of the Minerals, Metals & Materials Society*, 2020, 72: p.485–495
11. P. Singh, V.K. Balla, A. Tofangchi, S.V. Atre, K.H. Kate, Printability studies of Ti-6Al-4 V by metal fused filament fabrication (MF³), *International Journal of Refractory Metals and Hard Materials*, 2020, 91: p.105249
12. K. Sudan, P. Singh, A. Gökçe, V.K. Balla, K.H. Kate, Processing of hydroxyapatite and its composites using ceramic fused filament fabrication (CF³), *Ceramics International*, 2020, 46: p.23922–23931
13. A. Cattenone, S. Morganti, G. Alaimo, F. Auricchio, Finite element analysis of additive manufacturing based on fused deposition modeling (FDM): distortions prediction and comparison with experimental data, *Journal of Manufacturing Science and Engineering*, 2019, 141 (011010): p.1-17
14. A. Armillotta, M. Bellotti, M. Cavallaro, Warpage of FDM parts: experimental tests and analytic model, *Robotics and Computer-Integrated Manufacturing*, 2018, 50: p.140–152

15. N. Watanabe, M.L. Shofner, N. Treat, D.W. Rosen, A model for residual stress and part warpage prediction in material extrusion with application to polypropylene, *Int Solid Freeform Fabrication Symposium*, 2016, Austin, 27th Edition: p.2437-2455
16. C. Li, J.F. Liu, X.Y. Fang, Y.B. Guo, Efficient predictive model of part distortion and residual stress in selective laser melting, *Additive Manufacturing*, 2017, 17: p.157-168
17. J. Song, W. Wu, L. Zhang, H. Beibei, L. Lin, N. Xiaoqing, L. Qianlei, Z.L. Guoliang, Role of scanning strategy on residual stress distribution in Ti-6Al-4V alloy prepared by selective laser melting, *Optik - International Journal of Light and Electron Optics*, 2018, 170: p.342-352
18. Y. Zhou, G. Xiong, T. Nyberg, D. Liu, Temperature analysis in the fused deposition modeling process, *International Conference on Information Science and Control Engineering*, 3rd ed., July 8-10, 2016, Beijing, China, 978-1-5090-2534-3 /16
19. D. Croccolo, M. DeAgostinis, G. Olmi, Experimental characterization and analytical modelling of the mechanical behaviour of fused deposition processed parts made of ABS-M30, *Computational Material Science*, 2013, 79: p.506-518
20. D.D. Phan, J.S. Horner, Z.R. Swain, Z.R. Swain, A.N. Berisa, M.E. Mackay, Computational Fluid Dynamics Simulation of the Melting Process in the Fused Filament Fabrication Additive Manufacturing Technique, *Additive Manufacturing*, 2020, 33: 101161
21. J. Zhang, X.Z. Wang, W.W. Yu, H.D. Yu, Numerical investigation of the influence of process conditions on the temperature variation in fused deposition modeling, *Materials Design*, 2017, 130: p.59-68

22. B. Brenken, E. Barocio, A. Favaloro, V. Kunc, R.B. Pipes, Development and validation of extrusion deposition additive manufacturing process simulations, *Additive Manufacturing*, 2019, 25: p.218-226
23. J. Abel, U. Scheithauer, T. Janics, S. Hampel, S. Cano, A. Müller-Köhn¹, A. Günther, C. Kukla, T. Moritz¹, Fused Filament Fabrication (FFF) of metal-ceramic components, *Journal of Visualized Experiments*, 2019, 143: 57693
24. M. Nikzad, S.H. Masood, I. Sbarski, Thermo-mechanical properties of a highly filled polymeric composites for fused deposition modeling, *Materials and Design*, 2011, 32(6): p.3448-3456
25. e-Xstream, Digimat-AM simulation solution for Additive Manufacturing, <https://www.e-xstream.com/product/digimat-am>, Accessed 10 September 2020
26. Y. Zhang, Y.K. Chou, 3D FEA simulations of fused deposition modeling process, *ASME International Conference on Manufacturing Science and Engineering*, 1st ed., October 8-11, 2006, 2006, Ypsilanti, MI, USA, MSEC2006-21132
27. M. Domingo-Espin, J.M. Puigoriol-Forcada, A.A. Garcia-Granada, L. Jordi, B. Salvador, R. Guillermo, Mechanical property characterization and simulation of fused deposition modeling Polycarbonate parts, *Materials and Design*, 2015, 83: p.670-677
28. A.E. Moumen, M. Tarfaoui, K. Lafdi, Modelling of the temperature and residual stress fields during 3D printing of polymer composites, *International Journal of Advanced Manufacturing Technology*, 2019, 104: p.1661-1676
29. S.F. Costa, F.M. Duarte, J.A. Covas, Thermal conditions affecting heat transfer in FDM/FFE: a contribution towards the numerical modelling of the process, *Virtual and Physical Prototyping*, 2015, 10 (1): p.35-46

30. R. Q. De Macedo, R.T. Luiz Ferreira, J. Kuzhichalil, Determination of mechanical properties of FFF 3D printed material by assessing void volume fraction, cooling rate and residual thermal stresses, *Rapid Prototyping Journal*, 2019, 25(10): p.1661-1683
31. Q. Sun, G.M. Rizvi, C.T. Bellehumeur, P. Gu, Effect of processing conditions on the bonding quality of FDM polymer filaments, *Rapid Prototyping Journal*, 2008, 14(2): p.72–80
32. C. Bellehumeur, L. Li, Q. Sun, P. Gu, Modeling of Bond Formation Between Polymer Filaments in the Fused Deposition Modeling Process, *SME Journal of Manufacturing Processes*, 2004, 6(2): p.170-178
33. L. Ren, X. Zhou, Z. Song, C. Zhao, Q. Liu, J. Xue, X. Li, Process parameter optimization of extrusion-based 3D metal printing utilizing PW–LDPE–SA binder system, *Materials*, 2017. 10(3): p. 305
34. S. Ahn, S.J. Park, S. Lee, S.V. Atre, R.M. German, Effect of powders and binders on material properties and molding parameters in iron and stainless-steel powder injection molding process, *Powder Technology*, 2009, 193: p.162–169
35. P. Parandoush, D. Lin, A review on additive manufacturing of polymer-fiber composites, *Composite Structures*, 2017, 182: p.36–53
36. R.Q. de Macedo, R.T. Ferreira, Residual thermal stress in fused deposition modelling, *ABCM International Congress of Mechanical Engineering*, 24th edition, December 3-8, 2017, Curitiba, Brazil, COBEM-2017-0124
37. H. Xia, J. Lu, S. Dabiri, G. Tryggvason, fully resolved numerical simulations of fused deposition modeling. Part I: fluid flow, *Rapid Prototyping Journal*, 2018, 24(2): p.463–476

38. B. Barmore, Fused Filament Fabrication of Filled Polymers for Metal Additive Manufacturing, Master's Thesis, Mechanical Engineering, Oregon State University, 2016
39. T.W. Kerekes, H. Lim, W.Y. Joe, G.J. Yun, Characterization of process–deformation/damage property relationship of fused deposition modeling (FDM) 3D-printed specimens, *Additive Manufacturing*, 2019, 25: p.532–544
40. F. Górski, W. Kuczko, R. Wichniarek, Influence of process parameters on dimensional accuracy of parts manufactured using fused deposition modelling technology, *Advances in Science and Technology*, 2013, 7(19): p.27–35
41. J. Giannatsis, K. Sofos, V. Canellidis, D. Karalekas, V. Dedoussis, Investigating the influence of build parameters on the mechanical properties of FDM parts, *Innovative Developments in Virtual and Physical Prototyping*, 2012, Taylor & Francis Group, London, ISBN 978-0-415-68418-7
42. G. Jothibabua, S. K. Gurunathanb, Surrogate Based Sensitivity Analysis of Part Strength due to Process Parameters in Fused Deposition Modelling, *Procedia Computer Science*, 2018 (133): p.772–778
43. B.H. Lee, J. Abdullah, Z.A. Khan, Optimization of rapid prototyping parameters for production of flexible ABS object, *Journal of Materials Processing Technology*, 2005, 169: p.54–61
44. E.R. Fitzharris, N. Watanabe, D.W. Rosen, M.L. Shofner, Effects of material properties on warpage in fused deposition modeling parts, *The International Journal of Advanced Manufacturing Technology*, 2018, 95: p.2059–2070

45. B. Vasudevarao, D.P. Natarajan, M. Henderson, A. Razdan, Sensitivity of RP surface finish to process parameter variation, 2000, <https://www.researchgate.net/publication/2467464>
46. S.V. Atre, S.J. Park, R. Zauner, R.M. German, Process simulation of powder injection moulding: Identification of significant parameters during mould filling phase, *Powder Metallurgy*, 2007, 50(1): p.76-85
47. M.Q. Shaikh, P. Singh, K.H. Kate, M. Freese, S.V. Atre, Finite Element-Based Simulation of Metal Fused Filament Fabrication Process: Distortion Prediction and Experimental Verification, *Journal of Materials Engineering and Performance*, 2021, <https://doi.org/10.1007/s11665-021-05733-0>
48. A. Kumar, S. Verma, J.Y. Jeng, Supportless Lattice Structures for Energy Absorption Fabricated by Fused Deposition Modeling, *3D Printing And Additive Manufacturing*, 2020, 7(2): p.85-96
49. G. Dong, G. Wijaya, Y. Tang, Y.F. Zhao, Optimizing process parameters of fused deposition modeling by Taguchi method for the fabrication of lattice structures, *Additive Manufacturing*, 2018, 19: p.62–72
50. S. Park, D.W. Rosen, Quantifying effects of material extrusion additive manufacturing process on mechanical properties of lattice structures using as-fabricated voxel modeling, *Additive Manufacturing*, 2016, 12: p.265–273
51. M.F. Ashby, *The Mechanical Properties of Cellular Solids*, *Metallurgical Transactions A*, 1983, 14: p.1755-1769
52. V.S. Deshpande, Effective properties of the octet-truss lattice material, *Journal of the Mechanics and Physics of Solids*, 2001, 49: p.1747 – 1769

53. J. Lehman, R. Lakes, Stiff lattices with zero thermal expansion and enhanced stiffness via rib cross section optimization, *International Journal of Mechanics and Materials in Design*, 2013, 9: p.213–225
54. L. Yang, D. Cormier, H. West, O. Harrysson, K. Knowlson, Non-stochastic Ti–6Al–4V foam structures with negative Poisson’s ratio, *Materials Science & Engineering A*, 2012, 558: p.579–585
55. Z. QianCheng, H. YunJie, C. ChangQing, L. TianJian, Ultralight X-type lattice sandwich structure (I): Concept, fabrication and experimental characterization, *Science in China Series E: Technological Sciences*, 2009, 52(8): p.2147-2154
56. J. Lehman, R. Lakes, (2014), Stiff, strong, zero thermal expansion lattices via material hierarchy, *Composite Structures*, 2014, 107: p.654–663
57. D.W. Rosen, Computer-Aided Design for Additive Manufacturing of Cellular Structures, *Computer-Aided Design & Applications*, 2007, 4(5): p.585-594
58. Y. Tang, A. Kurtz, Y.F. Zhao, Bidirectional Evolutionary Structural Optimization (BESO) based design method for lattice structure to be fabricated by additive manufacturing, *Computer-Aided Design*, 2015, 69: p.91–101
59. H. Brooks, K. Brigden, Design of conformal cooling layers with self-supporting lattices for additively manufactured tooling, *Additive Manufacturing*, 2016, 11: p.16–22
60. Z. Ozdemir, E. Hernandez-Nava, A. Tyas, J.A. Warren, S.D. Fay, R. Goodall, I. Todd, H. Askes, Energy absorption in lattice structures in dynamics: Experiments, *International Journal of Impact Engineering*, 2016, 89: p.49–61

61. O.E. Sotomayor, H.V. Tippur, Role of cell regularity and relative density on elastoplastic compression response of 3-D open-cell foam core sandwich structure generated using Voronoi diagrams, *Acta Materialia*, 2014, 78: p.301–313
62. S.H. Masood, J.P. Singh, Y. Morsi, The design and manufacturing of porous scaffolds for tissue engineering using rapid prototyping, *International Journal of Advanced Manufacturing Technology*, 2005 27: p.415–420
63. C.K. Chua, K.F. Leong, C.M. Cheah, S.W. Chua, Development of a Tissue Engineering Scaffold Structure Library for Rapid Prototyping. Part 1: Investigation and Classification, *International Journal of Advanced Manufacturing Technology*, 2003, 21: p.91–301
64. S.A. Khanoki, D. Pasini, (2013), Fatigue design of a mechanically biocompatible lattice for a proof-of-concept femoral stem, *Journal of the Mechanical Behavior of Biomedical Materials*, 2013, 22: p.65–83
65. K. Wei, Q. Yang, B. Ling, H. Xie, Z. Qu, D. Fang, Mechanical responses of titanium 3D kagome lattice structure manufactured by selective laser melting, *Extreme Mechanics Letters*, 2018, 23: p.41–48
66. H.N. Wadley, Multifunctional periodic cellular metals, *Philosophical Transactions of the Royal Society A*, 2006, 364: p.31–68
67. H.N. Wadley, N.A. Fleck, A.G. Evans, Fabrication and structural performance of periodic cellular metal sandwich structures, *Composites Science and Technology*, 2003, 63: p.2331–2343
68. S.N. Khaderi, V.S. Deshpande, N.A. Fleck, (2014), The stiffness and strength of the gyroid lattice, *International Journal of Solids and Structures*, 2014, 51: p.3866–3877

69. F.N. Habib, P. Iovenitti, S.H. Masood, M. Nikzad, (2018), Fabrication of polymeric lattice structures for optimum energy absorption using Multi Jet Fusion technology, *Materials and Design*, 2018, 155: p.86-98
70. A. Cerardi, M. Caneri, R. Meneghello, G. Concheri, M. Ricotta, Mechanical characterization of polyamide cellular structures fabricated using selective laser sintering technologies, *Materials and Design*, 2013, 46: p.910–915
71. I. Gurrappa, Characterization of titanium alloy Ti-6Al-4V for chemical, marine and industrial applications, *Materials Characterization*, 2003, 51: p.131– 139
72. E. Brandl, B. Baufeld, C. Leyens, R. Gault, Additive Manufactured Ti-6Al-4V using welding wire: comparison of laser and arc beam deposition and evaluation with respect to aerospace material specifications, *Physics Procedia*, 2010, 5: p.595–606
73. H.M.A. Kolken, K. Lietaert, T. van der Sloten, B. Pouran, A. Meynen, G.V. Loock, H. Weinans, L. Scheys, A.A. Zadpoor, Mechanical performance of auxetic meta-biomaterials, *Journal of the Mechanical Behavior of Biomedical Materials*, 2020, 104: 103658
74. H. Bradley, J. Berthel, M. Frecker, T. W. Simpson, (2020), Mechanical properties of additively manufactured metal lattice structures: data review and design interface, *Additive Manufacturing*, 2020, 35: 101301
75. E. Atzeni, A. Salmi, Study on unsupported overhangs of AlSi10Mg parts processed by Direct Metal Laser Sintering (DMLS), *Journal of Manufacturing Processes*, 2015, 20: p.500–506

76. A.T. Gaynor, J.K. Guest, Topology optimization considering overhang constraints: Eliminating sacrificial support material in additive manufacturing through design, *Structural and Multidisciplinary Optimization*, 2016, 54: p.1157-1172
77. A. Kumar, L. Collini, A. Daurel, J.Y. Jeng, Design and additive manufacturing of closed cells from supportless lattice structure, *Additive Manufacturing*, 2020, 33: p.101168
78. W. Tao, M.C. Leu, Design Of Lattice Structure for Additive Manufacturing, International Symposium on Flexible Automation, 1 – 3 August 2016, Cleveland, Ohio, U.S.A. DOI: 10.1109/ISFA.2016.7790182, available at https://www.researchgate.net/publication/311756044_Design_of_lattice_structure_for_additive_manufacturing (accessed 10 December 2020)
79. T. Ziegler, R. Jaeger, C. Koplín, A design, mechanical rating, and load adaptation method for cellular components for additive manufacturing, *International Journal of Additive Manufacturing Technologies*, 2017, 90: p.2875–2884
80. S. Babae, J. Shim, J.C. Weaver, E.R. Chen, N. Patel, K. Bertoldi, 3D Soft Metamaterials with Negative Poisson's Ratio, *Advanced Materials*, 2013, 25: p.5044–5049
81. A. Bandyopadhyay, K.D. Traxel, Invited review article: Metal-additive manufacturing- Modeling strategies for application-optimized designs, *Additive Manufacturing*, 2018, 22: p.758–774
82. M.F. Ashby, The properties of foams and lattices, *Philosophical Transactions of the Royal Society A: Mathematical, Physical and Engineering Sciences*, 2006, 364(1838): p.15-30

83. M.Q. Shaikh, P.Y. Lavertu, K.H. Kate, S.V. Atre, Process Sensitivity and Significant Parameters Investigation in Metal Fused Filament Fabrication of Ti-6Al-4V, *Journal of Materials Engineering and Performance*, 2021, <https://doi.org/10.1007/s11665-021-05666-8>
84. X. Lu, Y. Lee, S. Yang, Y. Hao, J.R. Evans, C. G. Parini, Fine lattice structures fabricated by extrusion freeforming: Process variables, *Journal of Materials Processing Technology*, 2009, 209: p.4654–4661
85. J.M. Gere, B.J. Goodno, *Mechanics of Materials*, 2012, Brief Edition, Cengage Learning, Stamford, CT.
86. F. Tamimi, J. Torres, K. Al-Abedalla, E. Lopez-Cabarcos, M. H. Alkhraisat, D. C. Bassett, U. Gbureck, J. E. Barralet, Osseointegration of dental implants in 3D-printed synthetic onlay grafts customized according to bone metabolic activity in recipient site, *Biomaterials*, 2014, 35: p.5436-5445
87. R.B. Osman, A. J. van der Veen, D. Huiberts, D. Wismeijer, N. Alharbi, 3D-printing zirconia implants; a dream or a reality? An in-vitro study evaluating the dimensional accuracy, surface topography and mechanical properties of printed zirconia implant and discs, *Journal of the Mechanical Behavior of Biomedical Materials*, 2017, 75: p.521-528
88. T.T. Oliveira, A.C. Reis, Fabrication of dental implants by the additive manufacturing method: A systematic review, *Journal of Prosthetic Dentistry*, 2019, 122(3): p.270–274
89. S. Titsinides, G. Agrogiannis, T. Karatzas, Bone grafting materials in dentoalveolar reconstruction: A comprehensive review, *Japanese Dental Science Review*, 2019, 55: p.26-32

90. F. Batool., M. Strub, C. Petit, I. M. Bugueno, F. Bornert, F. Clauss, O. Huck, S. Kuchler-Bopp, N. Benkirane-Jessel, Periodontal Tissues, Maxillary Jaw Bone, and Tooth Regeneration Approaches: From Animal Models Analyses to Clinical Applications, *Nanomaterials*, 2018, 8(5): 337
91. E.E. Keller, N.B. Van Roekel, R.O. Desjardins, D.E. Tolman, Prosthetic-Surgical Reconstruction of the Severely Resorbed Maxilla With Iliac Bone Grafting and Tissue-Integrated Prostheses, *International Journal of Oral & Maxillofacial Implants*, 1987, 2(3): p.39-55
92. N. Gellrich, R.M. Zimmerer, S. Spalthoff, P. Jehn, P. Pott, M. Rana, B. Rahlf, A customised digitally engineered solution for fixed dental rehabilitation in severe bone deficiency: A new innovative line extension in implant dentistry, *Journal of Cranio-Maxillo-Facial Surgery*, 2017, 45: p.1632–1638
93. C. Mangano, A. Bianchi, F.G. Mangano, J. Dana, M. Colombo, I. Solop, O. Admakin, Custom-made 3D printed subperiosteal titanium implants for the prosthetic restoration of the atrophic posterior mandible of elderly patients: a case series, *3D Printing in Medicine*, 2020, 6: 1
94. M. Sokac, I. Budak, D. Miljanovic, Z. Santosi, D. Vukelic, Computer-aided modeling and additive manufacturing fabrication of patient-specific mandibular implant, *Lekar a tehnika – Clinician and Technology*, 2018, 48(4): p.113-117
95. R.R. Fry, I. Gargya, S. Goyal, J.P. Chawla, P.K. Pandher, G. Dhaliwal, P.S. Ghotra, Additive Manufacturing- An Enigma: the Future of Oral & Maxillofacial Surgery, *IOSR Journal of Dental and Medical Sciences*, 2016, 15(9): p.78-83

96. L.L. Dincă1, A. Banu, A. Vișan, Additive manufacturing in maxillofacial reconstruction, MATEC Web of Conferences, 2017, 137: 02001
97. D.J. Cohen, A.Cheng, A.Kahn, M. Aviram, A.J. Whitehead, S.L. Hyzy, R.M. Clohessy, B.D. Boyan, Z. Schwartz, Novel Osteogenic Ti-6Al-4V Device For Restoration Of Dental Function In Patients With Large Bone Deficiencies: Design, Development And Implementation, Scientific Reports, 2016, 6: 20493
98. T. Joda, F. Zarone, M. Ferrari, The complete digital workflow in fixed prosthodontics: a systematic review, BMC Oral Health, 2017, 17(1): 124
99. A.L. Jardini, M.A. Larosa, R.M. Filho, C.A. de Carvalho, L.F. Bernardes, C.S. Lambert, D.R. Calderoni, P. Kharmandayan, Cranial reconstruction: 3D biomodel and custom-built implant created using additive manufacturing, Journal of Cranio-Maxillo-Facial Surgery, 2-14, 42: p.1877-1884
100. M. Salmi, K. Paloheimo, J. Tuomi, J. Wolff, A. Mäkitie, Accuracy of medical models made by additive manufacturing (rapid manufacturing), Journal of Cranio-Maxillo-Facial Surgery, 2013, 41: p.603-609
101. P. Stoor, A. Suomalainen, K. Mesimäki, R. Kontio, Rapid prototyped patient specific guiding implants in critical mandibular reconstruction, Journal of Cranio-Maxillo-Facial Surgery, 2017, 45: p.63-70
102. Andreas Naros, Hannes Weise, Felix Tilsen, Sebastian Hoefert, Georgios Naros, Michael Krimmel, Siegmund Reinert, Joachim Polligkeit, Three-dimensional accuracy of mandibular reconstruction by patient-specific pre-bent reconstruction plates using an “in-house” 3D-printer, Journal of Cranio-Maxillo-Facial Surgery, 2018, 46: p.1645-1651

103. J. Parthasarathy, 3D modeling, custom implants and its future perspectives in craniofacial surgery, *Annals of Maxillofacial Surgery*, 2014, 4(1)
104. S. Bose, D. Ke, H. Sahasrabudhe, A. Bandyopadhyay, (2018), Additive manufacturing of biomaterials, *Progress in Materials Science*, 2018, 93: p.45-111
105. S.L. Sing, J. An, W.Y. Yeong, F.E. Wiria, Laser and Electron-Beam Powder-Bed Additive Manufacturing of Metallic Implants: A Review on Processes, Materials and Designs, *Journal of Orthopaedic Research*, 2016, 34(3): p.369-385
106. L. Bai, C. Gong, X. Chen, Y. Sun, J. Zhang, L. Cai, S. Zhu, S.Q. Xie, Additive Manufacturing of Customized Metallic Orthopedic Implants: Materials, Structures, and Surface Modifications, *Metals*, 2019, 9(9): 1004
107. D.J. Cohen, A. Cheng, K. Sahingur, R.M. Clohessy, L.B. Hopkins, B.D. Boyan, Z. Schwartz, Performance of laser sintered Ti-6Al-4V implants with bone-inspired porosity and micro/nanoscale surface roughness in the rabbit femur, *Biomedical Materials*, 2017, 12: 025021
108. R. Ramakrishnaiah, A.A. Kheraif, A. Mohammad, D.D. Divakar, S.B. Kotha, S.L. Celur, M.I. Hashem, P.K. Vallittu, I. Rehman, (2017), Preliminary fabrication and characterization of electron beam melted Ti-6Al-4V customized dental implant, *Saudi Journal of Biological Sciences*, 2017, 24: p.787-796
109. B.A. Szost, S. Terzi, F.Martina, D. Boisselier, A. Prytuliak, T. Pirling, M. Hofmann, D.J. Jarvis, A comparative study of additive manufacturing techniques: Residual stress and microstructural analysis of CLAD and WAAM printed Ti-6Al-4V components, *Materials and Design*, 2016, 89: p.559-567

110. M. Mounir, M. Atef, A. Abou-Elfetouh, M.M. Hakam, Titanium and polyether ether ketone (PEEK) patient-specific sub-periosteal implants: two novel approaches for rehabilitation of the severely atrophic anterior maxillary ridge, *International Journal of Oral and Maxillofacial Surgery*, 2018, 47(5): p.658-664
111. J. Chen, Z. Zhang, X. Chen, C. Zhang, G. Zhang, Z. Xu, Design and manufacture of customized dental implants by using reverse engineering and selective laser melting technology, *The Journal of Prosthetic Dentistry*, 2014, 112(5): p.1088-1095
112. F. Mangano, C. Mangano, A. Piattelli, G. Iezzi, (2017), Histological Evidence of the Osseointegration of Fractured Direct Metal Laser Sintering Implants Retrieved after 5 Years of Function, *BioMed Research International*, 2017: 9732136
113. S.L. Hyzy, A. Cheng, D.J. Cohen, G. Yatzkaier, A.J. Whitehead, R.M. Clohessy, R.A. Gittens, B.D. Boyan, Z. Schwartz, Novel hydrophilic nanostructured microtexture on direct metal laser sintered Ti–6Al–4V surfaces enhances osteoblast response in vitro and osseointegration in a rabbit model, *Journal of Biomedical Materials Research Part-A*, 2016, 104(8): p.2086-2098
114. Y. Kok, X.P. Tan, P. Wang, M.L. Nai, N.H. Loh, E. Liu, S.B. Tor, Anisotropy and heterogeneity of microstructure and mechanical properties in metal additive manufacturing: A critical review, *Materials and Design*, 2018, 139: p.565-586
115. J.J. Lewandowski, M. Seifi, *Metal Additive Manufacturing: A Review of Mechanical Properties*, *Annual Review of Materials Research*, 2016, 46: p.151-186
116. J. Damon, S. Dietrich, Process porosity and mechanical performance of fused filament fabricated 316L stainless steel, *Rapid Prototyping Journal*, 2019, 25(7): p.1319-1327

117. D. Godec, S. Cano, C. Holzer, J. Gonzalez-Gutierrez, Optimization of the 3D Printing Parameters for Tensile Properties of Specimens Produced by Fused Filament Fabrication of 17-4PH Stainless Steel, *Materials*, 2020, 13(3): 774
118. M.Q. Shaikh, S. Graziosi, S.V. Atre, Supportless printing of lattice structures by metal fused filament fabrication (MF3) of Ti-6Al-4V: Design and analysis, *Rapid Prototyping Journal*, 2021, accepted for publication
119. Y.Y. Yau, J.F. Arvier, T.M. Barker, Maxillofacial biomodelling—preliminary result, *British Institute of Radiology*, 2014, 68(809): 519
120. D.J. Thomas, M.A. Azmi, Z. Tehrani, 3D additive manufacture of oral and maxillofacial surgical models for preoperative planning, *International Journal of Advanced Manufacturing Technology*, 2014, 71: p.1643-1651
121. A. Suomalainen, P. Stoor, K. Mesimäki, R.K. Kontio, Rapid prototyping modelling in oral and maxillofacial surgery: A two year retrospective study, *Journal of Clinical and Experimental Dentistry*, 2015, 7(5): p.605-612
122. P. Singh, Materials-Processing Relationships for Metal Fused Filament Fabrication of Ti-6Al-4V Alloy, *Electronic Theses and Dissertations*, 2020: Paper 3388
123. M.M. Shalabi, A. Gortemaker, M.A. Van't Hof, J.A. Jansen, N.H. Creugers, Implant Surface Roughness and Bone Healing: a Systematic Review, *Journal Dental Research*, 2006, 85(6): p.496-500
124. A. Brizuela, M. Herrero-Climent, E. Rios-Carrasco, J.V. Rios-Santos, R.A. Pérez, J.M. Manero, J.G. Mur, Influence of the Elastic Modulus on the Osseointegration of Dental Implants, *Materials*, 2019, 12: 980

125. S. Tunchel, A. Blay, R. Kolerman, E. Mijiritsky, J.A. Shibli, 3D Printing/Additive Manufacturing Single Titanium Dental Implants: A Prospective Multicenter Study with 3 Years of Follow-Up, *International Journal of Dentistry*, 2016, 6: p.1-9
126. P. DeVasConCellos, V.K. Balla, S. Bose, R. Fugazzi, W.S. Dernell, A. Bandyopadhyay, Patient specific implants for amputation prostheses: Design, manufacture and analysis, *Veterinary and Comparative Orthopaedics and Traumatology*, 2012, 25(4): p.286-296
127. L.E. Murr, S.A. Quinones, S.M. Gaytan, M.I. Lopez, A. Rodela, E.Y. Martinez, D.H. Hernandez, E. Martinez, F. Medina, R.B. Wicker, Microstructure and mechanical behavior of Ti-6Al-4V produced by rapid-layer manufacturing, for biomedical applications, *Journal of the Mechanical Behavior of Biomedical Materials*, 2009, 2(1): p.20-32
128. C. Ohman, E. Dall'Ara, M. Baleani, S. Van Sint Jan, Marco Viceconti, The effects of embalming using a 4% formalin solution on the compressive mechanical properties of human cortical bone, *Clinical Biomechanics*, 2008, 23: p.1294-1298

APPENDIX A

ESTIMATING POWDER-POLYMER MATERIAL PROPERTIES USED IN DESIGN FOR METAL FUSED FILAMENT FABRICATION (DfMF³)

A.1. INTRODUCTION

Metal fused filament fabrication (MF³) is a hybrid 3D printing process to fabricate custom 3D metal components. MF³ provides an alternative to other energy-intensive metal additive manufacturing (AM) processes such as laser-powder bed fusion, selective laser sintering, and direct energy deposition. MF³ is a multi-step process that involves a) mixing and extrusion of a powder-polymer mixture into filaments, b) 3D printing of a green part, c) polymer removal from the 3D printed green part by debinding to get a brown part, and d) densifying the brown part to achieve dense metal parts by sintering. The powder-polymer mixtures used in MF³ are adapted from metal injection molding (MIM) and are processed by modifying fused filament fabrication (FFF) that typically fabricate polymeric parts [1, 2]. Although materials design rules are known for processing powder-polymer mixtures using MIM, they cannot be directly applied to formulate new MF³ materials owing to differences in physical phenomena involved in the two processes. Moreover, processing with polymers using FFF is well-known, but very limited literature exists on the processing of polymer systems with high solid loadings typically used for MF³ [1, 3-7]. For example, in MIM, powder-polymer feedstocks are melt-processed at high shear rates in the range of 10^2 to 10^5 s⁻¹ [2]. However, the FFF processing of a polymer is typically done at a shear-

rate in the range of $10\text{-}300\text{ s}^{-1}$ [8]. These differences pose significant processing challenges for powder-polymer mixtures that display shear thinning behavior. Further, other properties such as density, thermal, and mechanical and equation-of-state parameters (PVT) change with variation in powder-polymer concentrations that can affect the design of overhangs and support structures in the printed part. Any variations in powder-polymer composition, filament properties, filament processing, and process setup at the green stage can further introduce defects during subsequent debinding and sintering. Accordingly, material compositional variations can affect the design of not only component geometrical attributes but also overhangs and support structures in the printed part. **Figure A.1** represents our present approach for capturing material influences on processing and part attributes using a design-for-metal-fused-filament-fabrication (DfMF³) platform.

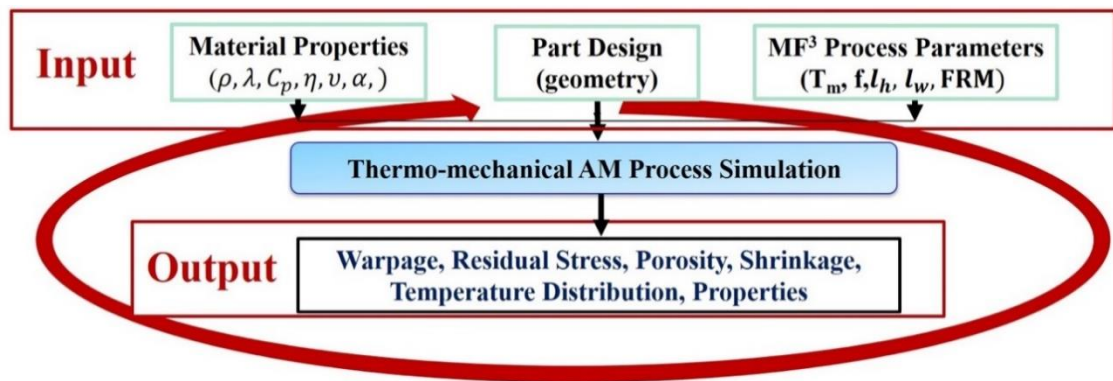


Figure A.1. The present work for determining the input material parameters for conducting process simulations

Our current work on processing Ti-6Al-4V powder-polymer mixtures with MF³ has enabled us examining such defects at different stages of MF³ processing. In **Figure A.2**,

common defects encountered during filament fabrication, printing, debinding and sintering are shown. **Figure A.2a** and **b** are imaged using scanning electron microscopy (TESCAN Vega 3) and **Figure A.2c** and **d** are imaged using optical microscopy (Olympus BX-51). **Figure A.2a** shows the presence of pores in the filament, leading to lower filament densities. These filaments were found to buckle and crack under pressures exerted by the pinch roller during 3D printing. **Figure A.2b** shows MF³ 3D printing defects such as gaps across layers within a cross-section resulting in low green density in 3D printed parts, which can magnify post-sintering. Typical cracks that occur during debinding due to the internal stress build-up in a part are presented in **Figure A.2c**. Similarly, **Figure A.2d** shows the distribution of inter and intra-bead porosity and gap between layers post sintering.

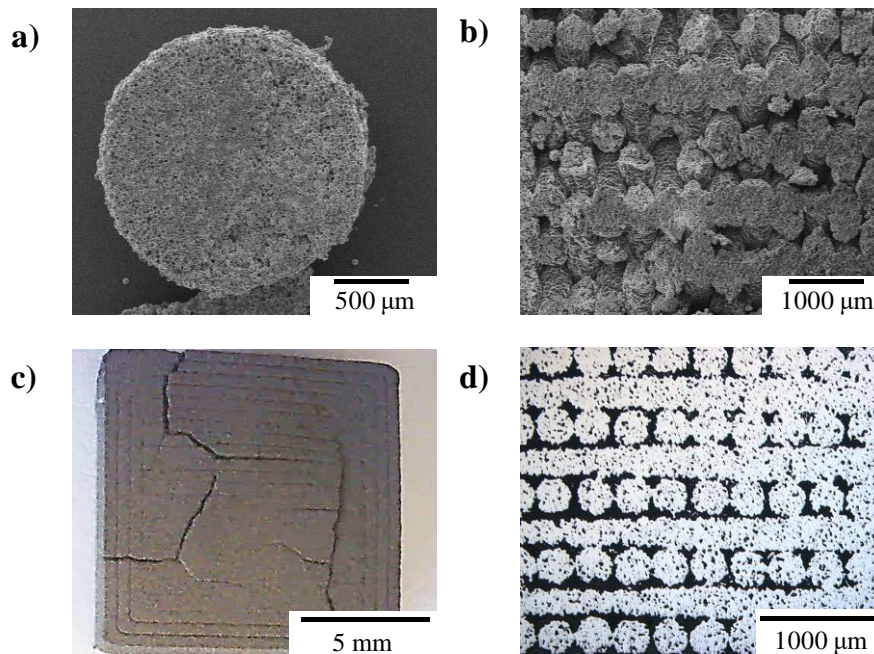


Figure A.2. Typical defects observed in MF³ 3D printing process demonstrated for Ti-6Al-4V alloy system fabricated by our group showing (a) dark regions representing pores within a cut-cross section of a powder-polymer filament, (b) gaps between layers within an MF³

fabricated green part, (c) crack propagation observed after debinding and (d) the presence of micro and macro pores present within the sintered MF³ part.

Understanding defect evolution during MF³ processing can be crucial for achieving desired material properties and part functionality. Specifically, simulation tools to correctly identify appropriate material compositions and process parameters for designing parts suitable for MF³ can help reduce the trial-and-error involved in producing defect-free parts. As the density and thermal properties for metals are higher than that of polymer binder, fabricating parts with high overhangs can be easily printed using standard polymers but MF³ of such parts with metal-polymer feedstocks could result in part sagging, differential heating/cooling rates during printing and subsequent debinding and sintering. The potential of the MF³ process in fabricating metal parts has been shown in some of the published work for 17-4 PH stainless steel, copper, WC-10Co, W-Cr and Cu-10Sn materials [1, 4, 5, 9-13]. However, the use of design tools to perform material and process simulations in MF³ has not yet been well-established, thereby limiting the widespread use of the MF³ process to manufacture parts with different materials for a variety of applications [12].

A few simulation tools for FFF such as Digimat from MSC Software and GENOA from Alphastar and GENESIS from Vanderplaats R&D are commercially available for conducting Design-for-MF³ (DfMF³) simulations. These simulation platforms require a range of powder-polymer mixture material properties such as physical, thermal, mechanical, rheological and equation-of-state parameters (PVT) as input parameters [14-16]. Compared to properties of more than 5000 different grades of plastics commonly used in injection molding simulation platforms, less than ten polymeric material systems are

available in the database of these platforms. Any variations in powder concentrations or changes in powder-polymer mixture material properties require new experimental measurements to be performed, which can be time-consuming and expensive.

The current work addresses the important gap in the availability of powder-polymer properties for DfMF³ by utilizing material models that predict the compound properties from literature data of powder properties and measured data of polymer matrix properties. To identify how material properties vary with powder content (solids loading), properties were estimated for density, thermal conductivity, specific heat, modulus, coefficient of thermal expansion, viscosity as a function of shear rate and temperature, and specific volume as a function of pressure and temperature. The estimated material properties were used to understand the simulation outputs such as residual stresses and warpages using the DfMF³ platform, Digimat. It is expected that the overall approach will help reduce significant trial-and-error in designing new materials that can be used to fabricate complex geometries using MF³.

A.2. MODELS FOR POWDER-POLYMER MATERIAL PROPERTIES

There are various models that can predict material thermophysical properties for powder-polymer mixtures [17-28]. Our recent work compared various models used to predict density, thermal conductivity, specific heat, viscosity, and specific volume and identifies models that provide the best fit to experimental measurements of powder-polymer properties [23-25]. From the set of models screened for predicting material properties, models that provided the best fit with experimental measurements in prior work were selected for subsequent sections for different material property estimations. In the current

work, a protocol was developed to use existing literature filler (powder) properties and experimentally measured binder properties in conjunction with the selected models to estimate powder-polymer properties that are required to perform DfM³ simulations. Material properties included density, thermal conductivity, specific heat, modulus, coefficient of thermal expansion, viscosity as a function of shear rate and temperature, and specific volume as a function of pressure and temperature. As a representative, high-impact material Ti-6Al-4V alloy was used as the filler phase while experimentally measured properties of a wax-polymer binder were used as matrix phase. **Table A.1** lists thermomechanical properties at room temperature for Ti-6Al-4V alloy collected from literature sources [31-40].

Table A.1. Material properties of Ti-6Al-4V alloy at room temperature

Property	Value	Reference
Density (kg/m ³)	4.42 ± 0.06	[29-36]
Specific heat, (J/kg·K)	560 ± 30	[34, 36-39]
Thermal conductivity (W/m·K)	6.5 ± 0.4	[34-39]
Coefficient of thermal expansion (x10 ⁻⁶ K ⁻¹)	8.8 ± 0.4	[34-36, 38, 40, 41]
Modulus (GPa)	110 ± 3	[34-38, 42, 43]

A.3. MATERIALS AND EXPERIMENTAL METHODS

The ti-6Al-4V powder has been considered as the filler phase for the current study with the assumption, that the particles are mono-sized and spherical. In this work, to perform material property estimations, effects of powder particle size distribution, flowability, and packing behavior are not considered. The binder used in this work comprised paraffin wax,

low-density polyethylene, polypropylene, and stearic acid. Binder thermomechanical property measurements including density, modulus, specific heat, thermal conductivity, coefficient of thermal expansion, viscosity and specific volume were made at Datapoint Labs (Ithaca, NY). These measurements were performed according to the ASTM standards listed in supplementary **Table A.2**. Solid density measurements were made for the binder using the Archimedes principle as laid out in ASTM standard D792. A Perkin Elmer differential scanning calorimetry (DSC) was used to measure specific heats for the binder following ASTM E1269 standard. Thermal conductivity measurements for the binder were made using a K-System II thermal conductivity system per ASTM standard D5930.

Table A.2. Experimental methods with respective ASTM standard for measuring the thermophysical properties of the binder system

Property	Instrument	Standard
Density	Gas pycnometer	ASTM B923
Young's modulus	Universal testing machine	ASTM D638
Specific heat	Differential scanning calorimetry	ASTM E1269
Thermal conductivity	Line source method	ASTM D5930
Coefficient of thermal expansion	Thermomechanical analyzer	ASTM E831
Viscosity	Capillary rheometer	ASTM D3835
Specific volume	High-pressure dilatometry	ASTM D792

Viscosity for the binder was measured according to ASTM D3835 using a Gottfert Rheograph capillary rheometer. Pressure-volume-temperature (PVT) measurements for the binder were made with a Gnomix PVT apparatus per ASTM D792. The feedstock

properties for the composite with Ti-6Al-4V as filler with polymer binder were estimated using models discussed in the later sections.

A.4. ESTIMATING PROPERTIES OF POWDER-POLYMER MIXTURES

The experimentally measured values of polymer binder and literature values of Ti-6Al-4V filler properties were used to estimate feedstock properties of Ti-6Al-4V powder-polymer composite from 56 to 60 vol.% solids loading.

A.4.1. DENSITY

The density of a filler-binder mixture is a critical parameter in determining the composition of a feedstock. The metal filler content in the polymer binder depends on several factors including the particle shape and size, polymer behavior and mixture homogeneity. The solid density of filler-polymer mixtures can be estimated using various available models [17, 18]. In this study, an inverse rule-of-mixtures was used to estimate the composite feedstock density, given in **Equation 1**. This model has previously been verified in published work from our group [26, 44] by comparing it with experimental density measurements for various fillers, yielding a high coefficient of determination (R^2) of 0.97, thereby confirming good applicability to make density estimations.

$$\frac{1}{\rho_c} = \frac{X_f}{\rho_f} + \frac{X_b}{\rho_b} \quad (1)$$

where ρ is the density, X is the mass fraction, and the subscripts c, b and f stand for the composite, binder, and filler, respectively.

Although the feedstock formulation is represented by weight fractions, for preparing powder-polymer mixtures, volumetric comparisons are more useful to compare powders of differing densities. Therefore, the volume fractions of powder and binder were estimated from the mass fractions using **Equations 2** and **3**, respectively:

$$\phi_f = \frac{\frac{X_f}{\rho_f}}{\frac{X_f}{\rho_f} + \frac{X_b}{\rho_b}} \quad (2)$$

$$\phi_b = 1 - \phi_f \quad (3)$$

where, ϕ_f and ϕ_b are the volume fractions of the filler and binder, respectively.

The solid density for the formulated binder system (ρ_b) was experimentally obtained (available in **Table A.3**) and the filler properties were found from literature provided in **Table A.1**, while the values for intermediate volume fractions were estimated using **Equation 1**. A comparison of density as a function of volume fraction of powder is shown in **Figure A.3a**. It was observed that for a change from 0.56 to 0.60 volume fraction of Ti-6Al-4V, the composite solid density increased from 2860 to 3000 kg/m³. Further applicability of the model was verified by experimental density measurements for Ti-6Al-4V powder-binder feedstock at 0.59 volume fraction, which was found to be 2950 kg/m³, representing a deviation below 0.6% from the estimated value of 2965 kg/m³.

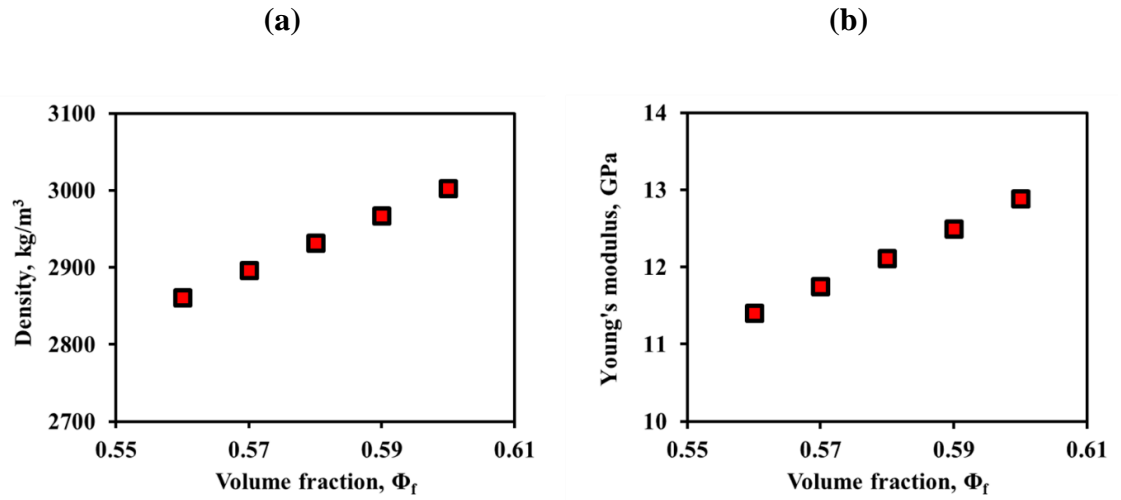


Figure A.3. Estimated (a) Feedstock density, and (b) Young's modulus for Ti-6Al-4V filler-binder feedstock at different volume fractions

Table A.3. Experimentally determined binder thermophysical properties

Property	Value							
Density (kg/m ³)	880							
Modulus (GPa)	2.560							
Specific heat (J/kg·K)	Temperature (K)							
	303	305	322	331	384	443		
	3160	3521	3665	4477	2395	2598		
Thermal conductivity (W/m·K)	Temperature (K)							
	316	337	357	378	398	418	438	
	0.192	0.186	0.193	0.167	0.166	0.159	0.160	
Coefficient of thermal expansion (10 ⁻⁶ K ⁻¹)	56.5							
Viscosity (Pa·s)	Temperature (K)							
	413				423			
	Shear rate (s ⁻¹)				Shear rate (s ⁻¹)			
	20	160	800	1600	20	160	800	1600
	102	34	13	8	32	13	5	4
Specific volume (10 ⁻⁴ m ³ /kg)	Pressure (MPa)							
	0				50			
	Temperature (K)				Temperature (K)			
	300	350	400	450	300	350	400	450
	11.4	12.7	13.4	14.0	11.2	12.4	12.9	13.4

A.4.2. YOUNG'S MODULUS

The Young's modulus of the feedstock has a direct influence on the strength and distortion of parts fabricated by MF³. Good adhesion between metal particles and the polymer is very essential to achieve a high Young's modulus. Furthermore, solids loading, binder compositions, and temperature strongly influence Young's modulus. Among various models available [19-21] to predict Young's modulus of a filler-polymer mixture, Halpin and Tsai [19] developed a widely accepted model that takes into account the filler shape and loading direction. It has been widely used in studies in predicting the modulus and provides estimations comparable to experimental data for filled polymer systems [45, 46]. This model is as shown in **Equation 4**:

$$\frac{E_c}{E_b} = \frac{1 + \xi\eta\phi_f}{1 - \eta\phi_f} \quad (4)$$

where E is the elastic modulus, ξ is a shape parameter dependent on the geometry and loading direction, ϕ is volume fraction, subscripts c, b and f stand for the composite, binder, and filler respectively.

The parameter η is given by **Equation 5**:

$$\eta = \frac{E_f/E_b - 1}{E_f/E_b + \xi} \quad (5)$$

The parameter, ξ can be approximated to 2 for spherical particles [19]. The Young's modulus for binder (E_b) was determined experimentally at room temperature (available in supplementary **Table A.3**). The Ti-6Al-4V filler properties were collected from the literature as shown in **Table A.1**. The Young's modulus for intermediate volume fractions

was estimated using **Equations 4** and **5**. As seen in **Figure A.3b**, the modulus changed from 11.4 GPa to 12.8 GPa with the change in volume fraction from 0.56 to 0.60.

A.4.3. SPECIFIC HEAT

For polymers and metal powder feedstocks, the heat capacity is dependent on the processing temperature. The polymer melting results in phase change and further changes the heat capacity. For MF³ it is critical to understand the trends that occur in the entire range of processing temperatures. In the current work, a modified rule-of-mixtures was used [22] as given in **Equation 6** to determine the specific heat of powder-polymer mixture and this equation has been successfully applied to mixtures with high volume fraction fillers. In our previous work [26-28, 44], the predicted values from this model have been evaluated against experimental specific heat measurements and it has produced a high coefficient of determination, (R^2) of 0.97, asserting good applicability.

$$C_{p_c} = [C_{p_b}X_b + C_{p_f}X_f] * [1 + A * X_bX_f] \quad (6)$$

where A is a correction factor assumed to be 0.2 for spherical particles.

The specific heat for the binder system (C_{p_b}) was experimentally obtained at different temperatures (available in **Table A.3**) and the filler properties were found from literature (**Table A.1** and supplementary **Table A.4** for each temperature). The values were used to estimate the specific heat capacity over a range of filler volume fractions using **Equation 6** and are plotted in **Figure A.4a**. It can be observed that for a change from 0.56 to 0.60 volume fraction of Ti-6Al-4V powder at 303 K, the specific heat decreased from 983 to 926 J/kg·K. With an increase in temperature from 303 K to 443 K, the specific heat first

increased from 983 to 1173 J/kg·K at 322 K and then decreased to 855 J/kg·K. More details for specific heat estimation for each volume fraction and temperature are provided in **Table A.4**.

Table A.4. Specific heat of Ti-6Al-4V powder-binder feedstock at different filler volume fractions for different temperatures

Volume fraction of filler, Φ_f	Temperature (K)						
	298	303	305	322	331	384	443
	Specific heat capacity C_p , J/kg·K						
0.56	933	983	1003	1173	1115	827	855
0.57	920	968	987	1152	1096	818	845
0.58	907	954	972	1131	1077	809	835
0.59	895	940	957	1110	1058	800	825
0.60	883	926	943	1090	1040	791	815
1 (for Ti6Al-4V powder)	565	565	565	565	565	566	571

A.4.4. THERMAL CONDUCTIVITY

The addition of metal particles in the polymer matrix improves the overall thermal conductivity of feedstock due to the high thermal conductivity of the metal. In MF³, it is vital to understand the thermal conductivity behavior of feedstock to ensure strong layer-to-layer and bead-to-bead adhesion by the proper selection of extrusion and build platform temperatures. The Bruggeman model has been found to provide better predictions for filled-polymer feedstock systems comparable to experimental measurements at high filler loadings [22, 26-28, 47]. **Equation 7** was used to estimate the thermal conductivity of powder-polymer mixture:

$$1 - \phi_f = \left(\frac{\lambda_f - \lambda_c}{\lambda_f - \lambda_b} \right) \left(\frac{\lambda_b}{\lambda_c} \right)^{1/3} \quad (7)$$

where λ is the thermal conductivity, ϕ is the volume fraction of powder, and the subscripts c, b and f stand for the composite, binder and filler, respectively.

Table A.5. Thermal conductivity of Ti-6Al-4V powder-binder feedstock at different filler volume fractions for different temperatures

Volume fraction of filler, Φ_f	Temperature (K)						
	316	337	357	378	398	418	438
	Thermal conductivity λ , W/m·K						
0.56	1.301	1.289	1.332	1.229	1.240	1.220	1.238
0.57	1.353	1.341	1.386	1.280	1.293	1.272	1.292
0.58	1.409	1.397	1.444	1.336	1.350	1.330	1.351
0.59	1.466	1.455	1.504	1.395	1.411	1.392	1.414
0.60	1.526	1.516	1.567	1.457	1.475	1.456	1.480
1 (for Ti6Al-4V powder)	6.82	7.02	7.21	7.49	7.81	8.13	8.42

The binder thermal conductivity (λ_b) was experimentally determined (available in **Table A.3**), and the filler properties were taken from the literature (**Table A.1**). The intermediate volume fractions were estimated using **Equation 7** (available in **Table A.4**). It can be inferred from **Figure A.4b** that for a change in volume fraction from 0.56 to 0.60 for Ti-6Al-4V powder at 316 K, the thermal conductivity increased from 1.3 to 1.53 W/m·K. With an increase in temperature from 316 K to 438 K at 0.56 volume fraction, the thermal conductivity first increased from 1.3 to 1.33 W/m·K at 357 K and then decreased to 1.24 W/m·K at 438 K. The trend was similar for other volume fractions of Ti-6Al-4V feedstocks.

The trend of the curve for composite feedstock is dominated by the thermal conductivity of the matrix/binder material. The typical crest and trough observed in the curve are due to the changes in the binder state from solid to liquid while heated to a definitive temperature.

A.4.5. COEFFICIENT OF THERMAL EXPANSION (CTE)

The 3D printed components expand and shrink during the heating and cooling stages of the process. Big differences in powder-polymer CTE can cause warping in parts due to the buildup of residual thermal stresses while cooling. The CTE of powder-polymer mixtures can be calculated by several models [24-28]. The general rule-of-mixtures is a simple approach [26] (shown in **Equation 8**) which requires fewer empirical constants, and in our previous work [26] when evaluated against experimental values it yielded regression coefficient of determination (R^2) in the range of 0.87-0.97, indicating a good fit.

$$\alpha_c = \phi_f \alpha_f + \alpha_b (1 - \phi_f) \quad (8)$$

where α is the thermal expansion coefficient, ϕ is the volume fraction, and the subscripts c, f and b stand for composite, filler, and binder respectively.

The CTE for binder (α_b) was experimentally obtained (available in **Table A.3**) and the filler properties were found from literature provided in **Table A.1** while the values for intermediate volume fractions were estimated using **Equation 8**. In **Figure A.4c**, for a change in volume fraction from 0.56 to 0.60, the CTE decreased from 29.7×10^{-6} to $27.8 \times 10^{-6} \text{ K}^{-1}$.

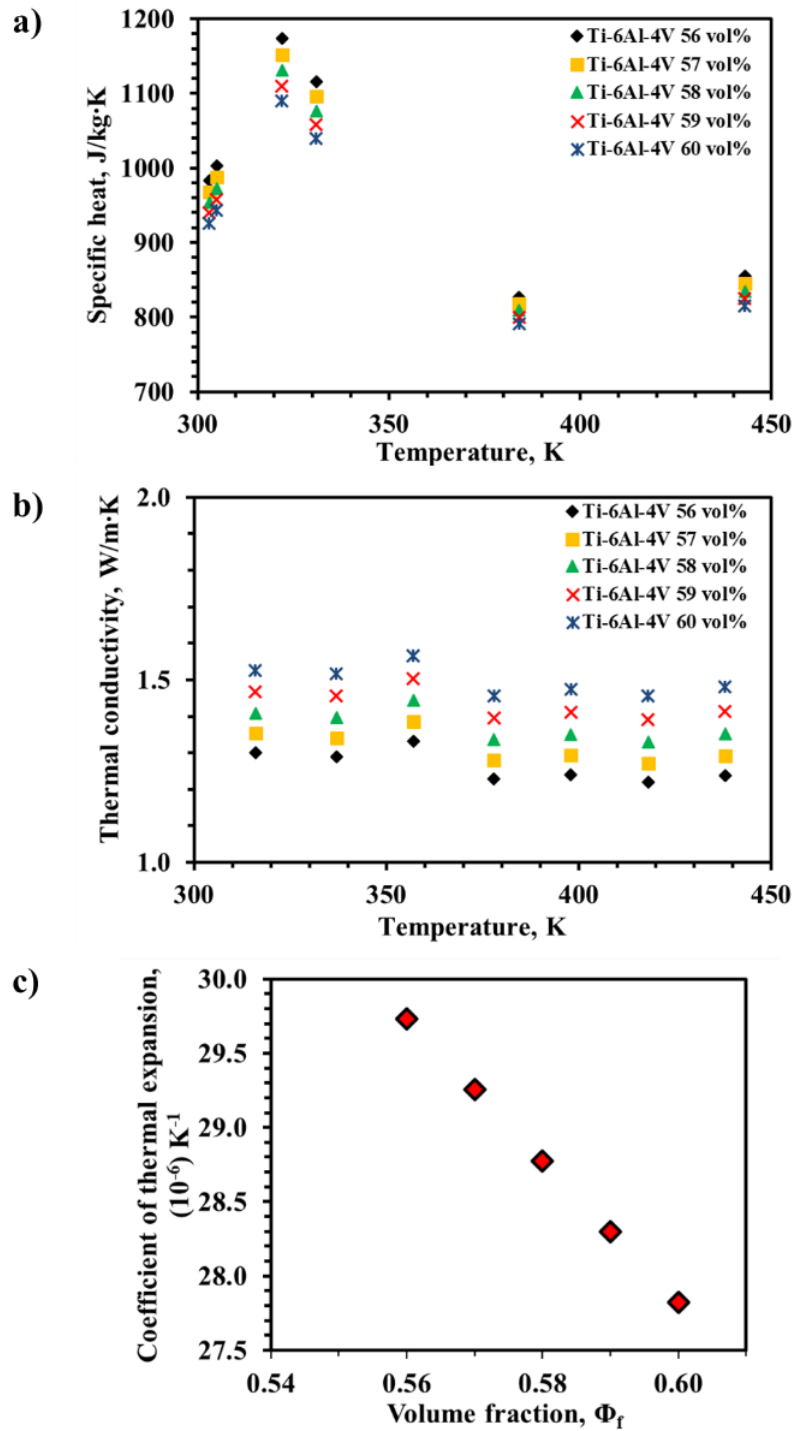


Figure A.4. Estimated thermal properties of composite Ti-6Al-4V powder-binder feedstock at different volume fractions for (a) specific heat and (b) thermal conductivity as a function of temperature, and (c) coefficient of thermal expansion

A.4.6. VISCOSITY

MF³ operates with the flow of molten feedstock material through the nozzle to form the desired geometry. The rheological understanding of powder-polymer mixtures is crucial since at higher powder loadings the feedstock viscosity increases. The typical filler content ranges between 50-65 vol.%, and the viscosity varies as the inverse of powder particle size. Rheological characteristics provide a clear understanding related to flow instabilities while printing and thereby the influence of powder loading, shear rate and temperature on the material flow properties.

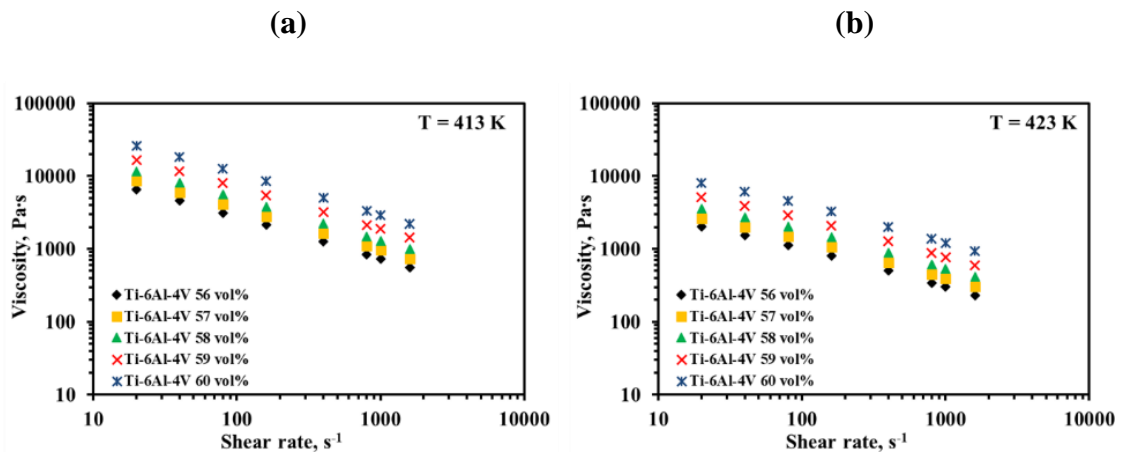


Figure A.5. Estimated viscosity of the Ti-6Al-4V powder-binder feedstock for a shear rate of 20-1600s⁻¹ at (a) 413K and (b) 423K with different volume fractions

The Krieger-Dougherty model [26-28, 48] has been found to be suitable for predicting viscosity values for highly filled powder-polymer mixtures from our previous work, generating coefficient of determination (R^2) ranging 0.94-0.99, compared to experimental viscosity measurements. A simplified form of the model is given in **Equation 9**:

$$\eta_c = \frac{\eta_b}{\left[1 - \frac{\phi_f}{\phi_m}\right]^2} \quad (9)$$

where η is the viscosity with subscript c and b stand for composite and binder, respectively. ϕ_m stands for the maximum packing fraction of the filler and is approximated to be 0.64 for randomly packed spheres [49], and ϕ_f is the filler volume fraction.

Figure A.5 shows the variation in viscosity as a function of powder volume fraction, shear rate and temperature (tabulated data provided in **Table A.6**). At 413K and a shear rate of 800s^{-1} , increasing the volume fraction of powder from 0.56 to 0.60 increases the viscosity from 840 to 3350 Pa.s. For example, with a volume fraction of 0.56 at 413K with an increasing shear rate from 20 to 1600 s^{-1} , the viscosity decreases from 6520 to 560 Pa.s. Similarly, increasing temperature from 413 to 423 K decreases the viscosity from 840 to 350 Pa.s for 0.56 volume fraction at 800s^{-1} . For processes operating under low shear rates, it is highly important to have low feedstock viscosity for successful flowability, especially for the MF³ process where the filament strength properties provide enough force for a continuous flow through the nozzle and successful printing operation. Further applicability of the model was verified by experimental viscosity measurements for Ti-6Al-4V powder-binder feedstock at 0.59 volume fraction utilizing a similar binder at 140 °C for 160s^{-1} , which was found to be 600 Pa.s, representing a wide deviation from the estimated value of 5450 Pa.s. The difference can majorly be attributed to the particle attributes related to size distribution and packing behavior which are not considered for the viscosity predictions by any of the available models, resulting in a discrepancy in estimations where particles are assumed to be mono-sized spheres.

Table A.6. Viscosity of Ti-6Al-4V powder-binder feedstock as a function of filler volume fraction, temperature, and shear rate

Volume fraction of filler, Φ_f	Temperature (K)							
	413				423			
	Shear rate (s ⁻¹)				Shear rate (s ⁻¹)			
	20	160	800	1600	20	160	800	1600
Viscosity (Pa's)								
0.56	6520	2130	840	560	2000	810	340	230
0.57	8520	2780	1100	730	2620	1060	450	300
0.58	11600	3780	1490	990	3560	1440	610	410
0.59	16700	5450	2140	1430	5130	2070	880	590
0.60	26100	8500	3350	2230	8010	3290	1370	930

Viscosity is sensitive to shear rate and temperature. At low temperatures, the mixture viscosity is too high making it impossible to extrude material to print. While at very high temperatures the powder-binder separation can occur during extrusion through the nozzle because of the binder being too thin causing nozzle clogging. In order to predict the viscosity at the typical MF³ printing temperatures and shear rates, the Cross-WLF equation can be used to numerically capture the shear-rate and temperature changes in viscosity [50], shown in **Equation 10**:

$$\eta = \frac{\eta_o}{1 + \left(\frac{\eta_o \dot{\gamma}}{\tau^*}\right)^{1-n}} \quad (10)$$

where η is the melt viscosity (Pa·s), η_0 is the zero-shear viscosity (Pa·s), $\dot{\gamma}$ is the shear rate (s^{-1}), τ^* is the critical stress level at the transition to shear thinning (Pa), which is determined by curve fitting, and n is the power-law index in the high shear rate regime, also determined by curve fitting. The viscosity of a filled polymer mixture and its temperature dependence can be calculated using **Equation 11**:

$$\eta_0 = D_1 \exp \left[- \frac{A_1(T - T^*)}{A_2 + (T - T^*)} \right] \quad (11)$$

where T is the temperature (K), T^* , D_1 , and A_1 are curve fitted coefficients, A_2 (assumed as 51.6 K) is the WLF constant. The values of these coefficients can be obtained by curve-fitting the estimated viscosity for different volume fractions of powder at various shear rates and temperatures. Representative extracted Cross WLF constants for 60 vol.% solids loading Ti-6Al-4V feedstock are provided in **Table A.7**.

Table A.7. Cross-WLF constants to determine viscosity at varying shear-rate and temperature for binder and 0.60 volume fractions of Ti-6Al-4V powder in the feedstock

Cross WLF constants	volume fraction, Φ_f	
	0	0.60
n	0.4	0.40
τ , Pa	793.46	203324.34
D_1 , Pa·s	4.29E+23	1.67E+15
T^* , K	333	364
A_1	78.13	46.37
A_2 , K	51.6	51.6

A.4.7. SPECIFIC VOLUME

Residual stresses are generated during MF³ as a result of differential heat transfer during layer deposition and subsequent cooling process. Warpage and non-uniform shrinkage have been some of the reported issues in the polymer FFF process which are equally important in MF³. The changes in material-specific volume, at certain powder volume fractions, as a function of temperature and pressure help providing substantial information in mitigating such defects in MF³ parts. The composite specific volume at different filler volume fractions was calculated using the rule-of-mixtures [17] and is shown in **Equation 12**. The rule of mixture has been found to be a reliable method in predicting the specific volume of polymer-filled systems, with our previous work [26] producing a high coefficient of determination (R^2) of 0.99 when compared to experimental results.

$$v_c = X_f v_f + v_b (1 - X_f) \quad (12)$$

where v is the specific volume, X is the mass fraction, and the subscripts c, f, and b refer to the composite, filler, and binder respectively.

From the estimations in **Figure A.6**, it can be seen that specific volume not only depends on temperature and pressure but also on powder volume fraction (data available in **Table A.8**). Increasing the volume fraction from 0.56 to 0.60 at 0 MPa decreased the specific volume from 4.6×10^{-4} to 4.4×10^{-4} m³/kg at 300K. When the temperature was increased from 300 to 450 K, at 0 MPa, the specific volume increased from 4.6×10^{-4} to 4.95×10^{-4} m³/kg for feedstock with 0.56 volume fraction of Ti-6Al-4V powder. However, with increasing pressure from 0 to 50 MPa (at 300 K) and 0.56 volume fraction, the specific volume was found to decrease from 4.6×10^{-4} to 4.5×10^{-4} m³/kg.

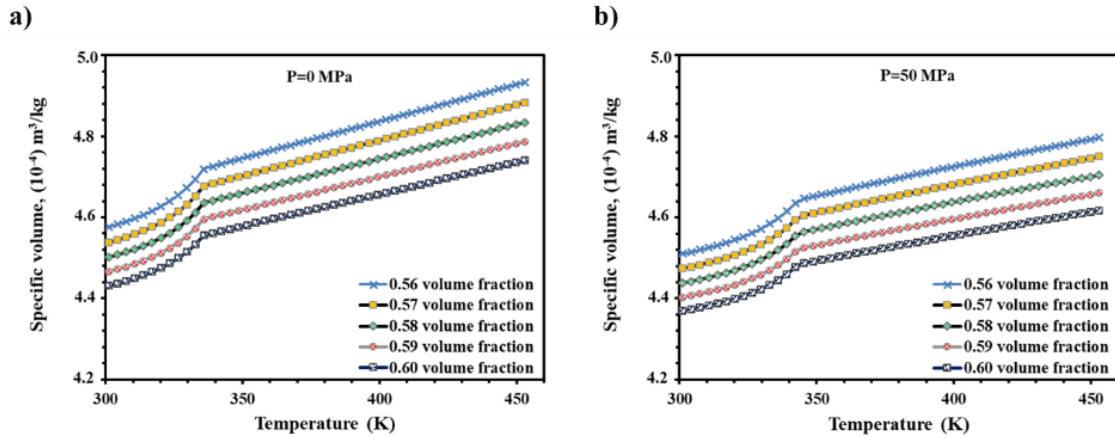


Figure A.6. Estimated specific volume of Ti-6Al-4V powder-binder feedstock at different filler volume fractions for (a) 0 MPa and (b) 50 MPa

Table A.8. Specific volume of Ti-6Al-4V powder-binder feedstock as a function of filler volume fraction, temperature, and pressure

Volume fraction of filler, Φ_f	Pressure (MPa)							
	0				50			
	Temperature (K)				Temperature (K)			
	300	350	400	450	300	350	400	450
	Specific volume ($10^{-4} \text{m}^3/\text{kg}$)							
0.56	4.60	4.75	4.84	4.9	4.50	4.66	4.72	4.79
0.57	4.55	4.71	4.79	4.87	4.47	4.61	4.68	4.75
0.58	4.50	4.66	4.74	4.83	4.043	4.57	4.64	4.70
0.59	4.45	4.62	4.70	4.78	4.40	4.53	4.60	4.66
0.60	4.40	4.58	4.66	4.74	4.37	4.5	4.55	4.61

A two-domain Tait [50] model (**Equation 13**) can be utilized for generating specific volume data as a function of temperature and pressure pertaining to the MF³ processing conditions:

$$v(T, p) = v_o(T) \left[1 - C \ln \left(1 + \frac{p}{B(T)} \right) + v_t(T, p) \right] \quad (13)$$

where, $v(T, p)$ is the specific volume at a given temperature and pressure, $v_o(T)$ is the specific volume at zero gauge pressure, T is the temperature in K, p is pressure in Pa, and C is a constant assumed to be 0.0894 for two-domain Tait model. The parameter $B(T)$, accounts for the pressure sensitivity of the material and is separately defined for the solid and melt regions. For the upper bound [50] when $T > T_t$ (volumetric transition temperature), B is given by **Equation 14, 15, 16**, respectively:

$$v_o = b_{1m} + b_{2m}(T - b_5) \quad (14)$$

$$B(T) = b_{3m} e^{[-b_{4m}(T - b_5)]} \quad (15)$$

$$v_t(T, p) = 0 \quad (16)$$

where, b_{1m} , b_{2m} , b_{3m} , b_{4m} , and b_5 are curve-fitted coefficients. For the lower bound [50], when $T < T_t$, the parameter, B , is given by **Equation 17, 18, 19**, respectively:

$$v_o = b_{1s} + b_{2s}(T - b_5) \quad (17)$$

$$B(T) = b_{3s} e^{[-b_{4s}(T - b_5)]} \quad (18)$$

$$v_t(T, p) = b_7 e^{[b_8(T-b_5)-(b_9p)]} \quad (19)$$

where, b_{1s} , b_{2s} , b_{3s} , b_{4s} , b_5 , b_7 , b_8 , and b_9 are curve-fitted coefficients. The dependence of the volumetric transition temperature, T_t on pressure can be given by **Equation 20**:

$$T_t(p) = b_5 + b_6(p) \quad (20)$$

Representative extracted dual-domain Tait constants for 60 vol.% solids loading Ti-6Al-4V feedstock are provided in supplementary **Table A.9**.

Table A.9. Dual-domain Tait constants for Ti-6Al-4V powder-binder feedstock at 0 and 0.59 volume fractions

Dual-domain Tait constants	volume fraction, ϕ_f	
	0	0.59
b_5 , K	336.15	321
b_6 , K/Pa	1.47E-07	1.14E-06
b_{1m} , m ³ /kg	0.001255	4.53E-04
b_{2m} , m ³ /kg·K	1.34E-06	1.26E-07
b_{3m} , Pa	1.26E+08	7.21E+08
b_{4m} , K ⁻¹	0.005867	1.99E-03
b_{1s} , m ³ /kg	0.00117	4.45E-04
b_{2s} , m ³ /kg·K	8.57E-07	1.46E-07
b_{3s} , Pa	2.40E+08	6.57E+08
b_{4s} , K ⁻¹	0.004155	3.94E-06
b_7 , m ³ /kg	8.46E-05	3.23E-05
b_8 , K ⁻¹	0.06688	9.12E-02
b_9 , Pa ⁻¹	1.39E-08	2.05E-08

A.5. SIMULATION CASE STUDY RESULTS

In the current study, Digimat-AM was utilized as the simulation tool which takes material thermophysical properties as the input parameters. Here the estimated values of Young's modulus, specific volume, thermal conductivity, specific heat capacity and coefficient of thermal expansion for 59 vol.% Ti-6Al-4V + binder feedstock system was used as input parameters to predict output as warpage/dimensional changes. A comparison was drawn with Acrylonitrile butadiene styrene (ABS), a common polymer for FFF printing with a readily available database for material properties in Digimat-AM.

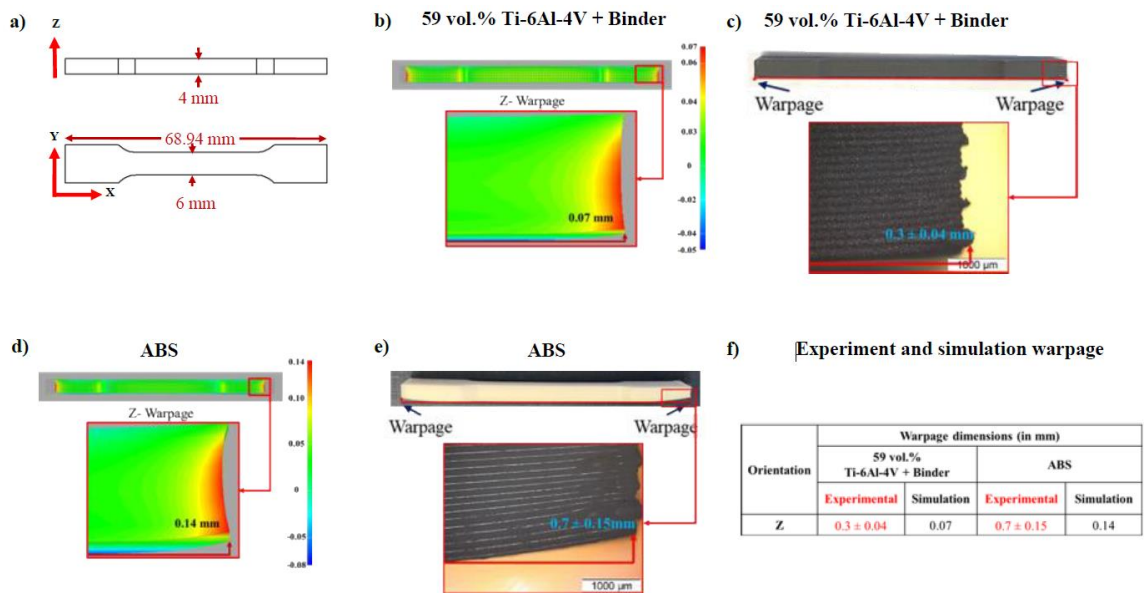


Figure A.7. Experimental and simulation result verifications using estimated values: (a) CAD file for ASTM E8 tensile sample with dimensions, (b) Simulation of the part using the estimated material properties for 59 vol.% Ti-6Al-4V + binder feedstock (c) Printed green parts with 0.59 vol.% of Ti-6Al-4V + binder feedstock, (d) Simulation of the ABS part using the available material database in Digimat-AM, (e) Printed part with ABS

material filament, (f) Warpage analysis resulting from experiments and simulation for 59 vol.% Ti-6Al-4V+ binder feedstock and ABS

Figure A.7a shows the CAD file with dimensions for an ASTM E8 tensile sample. The part dimensions of this geometry obtained from simulations and MF³ experiments were in excellent agreement (data provided in **Figure A.8**). Warpage analysis of simulated and fabricated samples of 59 vol.% Ti-6Al-4V MF³ samples are shown in **Figures A.7b** and **c**, respectively. Simulation results predicted the maximum warpage to be located at the edge of the tensile bar and the magnitude of the warpage at this location along the Z direction to be 0.07 mm. In close agreement to simulations, the MF³ experiments with the green parts verified that the location of the maximum warpage was identical. However, the magnitude of the warpage at this location in the Z direction was slightly higher at 0.3 ± 0.04 mm. In order to further, assess the differences between MF³ and FFF results, simulations and experiments were also conducted on a standard ABS polymer for the same tensile bar specimen and are represented in **Figures A.7d** and **e**. For ABS parts from simulations, the location of the maximum warpage was identical to the MF³ simulation result. However, the magnitude of the warpage at this location in the Z direction was comparatively higher at 0.14 mm. In FFF experiments with ABS, the location of maximum warpage correlated with the ABS simulation. However, the magnitude measured in the Z direction was also slightly higher 0.7 ± 0.15 mm. The warpage results obtained from simulations as well as experiments are summarized in **Figure A.7f**. These results indicate that the location of the maximum warpage is accurately predicted for both material systems. However, the magnitude of warpage is under-estimated by the Digimat-AM simulation platform for both

the systems and needs further analysis and refinement in the future. Typically, uneven heat distribution creates internal stresses within a part, resulting in warpage [43, 124]. Several material properties are known to contribute to the overall warpage. However, the CTE value of 59 vol. % Ti-6Al-4V powder-binder system ($2.8 \times 10^{-5} \text{ K}^{-1}$) is lower than that for ABS ($9 \times 10^{-5} \text{ K}^{-1}$) and is concluded to be the major reason for the differences in the extent of warpage in the two material systems.

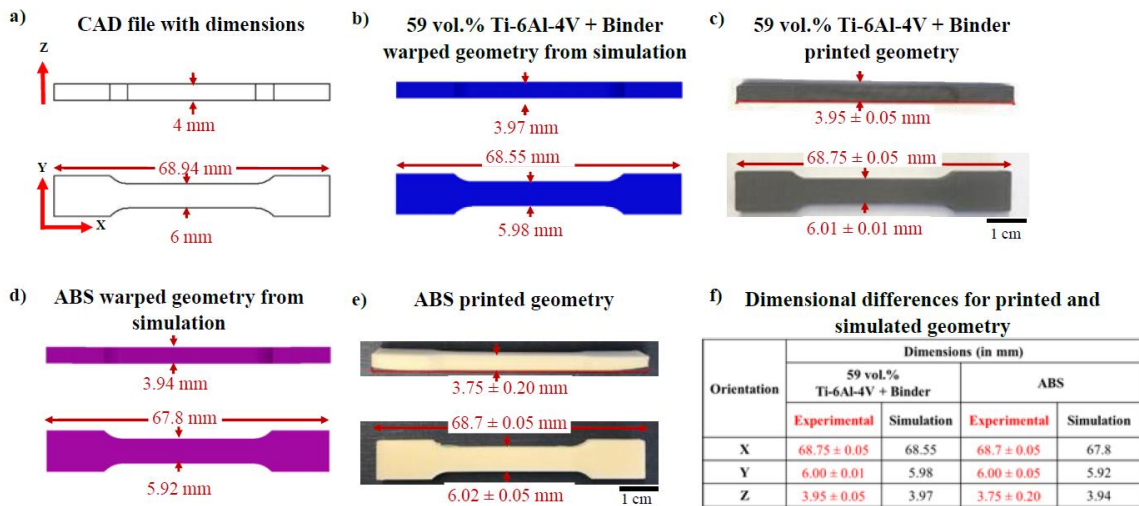


Figure A.8. Dimensions for an ASTM E8 tensile sample obtained from simulations and experiments for 59 vol. % solids loading Ti-6Al-4V feedstock and ABS

The above results suggest the potential for using the material property estimation protocol for analyzing complex geometries using other output parameters of the MF³ process including warpage, residual stresses, porosity, and distortion. Preliminary results to demonstrate the geometry capability of the process simulation are shown in **Figure A.9**. These studies are currently underway in our group and will be reported in the future. **Table**

A.10 provides material properties for other most commonly used metals that can be used to estimate input material properties for other MF³ systems based on the protocols presented in the present study. These studies are also currently underway in our group and will be reported in future publications.

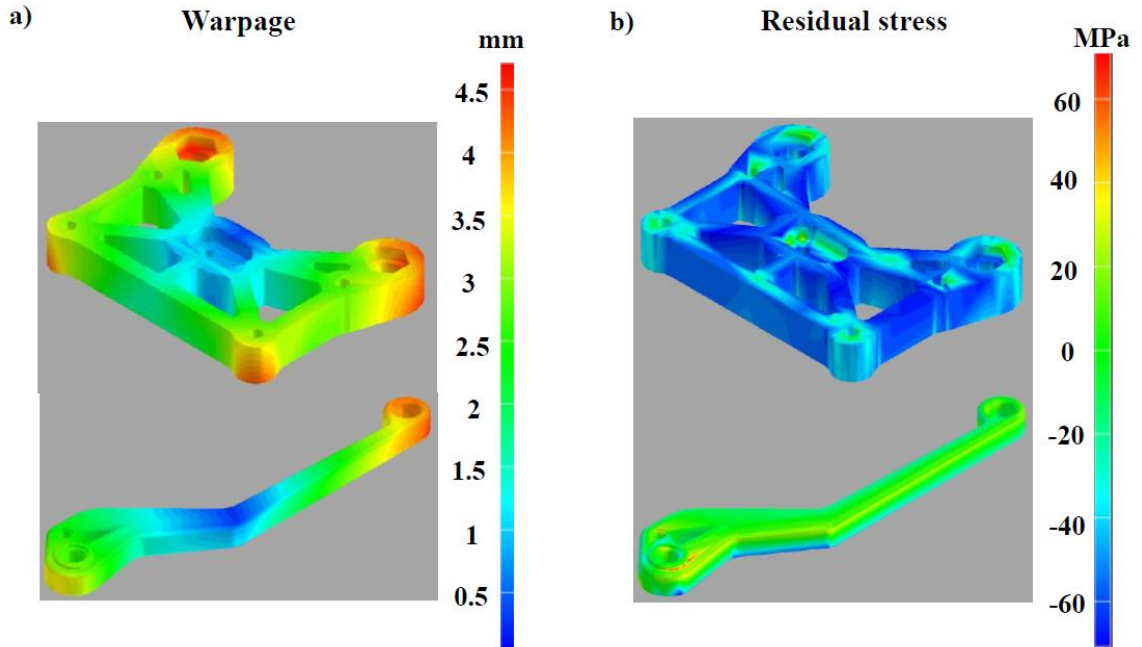


Figure A.9. Examples for Digimat-AM simulations that show typical outputs such as (a) warpage, and (b) residual stress in case studies for parts an end-of-arm tool (top) and automotive brake lever (bottom)

Table A.10. Thermo-physical properties for major commercially used metals [33]

Material	Density kg/m³	Specific heat J/kg.K	Thermal conductivity W/m.K	Coefficient of thermal expansion 10⁻⁶/K⁻¹	Elastic modulus GPa
Aluminum	2700	900	180	23	70
Copper	8750	<u>385</u>	360	13	130
W-10Cu	17000	160	209	6	340
Co-28Cr-4W-3Ni	8800	--	14.7	12.8	235
Inconel 718	8230	--	11.4	12.8	200
17-4PH stainless steel	7810	460	14	10.8	190
316L stainless steel	8010	500	15.9	17	190
420 stainless steel	7860	460	24.9	12.2	190

A.6. CONCLUSIONS

Based on the estimated metal-polymer mixture properties and their use in process simulations, the following conclusions can be drawn:

- The variation of material properties related to dimensional changes as a function of filler attributes and filler volume fraction can be estimated for Ti-6Al-4V powder-polymer mixtures.
- The properties estimated using various models enable the evaluation of component-level attributes fabricated by MF³ using DfMF³ platforms. The component-level attribute included here is warpage/shrinkage. A future extension can be done to relate the existing residual stresses in the part and its effect on part distortion.

- The overall approach enables the understanding of the dependence of MF³ processing of complex Ti-6Al-4V components on the material composition and printing parameters.
- The experimental protocols for verifying the estimated material properties presented in this work can help in further refining the estimation models and analyzing their influence on successfully predicting MF³ outcomes.
- It is expected that the overall approach will help reduce significant trial-and-error in designing new materials that can be used to fabricate complex geometries using MF³.

REFERENCES

1. J. Gonzalez-Gutierrez, S. Cano, S. Schuschnigg, C. Kukla, J. Sapkota, C. Holzer, Additive manufacturing of metallic and ceramic components by the material extrusion of highly-filled polymers: a review and future perspectives, *Materials* 11(5) (2018) 840.
2. R.M. German, Injection molding of metals and ceramics, *Metal powder industries federation* 3 (1997).
3. S. Rangarajan, G. Qi, N. Venkataraman, A. Safari, S.C. Danforth, Powder processing, rheology, and mechanical properties of feedstock for fused deposition of Si₃N₄ ceramics, *Journal of the American Ceramic Society* 83(7) (2000) 1663-1669.
4. G. Wu, N.A. Langrana, R. Sadanji, S. Danforth, Solid freeform fabrication of metal components using fused deposition of metals, *Materials & Design* 23(1) (2002) 97-105.
5. W. Lengauer, I. Duretek, M. Fürst, V. Schwarz, J. Gonzalez-Gutierrez, S. Schuschnigg, C. Kukla, M. Kitzmantel, E. Neubauer, C. Lieberwirth, Fabrication and properties of

- extrusion-based 3D-printed hardmetal and cermet components, *International Journal of Refractory Metals and Hard Materials* 82 (2019) 141-149.
6. S. Masood, W. Song, Development of new metal/polymer materials for rapid tooling using fused deposition modelling, *Materials & design* 25(7) (2004) 587-594.
 7. M. Nikzad, S. Masood, I. Sbarski, Thermo-mechanical properties of a highly filled polymeric composites for fused deposition modeling, *Materials & Design* 32(6) (2011) 3448-3456.
 8. D.A. Anderegg, H.A. Bryant, D.C. Ruffin, S.M. Skrip Jr, J.J. Fallon, E.L. Gilmer, M.J. Bortner, In-situ monitoring of polymer flow temperature and pressure in extrusion based additive manufacturing, *Additive Manufacturing* 26 (2019) 76-83.
 9. M.K. Agarwala, V.R. Jamalabad, N.A. Langrana, A. Safari, P.J. Whalen, S.C. Danforth, Structural quality of parts processed by fused deposition, *Rapid Prototyping Journal* 2(4) (1996) 4-19.
 10. A. Bose, C.A. Schuh, J.C. Tobia, N. Tuncer, N.M. Mykulowycz, A. Preston, A.C. Barbati, B. Kernan, M.A. Gibson, D. Krause, Traditional and additive manufacturing of a new tungsten heavy alloy alternative, *International Journal of Refractory Metals and Hard Materials* 73 (2018) 22-28.
 11. J. Gonzalez-Gutierrez, F. Arbeiter, T. Schlauf, C. Kukla, C. Holzer, Tensile properties of sintered 17-4PH stainless steel fabricated by material extrusion additive manufacturing, *Materials Letters* 248 (2019) 165-168.

12. B. Barmore, Fused Filament Fabrication of Filled Polymers for Metal Additive Manufacturing, (2016).
13. L. Ren, X. Zhou, Z. Song, C. Zhao, Q. Liu, J. Xue, X. Li, Process parameter optimization of extrusion-based 3D metal printing utilizing PW-LDPE-SA binder system, *Materials* 10(3) (2017) 305.
14. e-xstream, Digimat-FE. <https://www.e-xstream.com/products/tools/digimat-fe>. (Accessed July 30, 2019).
15. Alphastar, Genoa. <http://www.alphastarcorp.com/products/genoa-3dp-simulation/>. (Accessed July 30, 2019).
16. Vanderplaats, Genesis. <http://www.vrand.com/products/genesis/>. (Accessed July 30, 2019).
17. L.E. Nielsen, Predicting the properties of mixtures, M. Dekker1978.
18. S. McGee, R. McGullough, Combining rules for predicting the thermoelastic properties of particulate filled polymers, polymers, polyblends, and foams, *Polymer Composites* 2(4) (1981) 149-161.
19. W. Wu, K. Sadeghipour, K. Boberick, G. Baran, Predictive modeling of elastic properties of particulate-reinforced composites, *Materials Science and Engineering: A* 332(1-2) (2002) 362-370.
20. T.J. Wooster, S. Abrol, J.M. Hey, D.R. MacFarlane, Thermal, mechanical, and conductivity properties of cyanate ester composites, *Composites Part A: Applied science and manufacturing* 35(1) (2004) 75-82.

21. I. Balać, M. Milovančević, C.-y. Tang, P.S. Uskoković, D.P. Uskoković, Estimation of elastic properties of a particulate polymer composite using a face-centered cubic FE model, *Materials letters* 58(19) (2004) 2437-2441.
22. Y.P. Mamunya, V. Davydenko, P. Pissis, E. Lebedev, Electrical and thermal conductivity of polymers filled with metal powders, *European polymer journal* 38(9) (2002) 1887-1897.
23. L. Kowalski, J. Duszczyk, L. Katgerman, Thermal conductivity of metal powder-polymer feedstock for powder injection moulding, *Journal of materials science* 34(1) (1999) 1-5.
24. A. Boudenne, L. Ibos, M. Fois, E. Gehin, J.C. Majeste, Thermophysical properties of polypropylene/aluminum composites, *Journal of Polymer Science Part B: Polymer Physics* 42(4) (2004) 722-732.
25. T. Zhang, J. Evans, K. Dutta, Thermal properties of ceramic injection moulding suspensions in the liquid and solid states, *Journal of the European Ceramic Society* 5(5) (1989) 303-309.
26. K.H. Kate, R.K. Enneti, S.-J. Park, R.M. German, S.V. Atre, Predicting powder-polymer mixture properties for PIM design, *Critical Reviews in Solid State and Materials Sciences* 39(3) (2014) 197-214.
27. K.H. Kate, R.K. Enneti, V.P. Onbattuvelli, S.V. Atre, Feedstock properties and injection molding simulations of bimodal mixtures of nanoscale and microscale aluminum nitride, *Ceramics International* 39(6) (2013) 6887-6897.

28. K.H. Kate, V.P. Onbattuvelli, R.K. Enneti, S.W. Lee, S.-J. Park, S.V. Atre, Measurements of powder–polymer mixture properties and their use in powder injection molding simulations for aluminum nitride, *JOM* 64(9) (2012) 1048-1058.
29. N.M. Nor, N. Muhamad, M. Ibrahim, M. Ruzi, K. Jamaludin, Optimization of injection molding parameter of Ti-6Al-4V powder mix with palm stearin and polyethylene for the highest green strength by using Taguchi method, *International Journal of Mechanical and Materials Engineering* 6(1) (2011) 126-132.
30. G. Shibo, Q. Xuanhui, H. Xinbo, Z. Ting, D. Bohua, Powder injection molding of Ti–6Al–4V alloy, *Journal of Materials Processing Technology* 173(3) (2006) 310-314.
31. G. Obasi, O. Ferri, T. Ebel, R. Bormann, Influence of processing parameters on mechanical properties of Ti–6Al–4V alloy fabricated by MIM, *Materials Science and Engineering: A* 527(16-17) (2010) 3929-3935.
32. E. Ergül, H. Özkan Gülsoy, V. Günay, Effect of sintering parameters on mechanical properties of injection moulded Ti–6Al–4V alloys, *Powder Metallurgy* 52(1) (2009) 65-71.
33. H.Ö. Gülsoy, N. Gülsoy, R. Çalışıcı, Particle morphology influence on mechanical and biocompatibility properties of injection molded Ti alloy powder, *Bio-medical materials and engineering* 24(5) (2014) 1861-1873.
34. K.C. Mills, Recommended values of thermophysical properties for selected commercial alloys, Woodhead Publishing 2002.

35. G. Welsch, R. Boyer, E. Collings, Materials properties handbook: titanium alloys, ASM international 1993.
36. R. Enneti, V. Onbattuvelli, O. Gulsoy, K. Kate, S. Atre, Powder-binder formulation and compound manufacture in metal injection molding (MIM), Handbook of metal injection molding, Elsevier 2019, pp. 57-88.
37. G. Chen, C. Ren, X. Yang, X. Jin, T. Guo, Finite element simulation of high-speed machining of titanium alloy (Ti-6Al-4V) based on ductile failure model, The International Journal of Advanced Manufacturing Technology 56(9-12) (2011) 1027-1038.
38. C.J. Smithells, Metals reference book, Elsevier 2013.
39. V. Wagner, M. Baili, G. Dessein, D. Lallement, Experimental characterization of behavior laws for titanium alloys: application to Ti5553, Key Engineering Materials, Trans Tech Publ, 2010, pp. 147-155.
40. J. Elmer, T. Palmer, S. Babu, E. Specht, In situ observations of lattice expansion and transformation rates of α and β phases in Ti-6Al-4V, Materials Science and Engineering: A 391(1-2) (2005) 104-113.
41. R. Rai, J. Elmer, T. Palmer, T. DebRoy, Heat transfer and fluid flow during keyhole mode laser welding of tantalum, Ti-6Al-4V, 304L stainless steel and vanadium, Journal of physics D: Applied physics 40(18) (2007) 5753.
42. M. Niinomi, Mechanical properties of biomedical titanium alloys, Materials Science and Engineering: A 243(1-2) (1998) 231-236.

43. Y. Lee, G. Welsch, Young's modulus and damping of Ti-6Al-4V alloy as a function of heat treatment and oxygen concentration, *Materials Science and Engineering: A* 128(1) (1990) 77-89.
44. K.H. Kate, R.K. Enneti, T. McCabe, S.V. Atre, Simulations and injection molding experiments for aluminum nitride feedstock, *Ceramics International* 42(1) (2016) 194-203.
45. Y.-P. Wu, Q.-X. Jia, D.-S. Yu, L.-Q. Zhang, Modeling Young's modulus of rubber-clay nanocomposites using composite theories, *Polymer Testing* 23(8) (2004) 903-909.
46. C.L. Tucker III, E. Liang, Stiffness predictions for unidirectional short-fiber composites: review and evaluation, *Composites science and technology* 59(5) (1999) 655-671.
47. C. Wong, R.S. Bollampally, Thermal conductivity, elastic modulus, and coefficient of thermal expansion of polymer composites filled with ceramic particles for electronic packaging, *Journal of applied polymer science* 74(14) (1999) 3396-3403.
48. A. Metzner, Rheology of suspensions in polymeric liquids, *Journal of rheology* 29(6) (1985) 739-775.
49. R.M. German, Homogeneity effects on feedstock viscosity in powder injection molding, *Journal of the American Ceramic Society* 77(1) (1994) 283-285.
50. H. Chiang, C. Hieber, K. Wang, A unified simulation of the filling and postfilling stages in injection molding. Part I: Formulation, *Polymer Engineering & Science* 31(2) (1991) 116-124.

51. A.H. Peng, Research on the interlayer stress and warpage deformation in FDM, Advanced Materials Research, Trans Tech Publ, 2012, pp. 1564-1567.
52. B.N. Turner, S.A. Gold, A review of melt extrusion additive manufacturing processes: II. Materials, dimensional accuracy, and surface roughness, Rapid Prototyping Journal 21(3) (2015) 250-261.

APPENDIX B-I

SUPPLEMENTARY MATERIALS:

PROCESS SENSITIVITY AND SIGNIFICANT PARAMETERS INVESTIGATION IN METAL FUSED FILAMENT FABRICATION (MF³) OF TI-6AL-4V

This section consists of some valuable raw data that was generated during the MF³ sensitivity analyses (Chapter 3). A total of 78 simulation jobs were conducted in this study for three different part designs. The data includes simulation results used for sensitivity factor calculations of all the designs.

Table B-I.1. Design I - Simulation results used for sensitivity factor calculation

	Variables	Variations	Print time (s)	Max Deflection, All (mm)	Z-warpage (mm)	Residual Stress (MPa)	Min. substrate temp. (°C)
Component geometry parameters	Part wall thickness	1mm	3873	0.3113	0.3286	9.831	36.578
		1.5mm	7388	0.3164	0.3342	10.900	32.136
		2mm	7164	0.3156	0.3410	11.150	35.425
	Part Z-height	10mm	4196	0.2781	0.2657	7.738	44.413
		20mm	7388	0.3164	0.3342	10.900	32.136
		30mm	10580	0.3116	0.3419	11.640	28.541
Process parameters	Layer thickness	0.1mm	14381	0.3131	0.3321	10.730	28.543
		0.2mm	7388	0.3164	0.3342	10.900	32.136
		0.3mm	4996	0.3129	0.3283	10.730	35.043
	Layer width	0.36mm	7603	0.3084	0.3247	10.600	32.412
		0.48mm	7388	0.3164	0.3342	10.900	32.136
		0.60mm	3975	0.2907	0.3026	8.755	31.109
	Extrusion temperature	220°C	7388	0.2720	0.2857	9.360	31.660
		240°C	7388	0.3164	0.3342	10.900	32.136
		260°C	7388	0.3623	0.3840	12.480	32.596
	Build plate temperature	45°C	7388	0.3134	0.3328	10.970	30.031
		65°C	7388	0.3164	0.3342	10.900	32.136
		85°C	7388	0.3212	0.3388	10.940	34.228
	Printing speed	5mm/s	7388	0.3164	0.3342	10.900	32.136
		10mm/s	3696	0.3087	0.3214	10.530	38.726
		15mm/s	2465	0.3005	0.3083	10.140	44.911
Toolpath	0 – 90	7388	0.3164	0.3342	10.900	32.136	
	45 - 135	7324	0.3164	0.3340	10.890	32.263	
Feedstock material properties	Thermal conductivity	1.1728	7388	0.3174	0.3367	10.930	31.436
		1.466	7388	0.3164	0.3342	10.900	32.136
		1.7592	7388	0.3154	0.3317	10.860	32.952
	Coefficient of thermal expansion	2.26E-05	7388	0.2511	0.2658	8.653	32.128
		2.83E-05	7388	0.3164	0.3342	10.900	32.136
		3.40E-05	7388	0.3829	0.4034	13.170	32.144
	Specific heat capacity	7.16E+08	7388	0.3177	0.3364	10.960	30.725
		8.95E+08	7388	0.3164	0.3342	10.900	32.136
		1.07E+09	7388	0.3150	0.3318	10.830	33.514
	Young's modulus	164	7388	0.3164	0.3342	8.718	32.136
		205	7388	0.3164	0.3342	10.900	32.136
		246	7388	0.3164	0.3342	13.080	32.136
Specific volume	2.70E+08	7388	0.3147	0.3312	10.810	33.855	
	3.38E+08	7388	0.3164	0.3342	10.900	32.136	
	4.06E+08	7388	0.3175	0.3360	10.950	30.963	

Table B-I.2. Design II - Simulation results used for sensitivity factor calculation

	Variables	Variations	Print time (s)	Max Deflection, All (mm)	Z-warpage (mm)	Residual Stress (MPa)	Min. substrate temp. (°C)
Component geometry parameters	Part wall thickness	1mm	3896	0.2883	0.3434	6.761	35.711
		1.5mm	7498	0.2957	0.3517	7.467	31.178
		2mm	7263	0.2929	0.3538	7.760	34.730
	Part Z-height	10mm	4246	0.2534	0.2535	5.009	43.031
		20mm	7498	0.2957	0.3517	7.467	31.178
		30mm	10749	0.2973	0.3841	8.404	28.023
Process parameters	Layer thickness	0.1mm	15482	0.2969	0.3572	7.168	27.864
		0.2mm	7498	0.2957	0.3517	7.467	31.178
		0.3mm	5335	0.2480	0.2643	8.593	35.171
	Layer width	0.36mm	7681	0.2955	0.3508	7.087	31.643
		0.48mm	7498	0.2957	0.3517	7.467	31.178
		0.60mm	4006	0.2782	0.3267	7.414	30.994
	Extrusion temperature	220°C	7498	0.2257	0.3033	6.429	30.737
		240°C	7498	0.2957	0.3517	7.467	31.178
		260°C	7498	0.3366	0.3989	8.536	31.600
	Build plate temperature	45°C	7498	0.3088	0.3716	8.009	29.463
		65°C	7498	0.2957	0.3517	7.467	31.178
		85°C	7498	0.3044	0.3600	7.526	33.106
	Printing speed	5mm/s	7498	0.2957	0.3517	7.467	31.178
		10mm/s	3751	0.2892	0.3410	7.237	37.315
		15mm/s	2502	0.2820	0.3293	6.978	43.108
	Toolpath	0 - 90	7498	0.2957	0.3517	7.467	31.178
		45 - 135	7813	0.2961	0.3521	7.478	30.949
	Feedstock material properties	Thermal conductivity	1.1728	7498	0.2968	0.3538	7.487
1.466			7498	0.2957	0.3517	7.467	31.178
1.7592			7498	0.2947	0.3497	7.444	32.003
Coefficient of thermal expansion		2.26E-05	7498	0.2366	0.2823	5.940	31.172
		2.83E-05	7498	0.2957	0.3517	7.467	31.178
		3.40E-05	7498	0.3594	0.4210	9.009	31.184
Specific heat capacity		7.16E+08	7498	0.2968	0.3534	7.505	29.874
		8.95E+08	7498	0.2957	0.3517	7.467	31.178
		1.07E+09	7498	0.2946	0.3498	7.426	32.456
Young's modulus		164	7498	0.2957	0.3517	5.973	31.178
		205	7498	0.2957	0.3517	7.467	31.178
		246	7498	0.2957	0.3517	8.960	31.178
Specific volume		2.70E+08	7498	0.2943	0.3493	7.415	32.772
		3.38E+08	7498	0.2957	0.3517	7.467	31.178
		4.06E+08	7498	0.2966	0.3531	7.499	30.093

Table B-I.3. Design III - Simulation results used for sensitivity factor calculation

	Variables	Variations	Print time (s)	Max Deflection, All (mm)	Z-warpage (mm)	Residual Stress (MPa)	Min. substrate temp. (°C)
Component geometry parameters	Part wall thickness	1mm	3366	0.2461	0.2686	6.398	42.146
		1.5mm	6475	0.2591	0.3031	7.242	35.901
		2mm	6466	0.2627	0.3070	7.448	39.125
	Part Z-height	10mm	4246	0.2242	0.1950	5.088	47.847
		20mm	6475	0.2591	0.3031	7.242	35.901
Process parameters	Layer thickness	30mm	8704	0.2662	0.3196	8.361	32.130
		0.1mm	11564	0.2615	0.3098	7.375	31.691
		0.2mm	6475	0.2591	0.3031	7.242	35.901
	Layer width	0.3mm	4327	0.2562	0.2951	7.070	40.412
		0.36mm	6859	0.2584	0.3010	7.195	37.209
		0.48mm	6475	0.2591	0.3031	7.242	35.901
	Extrusion temperature	0.60mm	3707	0.2517	0.2827	6.788	47.147
		220°C	6475	0.2245	0.2615	6.231	35.205
		240°C	6475	0.2591	0.3031	7.242	35.901
	Build plate temperature	260°C	6475	0.2945	0.3455	8.279	36.563
		45°C	6475	0.2572	0.3006	7.277	33.500
		65°C	6475	0.2591	0.3031	7.242	35.901
	Printing speed	85°C	6475	0.2626	0.3097	7.277	38.291
		5mm/s	6475	0.2591	0.3031	7.242	35.901
		10mm/s	3239	0.2533	0.2866	6.880	45.005
Toolpath	15mm/s	2161	0.2481	0.2715	6.528	53.340	
	0 – 90	6475	0.2591	0.3031	7.242	35.901	
Feedstock material properties	Thermal conductivity	45 - 135	6629	0.2593	0.3037	7.254	35.556
		1.1728	6475	0.2596	0.3046	7.257	35.292
		1.466	6475	0.2591	0.3031	7.242	35.901
	Coefficient of thermal expansion	1.7592	6475	0.2587	0.3018	7.223	36.640
		2.26E-05	6475	0.2072	0.2430	5.761	35.882
		2.83E-05	6475	0.2591	0.3031	7.242	35.901
	Specific heat capacity	3.40E-05	6475	0.3110	0.3629	8.731	35.919
		7.16E+08	6475	0.2602	0.3062	7.305	33.948
		8.95E+08	6475	0.2591	0.3031	7.242	35.901
	Young's modulus	1.07E+09	6475	0.2580	0.2999	7.173	37.807
		164	6475	0.2591	0.3031	5.793	35.901
		205	6475	0.2591	0.3031	7.242	35.901
	Specific volume	246	6475	0.2591	0.3031	8.690	35.901
		2.70E+08	6475	0.2577	0.2991	7.156	38.277
		3.38E+08	6475	0.2591	0.3031	7.242	35.901
		4.06E+08	6475	0.2600	0.3057	7.295	34.277

APPENDIX B-II

SUPPLEMENTARY MATERIALS:

SUPPORTLESS PRINTING OF LATTICE STRUCTURES BY METAL FUSED FILAMENT FABRICATION (MF³) OF TI-6AL-4V: DESIGN AND ANALYSIS

Data from lattice structure fabrication experiments and characterization (Chapter 4).



Table B-II.1. Square cross-section unit cell green part characterization

Element thickness	Element length	CAD volume (mm ³)	Weight (g)		Green part relative density (%)	Shrinkage (Green part) (%)		
			CAD	Green part		Thickness	X/Y	Z
3mm	8mm	756	2.28312	2.0196	88.5	2.3	0.9	0.9
	7mm	648	1.95696	1.7845	91.2	2.0	0.7	-1.0
	6mm	540	1.6308	1.3473	87.4	5.0	0.9	0.1
2.5mm	8mm	537	1.62174	1.5517	95.7	4.4	0.1	0.1
	7mm	462	1.39524	1.2147	87.1	7.2	1.3	1.2
	6mm	387	1.16874	1.0061	86.1	4.8	1.6	0.2
2mm	8mm	352	1.06304	0.9751	91.7	5.0	0.0	-0.1
	7mm	304	0.91808	0.8222	89.6	7.0	0.9	0.2
	6mm	256	0.77312	0.6499	84.1	6.0	1.8	0.5

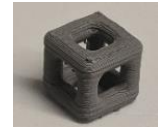


Table B-II.2. Circular cross-section unit cell green part characterization

Element thickness	Element length	CAD volume (mm ³)	Weight (g)		Green part relative density (%)	Shrinkage (Green part) (%)		
			CAD	Green part		Thickness	X/Y	Z
3mm	8mm	637	1.92374	1.7137	89.1	5.0	1.2	0.5
	7mm	552	1.66704	1.4496	87.0	6.3	1.8	-0.3
	6mm	431	1.30162	1.1235	87.5	5.7	1.7	0.6
2.5mm	8mm	447	1.34994	1.1654	86.3	8.4	2.0	0.3
	7mm	388	1.17176	1.0189	87.0	13.6	2.0	0.9
	6mm	329	0.99358	0.8942	90.0	7.6	2.1	0.0
2mm	8mm	289	0.87278	0.7285	83.5	19.5	2.0	-0.1
	7mm	252	0.76104	0.6966	91.5	17.0	1.4	0.2
	6mm	214	0.64628	0.5647	87.4	14.5	1.9	0.9

Table B-II.3. Square cross-section unit cell (3 mm thickness) sintered part characterization

Element thickness		3 mm		
Overhang		8 mm	7 mm	6 mm
Weight (g)	CAD volume (mm ³)	637	552	431
	CAD weight	1.92374	1.66704	1.30162
	Green part	1.7137	1.4496	1.1235
	Solvent debound	1.6401	1.3877	1.0743
	Sintered	1.482	1.2565	0.9738
Green part relative density (%)		89.1	87.0	86.3
Solvent debinding binder loss (%)		4.3	4.3	4.4
Thermal debinding-sintering binder loss (%)		9.2	9.1	8.9
Sintered part Archimedes density		4.17	4.13	4.13
Sintered part relative density		94.1	93.2	93.2
Dimension (CAD) (mm)	Thickness	3.00	3.00	3.00
	X/Y	11.00	10.00	9.00
	Z	11.00	10.00	9.00
Dimension (Green part) (mm)	Thickness	2.85	2.81	2.83
	X/Y	10.87	9.82	8.85
	Z	10.95	10.03	8.95
Shrinkage (Green part) (%)	Thickness	5.0	6.3	5.7
	X/Y	1.2	1.8	1.7
	Z	0.5	-0.3	0.6
Dimension (sintered part) (mm)	Thickness	2.5	2.36	2.33
	X/Y	9.25	8.29	7.38
	Z	9.35	8.46	7.58
Shrinkage (Sintered part) (%)	Thickness	16.7	21.3	22.3
	X/Y	15.9	17.1	18.0
	Z	15.0	15.4	15.8

Table B-II.4. Circular cross-section unit cell (3mm thickness) sintered part characterization

Element thickness		3 mm		
Overhang		8 mm	7 mm	6 mm
CAD volume (mm ³)		756	648	540
Weight (g)	CAD	2.28312	1.95696	1.6308
	Green part	2.0196	1.7845	1.3473
	Solvent debound	1.9301	1.7068	1.2858
	Sintered	1.7511	1.5495	1.1686
Green part relative density (%)		88.5	91.2	82.6
Solvent debinding binder loss (%)		4.4	4.4	4.6
Thermal debinding-sintering binder loss (%)		8.9	8.8	8.7
Sintered part Archimedes density		4.20	4.21	4.13
Sintered part relative density		94.8	95.1	93.1
Dimension (CAD) (mm)	Thickness	3.00	3.00	3.00
	X/Y	11.00	10.00	9.00
	Z	11.00	10.00	9.00
Dimension (Green part) (mm)	Thickness	2.93	2.94	2.85
	X/Y	10.90	9.93	8.92
	Z	10.90	10.10	8.99
Shrinkage (Green part) (%)	Thickness	2.3	2.0	5.0
	X/Y	0.9	0.7	0.9
	Z	0.9	-1.0	0.1
Dimension (sintered part) (mm)	Thickness	2.53	2.51	2.39
	X/Y	9.35	8.43	7.53
	Z	9.22	8.58	7.75
Shrinkage (Sintered part) (%)	Thickness	15.7	16.3	20.3
	X/Y	15.0	15.7	16.3
	Z	16.2	14.2	13.9

APPENDIX C-I

RESIDUAL STRESSES IN MF³ PRINTED PART: PREDICTIVE SIMULATION AND EXPERIMENTAL MEASUREMENT

1. INTRODUCTION

This section presents the work done towards verification of simulation results of residual stresses developed in MF³ printing. An experimental approach based on the ‘Crack Compliance’ method is used. It employs micro-strain measurement using strain gauge by incremental slotting of the specimen and using structural simulation using the ABAQUS tool. Estimation by Digimat-AM showed a correlation with experimental measurement.

1.1. RESEARCH OBJECTIVE

To investigate the residual stresses developed in MF³ printing using predictive simulations and experimental measurement for verification.

1.2. RESEARCH BACKGROUND

- Layer-by-layer fabrication in AM develops a thermal gradient resulting in residual stresses. Part quality and performance are affected by residual stresses.
- In particular, residual stresses developed in MF³ printing may affect the subsequent debinding and sintering processes in the form of part distortion or cracks.

- Part design and process parameters can be optimized to minimize the residual stresses if they can be estimated. Printing process simulation provides an estimation of residual stresses. However, verification of these results has been a challenge due to the difficulty associated with experimental measurement methods.
- Moreover, no publication has been found on such investigations in MF³.
- The previously investigated simulation tool (Digimat) provides an estimation of residual stresses in the MF³ printing process. To verify these estimations, an experimental measurement using the Crack Compliance method has been investigated in this study.
- The Crack Compliance method involves experimental measurement by strain gauge and FEA structural simulations.

1.3. METHODOLOGY

MF3 Process Simulation: Residual stresses estimation

Thermo-mechanical Process simulation (Digimat-AM)

Simulation setup: Geometry (STL), print parameters GCode, material properties, voxel meshing, FEA simulation

Crack Compliance Method: Experimental measurement

Experimental setup: Test specimen, strain gauges

Micro-strain measurement from incremental slotting

Legendre polynomial basis assumed for residual stress distribution

FEA Structural simulation (ABAQUS):

Simulation setup: FE meshing, varying pressure load, boundary conditions

Strain estimation for incremental slotting

Calculation of 'Compliance matrix [C]' and 'Unknown Amplitude vector [A]'

Estimation of stress distribution using measured micro-strain, unknown amplitude vector and Legendre polynomial basis

Figure C-I.1. Methodology followed for estimation of residual stresses through process simulation, and verification by experimental measurement

2. MF³ PROCESS SIMULATION

2.1. SIMULATION SETUP

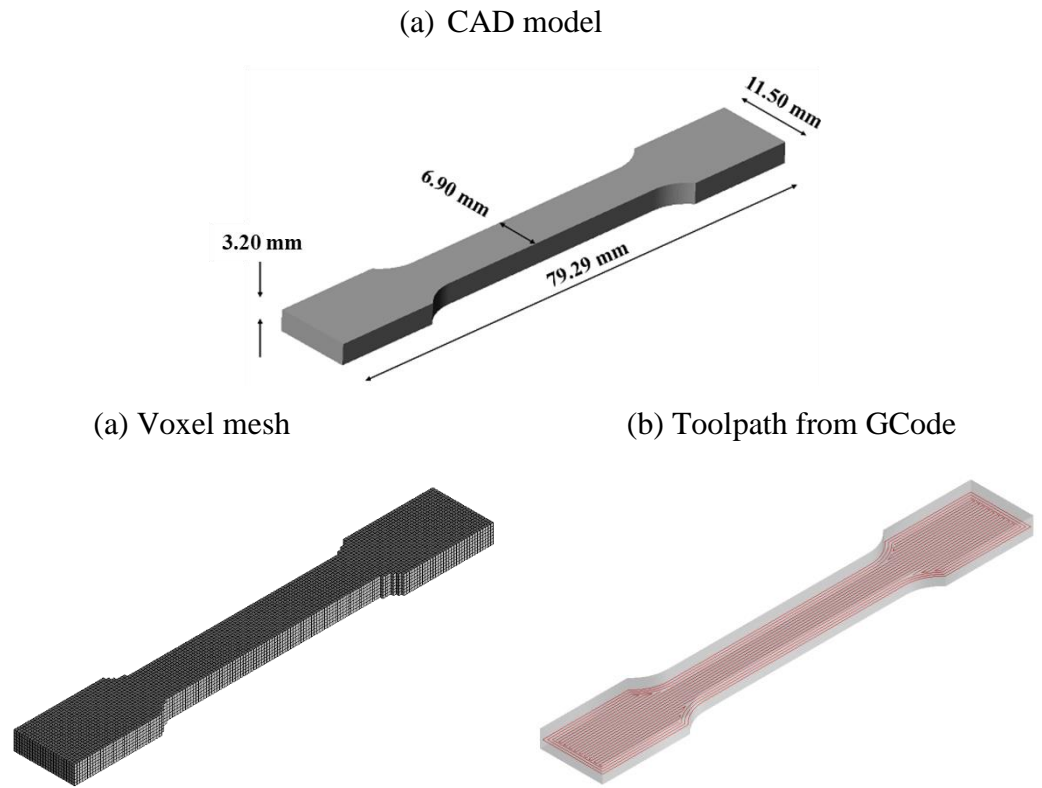


Figure C-I.2. (a) ASTM E8 tensile bar dimensions (a) meshed model with voxel element size 0.3mm (b) GCode data defines the 0-90° toolpath generated in slicing tool

Table C-I.1. Printing process parameters

Process parameters	Variations
Layer thickness (mm)	0.15
Layer width (mm)	0.48
Extrusion temperature (°C)	240
Build plate temperature (°C)	65
Build chamber temperature (°C)	20
Printing speed (mm/s)	5
Toolpath (°)	0 – 90

2.2. MATERIAL PROPERTIES: TI-6AL-4V

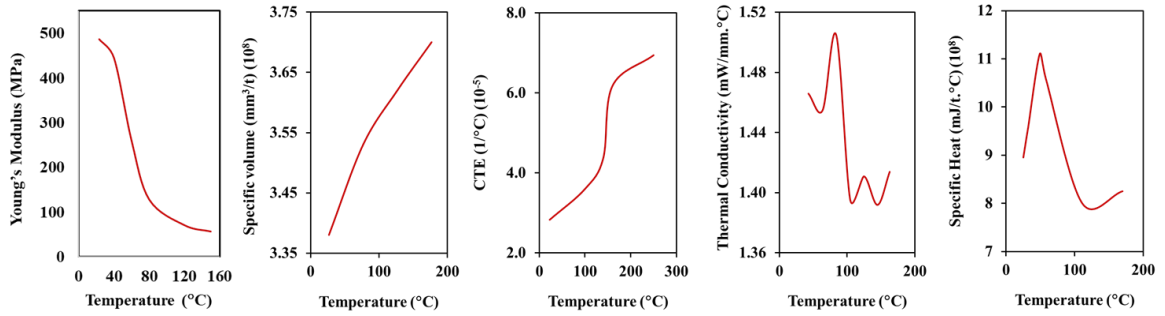


Figure C-I.3. Mechanical and thermal properties of Ti-6Al-4V feedstock over a range of temperatures used in printing process simulations

2.3. SIMULATION RESULTS: RESIDUAL STRESS

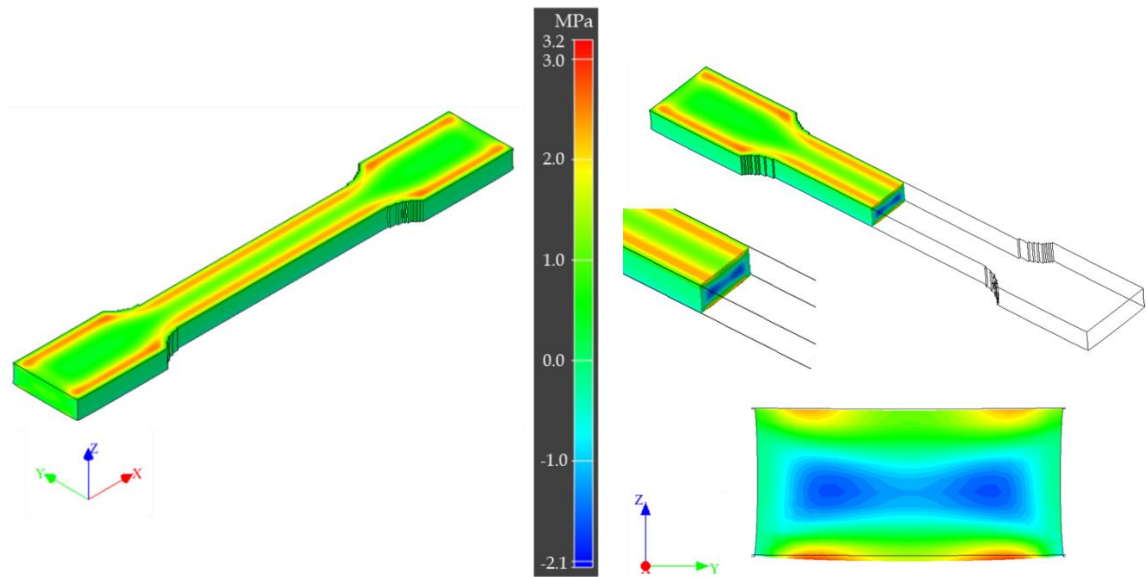


Figure C-I.4. Residual stresses (maximum principal stresses) estimation for Ti-6Al-4V feedstock part

3. CRACK COMPLIANCE METHOD

The general procedure for the slitting method is to gradually extend a slit into the specimen surface and measure near-slit strain as a function of slit depth.

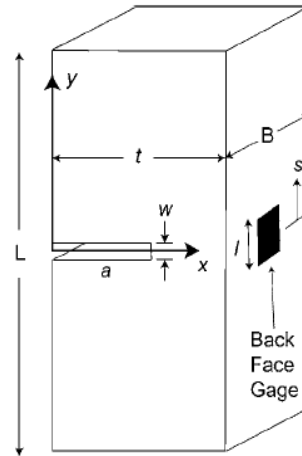


Figure C-I.5. Full block geometry model showing cut slot and strain gauge on the opposite side. *References:* - (Prime, M., *Appl Mech Rev*, vol. 52 no. 2, 1999)

Solving for the residual stress profile from measured strain data requires the solution of an elastic inverse problem. The inverse problem is solved by first representing the unknown residual stress profile in the Legendre polynomial basis, and then finding the coefficients of the basis from the measured strain data. The residual stress distribution is assumed to follow a Legendre polynomial basis;

$$\begin{aligned}P_0(x) &= 1 \\P_1(x) &= x \\P_2(x) &= \frac{1}{2}(3x^2 - 1) \\P_3(x) &= \frac{1}{2}(5x^3 - 3x) \\P_4(x) &= \frac{1}{8}(35x^4 - 30x^2 + 3) \\P_5(x) &= \frac{1}{8}(63x^5 - 70x^3 + 15x) \\P_6(x) &= \frac{1}{16}(231x^6 - 315x^4 + 105x^2 - 5)\end{aligned}$$

Taking 'X' as the coordinate along the depth direction, the unknown residual stress profile $\sigma_{RS}(X)$ is written as a sum of Legendre polynomial terms $P_j(X)$, each with a corresponding amplitude A_j ;

$$\sigma_{RS}(x) = \sum_{i=0}^m A_j P_j(x) \quad (1)$$

where m is the order of the highest term in the polynomial series.

A solution of the equations of elasticity is then developed to relate the stress given by a particular basis function (with unit amplitude) $P_j(X)$ to strain at a near-slit gage location.

If residual stress were given exactly by the basis function $P_j(x)$, the strain that would occur at cut depth a_i is provided by the elasticity solution. This strain is an element C_{ij} of a compliance matrix $[C]$ defined as

$$C_{ij} \equiv \varepsilon(a_i) |_{\sigma = P_j(x)} \quad (2)$$

Solving the elasticity problem for all basis functions and all cut depths, and invoking the principle of elastic superposition, results in a linear system relating basis function amplitudes to strain as a function of cut depth:

$$\varepsilon(a_i) = \sum_{j=0}^m C_{ij} A_j \quad (3)$$

using matrix notation:

$$\{\varepsilon\} = [C]\{A\} \quad (4)$$

Given this system, and strains measured experimentally during cutting, the amplitudes of the stress expansion are found by inversion of Eq. (4) in a least-squares sense:

$$\{A\} = ([C]^T[C])^{-1}[C]^T\{\varepsilon_{\text{meas}}\} \quad (5)$$

where $\{\varepsilon_{\text{meas}}\}$ is a vector of measured strain data. With the amplitude vector $\{A\}$ determined, the stress state existing before cutting is obtained from the equation

$$\sigma_{\text{RS}}(x) = \sum_{i=0}^m A_j P_j(x) \quad (6)$$

3.1. EXPERIMENTAL SETUP

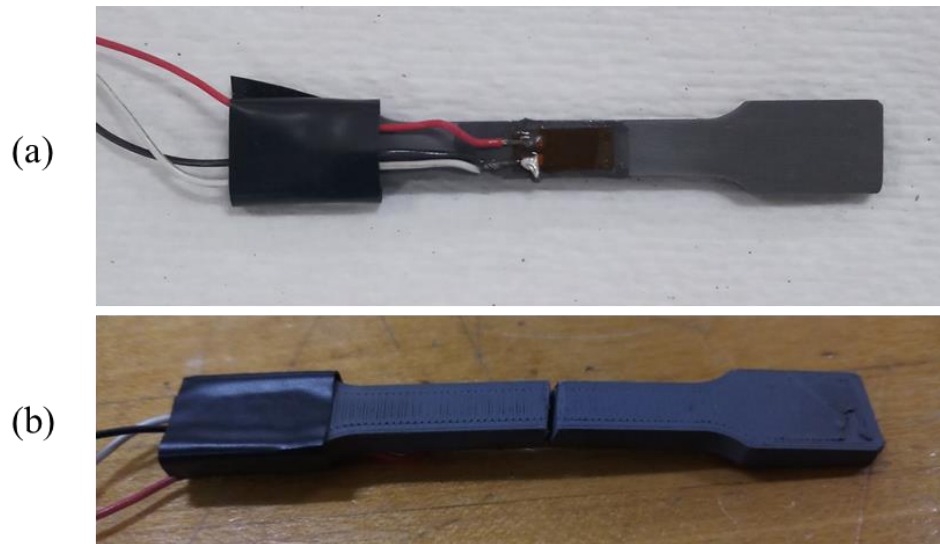


Figure C-I.6. Experimental setup: (a) strain gauges connected to test specimen (b) specimen broken after slotting

Note: The specimen got broken at a slot depth of 2.5mm, hence data up to 2.4mm depth was available and used in calculations.

Table C-I.2. Micro-strain measured experimentally with incremental slotting

Depth of cut (mm)	Micro-strain	Strain (ϵ_{exp})
0.1	215	0.000215
0.2	240	0.00024
0.3	84	0.000084
0.4	82	0.000082
0.5	203	0.000203
0.6	175	0.000175
0.7	260	0.00026
0.8	340	0.00034
0.9	368	0.000368
1	355	0.000355
1.1	380	0.00038
1.2	346	0.000346
1.3	352	0.000352
1.4	244	0.000244
1.5	215	0.000215
1.6	266	0.000266
1.7	346	0.000346
1.8	304	0.000304
1.9	360	0.00036
2	360	0.00036
2.1	223	0.000223
2.2	380	0.00038
2.3	186	0.000186
2.4	103	0.000103
2.5	-55	-0.000055
2.6	Part broken	
2.7	N/A	
2.8	N/A	
2.9	N/A	
3	N/A	
3.1	N/A	
3.2	N/A	

3.2. LEGENDRE POLYNOMIAL BASIS MATRIX [Pij]

Polynomials P2 to P5 were used in this study. P0 gives unity and P1 gives a constant value.

Table C-I.3. Legendre polynomial basis matrix [Pij]

Slot depth	$x = \text{Slot depth} / 3.2$	P2	P3	P4	P5
0.2	0.06	-0.49	-0.09	0.36	0.12
0.4	0.13	-0.48	-0.18	0.32	0.22
0.6	0.19	-0.45	-0.26	0.25	0.30
0.8	0.25	-0.41	-0.34	0.16	0.34
1.0	0.31	-0.35	-0.39	0.05	0.34
1.2	0.38	-0.29	-0.43	-0.07	0.30
1.4	0.44	-0.21	-0.45	-0.18	0.21
1.6	0.50	-0.13	-0.44	-0.29	0.09
1.8	0.56	-0.03	-0.40	-0.37	-0.06
2	0.63	0.09	-0.33	-0.42	-0.21
2.2	0.69	0.21	-0.22	-0.42	-0.34
2.4	0.75	0.34	-0.07	-0.35	-0.42

Simulation (in ABAQUS) was conducted for every 0.2mm cut depth increment instead of 0.1mm due to high computational requirements. Total $12 \times 4 = 48$ simulation jobs were conducted.

3.3. FEA Setup: ABAQUS

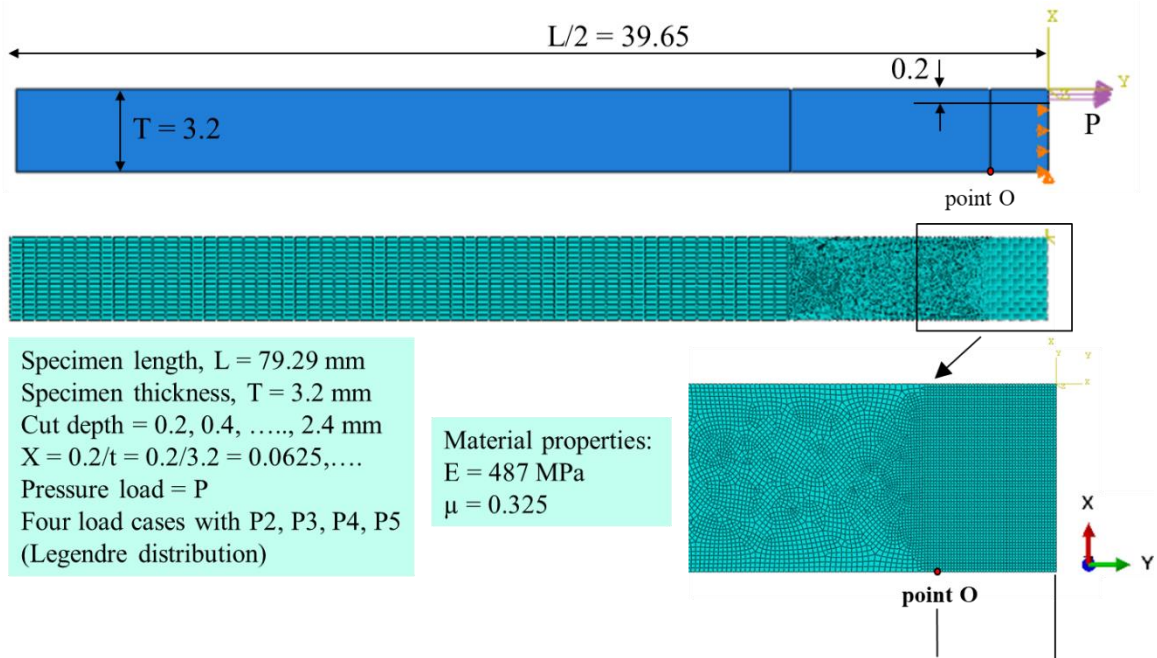


Figure C-I.7. FEA simulation setup: pressure load applied along Y-axis on 0.2mm slotted face, symmetry boundary condition applied at the cutting plane

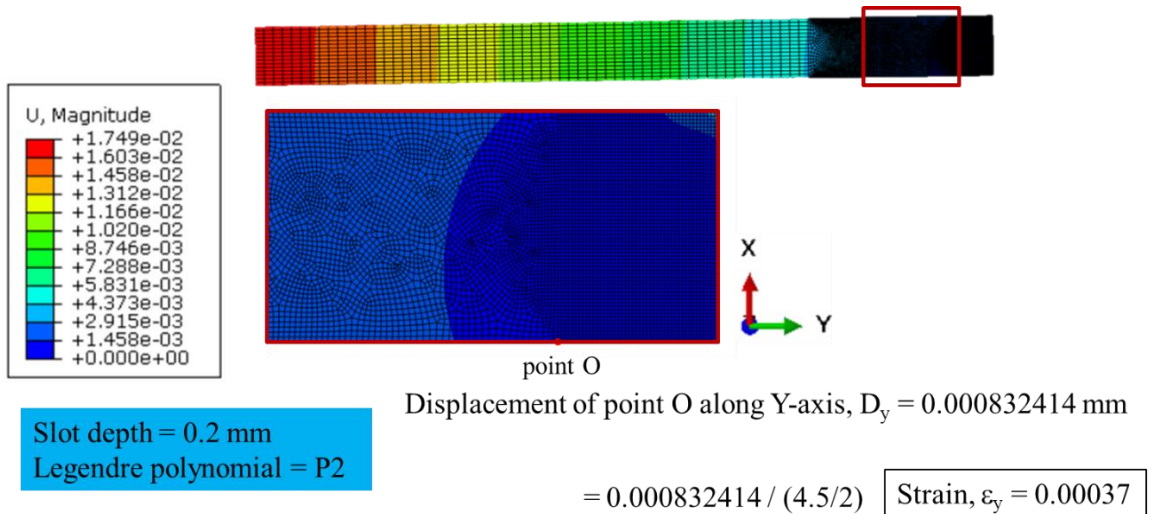


Figure. C-I.8. Displacement results from ABAQUS. Strain along Y-axis calculated at $Y=2.25$ mm (representing strain gauge length used in experimental measurement)

Similarly, ϵ_y is estimated for P3, P4, P5 pressure load and slot depth of 0.2 mm, hence four simulation jobs for 0.2 mm slot depth. Likewise, for 0.4, 0.6, ..., 2.4 mm, so a total of 48 simulation jobs conducted in ABAQUS, and respective strain value estimated.

3.4. COMPLIANCE MATRIX [Cij]

Table C-I.4. Strain value estimated from simulations (ABAQUS) represent the Compliance matrix [C] elements Cij

		Pj (Legendre polynomial basis)			
		P2	P3	P4	P5
a_i (normalized depth of cut)	$a_2 = 0.2/3.2$	4.1E-05	3.3E-06	3.3E-05	4.1E-06
	$a_4 = 0.4/3.2$	1.6E-04	2.5E-05	1.2E-04	3.1E-05
	$a_6 = 0.6/3.2$	3.7E-04	8.3E-05	2.7E-04	1.0E-04
	$a_8 = 0.8/3.2$	6.9E-04	2.0E-04	4.8E-04	2.4E-04
	$a_{10} = 1.0/3.2$	1.1E-03	4.2E-04	7.5E-04	4.7E-04
	$a_{12} = 1.2/3.2$	1.8E-03	7.8E-04	1.1E-03	8.4E-04
	$a_{14} = 1.4/3.2$	2.7E-03	1.4E-03	1.5E-03	1.4E-03
	$a_{16} = 1.6/3.2$	4.1E-03	2.3E-03	2.0E-03	2.2E-03
	$a_{18} = 1.8/3.2$	6.2E-03	3.9E-03	2.7E-03	3.4E-03
	$a_{20} = 2.0/3.2$	9.5E-03	6.6E-03	3.6E-03	5.2E-03
	$a_{22} = 2.2/3.2$	1.5E-02	1.1E-02	4.9E-03	8.1E-03
	$a_{24} = 2.4/3.2$	2.6E-02	2.1E-02	7.0E-03	1.3E-02

Stress Amplitude '{A}'

To find stress amplitude from equation 5,

$$\{A\} = ([C]^T[C])^{-1}[C]^T\{\epsilon_{meas}\}$$

where $\{\epsilon_{\text{meas}}\}$ is a vector of measured strain data. With the amplitude vector $\{A\}$ determined, the stress state existing before cutting is obtained from equation 6.

Calculate the following;

- Transpose of Compliance matrix, $[C]^T$
- Matrix multiplication, $[C]^T [C]$
- Inverse matrix, $[[C]^T [C]]^{-1}$
- Pseudo-inverse matrix, $[[[C]^T [C]]^{-1}] [C]^T$
- Stress amplitude

$$\{A\} = ([C]^T [C])^{-1} [C]^T \{\epsilon_{\text{meas}}\}$$

Pseudo-inverse matrix, $[[[C]^T [C]]^{-1}] [C]^T$												$\{\epsilon_{\text{measure}}\}$ Cumulative Strain (experimental)	
$\{A\} =$	40236	23589	-6814	-1586	16408	-16978	-3911	339	3087	2958	-1970	112	0.00024
	158848	47158	-90915	23494	-18690	21868	-1656	719	-1440	-2724	1384	48	0.00032
	-44823	-21052	11039	2734	-19284	19745	4333	-421	-3718	-3541	2408	-141	0.00050
	-228645	-85929	116975	-28033	6853	-10068	6225	-1128	-1105	584	116	-135	0.00084
													0.00119
													0.00154
													0.00178
													0.00205
													0.00235
													0.00271
													0.00309
													0.00320

$\{A\}$ Stress amplitude
0.718
0.781
3.575
-4.985

$\{A\} =$

Residual Stress ' σ_{RS} '

$$\sigma_{RS}(x) = \sum_{i=0}^m A_j P_j(x)$$

$\sigma_{RS}(x) =$

Slot depth	$x = \text{Slot depth}/3.2$	P2	P3	P4	P5
0.2	0.06	-0.49	-0.09	0.36	0.12
0.4	0.13	-0.48	-0.18	0.32	0.22
0.6	0.19	-0.45	-0.26	0.25	0.30
0.8	0.25	-0.41	-0.34	0.16	0.34
1	0.31	-0.35	-0.39	0.05	0.34
1.2	0.38	-0.29	-0.43	-0.07	0.30
1.4	0.44	-0.21	-0.45	-0.18	0.21
1.6	0.50	-0.13	-0.44	-0.29	0.09
1.8	0.56	-0.03	-0.40	-0.37	-0.06
2	0.63	0.09	-0.33	-0.42	-0.21
2.2	0.69	0.21	-0.22	-0.42	-0.34
2.4	0.75	0.34	-0.07	-0.35	-0.42

{A}
0.718
0.781
3.575
-4.985

$\sigma_{RS}(x) =$

Thickness	σ_{RS}
0.2	0.29
0.4	-0.43
0.6	-1.11
0.8	-1.68
1	-2.09
1.2	-2.28
1.4	-2.22
1.6	-1.91
1.8	-1.37
2	-0.64
2.2	0.20
2.4	1.02

3.5. STRESS DISTRIBUTION: EXPERIMENTAL MEASUREMENT

Table C-I.5. Residual stresses distribution: Experimental measurement

Thickness (mm)	Residual Stress (MPa)
0.2	0.29
0.4	-0.43
0.6	-1.11
0.8	-1.68
1	-2.09
1.2	-2.28
1.4	-2.22
1.6	-1.91
1.8	-1.37
2	-0.64
2.2	0.20
2.4	1.02

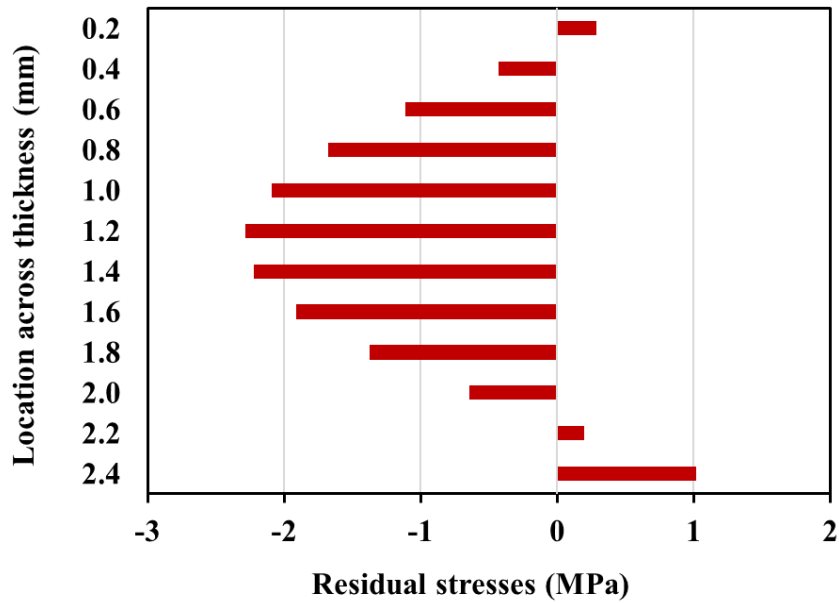


Figure C-I.9. Residual stresses distribution across thickness: Experimental measurement

3.6. STRESS DISTRIBUTION: SIMULATION ESTIMATION

Table C-I.6. Residual stresses distribution: Process simulation prediction

Thickness (mm)	Residual Stress (MPa)
0.3	1.37
0.6	0.69
0.9	-0.20
1.2	-0.86
1.5	-1.26
1.8	-1.39
2.1	-1.21
2.4	-0.68
2.7	0.24
3.0	1.15

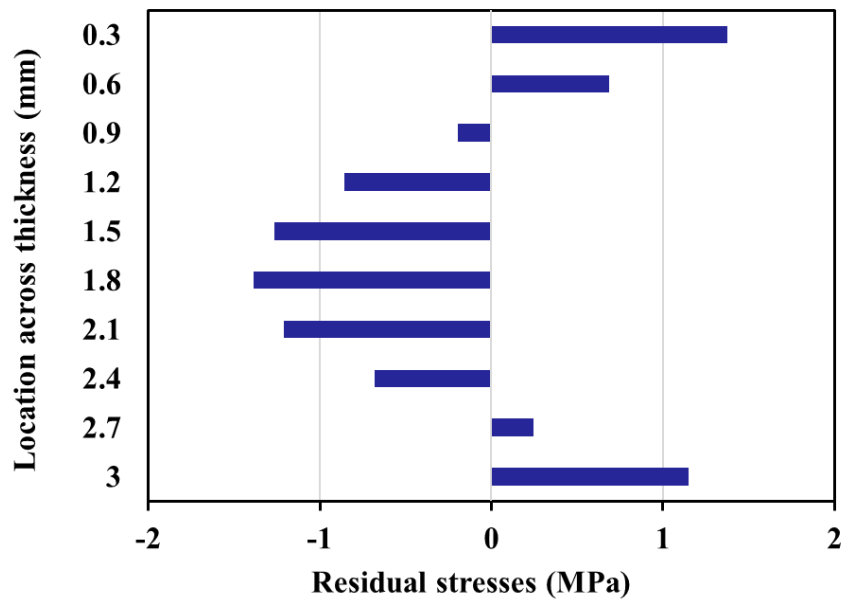


Figure C-I.10. Residual stresses distribution across thickness: Process simulation prediction

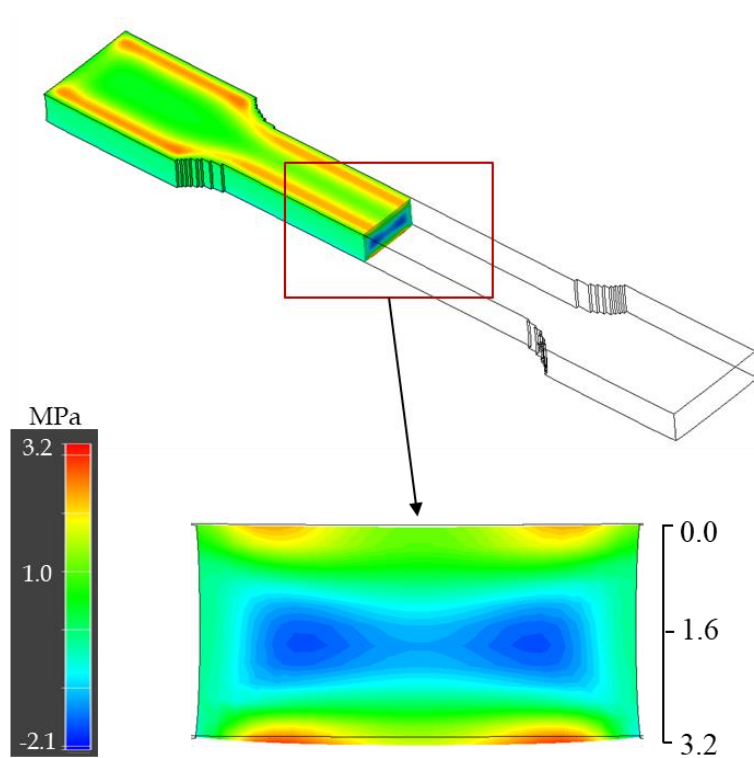


Figure C-I.11. Residual stresses distribution at cutting plane cross-section: Process simulation prediction

4. CONCLUSIONS

- The thermo-mechanical process simulation provided an estimation of residual stresses developed in MF³ printed parts.
- The crack compliance method was used for the first time for the experimental measurement of residual stresses in the green parts from MF³ of Ti-6Al-4V.
- The experimental measurement showed the residual stresses varying between 1.02 MPa (tension) and -2.28 MPa (compression). The simulation predicted residual stresses varying between 1.37 MPa (tension) and -1.39 MPa (compression).

- Simulation and experimental results showed a similar pattern of residual stress distribution at the slotted section.
- Both simulation and experiments showed tensile stresses in the outer surfaces and compressive stresses in the core.
- Simulation results have been verified by the experimental measurement with reasonable agreement. However, the accuracy of prediction needs to be further enhanced.

APPENDIX C-II

TEMPERATURE DISTRIBUTION AND THERMAL HISTORY IN MF³ PRINTING: PREDICTIVE SIMULATION AND EXPERIMENTAL MEASUREMENT

This section comprises some preliminary work on the real-time measurement of temperature distribution during MF³ printing. This facilitates the evaluation of thermal gradient and temperature history and enhanced understanding of their relationship with resulting part quality and performance. It will also enable verification of simulation results.

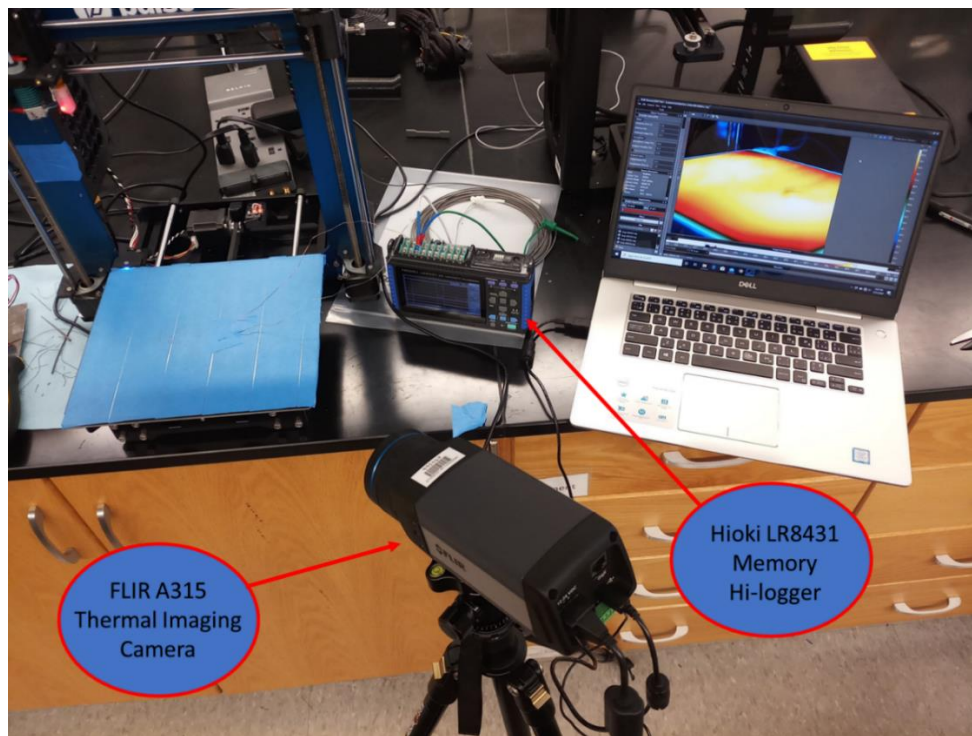
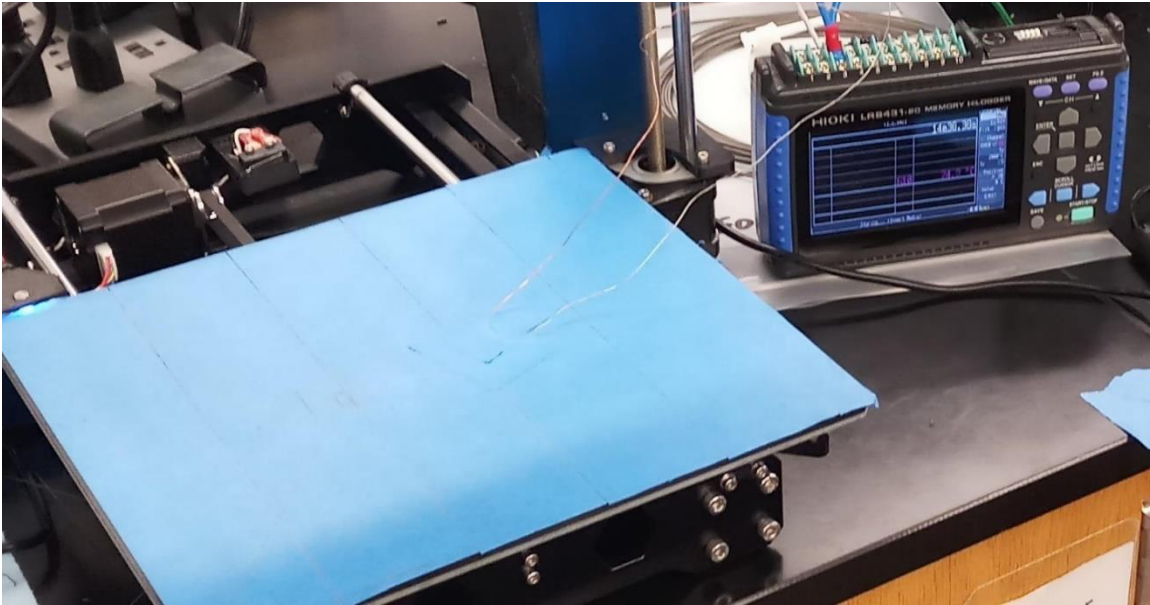


Figure C-II.1. Experimental setup for real-time measurement calibration of the thermal imaging camera using memory logger and FLIR ResearchIR Max software

(a)



(b)

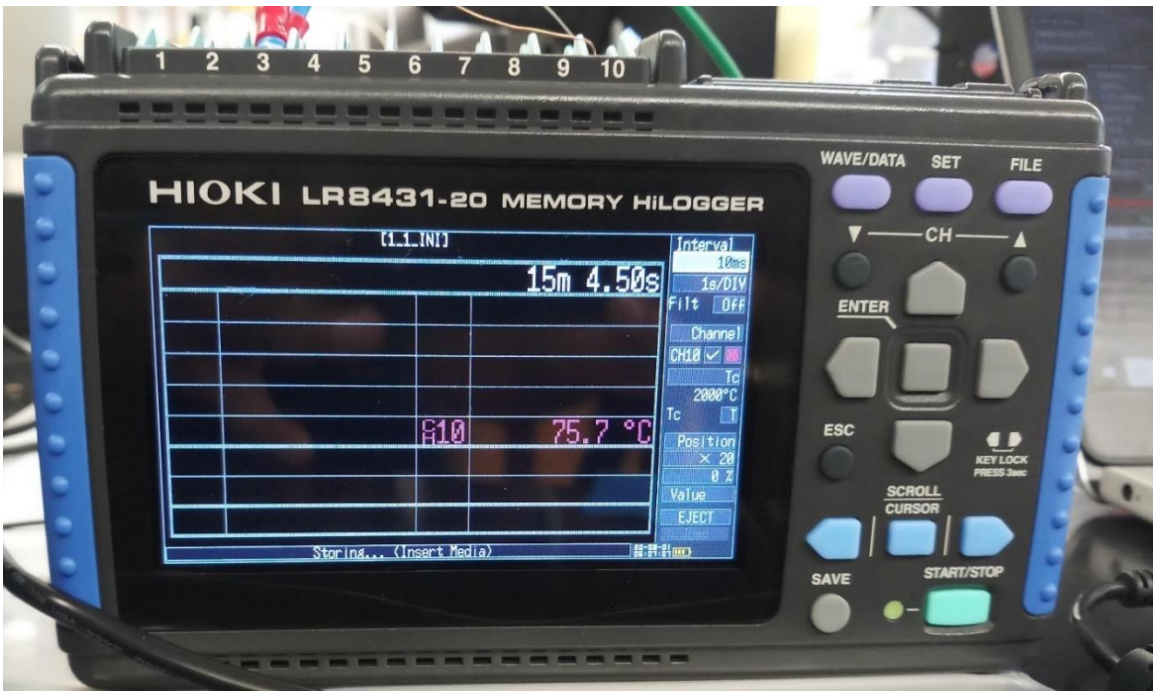


Figure C-II.2. (a) Thermocouple connected to the print bed reading temperature in the memory logger (b) Memory logger showing print bed temperature 75.7 °C

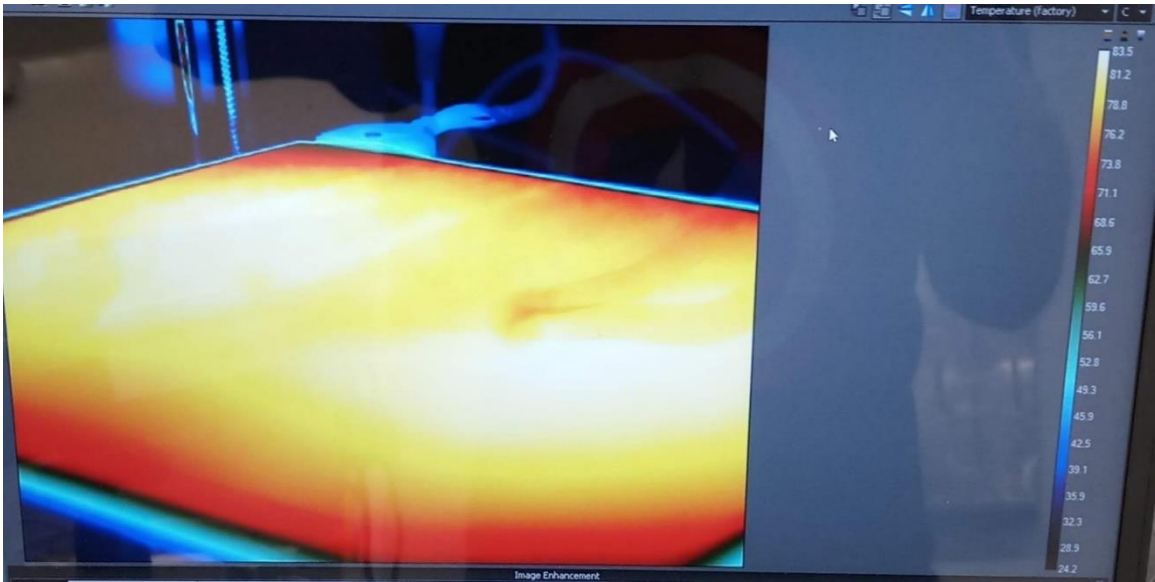
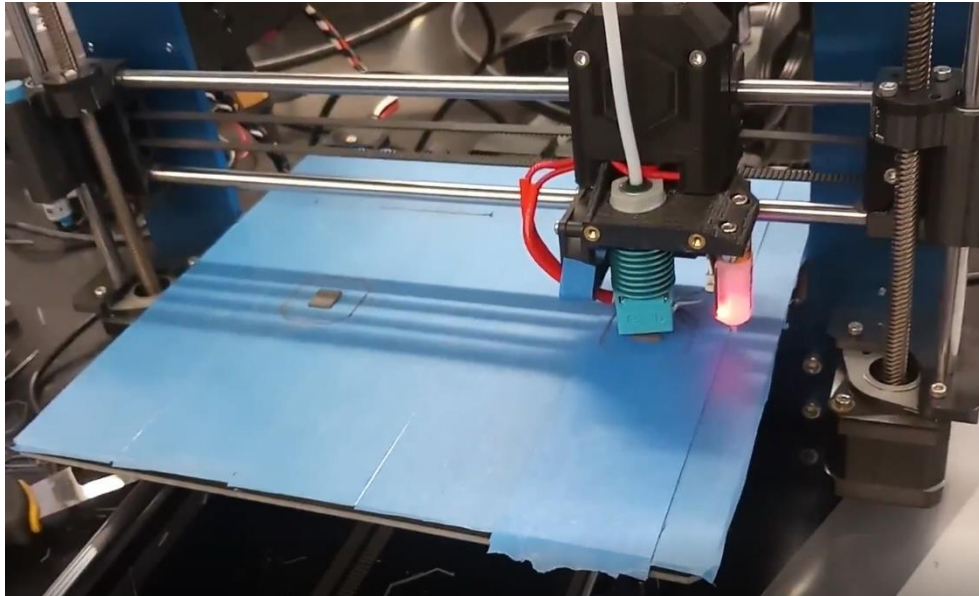


Figure C-II.3. FLIR software showing real-time measurement of print bed temperature distribution ranging between 24.2 °C and 83.5 °C



Figure C-II.4. Two square bars placed at a distance were chosen as test specimen to allow sufficient time for clear reading of the latest layer temperature and evaluate temperature drop between two layers

(a)



(b)

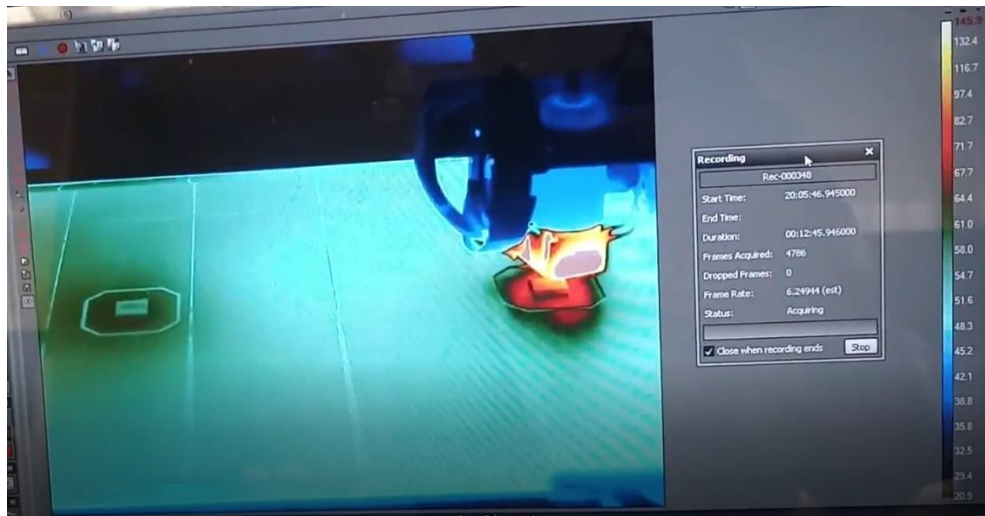


Figure C-II.5. (a) MF³ printing (b) FLIR software recording the real-time temperature measurement of the print bed, printed layers, nozzle and extruder, temperature distribution ranging between 20.9 °C and 145.9 °C

Future work will include estimation of temperature distribution and thermal history using simulation, and verification with experimental results.

APPENDIX C-III

POROSITY DISTRIBUTION IN MF³ PRINTING: PREDICTIVE SIMULATION

This section briefs about the initial progress towards having the capability to estimate porosity distribution in the MF³ printed green part, which will also provide an estimation of relative density distribution within the part. Apart from Digimat-AM, another simulation tool GENOA (AlphaStar) was investigated in this work.

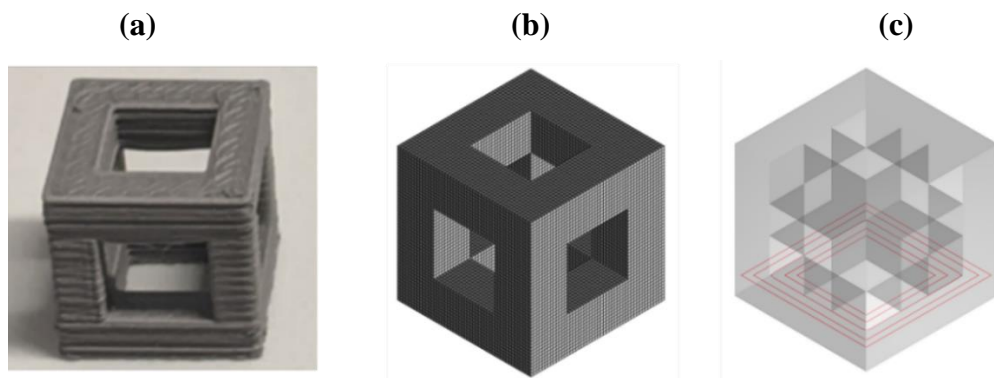


Figure C-III.1. Unit lattice cell (a) MF³ printed green part (b) voxel mesh (c) toolpath

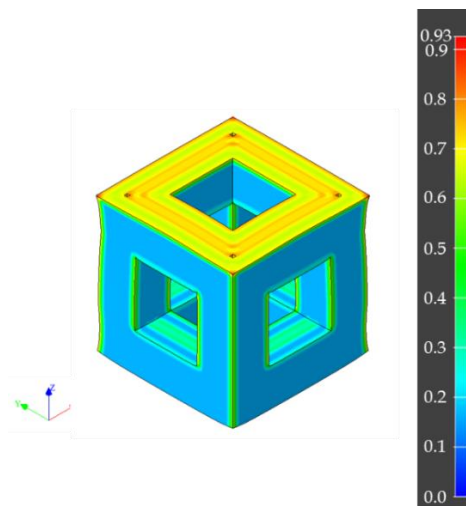


Figure C-III.2. Porosity estimation by Digimat-AM

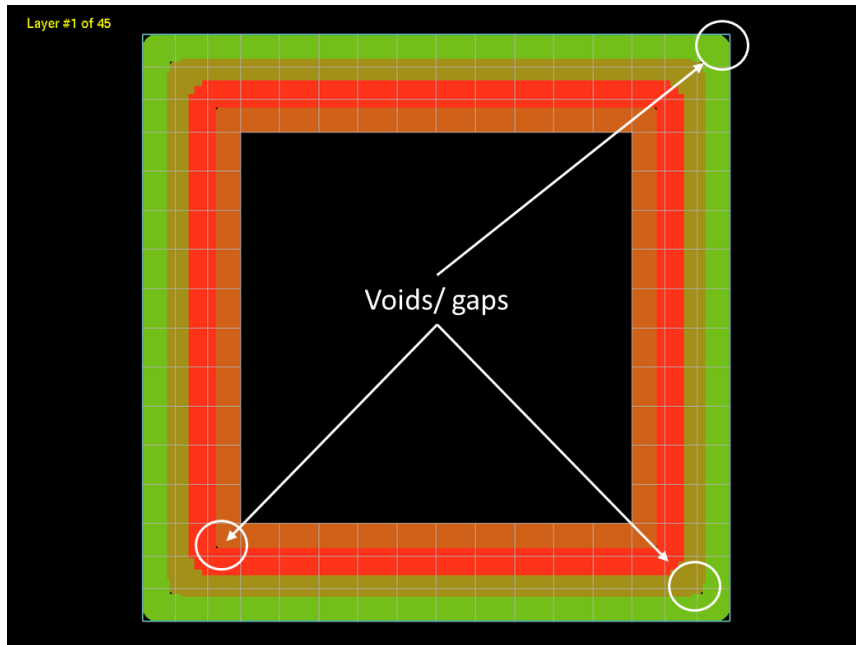


Figure C-III.3. PathCoverage results from GENOA: considerable voids/ porosity between tracks found at the corners within a single layer

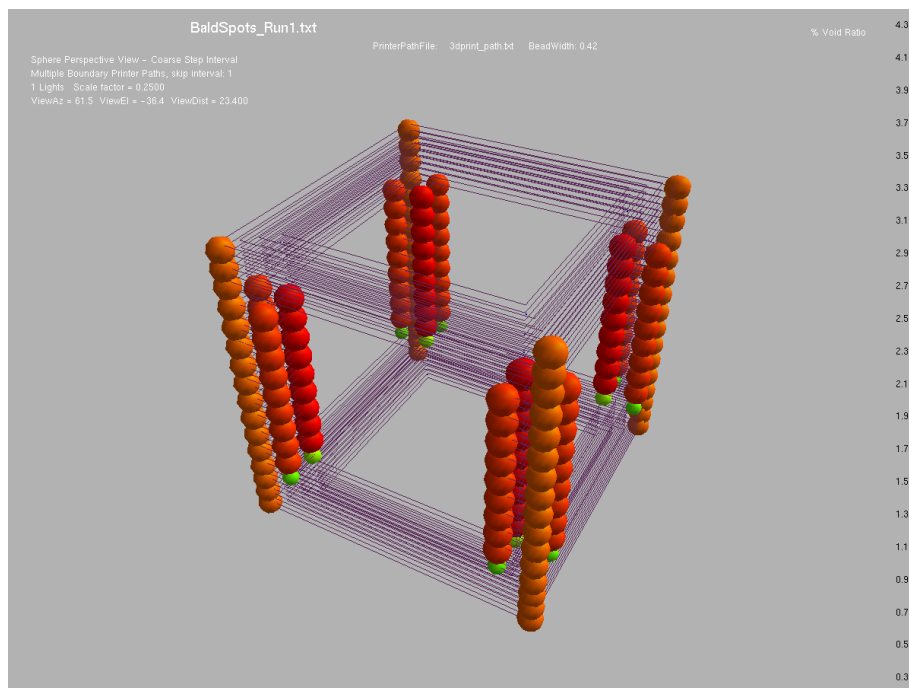


Figure C-III.4. EmptySpots results from GENOA: considerable voids/ porosity observed at the corners between tracks as well as between layers

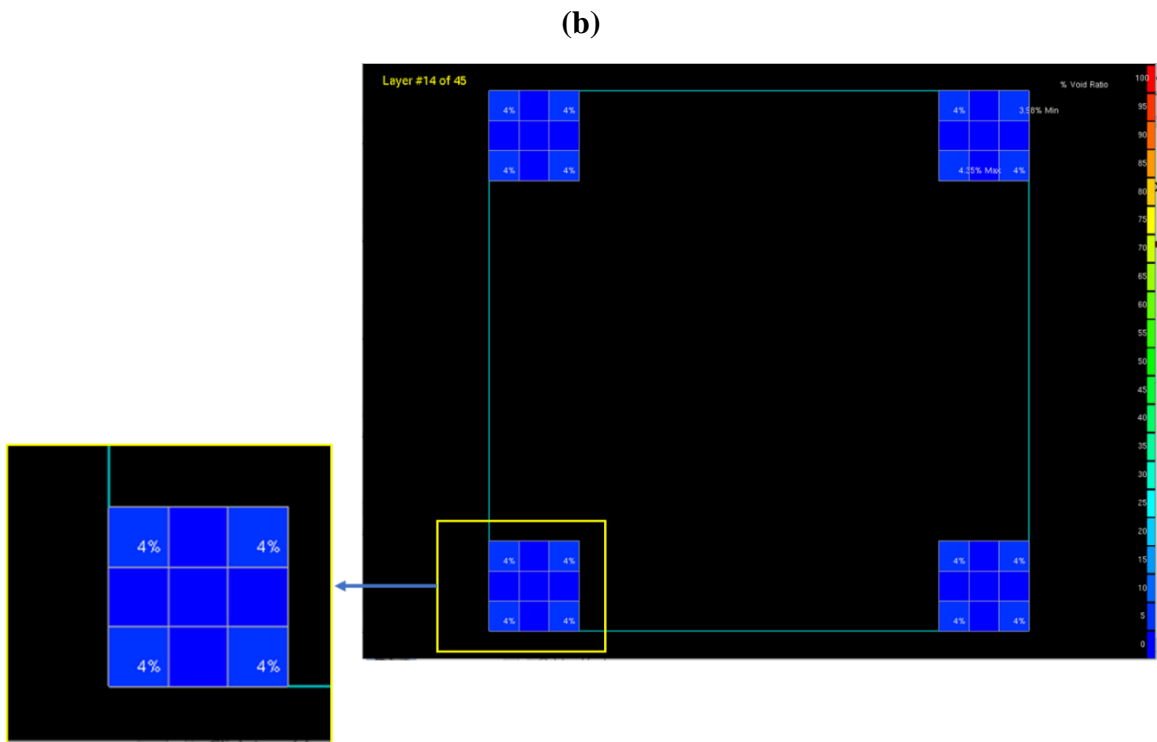
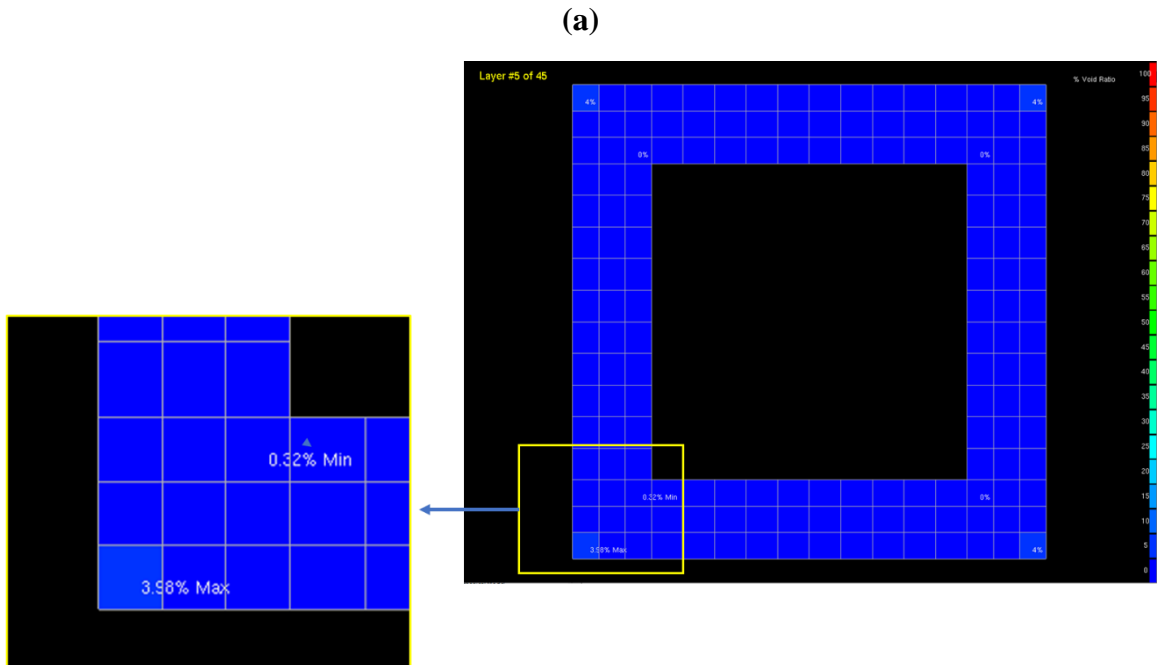


Figure C-III.5. VoidRatio results from GENOA: 0.3~4% voids observed at macro level (a) bottom of the unit cell (b) mid-section along the vertical axis

APPENDIX C-IV

MF³ SINTERING PROCESS SIMULATION: SIMUFACT ADDITIVE

This section presents the demonstration of the sintering simulations model developed through collaboration between MSC Software and the University of Louisville. A new module has been added in Simufact Additive simulation software and is presently being tested. This development underlines the extension of MF³ printing simulation to the sintering process.

➤ FULLY COUPLED THERMO-MECHANICAL ANALYSES

- *Phenomenological models based on continuum mechanics*
- *Thermo-viscoplastic formulations:* Linear viscous law to describe the shrinkage & deformation during sintering
- *Density of the green part considered homogeneous:* Inhomogeneous density distribution can predict anisotropic shrinkage accurately
- *Experimental data such as dilatation curve to determine the required parameters:* Sintering stress, bulk viscosity modulus, shear viscosity modulus, etc.

➤ PROCESS SIMULATION APPROACH

- Phenomenological
- Thermo-viscoplastic multi-physics to calculate the total strain, strain rate

- Densification, deformation is the net effect of combined local strains
- Important parameters include: Layer thickness, sintering temperature, sintering time, heating rate, binder saturation, friction between specimen & sintering plate

➤ INCLUDED PHYSICS

- Thermal gradients
- Diffusion process
- Grain growth
- Creep
- Surface tension effects
- Gravity and friction

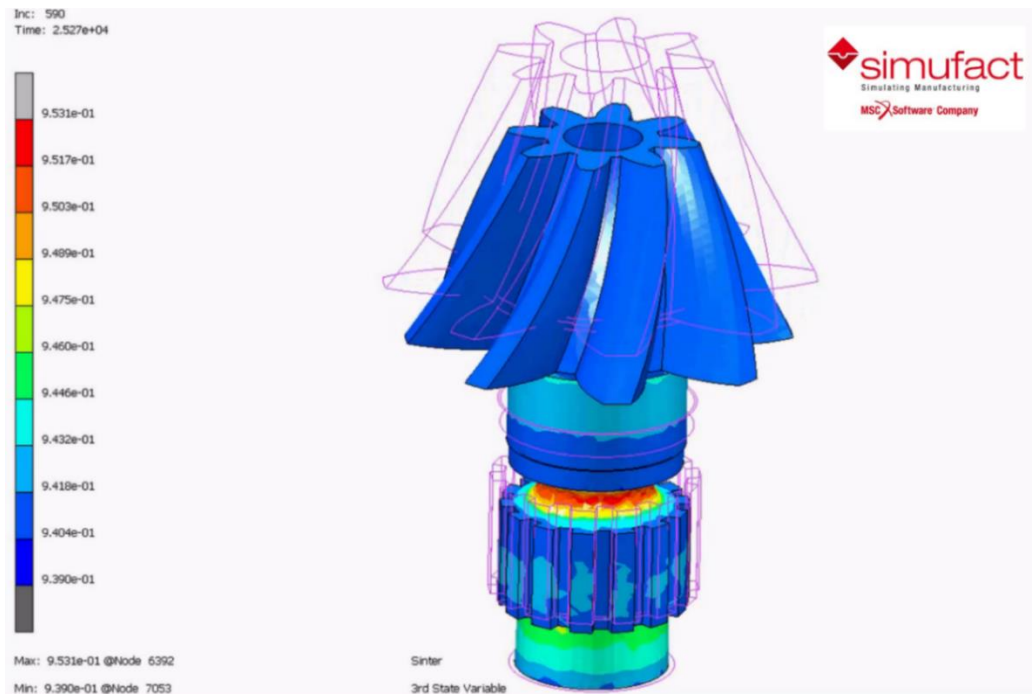


Figure C-IV.1. Shrinkage and distortion predicted by sintering simulation using Simufact
Additive: Helical Bevel Gear

➤ PREDICTION CAPABILITIES

- Shrinkage and distortion
- Relative density before and after sintering
- Gravity and friction effects
- Geometry compensation

Experimental validation and sensitivity analysis in progress.

➤ GEOMETRY COMPENSATION

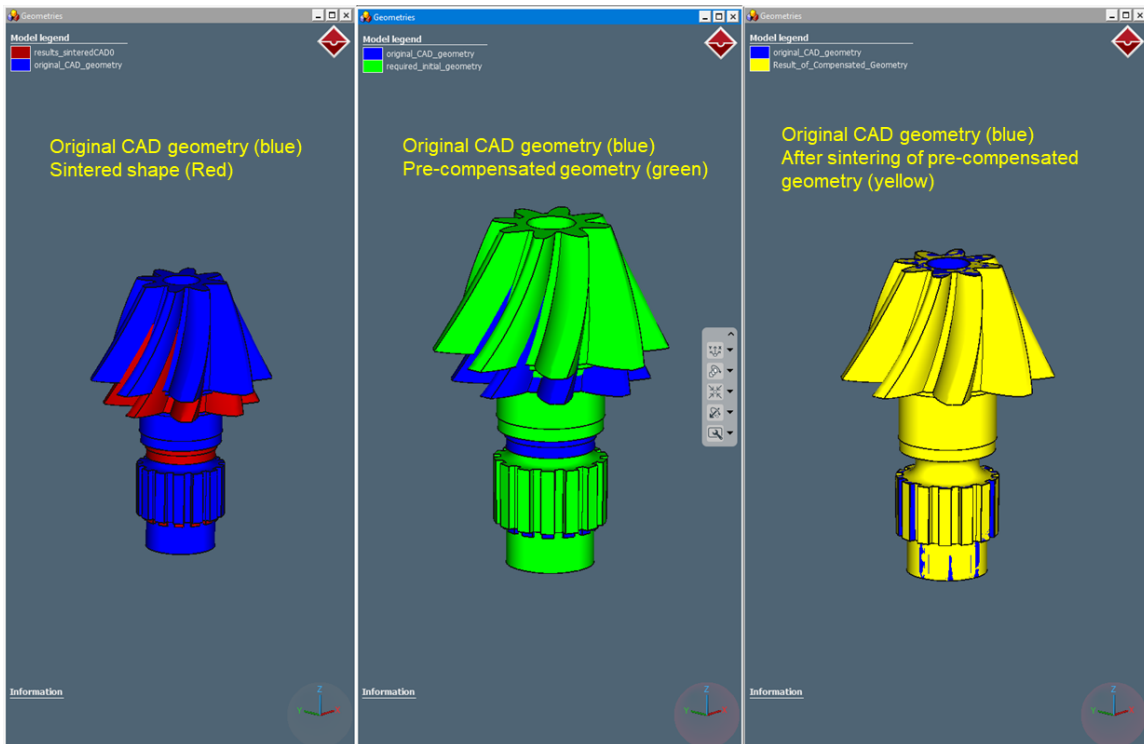


Figure C-IV.2. Geometry compensation taking into account the predicted shrinkage and distortions: (a)Original CAD geometry and after sintered geometry (b) pre-compensated geometry and original CAD geometry (c) final sintered shape of pre-compensated geometry and original CAD geometry

- Automated shape compensation in Simufact Additive to achieve the correct dimensions after shrinkage
- Geometry compensation achieved up to an accuracy of 97% (~ 1mm tolerance)
- Required 3 cycles to achieve the compensated geometry to the given tolerance

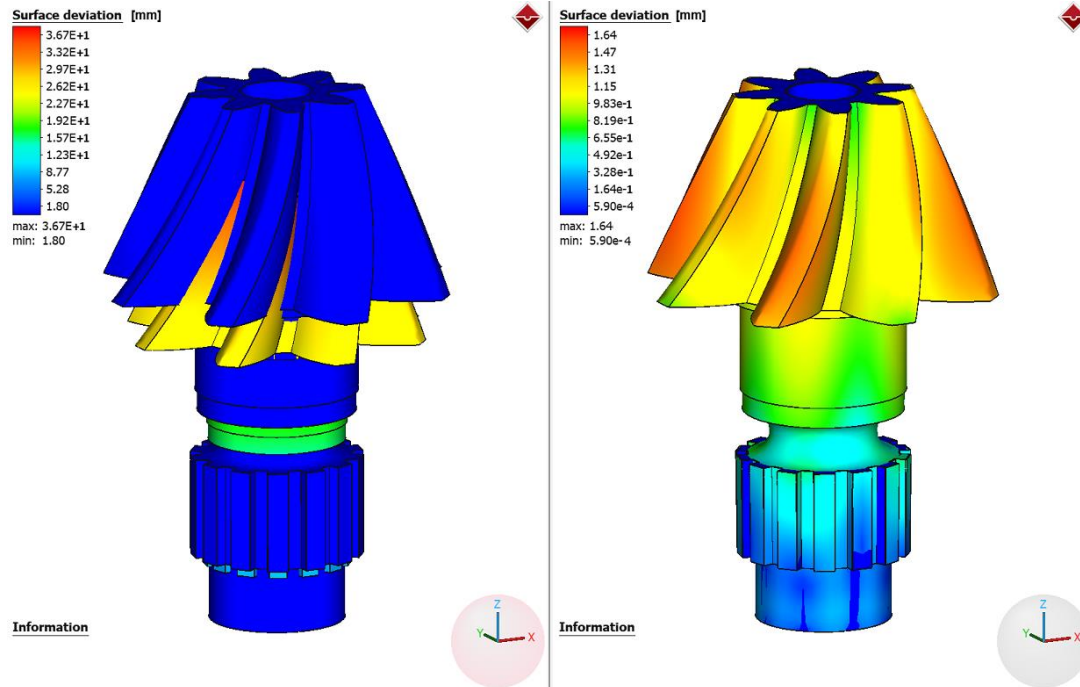
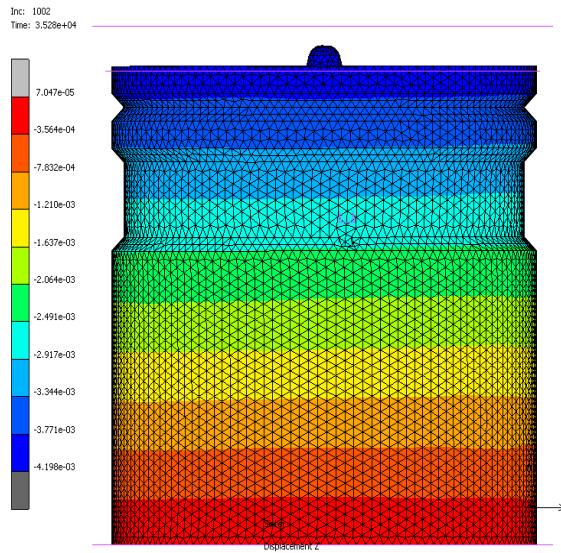


Figure C-IV.3. Comparison of surface deviation of the original CAD geometry with the after sintered shape (left) and original CAD geometry and after-sintered shape of pre-compensated geometry (right)

It is seen that the pre-compensated geometry matches with the original CAD geometry within a tolerance of ~ 1.6 mm.

➤ SHRINKAGE AND DISTORTION PROFILES

(a)



(b)

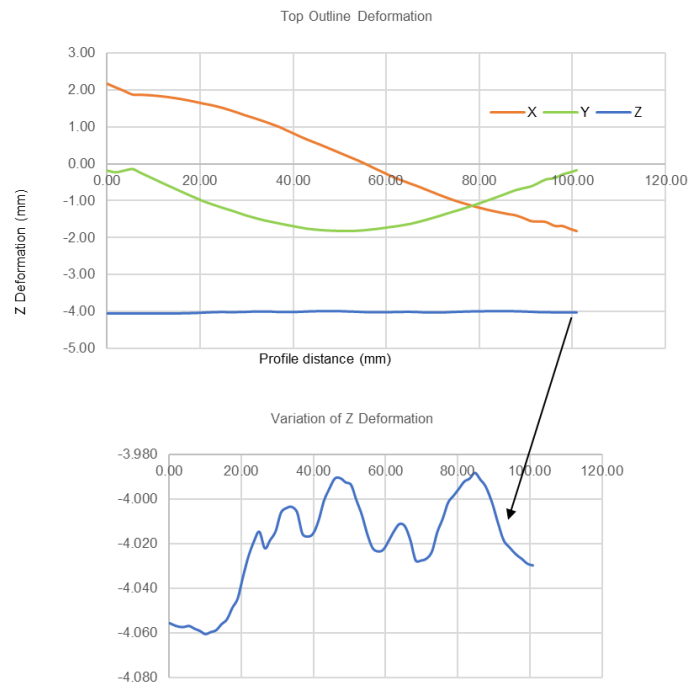


Figure C-IV.4. (a) Deformation along Z-axis (b) Deformation profiles at the top surface (half the circumference)

➤ FUTURE CAPABILITIES

- Residual stresses
- Microstructure

SUPPLEMENTARY DATA:

Table C-IV.1. Material properties input

Sr. no.	Description	Green Part	Sintered Part		Source
1	Young's modulus	170 MPa	110	GPa	Experiments
	Poisson's ratio	0.325	0.34		Literature
2	Temperature-dependent Young's modulus.	Table #4	Please see Table #5		Literature
3	Thermal expansion coefficient with temperature	Table #4	0.0000088	K ⁻¹	Literature
4	Specific heat capacity vs temperature	Table #4	560	J/kg·K	Literature
	Thermal conductivity vs temperature	Table #4	6.5	W/m·K	Literature
5	Viscosity	Table #4	NA	NA	NA
6	Relative density	98.50%	4.17306	g/cm ³	Experiments
7	Grain size	NA	140	micron (prior beta)	Experiments
8	Surface energy of the powder or the sintered part	NA	62	mN/m	Literature

Table C-IV.2. Validation experimental data

Sr. no.	Description	Data (Sintered Part)	Source
1	Measured shrinkage and distortion profiles	14%, 15%, 15.5% (X, Y, Z) for tensile bar	Experiments
2	Surface deviation measurement (if available)	Data not available	
3	Final relative density distribution (fully sintered part)	4.17306 g/cm ³	Experiments

Table C-IV.3. Sintering process parameters

Sr no.	Description	Data	Source
1	Sintering thermal cycle details	1250°C - 4hrs	Experiments
2	Surrounding atmosphere during sintering	0.15 torr, Argon purge	Experiments
3	Thermal distribution on the part	No data available	
4	Part geometry	ASTM E8 Tensile Bar	Experiments
5	Part placement in the furnace	No data available	
6	Gravitational force	1G	Experiments
7	Strain	No data available	

Table C-IV.4. Green part properties considered equivalent to that of Ti-6Al-4V feedstock

Temp. (°C)	Young's Modulus (MPa)	Temp. (°C)	CTE (1/°C)	Temp. (°C)	Specific Heat (mJ/t·°C)	Temp. (°C)	Thermal conductivity (mW/mm·°C)
23	205	23	2.83E-05	25	8.95E+08	43	1.466
		100	3.6E-05	30	9.40E+08	64	1.455
		140	4.37E-05	32	9.57E+08	84	1.504
		150	5.66E-05	49	1.11E+09	105	1.395
		160	6.18E-05	58	1.06E+09	125	1.411
		250	6.95E-05	111	8.00E+08	145	1.392
				170	8.25E+08	163	1.414

Table C-IV.5. Ti-6Al-4V feedstock viscosity

160C			170C		
Shear Rate (1/s)	Average Viscosity (Pa-s)	Std Dev	Shear Rate (1/s)	Average Viscosity (Pa-s)	Std. Dev.
20	634	34	20	546	4
40	567	22	40	490	6
80	445	11	80	400	0
160	352	5	160	310	3
400	253	3	400	216	2
800	193	3	800	166	1

Table C-IV.6. Sintered part - Young's modulus

Temperature (°C)	Young's Modulus (GPa)
20	106
100	102
200	96
300	90
400	85
500	79

APPENDIX C-V

MF³ PRINTING SIMULATION OF PARTS FROM NASA

MF³ printing some of the parts from NASA was simulated as part of the FabLab project. These simulation results were used in design analysis from a printing standpoint. NASA also wanted to conduct sintering simulations on these parts to predict the final part quality.

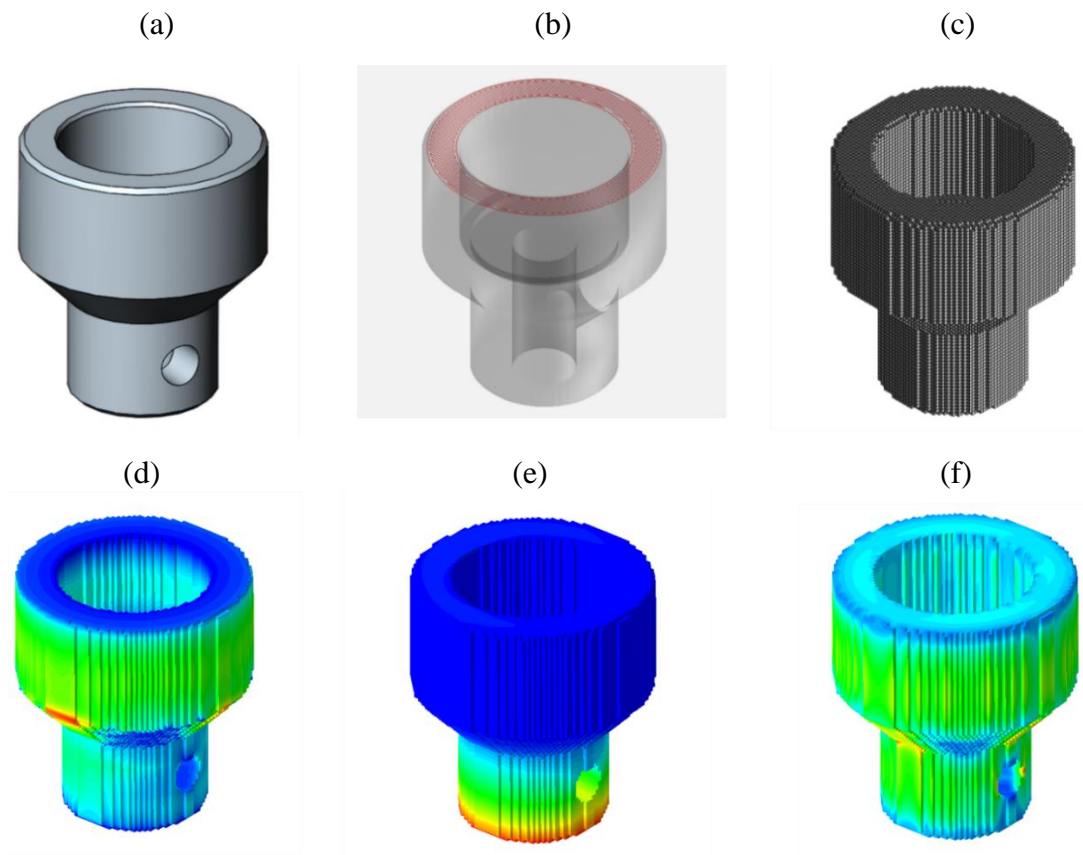


Figure C-V.1. Clutch adaptor (a) CAD in STL format (b) toolpath from slicer software imported in Digimat-AM (c) voxel mesh (d) residual stresses (e) thermal history (f) deformation

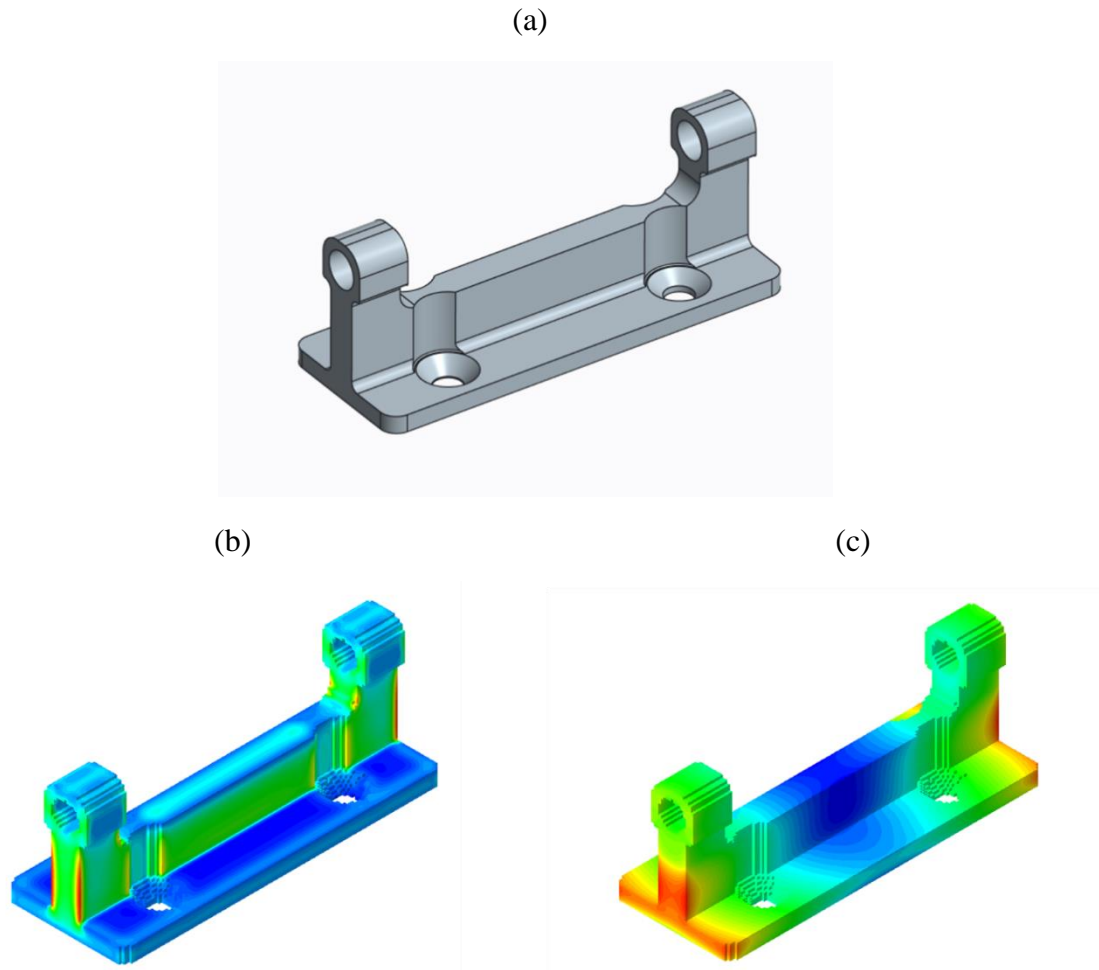


Figure C-V.2. Hinge base (a) CAD in STL format ((b) residual stresses (c) deformation

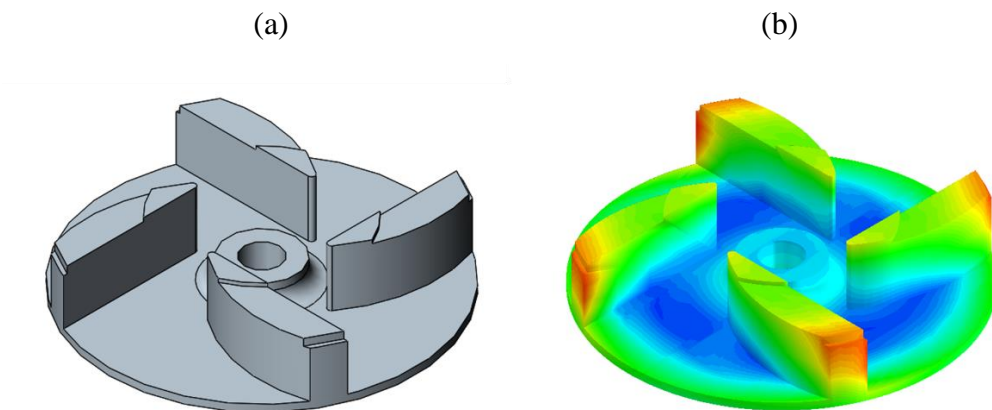


Figure C-V.3. Impellor (a) CAD in STL format (b) deformation

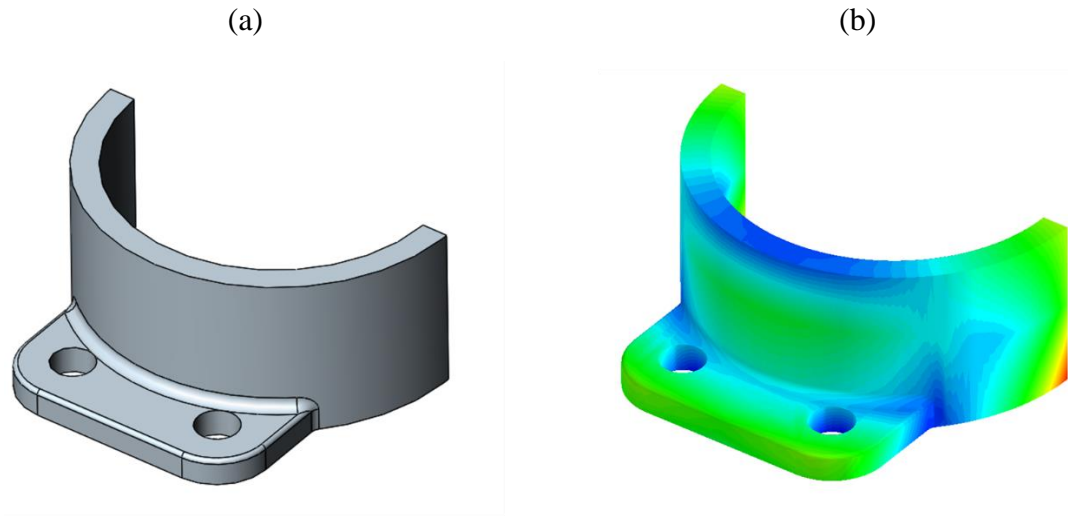


Figure C-V.4. Motor Support (a) CAD in STL format (b) deformation

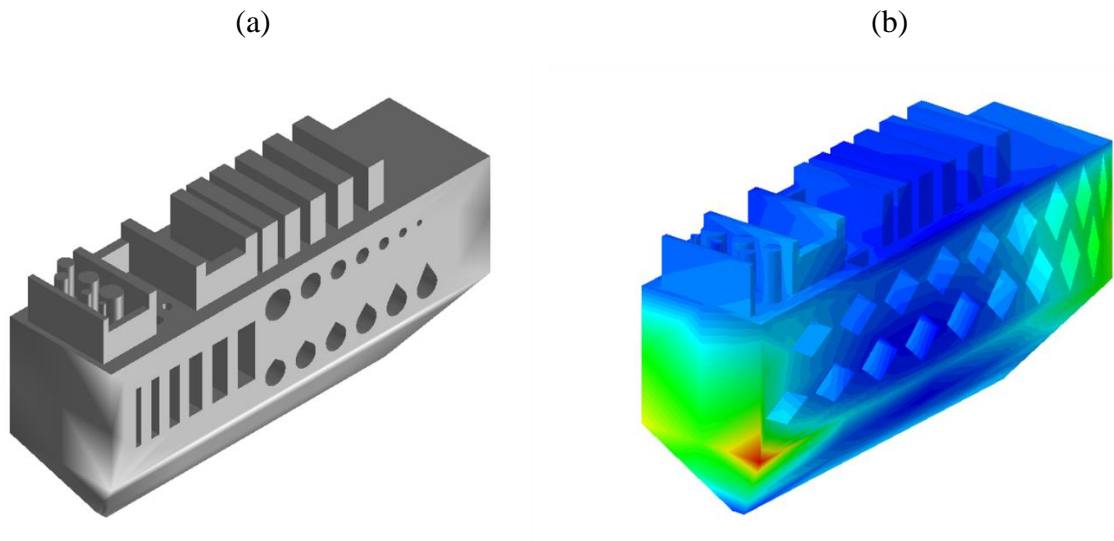


Figure C-V.5. Test artifact (a) CAD in STL format (b) deformation

CURRICULUM VITAE

Mohammad Qasim Shaikh

860 Pressing Drive,
Alpharetta, GA 30004, USA

jabbar.qasim@gmail.com
+1-803-493 2248

Application Development and Customer Technical Support (CTS) Manager with 12+ years of industrial experience in engineering polymers at BASF and Solvay, having expertise in Applications Development, Key Account Management (technical), Process Support/ Troubleshooting, Product Design, CAE/ FEA Simulations, Additive Manufacturing, Prototype Development and Testing, and Collaborative Project Management experience for a wide range of applications and markets in Automotive, E&E, Consumer & Industrial segments. Ph.D. Candidate at the University of Louisville in Mechanical Engineering specializing in Additive Manufacturing. New Business Development experience, MBA in Marketing.

Professional Experience

Company: 3D Systems, USA

Designation: Materials and Process Development Engineer (08/2020 – till date)
(R&D – Polymer Materials Engineering)

Roles and responsibilities:

- Supported materials and print process development for selective laser sintering (SLS) products involving thermoplastic polymers, polymer blends & polymer composites (such as PA12 GF, PP, PA6, CoPA, TPU)
- Tested various product formulations and identified feasible process window, evaluated mechanical performance to develop a Low-Cost PA12 GF solution
- Established SLS process settings for new materials via printing trials, specimen testing, properties validation, shrinkage calibration
- Conducted material testing like PSD, Bulk/ Tap Density, DSC, TGA, MFI, SEM, moisture content and other mechanical testing to establish optimal material and processing parameters
- Monitored material performance and evaluated material deterioration over multiple cycles of print process, and recommended recycling blend ratio.
- Hands-on experience with various platforms of 3D Systems polymer powder bed fusion machines (sPro 60, ProX 6100, ProX 500)
- Leveraged CAE simulations to predict SLS process outcome using Digimat-AM tool
- Provided guidance to technicians on build preparation, part printing, secondary operations, quality issues and troubleshooting
- Interacted and collaborated with Manufacturing, Hardware, Software, Product Management, Marketing & Sales

Institute: Materials Innovation Guild (MIG), University of Louisville, KY, USA

Designation: Research Assistant - Additive Manufacturing (01/2019 – 08/2020)

Additive Manufacturing (AM) research in polymer and metal, material-process-application development for AM, Design for AM (DfAM). Advanced research on material modeling, formulation development, compounding, filament extrusion and AM process simulation using Digimat to predict part quality and

performance. Hands-on experience in processing PA, PBT, ABS, TPU materials using SLS, FDM, MJF, SLA technologies.

Projects:

- **FabLab project:** Funded by NASA's in-space manufacturing initiative overcoming microgravity using MF³ with polymer-metal feedstock. Industrial collaboration with Techshot, nScript, DSH alongside NASA
- **Biomedical Probe:** Design and fabrication of a 3D printed device for intraoperative measurement and interpretation of bone strength during spinal surgery
- **Maxillofacial for Dental Implant:** Development of patient-specific maxillofacial implant by MF³ from patient's scanned data (DICOM)
- **End-of-Arm-Tooling (EoAT)** fabricated by AM for robotic automation on injection molding machine. Collaboration with industrial partner Bluestar Plastics (Tier1) and Toyota (OEM) for automotive mirror application
- **Collaboration with MSC Software** on multi-scale material simulation using Digimat to investigate material-process-properties interrelationships in AM
- Development and characterization of lattice structures by **Design for Additive Manufacturing (DfAM)** (collaboration with Politecnico di Milano, Italy)

Company: Solvay (Rhodia Polymers), India

Designation: Application Development & Customer Technical Support Manager (05/2015 – 01/2019)

Applications: Automotive (Under-the-hood, interior, exterior applications) and other applications in Consumer and Industrial segments

Roles and responsibilities:

- Managed AD & Customer Technical Support (CTS) team (4 members) in PePol GBU, India
- Managed technical resources/ services utilization for diversified customers (OEMs, GKAs, Tiers, Molders, Distributors) in line with business strategy
- Identified new opportunities and customer needs and provided solutions with differentiating technical and commercial value propositions via customer collaboration
- Provided technical support from concept or feasibility stage to material selection until commercialization stage of application development through PPAP
- Led metal-to-plastics replacement and VAVE projects with engineering solutions on material, design, simulation, process, testing validation (DVP & PVP) in line with customer needs
- Provided CAE simulation & design optimization support using Digimat, Ansys, Hypermesh
- Polymer processing support on injection molding, extrusion, blow molding, assembly operations (e.g., vibration welding, ultrasonic welding)
- Supported mold development through injection molding simulations (Moldflow), molding trials (T0, T1), process recommendations/ optimization and material qualification
- On-site customer support in handling material complaints and process troubleshooting
- Supported customer applications in proto development, proto testing (at Solvay labs)
- Coordinated on material testing like DSC, TGA, FTIR, MFI/ VI, SEM, UV, moisture content and other mechanical testing to address processing and product quality issues
- Led Solvay's Additive Manufacturing solution with Sinterline (PA6+GB40) for SLS
- Organized and led specific tech events/ tech shows/ tear-down activities with selected strategic customers to capture opportunities and reinforce the reputation of Solvay
- Responsible for managing key development projects funnel (Opportunity Pipe) through SFDC/ CRM tools, monthly review and follow up actions with internal teams
- Contributed to India business growth through New Market/ Business Development

Company: BASF, India (03/2008 – 05/2015)

Designation: Application Development/ CAE Engineer, Performance Materials BU

Applications: Automotive (Under-the-hood, interior, exterior applications) and other applications in E&E, Consumer and Industrial segments

Roles and responsibilities:

- Application Development and CAE simulations support for engineering plastic compounds of PA6, PA66,

- PBT, POM, TPU in Transportation, Consumer and Industrial segments
- Supported global technical centers as well as India business growth via R&D and customer projects, respectively
 - Supported techno-commercial feasibility study, material selection, design optimization, CAE simulations, part testing and validation (DVP & PVP), process establishment (PPAP)
 - Performed injection molding simulations (Moldflow), on-site molding trials (T9, T1), process troubleshooting
 - CAE studies/ design optimization using tools like Hyperworks, Abaqus, ULTRASIM
 - Collaborate with OEMs and Tiers for new development as well as VAVE opportunities for weight/ cost reduction through metal-replacement

Company: AurionPro Solutions (IIT Bombay), India (06/2007 – 03/2008)

Designation: CAE/ Application Engineer, Projects Division

- Design and analysis of Carbon Reinforced Composite Laminate structures
- Structural study of metallic CNG cylinder and development of composite cylinder
- Development of APDL for ply-by-ply composite analysis and fatigue life prediction
- Validation of FEAST Composite Analyzer using FEM

Educational Qualifications

Degree	Year	University	Grade
Ph.D. (Mech Engg)	-	University of Louisville, Kentucky, USA	3.94/4.0
MBA-Marketing	2013	Mumbai University, Mumbai, India	68%
Master of Tech. (Mech Engg –CAE/CAD/CAM)	2007	SRTM University, Nanded, India	CGPA-8.75/10
Bachelor of Engg. (Mech Engg)	2005	North Maharashtra University, Dhule, India	70.85%

Software Skills

FEA Tools: Digimat, Ansys, ABAQUS, RADIOSS, MoldFlow, Hypermesh, nTopology (Generative design), ULTRASIM, MMI

Other Tools: SolidWorks, Minitab, APDL, C++, MS Office

Accomplishments

Fellowship / Grant Awards

- MPIF grant recipient, Spring 2019
- GRA award at MIG, University of Louisville

Achievements:

- Exceptional Performance award at Solvay in 2016 & 2017
- Performance Appreciation award twice at BASF
- Represented India technical team at Global Exchange meetings at BASF and Solvay in Germany, France, China, Japan, Korea, Thailand and Vietnam
- Mentored high school kids in a workshop to develop engineering solutions to enable physically challenged individuals. The workshop was organized by Minority Business Development Agency (MBDA) of the US Department of Commerce to promote 3D printing